

LOW LOSS PASSIVE COMPONENT TECHNOLOGIES FOR HIGH PERFORMANCE
RADIO FREQUENCY CIRCUITS USING MICRO/NANO MACHINING

By

ARIAN RAHIMI

A DISSERTATION PRESENTED TO THE GRADUATE SCHOOL
OF THE UNIVERSITY OF FLORIDA IN PARTIAL FULFILLMENT
OF THE REQUIREMENTS FOR THE DEGREE OF
DOCTOR OF PHILOSOPHY

UNIVERSITY OF FLORIDA

2016

© 2016 Arian Rahimi

To my wife, Melina, and my family

ACKNOWLEDGMENTS

I would like to thank my Ph.D. advisor, Dr. Yong-Kyu Yoon, at the University of Florida; without his support, motivation, and, patience, this work never could have come true. I'm highly grateful to Dr. Yoon for editing all my publications and papers, even though there was a very short time to the deadlines, supporting me when coming up with new ideas and letting me feel like a manager working on multiple different projects, and supporting me to attend multiple conferences throughout my Ph.D. Also, I would like to thank my wife, Parisa (Melina) Tahafchi, and my family including my mom, Shahla Mohammadi, my dad, Asadollah Rahimi, and my sisters, Armita Rahimi and Rozita Rahimi, who continuously supported me in my Ph.D. life.

I would like to thank my committee members for editing, helpful comments and suggestions and valuable discussions including Dr. Yong-Kyu Yoon, Dr. Jianshan Lin, Dr. Brent Gila, and Dr. Toshikazu Nishida.

I would like to thank Dr. Aric Shorey, Corning Incorporated, for supporting us by providing the glass interposer substrates and the through glass via technology. Also, I'm grateful to the staff members in Nanoscale Research Facility (NRF), University of Florida Cleanroom, and Major Analytical and Particle Analysis Instrumentation Center (MAIC) who always were supportive and helped me on various trainings of the tools, troubleshooting, and microfabrication hints including Andres Trucco, David Hays, Bill Lewis, Dr. Brent Gila, Dr. Nicholas Rudawski, and Mr. Al Ogden.

This work never would have been possible without the help and support from my group members at the Interdisciplinary Microsystems Group (IMG) and Multidisciplinary nano and Microsystems (MnM) Laboratory at the University of Florida including Dr. David E. Senior, Dr. Cheolbok Kim, and all other members. Furthermore, I would like to thank Dr. David Arnold and

Mr. Camilo Velez for their assistance for letting us use their magnetic measurements setup and Dr. Jenshan Lin for high frequency measurements equipment. Also, I would like to thank Dr. Jing Wang, at the University of South Florida, for letting us use their VNA and high frequency test equipment.

This work is partially supported by NSF ECCS (1132413), in part supported by the Global R&D program of MOTIE/KIAT (N0000686), Korea, and in part supported by Corning Incorporated, USA.

TABLE OF CONTENTS

	<u>page</u>
ACKNOWLEDGMENTS	4
LIST OF TABLES	9
LIST OF FIGURES	10
LIST OF ABBREVIATIONS	19
ABSTRACT	21
CHAPTER	
1 INTRODUCTION	23
Motivation and Challenges	23
Frequency Bands and Requirements for Future Communication Systems	26
Ferromagnetic Materials in Radio Frequency Systems	27
Proposed Solutions, Research Objectives and Contributions	28
Dissertation Organization	32
2 BACKGROUND AND ANALYSIS.....	33
The Sources of Loss in Microwave Regime.....	33
Towards RF Loss Reduction	36
RF Loss Studies Using an Analytical Model for RF Inductors	39
The First-Generation RF Inductors in CMOS Process	44
The Conductor Loss and Ohmic Loss Reduction in Microwave Regime	48
Ferromagnetic Materials	52
Summary	58
3 LOW LOSS RADIAL CONDUCTORS FOR RF COMPONENTS	59
The Proposed Cylindrical Radial Superlattice Conductor Architecture	60
Simulations and Modeling of the CRS Unit Cell	62
The Effect of Layer Thickness on Resistance Spectra	66
The Radial Inductors Using the CRS Conductors	69
The CRS Conductors Using Electrodeposition	70
The CRS Conductors Using Physical Vapor Deposition	77
Analysis and Design	78
Microfabrication and Measurement Results	80
Summary	85
4 LOW LOSS PLANAR CONDUCTORS FOR RF COMPONENTS.....	86

Study on Width and Thickness of the Planar Superlattice Conductors	86
Analysis and Simulation Results	87
Fabrication and Experimental Results.....	89
Planar Superlattice Conductors Using Cu/Ni Multi-Layer Structure	94
Inductor Design	94
Fabrication and Experimental Results.....	95
Cu/Ni Multi-Layer Devices with Magnetic Alignments	97
Planar Superlattice Conductors Using Cu/NiFe Multi-Layer Structure	98
Summary.....	101
5 MAGNETIC FIELD EFFECT TRANSCONDUCTORS	102
Theory.....	102
Design and Analysis	105
Skin Depth in Ferromagnetic Materials and μ_r -Frequency Relationship	106
M-FET Conductor Architecture	107
Tunability Using an External DC Magnetic Field.....	109
Comparison of M-FET and MOSFET.....	110
Material Characterizations.....	112
Effect of Ferromagnetic Material on Resonance Frequency Tunability	118
Physical Characterizations.....	120
Fabrication and Experimental Results	123
RF Measurements	126
The Effect of Ferromagnetic Material	127
Measurement Results.....	129
The Effects of the Layer Thickness.....	133
The Effect of Line Width	137
Applied Magnetic Field in Hard Axis	138
Summary.....	139
6 LOW LOSS DIELECTRIC MATERIALS FOR RF COMPONENTS	140
Introduction.....	140
Implemented Passive Components on LCP	142
Substrate-Integrated Waveguide Structures	142
Filter Design Methodology.....	144
External Quality Factor	144
Internal Coupling Coefficients	145
Two-Pole and Three-Pole Filter Implementation	146
Implementation and Experimental Results.....	147
Implemented Passive Components Using BCB	150
Implementation and Experimental Results.....	151
Summary.....	154
7 PACKAGING AND INTERPOSER TECHNOLOGY	155
Proposed Packaging Schemes.....	156

Wire Bonding	156
Interposer Technology.....	156
TGV Technology and Proposed Microfabrication Processes.....	160
Photosensitive Glass Interposer.....	160
Corning Glass Interposer	161
Glass Interposer Characterizations	163
Ring Resonator Design.....	164
Glass Characterization.....	165
Micromachined Components on Corning Glass Substrates	168
Resonator Design.....	169
Bandpass Filter Design.....	171
Fabrication and Experimental Results.....	172
Towards Compactness for Higher Integration.....	174
Ultra-Compact Multi-Layer Micromachined Components on Corning Glass Substrates	176
Design and Simulations	176
Fabrication and Experimental Results	178
In-Substrate Resonators and Bandpass Filters with Improved Insertion Loss in K-band	180
Design and Characterization.....	181
RF Passive Components Design in K-Band.....	184
Fabrication and Measurement Results.....	187
Dual-Band Passives Using Cu/NiFe Conductors	193
Summary.....	197
8 CONCLUSIONS	198
LIST OF REFERENCES	202
BIOGRAPHICAL SKETCH	207

LIST OF TABLES

<u>Table</u>		<u>page</u>
2-1	The summary of the CMOS implemented inductors in 0.5 µm CMOS process and their dimensions.....	46
3-1	The comparison of common manufacturing metals and their electrical/mechanical properties.....	59
3-2	The composition of the utilized Ni ₈₀ Fe ₂₀ electrolyte.....	72
3-3	Comparison of the state-of-the-art inductors with multilayer conductors.....	77
4-1	The state-of-the-art comparison of multi-layer conductors.....	94
5-1	The skin depth, δ, comparison in different frequencies. The units are in [µm].....	106
5-2	The comparison of the MOSFET and the proposed M-FET.....	112
5-3	Comparison of the material properties of pure Ni and Ni ₈₀ Fe ₂₀	120
6-1	The comparison of some common manufacturing dielectric materials.....	140
6-2	The summary of design parameters for the bandpass filters on LCP.....	147
6-3	The summary of design parameters for the bandpass filters using BCB.....	151
7-1	Dimensions of the implemented ring resonators using the glass interposer layer.....	165
7-2	The extracted characterization data for Corning SGW3 glass.....	168
7-3	Summary of dimensions of the designed RF components in [mm].....	172
7-4	Summary of design parameters for the RF passive components. The given dimensions are in mm.....	187
7-5	The summary of insertion loss values for the passive resonators and bandpass filters using Cu/NiFe and reference Cu conductors.....	196

LIST OF FIGURES

<u>Figure</u>		<u>page</u>
1-1	The illustration of motivation on higher operation frequencies.....	24
1-2	The electromagnetic spectrum with the magnified RF range and frequency bands defined by IEEE	26
1-3	The proposed passive component technologies for implementation of high performance RF circuits and systems.	198
1-4	The components of an RF heterodyne system and the level of integration of each component.....	29
2-1	The equivalent circuit lumped-element models for integrated inductors. A) Simple one-port model, B) the π -model, C) the π -model assuming a conductive substrate, and D) the π -model with a non-conductive substrate.	41
2-2	The demonstration of skin effect in a conductor handling ac current.....	42
2-3	The simulation results of the Q-factor of a 1-nH inductor assuming a shunt parasitic capacitance of A) 1 pF, B) 0.5 pF, and C) 0.1 pF.	43
2-4	The 3D schematic view of the inductors in ANSYS HFSS v. 15.0. A) A 10-turn one-port inductor, B) a 3-turn two-port inductor.	45
2-5	The optical micrographs of the implemented inductors in 0.5 μm CMOS process.....	45
2-6	The comparison of the simulations and measurement results of the spiral inductor in 0.5 μm CMOS process with 10 number of turns.	47
2-7	The main sources of RF loss reducing the Q-factor of the integrated inductors in 0.5 μm CMOS process using the cross section view.....	47
2-8	The planar superlattice conductors with alternating ferromagnetic/non-ferromagnetic thin films.	50
2-9	The comparison between the ohmic resistances of a single-layer (solid) conductor vs. a multi-layer (superlattice) conductor in microwave regime. The insets show the schematic of the conductors with the resulting current distribution in their cross section.	51
2-10	The typical hysteresis loop of a ferromagnetic material where the easy and hard axes are shown.	52
2-11	The RF applications of ferromagnetic materials as thin films.....	53

2-12	The calculated permeability values. A) Ni ₈₀ Fe ₂₀ assuming no external magnetic field. The inset shows the real part, μ' , for the frequency between 12 to 16 GHz, B) the calculated real part of the permeability for different external magnetic fields.....	56
3-1	The schematic of superlattice conductor unit cells. A) The planar, B) the cylindrical radial superlattice conductor. The t_N and t_F are the thickness of the nonferromagnetic and ferromagnetic thin film layers, respectively.....	60
3-2	The illustration of eddy currents in a radial conductor carrying high frequency current	61
3-3	The simulation models. A) The two-port CRS conductor under study, B) the equivalent lumped element circuit model of the CRS conductor.	63
3-4	The resistance of a CRS conductor.....	64
3-5	Current distribution of the 16-layer Cu/Ni ₈₀ Fe ₂₀ CRS conductor (solid lines) with 125 nm Cu and 50 nm Ni ₈₀ Fe ₂₀ and its solid Cu reference (dashed lines) at the frequencies: A) 6 GHz, B) 10 GHz, C) 15 GHz, and D) 25 GHz.....	65
3-6	The conductors with different number of layers. A) The schematic view, B) the resistance spectra of CRS conductors with the different number of layers, with the same total diameter dimension and the same thickness ratio of Cu/ Ni ₈₀ Fe ₂₀ of 4:1.....	67
3-7	Resistance spectra of CRS conductors with the different thickness ratio of Cu/Ni ₈₀ Fe ₂₀ and the same total diameter dimension.....	68
3-8	The resistance spectra of a CRS conductor.....	68
3-9	The simulation results of the air-lifted radial inductors.....	69
3-10	The microfabrication process steps for the CRS conductors made of Cu/NiFe layers using a gold conductor core.	71
3-11	The optical micrographs of the fabricated radial inductors with different shapes. A) Prior to multi-step electroplating, B) after deposition of 160 nm NiFe, C) after deposition of 400 nm Cu.....	72
3-12	The SEM micrograph of the gold wire. A) Prior to electroplating process, B) after 21 layers of Ni ₈₀ Fe ₂₀ /Cu (160 nm/400 nm) electroplating, and C) cross section view of the CRS conductors in SEM.	73
3-13	The SEM of the air-lifted radial inductors with A) L=0.5mm, and B) L=1.5mm.....	74
3-14	The measurement results of the A) extracted inductance and resistance of the CRS conductor compared to the reference solid Cu conductor, and B) quality factor	75

3-15	The estimated real part (solid line) and imaginary part (dashed line) of the permeability spectra of a Ni ₈₀ Fe ₂₀ thin film in the frequency range of 0 to 20 GHz.....	76
3-16	The measurement results of the 1 mm long CRS and regular wire inductors, A) the measured inductance, and B) the measured Q-factor.	77
3-17	The cylindrical radial superlattice conductors. A) Full CRS conductor, B) the proposed hybrid cylindrical radial superlattice (<i>h</i> -CRS) conductor. Gray and white colors denote the ferromagnetic and non-ferromagnetic thin films, respectively	79
3-18	The concept of the dual-band improved Q-factor using a hybrid conductor consisting of the lower regular solid conductor for the first band and the upper superlattice conductor for the higher band.	79
3-19	The comparison of the CRS conductors.	80
3-20	The fabrication process for CRS inductors utilizing Cu/NiFe conductors. The insets show the schematic of the directional sputtering and the detailed TEM cross section view of multiple metallic stacked thin films making the pads.....	81
3-21	The SEM micrographs of the two-port inductors using Cu/NiFe nano-superlattice conductor architecture with L = 2 mm.....	82
3-22	The measurement results of the <i>h</i> -CRS inductor.	83
3-23	The measured Q-factor of the fabricated air-lifted <i>h</i> -CRS conductor-based inductor with L = 2 mm.	84
4-1	The schematic of the coplanar waveguide (CPW) transmission line.	87
4-2	The current distribution into the volume of the conductors. A) At an ECC frequency of 13 GHz, B) comparison of two multi-layer conductors with the same thickness ratio of t _{Cu} /t _{Ni} = 6 (same ECC operation frequency) but different film thicknesses.....	88
4-3	The simulation results of the RF ohmic resistance of two conductor unit cells, A) Cond_1 t _{Cu} = 150 nm, t _{Ni} = 25 nm, and B) Cond_2: t _{Cu} = 600 nm, t _{Ni} = 100 nm.....	89
4-4	The planar transmission lines using optimized superlattice conductors. A) The fabrication process B) the SEM micrographs of the fabricated transmission lines and interconnects where M shows the direction of magnetization.....	90
4-5	The magnetic characterization measurement results of 10 layers of Cu/Ni (150nm/30nm).....	91
4-6	The two-port planar transmission lines. A) Schematic of the ohmic resistance extraction method, B) the device under test.....	91

4-7	The measurement results of the fabricated transmission line with W=60 μm . A) The extracted ohmic resistance and the corresponding solid reference Cu conductor, B) the TEM micrographs of the nano-machined conductor's cross sectional view	92
4-8	The measurement results of the CPW transmission lines with W=30, 50, and 60 μm . The black dashed lines show the corresponding reference Cu conductor with W=30 μm	93
4-9	The two-port planar inductor. A) The schematic of the inductor and its cross section with r = 400 μm , D = 280 μm , and W = 60 μm , B) the fabrication process.	95
4-10	The SEM micrographs. A) The series of the fabricated high performance inductors with various dimensions and shapes using low loss multi-layer conductor, B) with different widths of the signal line.	96
4-11	The measurement results. A) The measured series resistance and B) inductance of the multi-layer and reference Cu inductors.....	97
4-12	The measured Q-factor of the fabricated planar inductors made of multi-layer and reference Cu versus frequency.....	97
4-13	The measurement results of the series resistance of the inductor after magnetic alignment of Ni films. A) Measured series resistance, B) inductance, and C) Q-factor.	98
4-14	The fabricated inductor using Cu/NiFe (360 nm/30 nm) on Corning glass substrate. A) The SEM micrograph of the device, B) the extracted ohmic resistance, C) the extracted inductance, and D) the extracted Q-factor.	100
4-15	The effect of number of substrate on the extracted ohmic resistance. A) The SEM micrograph of the fabricated CPW transmission line, B) the extracted ohmic resistance.....	100
5-1	The illustration of the movement of a magnetic moment under an applied magnetic field. A) Without damping with Larmor frequency, B) precessing damped movement of the magnetic moment trying to align to external magnetic field.	104
5-2	The theoretical permeability spectra of a Ni ₈₀ Fe ₂₀ thin film with a thickness of 30 nm before and after application of an external magnetic flux of 60 mT.	107
5-3	The proposed magnetically tunable superlattice conductor.....	108
5-4	The imaginary part of permeability expected by Kittel formula where the peak point values of the permeability versus operation frequency are shown.	110
5-5	The schematics comparing the regular FET and the proposed M-FET. A) The cross section view of the regular FET transistors working based on an applied E-field, B)	

the proposed M-FET where an H-field is applied for realization of tunable nano-superlattice conductors.....	112
5-6 The measurement results of B-H loops of a single layer Ni thin film with different thicknesses.	114
5-7 The B-H loop measurement results of the Cu/Ni multi-layer conductors.	115
5-8 The comparison of measured coercivity fields of Ni ferromagnetic thin films with different deposition thicknesses.....	115
5-9 The B-H loop measurement results of Cu/NiFe conductors of 10 and 15 layers.	116
5-10 The comparison of Cu/Ni and Cu/NiFe conductor samples with 10 number of layers and the same thicknesses of 180 nm/30 nm.....	117
5-11 The B-H loop measurement results of the Cu/NiFe samples. A) 10 layers with Cu/NiFe of 180 nm/60 nm, B) 10 layers with Cu/NiFe of 360 nm/30 nm.	117
5-12 The magnetic characterization B-H loops (upper) and theoretical permeability spectra (lower)	119
5-13 The TEM micrographs of the cross section view of the deposited multi-layer conductors.....	121
5-14 The zoomed in version of the Cu/NiFe of 180 nm/30 nm conductor sample on SGW3 Corning glass substrate.	122
5-15 The EDX characterization results of Cu/NiFe. A) Conductor of 360 nm/30 nm thickness, B) conductor of 180 nm/60 nm thickness.	123
5-16 The microfabrication process of the M-FETs. A) Method I using lift-off process, B) method II using wet etching process.....	124
5-17 The optical micrographs of the fabricated M-FETs. A) The devices which are made using a lift-off process, B) the edge of the conductor using the over-developed photoresist after the lift-off process.	125
5-18 The SEM micrographs of the fabricated transmission lines with a length of 2.0 mm. A) Width, W = 60 μm , B) W = 30 μm , and C) the detailed view of conductor's feeding line with 90° rotated angle.	125
5-19 The test setup for RF measurements of M-FETs using VNA.....	126
5-20 The actual measurement platform and device-under-test (DUT) under an applied DC magnetic field.....	126
5-21 The measured extracted resistance of the transmission lines before and after DC magnetic field of 0 and 100 Oe. A) Cu/Ni conductor, and B) Cu/NiFe conductor.	127

5-22	A) The measurement results of the extracted resistance of the Cu/Ni ₈₀ Fe ₂₀ (150 nm/25 nm) transmission lines with various DC magnetic fields, B) the SEM of the transmission lines with the direction of the applied magnetic field which is indicated.	.130
5-23	The peak point values versus applied magnetic field.	130
5-24	The correlation of the LLG theory and the measured samples with Cu/Ni ₈₀ Fe ₂₀ (150 nm/25 nm) in terms of the peak of the ohmic resistance near f_{FMR} .	131
5-25	The extracted ohmic resistance of the M-FET with Cu/Ni ₈₀ Fe ₂₀ (150 nm/25 nm) versus applied magnetic field. A) At 2.4 GHz, B) at 5.8 GHz.	132
5-26	The ferromagnetic nano-layers affecting neighboring Cu layers in Cu/NiFe superlattice conductors, showing two paired layers for each.	133
5-27	The measurement results of the M-FET conductors. A) The extracted ohmic resistance versus frequency given an applied DC magnetic field of 550 Oe, B) the schematic of the conductors.	134
5-28	The SEM micrographs of the M-FET conductors	135
5-29	The tunability of the M-FET conductors. A) The M-FET 2 with Cu/NiFe (360 nm/30 nm), B) the M-FET 3 with Cu/NiFe (180 nm/60 nm).	136
5-30	The comparison of the M-FET conductors with different signal width, W	137
5-31	The effect of applied magnetic field in hard axis. A) The measurement results of the ohmic resistance of Cu/NiFe (360 nm/30 nm) M-FET, B) demonstration of the applied DC magnetic field in the direction of magnetic moment.	138
6-1	E-Field for the quasi-TE ₁₀₁ mode.	143
6-2	Frequency responses of the conventional QMSIW and the CSRR-loaded QMSIW cavities. Geometrical parameters are $L_Q = 1$ mm, $w_s = 0.26$ mm. A microstrip 50 Ω feeding line is used to excite the cavity.	145
6-3	The illustration of electromagnetic coupling between two identical resonators [36].	146
6-4	The schematic of the designed bandpass filters for 25 GHz frequency band, A) Two-pole bandpass filter, B) three-pole bandpass filter.	146
6-5	The fabrication process flow for the bandpass filters on LCP.	148
6-6	The SEM micrographs of the fabricated bandpass filters on LCP. A) two-pole filter, B) three-pole filter.	149
6-7	The Simulated and measured results of the implemented bandpass filters on LCP. A) Two-pole filter, B) three-pole filter.	149

6-8	The field distribution graphs. A) QMSIW module before at resonance (102 GHz), B) the QMSIW loaded with a CSRR structure with resonance at 60 GHz.....	150
6-9	The fabrication process flow of the broadband bandpass filters using BCB	153
6-10	The microfabricated bandpass filters for 60 GHz band. A) two-pole bandpass filter, B) three-pole bandpass filter.....	153
6-11.	The measurement results of A) Two-pole filter, B) three-pole filter. Less than 2 dB insertion loss is obtained in the passband.	154
7-1	The interposer-based packaging scheme for integration of RF components (off-chip) and other components (integrated on-chip) of a system front-end using glass interposer and through glass vias (TGV's).	157
7-2	The different types of device implementation using glass interposer technology.....	158
7-3	The fabrication process flow for the photosensitive glass.	160
7-4	The series of laser-machined TGV's on Corning SGW3 50 mm × 50 mm with a TGV diameter of 100 μm.....	161
7-5	The microfabrication process using the Corning glass substrates.	162
7-6	The SEM micrographs of a single TGV before and after thick metallization. A) The TGV before metallization, B) seed layer deposition and subsequent electroplating through the TGV.	163
7-7	The ring resonators. A) The schematic of the ring resonator for electrical characteristics extraction of the utilized glass interposers, B) the fabricated device with the magnified view of the electroplated TGV.	164
7-8	The measurement results of the insertion loss. A) RR_1 up to 40 GHz, and B) RR_2 & RR_3 up to 50 GHz. The inset in A shows the fabricated ring resonator RR_1.	167
7-9	The schematic view of the CSRR-loaded HMSIW resonator on glass interposer layer and its dimensions.....	170
7-10	The simulation results of the CSRR-loaded HMSIW resonator. A) The S-parameters versus frequency, B) the electric field distribution at resonance.	171
7-11	The schematic of the two-pole bandpass filter based on mutual coupling of two CSRR resonators.....	172
7-12	Optical micrographs of the fabricated 2.4 GHz devices. A) The CSRR-loaded resonator, B) the 2-pole bandpass filter.	172
7-13	The simulation and measurement results of the CSRR-loaded HMSIW resonator. A) The 2.4 GHz band, B) 5.8 GHz band.....	173

7-14	The SEM images of the fabricated resonator for the 5.8 GHz frequency band.....	174
7-15	The simulation and measurement results of the 5.8 GHz 2-pole band-pass filter.	174
7-16	The simulation and measurement results of the 5.8 GHz double-ring CSRR-loaded HMSIW resonator.....	175
7-17	The schematic and lumped-element equivalent circuit of a CSRR-loaded HMSIW resonator for 5.8 GHz band.....	176
7-18	The schematic and lumped-element equivalent circuit of a CSRR-loaded HMSIW multi-layer and ultra-compact resonator for 5.8 GHz band.....	177
7-19	The proposed ultra-compact resonator. A) The cross section view of the multi-layer resonator, B) the bottom 3D view.....	177
7-20	The simulation results of the CSRR-loaded HMSIW multi-layer 5.8 GHz resonator.....	178
7-21	The fabrication process flow for the ultra-compact multi-layer resonators.....	179
7-22	The front view of the microfabricated 5.8 GHz resonator. A) The optical view after first mask, B) the optical view after simultaneous electroplating of top and bottom sides.....	180
7-23	The optical micrographs of the fabricated TGV's by Corning with 80 μm diameter. A) The front-side view, B) the back-side view of the interposer substrate.	182
7-24	The extracted measurement results of the glass electrical properties up to 30 GHz.	182
7-25	The simulation results of the planar Cu/NiFe (360 nm/30 nm) multi-layer (superlattice) conductor and the corresponding reference copper conductor in ANSYS HFSS v. 15.0.....	184
7-26	The schematic of the two-pole bandpass filter.	186
7-27	The microfabrication process for passive resonators and bandpass filters using Cu/NiFe conductors.	187
7-28	The SEM micrographs of the passive RF components.....	189
7-29	The measurement results of the resonator for 18 GHz band	190
7-30	The measurement results of the bandpass filter for 18 GHz band.....	192
7-31	The measurement results of the resonator for 25 GHz band. A) The comparison of the resonator made of solid Cu and Cu/NiFe conductors, B) the comparison of the insertion losses in the passband.	193

7-32	The dual-band capacitively-loaded HMSIW resonator. A) Simulation schematic, B) simulation results, and C) the equivalent circuit model.....	194
7-33	The SEM micrograph of the fabricated dual-band resonator for 18 GHz band.....	195
7-34	The measurement results of the dual-band resonator for 12 and 19 GHz band.....	196
8-1	The proposed passive component technologies for implementation of high performance RF circuits and systems.	198

LIST OF ABBREVIATIONS

Ag	Silver
Au	Gold
BCB	Benzocyclobutene
BW	Bandwidth
C	Capacitance
CMOS	Complementary metal oxide semiconductor
CPW	Coplanar waveguide
CRLH	Composite right/left-handed
CRS	Cylindrical radial superlattice
CSRR	Complementary split ring resonator
Cu	Copper
ECC	Eddy current cancelling
FBW	Fractional bandwidth
FEM	Finite element method
FM	Ferromagnetic
FMR	Ferromagnetic resonance frequency
HMSIW	Half-mode substrate-integrated waveguide
L	Inductance
LCP	Liquid crystal polymer
LEM	Lumped element model
MAR	Magnetic anti-resonance frequency
MEMS	Microelectromechanical systems
M-FET	Magnetic field effect transconductor
MIM	Metal-insulator-metal

Ni	Nickel
NiFe	Nickel-iron (Permalloy)
Oe	Oersted
PCB	Printed circuit board
Q	Quality factor
QMSIW	Quarter-mode substrate-integrated waveguide
RF	Radio frequency
RSV	Radial superlattice via
SEM	Scanning electron microscopy
Si	Silicon
SIW	Substrate-integrated waveguide
SOLT	Short-open-load-through
SRR	Split ring resonator
T	Tesla
TEM	Transmission electron microscopy
TEM	Transverse electromagnetic
TGV	Through glass via
Ti	Titanium
TL	Transmission line
TRL	Through-reflection-load
TSV	Through silicon via
UV	Ultraviolet
VNA	Vector network analyzer
VSM	Vibrating sample magnetometer

Abstract of Dissertation Presented to the Graduate School
of the University of Florida in Partial Fulfillment of the
Requirements for the Degree of Doctor of Philosophy

LOW LOSS PASSIVE COMPONENT TECHNOLOGIES FOR HIGH PERFORMANCE
RADIO FREQUENCY CIRCUITS USING MICRO/NANO MACHINING

By

Arian Rahimi

May 2016

Chair: Yong-Kyu Yoon

Major: Electrical and Computer Engineering

Design, fabrication, and characterization of high performance RF passive components including transmission lines, inductors, tunable transconductors, resonators and filters, typically occupying large on-chip area, are presented in which the RF loss mechanism is studied and the structure architectures, appropriate low loss materials, optimized fabrication methods, and packaging solutions are investigated. The micro/nano machining techniques are proposed and experimentally verified for RF passives to satisfy the major requirements of the next-generation communication circuits and systems, namely, high performance and low loss at high operation frequencies, compact size and being compatible with standard fabrication processes.

Ferromagnetic materials including Ni and NiFe are extensively studied and characterized for their applications in RF passives. The multi-layer ferromagnetic/non-ferromagnetic architecture is used to overpass the unavoidable skin effect in high operation frequencies and high quality inductors, interconnects and transmission lines for K and Ka bands are reported. The planar superlattice conductors with optimized physical dimensions employing Cu/NiFe and Cu/Ni are presented. Also, a cylindrical radial superlattice (CRS) conductor is demonstrated to overcome some drawbacks of the planar superlattice conductors, mainly electromagnetic discontinuity at the edge of the conductor. A magnetically-driven conductor with tunable ohmic

resistance in microwave regime, magnetic field-effect transconductor (M-FET), is proposed where the spin torque transfer of the magnetic moment to electromagnetic energy is used as a loss mechanism to design tunable conductors in RF regime.

Low dielectric loss materials compatible with standard microfabrication processes including the photo-sensitive Benzocyclobutene (BCB) and Liquid Crystal Polymer (LCP) are utilized to fabricate low loss RF passive resonators and band-pass filters for several operation frequencies. At last, the glass interposer technology using Corning glass substrates is proposed as a low loss packaging scheme for integration of high performance RF components. The characterization of the glass substrates up to 60 GHz has been performed paving the road for implementation of high frequency in-substrate passive components. The related through glass via (TGV) processing and optimized fabrication steps are detailed. Also, the passive RF components embedded inside the glass interposer substrates are designed and fabricated including a new ultra-compact multi-layer architecture with more than 10 times size reduction.

CHAPTER 1

INTRODUCTION

Motivation and Challenges

Internet of things (IoT) is the main theme for the next-generation communication systems where multiple integrated wireless/access solutions will enable a long-term networked society. This includes cellphone, mobile and device-to-device wireless communication, entertainment and consumer electronics, inter-vehicular and vehicular-road connectivity, and etc. As a result, development of complete RF systems with wireless data transfer capabilities while having a very compact size is a major requirement for such a networked society.

While the scale of integration in digital/logic integrated circuits (IC's) technology is ongoing following the Moore's law, the other required components in a comprehensive system such as analog/radio frequency (RF) circuits, microelectromechanical systems (MEMS), passive components, high performance interconnects, and related packaging are not progressing in a similar scaling pace. Therefore, creating a high performance platform with high scale integration is of great importance, which is especially true toward the More-than-Moore (MtM) roadmap.

RF passive components including inductors, capacitors, transmission lines, resonators and filters are highly demanded in RF frontend systems due to their applications in input/output impedance matching networks, intermediate frequency (IF) and RF filter applications and feeding networks. However, their on-chip implementation in a silicon-based technology is either consuming a large on-chip area resulting in a high system cost or accruing losses associated with the material loss in RF frequencies. For example, the dominant chip manufacturing processes including the complementary metal oxide semiconductor (CMOS) use silicon (Si) as a conductive substrate leading to high substrate losses in RF regime and a thin silicon dioxide (SiO_2) as the insulating layer resulting in relatively high dielectric losses. Therefore, developing

technologies to implement low loss and compact RF passive components is highly crucial improving the MtM law.

Also, with the growing need for the high performance, high-speed, and radio frequency (RF) electronic devices, the operation frequency of the new telecommunication, microelectronics and consumer electronic applications has reached the GHz range and tends to move to higher frequencies as the clock frequency of today's microprocessors has reached 3 GHz and tends to move to higher frequencies [1]. This continuous increase of the operation frequencies is expected to help mitigate the heavy traffic in the lower frequency bands (to reduce distortion), make the antenna system compacter facilitating system miniaturization, and enable realization of devices with higher data transfer rates which is more feasible operating in higher frequencies (Figure 1-1).

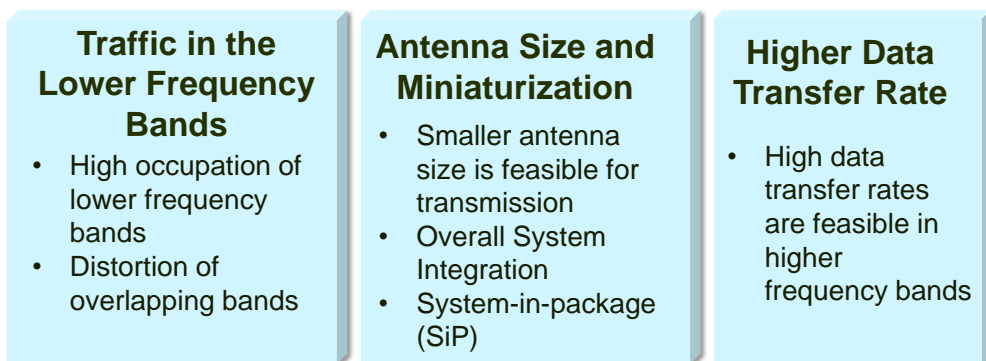


Figure 1-1. The illustration of motivation on higher operation frequencies.

One of the limiting factors of the operation in higher frequencies is the RF losses, including the conductor and dielectric loss, which are more prominent for the devices and circuits operating in the higher RF frequencies minimizing their performance and efficiency while increasing the power consumption. The mentioned losses together with the inherent parasitic capacitance in those circuits result in the so called RC time delay, preventing the operating frequencies from going higher. This will give rise to a great demand for development

of high performance materials including isolators (dielectric materials) and conductors for RF circuits and systems and passive components including inductors, capacitors, interconnects, antennas, etc. at those frequency bands. Another important impact of the next-generation RF and communication systems is that as their operation frequency is increasing, the wavelength decreases and as a result, the physical dimensions of the new components will shrink. So, the conventional machining and printed-circuit-board (PCB) implementations might not be either sufficient or fully optimized for high frequency circuits and systems and there will be a requirement for micromachining and development of microfabrication processes for high resolution, efficient, compact, and high performance development of next-generation RF components. Therefore, development and utilization of new materials which are compatible with standard microfabrication processes including Microelectromechanical Systems (MEMS) and Complementary Metal Oxide Semiconductor (CMOS) processes is an important requirement.

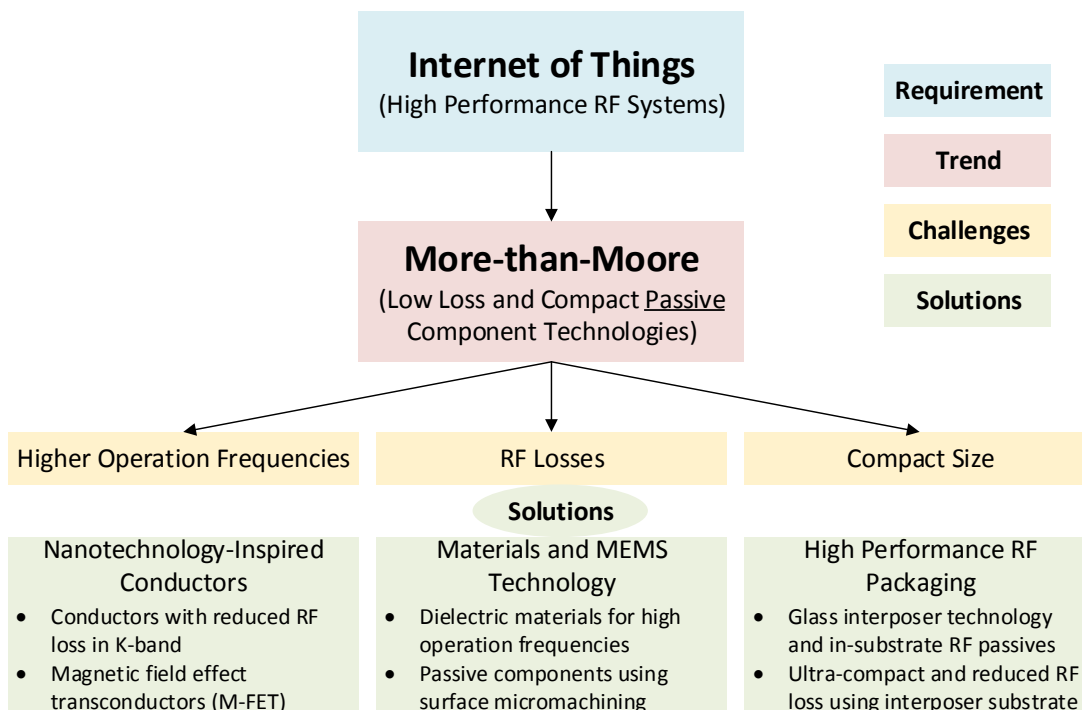


Figure 1-2. The flowchart showing the requirements, trend, challenges, and the proposed solutions for high performance RF passive component technologies.

In this dissertation, new architectures are proposed towards high performance, low loss and compact RF passive components compatible with the requirements for next-generation high frequency circuits and systems. The main challenges regarding the high conductor loss, development of photo-sensitive low loss dielectric materials compatible with standard RF MEMS fabrication processes and related low loss packaging issues using interposer technologies are addressed. Figure 1-2 shows a summary of the requirements, trend, challenges, and the solutions, proposed in this work, for the development of the high performance RF passive component technologies.

Frequency Bands and Requirements for Future Communication Systems

Based on the IEEE radio frequency (RF) definition, the RF regime is the frequency bands between 3 kHz and 300 GHz as the allocated frequency bands, their maximum power operation and maximum electric/magnetic field strengths are given by Federal Communications Commission (FCC). Figure 1-3 shows the electromagnetic spectrum with the highlighted allocated radio spectrum.

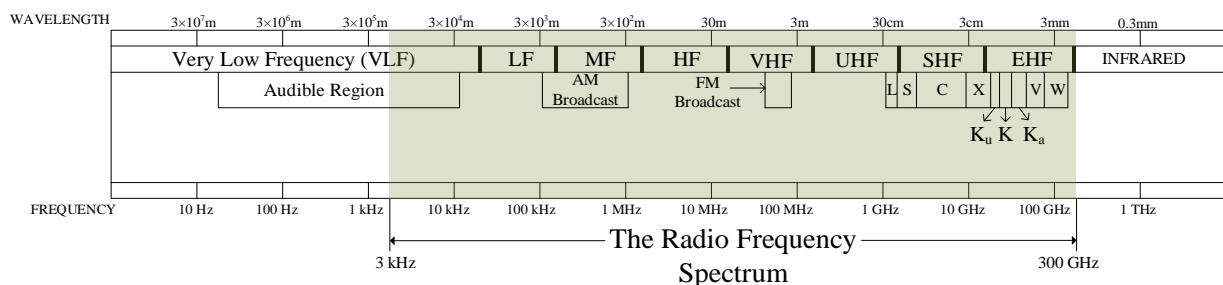


Figure 1-3. The electromagnetic spectrum with the magnified RF range and frequency bands defined by IEEE.

With the development of technology, electronic devices including the cellphones and smart phones, global positioning systems (GPS), satellite communication and radar systems work in the microwave range which makes regular daily life communications feasible and ongoing. These devices include 1.8 GHz 4G cellular communications, 2.4 GHz bluetooth, 3.5

GHz WiMAX and 5.8 GHz unlicensed ISM (Industrial, Scientific, and Medical) bands. Operation in higher frequencies will need a smaller antenna size for wireless communication and typically smaller physical dimensions for passive components. As a result, the technology node is moving towards higher frequencies due to the traffic in the lower frequency bands as mentioned above, higher data transfer rate, higher resolution and also the requirement for more compact and lower power consumption. As an instance, 20-30 GHz is expected as a plausible idle band for next generation cellular communications (5G cellular communication [2]). Also, in entertainment and consumer electronic applications where ultra-high data rate is intended such as high definition (HD) graphical wireless transfer, a 60 GHz frequency is selected.

In overall, because of the trend in operation frequencies of the RF circuits and systems which is towards higher frequencies (Figure 1-1), the loss mechanism in higher operation frequencies must be recognized and studied in order to implement high performance components for those frequencies and development of low loss conductors and materials in high frequencies compatible with standard microfabrication processes is the major requirement to be addressed.

Ferromagnetic Materials in Radio Frequency Systems

Ferromagnetic materials are needed to be because they are used to implement passive components with reduced loss. One of the objectives of this research work is to demonstrate the basic concept and potential applications of nanotechnology inspired multi-layer conductors consisting of alternating nano-superlattice structures for use in microwave passive components. Ferromagnetic materials, once deposited as thin films, have extremely dynamic frequency-dependent properties in frequencies ranging from DC to K-band (18–26 GHz) that could be used as conductor to realize passive components with extraordinary performance, that couldn't be achieved by conventional conductors as we call them metaconductors. Since ferromagnetic materials have much lower conductivity compared to regularly used high performance conductor

materials like copper or silver, they could not be used as solid conductors in RF components because of high conductor loss. However, combining the ferromagnetic materials with other non-ferromagnetic good conductors in a multi-layer nano-superlattice architecture which is the main objective in this research plan, will let us exploit those aforementioned dynamic properties of the ferromagnetic materials and build high performance RF components with new features and extra capabilities. The nanotechnology-inspired multi-layer conductors using ferromagnetic materials investigated and proposed in this work lie in the following device areas:

- Low Loss Conductors: Utilization of the multi-layer non-ferromagnetic/ferromagnetic conductors as eddy current cancelling conductors for the fabrication of ultra-high Q inductors in K-band.
- Magnetic Field Effect Transconductors: Introduction and fabrication of transmission lines with tunable ohmic resistance in microwave frequencies.
- Microwave and mm-wave Passive Components Using Nano-Superlattice Conductors: Demonstrating the passive components including the microwave and mm-wave resonators and bandpass filters which use the proposed conductor architecture for loss reduction.

Chapters 3, 4, and 5 of this dissertation will give an in-depth overview of each of the above mentioned items by giving the theoretical background, fabrication and measurement results.

Proposed Solutions, Research Objectives and Contributions

Figure 1-4 presents a typical RF heterodyne frontend which is a thorough representative of an RF system with different active and passive components where the level of integration is indicated. While some components like analog-to-digital converters could be fully integrated, some other components like low noise amplifiers (LNA) will require high performance RF inductors/capacitors for their input/output matching networks which will occupy large on-chip area. This will increase the total cost of the system (large chip area) and will limit the performance of the passive components due to the limitation forced by the CMOS processes

including the substrate losses (limited dielectric thickness and conductive substrates), and high dielectric loss (high loss tangent of silicone dioxide in CMOS chips). Therefore, off-chip implementation of the so called components and integration of them to the other components of the system using a low loss packaging scheme may increase the total efficiency of the system and save both cost and area. Also, some required passive components including the band-pass filters and resonators are almost impossible to be implemented on-chip. These effects will be more prominent in next-generation systems where the operation frequencies are moving toward higher values. As a result, a comprehensive research on the development of high performance components in high operation frequencies is mandatory.

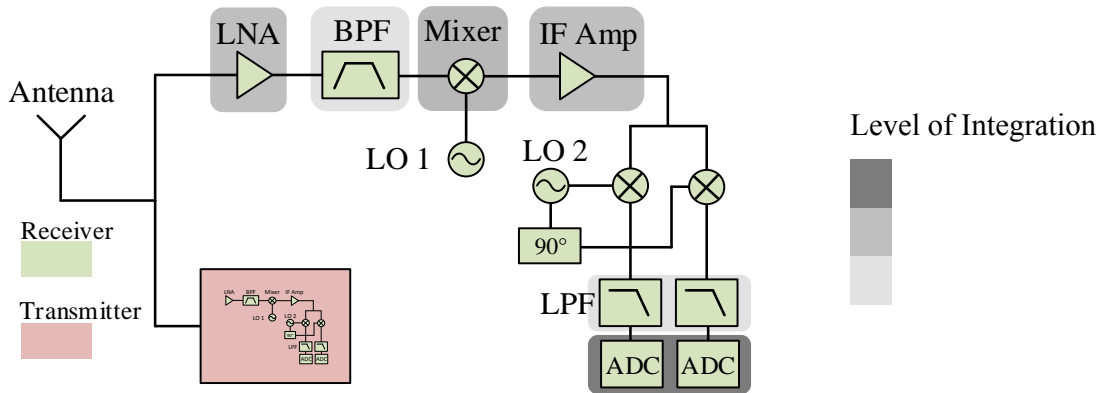


Figure 1-4. The components of an RF heterodyne system and the level of integration of each component.

In this research, the design, fabrication and characterization of high performance micromachined passive components including inductors, resonators, and band-pass filters in K and V bands are presented. A low loss RF packaging scheme is proposed where conventional wire-bonding could be skipped and some passive components are fabricated in-substrate allowing the 2.5D integration of passive and active components for maximum system performance and compactness. The major contributions include the devices with low conductor loss, low dielectric loss and low loss packaging solutions for RF as listed below:

The devices with low conductor loss:

- A new architecture, cylindrical radial superlattice (CRS) conductor, is proposed to overcome the limited conductor loss reduction performance of previously proposed planar superlattice conductors. The presented CRS conductors have inherently closed and uniform boundary conditions in the azimuthal direction of the radial shape. Therefore, the electromagnetic (EM) fields resulting in eddy current cancelling are confined inside the conductor fully contributing towards the ohmic loss reduction.
- The physical dimensions of the planar multi-layer conductors for eddy current cancelling have an important effect on the overall performance of the conductors for improving the conductor loss in a high frequency regime of operation. These effects are not studied before and as a result the work from previous publications does not exploit the maximum benefit that these high performance conductors could provide. In this work, for the first time, the effects of physical dimensions of the conductors are studied in nanometer range by use of accurate finite-element method (FEM) simulations which provide guidelines for designing high performance multi-layer conductors for RF circuits and systems.
- A study and the experimental utilization of different magnetic materials have been taken. The electroplating process has been adopted as the cost-effective, conformal deposition method which is suitable for the implementation of uniform radial CRS conductors. The pure Ni 99.99% has been employed as a new ferromagnetic material in eddy current cancelling (ECC) conductors has been introduced and experimentally verified. Ni is an abundant ferromagnetic material which could be deposited in most in-house fabrication facilities and has the advantage of high contrast between its in-plane and out-of-plane coercivities, making it suitable for ECC conductors. A magnetic characterization of the utilized ferromagnetic materials including the electroplated NiFe and sputtered NiFe and Ni is provided.
- A maximum peak Q-factor of 45 at 18 GHz for the radial inductors and a peak Q-factor of 60 at 23 GHz for the planar inductors are reported for the RF inductors.
- The fabrication methods are fully compatible with the standard Microelectromechanical Systems (MEMS) and Complementary Metal-Oxide-Semiconductor (CMOS) processes. Combination of the proposed method with the existing concurrent microfabrication processes could be applied as a long-term solution in low loss future high-speed microelectronic devices including digital microprocessors, analog-to-digital converters, RF inductors, interconnects, transmission lines, antennas, and metamaterials.

The development of magnetic field effect transconductors:

- The design and experimental demonstration of the magnetically-driven nano-superlattice conductors, called as M-FETs, is given.
- The comprehensive ferromagnetic and physical material characterizations are performed. The effects of number of layers and width of the signal line on the extracted ohmic resistance are studied.

- Cu/NiFe M-FETs with a thickness of 180 nm/30 nm have more than 3 times higher resistance near ferromagnetic resonance frequency, allowing implementation of tunable RF conductors; while M-FETs with a thickness of 180 nm/60 nm showed more than 6 times higher ohmic loss near ferromagnetic resonance frequency.

The devices with low dielectric loss:

- The RF resonators and band-pass filters are designed and implemented using low loss dielectric materials. The liquid crystal polymer (LCP) substrate has been used for the fabrication of components in 25 GHz and 40 GHz bands. A hybrid fabrication method is performed where vias are fabricated using mechanical milling followed by surface micromachining for realization of the devices. The half-mode and quarter-mode substrate-integrated-waveguide (HM/QMSIW) modules are used as the handling devices wherein complementary split ring resonators (CSRR's) are used to design compact resonators and filters. The wide-band two-pole and three-pole band-pass filters with low loss and 17% fractional BW in 25 GHz and less than 1.6 dB insertion loss are demonstrated.
- A modified fabrication process is developed for deposition and photo patterning of BCB where 30 μm BCB layers with a single coating are successfully deposited and patterned.
- The RF resonators and two-pole and three-pole band-pass filters for 60 GHz band are implemented by using BCB as the structural material featuring compact size and ultra-low loss. The metamaterial-based components (CSRR's) are used inside the SIW structures operating in evanescent mode below their cut-off frequency for size reduction. A maximum 1.7 dB insertion loss is achieved for the band-pass filters at 60 GHz with a fractional BW of 10%.

Low loss RF packaging:

- A glass interposer technology is proposed as the low loss packaging scheme for high performance RF integration. Two glass interposer layers, namely, Corning and photo-sensitive glass substrates, are characterized in high frequency up to 50 GHz to be used as the hosting medium for implementation of RF components.
- The design approaches together with fabrication techniques are proposed to realize high performance and compact microwave passive components on the glass interposer substrates.
- Half-mode substrate integrated waveguide (HMSIW) architecture loaded with the CSRR's is chosen to realize compact resonators and bandpass filters for two ISM bands of 2.4 GHz and 5.8 GHz. The through glass vias (TGV's) are fabricated using a laser fusion process on a glass interposer from Corning Incorporated Surface micromachining techniques are used for the fabrication of the proposed devices. The measurement results show less than 1.7 dB insertion loss for the 2-pole bandpass filters in 2.4 and 5.8 GHz bands.

- The 3D Microelectromechanical (MEMS) fabrication and interposer technology is combined with the design architectures using metamaterials to implement super-compact and high performance. The implemented resonators with a size of $0.04 \lambda_g \times 0.04 \lambda_g$ and band-pass filters with a size of $0.137 \lambda_g \times 0.04 \lambda_g$ at 2.4 GHz and 5.8 GHz bands are the smallest reported in the literature.
- Resonators and bandpass filters for higher operation frequencies including the K-band are designed using the glass interposer technologies and a multi-layer low loss conductor to improve the insertion loss in passband.

Dissertation Organization

The dissertation is organized in eight chapters as follows,

Chapter 1 is an introduction regarding the motivation description of the problems and issues regarding the losses present in the high frequency operation of next-generation circuits and systems and their feasible solutions. Also, the research objectives and contributions of this work are listed. Chapter 2 introduces the required background and theory on sources of RF loss and RF loss reduction. Chapters 3 and 4 give the conductor architectures for loss reduction in RF regime where the design and experimental demonstration are detailed. Chapter 5 introduces the proposed magnetic field effect transconductor (MFET) which are RF conductors with tunable ohmic resistance. Chapter 6 is on the components with suppressed dielectric loss and gives the fabrication techniques for implementation of RF components using insulators with low dielectric loss. Chapter 7 details the packaging techniques and the RF components implemented using glass interposer technology. Chapter 8 gives the conclusions and summarizes the planned future works.

CHAPTER 2

BACKGROUND AND ANALYSIS

In this chapter, the required theory which is necessary as the background for the research objectives of this thesis and the proposed solutions to improve them are presented. First, the sources of loss in microwave regime are recognized which are initially required to follow the steps towards how to suppress them. Inductors are selected as one of the main passive components required for implementation of RF systems which are used in this work as test vehicles for RF loss studies. The analytical modelling of the inductors followed by experimental studies highlight the RF losses providing the path for RF loss reduction. Next, the conductor loss and ohmic loss reduction in RF regime is discussed followed by an introduction to ferromagnetic materials which will be used in low loss conductors in Chapters 3 and 4. Also, the theory behind the dynamic modelling of the ferromagnetic materials using Landau-Lifshitz-Gilbert work is provided which will help understand the realization of M-FETs given in Chapter 5.

The Sources of Loss in Microwave Regime

The propagation of an electromagnetic wave in RF regime in any given medium is described by Maxwell's equations. The physical properties of the medium, namely electric permittivity and magnetic permeability, will be used as known parameters to solve for the Maxwell's equations and find the relationships between the electric and the magnetic fields as follows,

$$\nabla \cdot \mathbf{B} = 0 \quad (2-1)$$

$$\nabla \cdot \mathbf{D} = \frac{\rho}{\epsilon} \quad (2-2)$$

$$\nabla \times \mathbf{E} = -\frac{\partial \mathbf{B}}{\partial t} \quad (2-3)$$

$$\nabla \times \mathbf{H} = \frac{\partial \mathbf{D}}{\partial t} + \mathbf{J} \quad (2-4)$$

where \mathbf{D} is the electric flux density (Coul/m^2), \mathbf{H} is the magnetic field intensity (A/m), \mathbf{E} is the electric field intensity (V/m), ρ is the electric charge density (Coul/m^3), and \mathbf{J} is the electric current density (A/m^2). When electromagnetic fields exist in a given medium with known material properties, the field vectors are related to each other by constitutive relations. The following relationships hold between electric and magnetic field intensities and flux densities in free space,

$$\mathbf{D} = \epsilon_0 \mathbf{E} \quad (2-5)$$

$$\mathbf{B} = \mu_0 \mathbf{H} \quad (2-6)$$

For non-conductive dielectric materials, an electric field \mathbf{E} will cause a polarization of the atoms and molecules of the material to create electric dipole moments. The additional polarization vector will result in modification of (2-5) as follows,

$$\mathbf{D} = \epsilon_0 \mathbf{E} + \mathbf{P}_e \quad (2-7)$$

where \mathbf{P}_e is the electric polarization vector. Assuming that the dielectric material is linear, which is valid for most cases, the polarization vector will be a linear function of applied electric field and could be given as,

$$\mathbf{P}_e = \epsilon_0 \chi_e \cdot \mathbf{E} \quad (2-8)$$

where χ_e is the electric susceptibility. Then, (2-7) could be simplified as,

$$\mathbf{D} = \epsilon_0 (1 + \chi_e) \cdot \mathbf{E} = \epsilon \mathbf{E} \quad (2-9)$$

where,

$$\epsilon = \epsilon_0 (1 + \chi_e) = \epsilon' - j\epsilon'' \quad (2-10)$$

When \mathbf{E} is alternating, the dielectric material will be polarized as a result of the fluctuating fields where portion of the energy will be wasted as heat inside the dielectric material due to the damping of the electric dipoles. (2-10) is the complex permittivity of a medium where the imaginary part accounts for the loss in the dielectric medium.

Another loss associated with devices operating in RF frequencies is the conductor loss which exists due to utilization of conductors with limited conductivity. As a result, portion of the electromagnetic energy will be wasted as heat in terms of ohmic losses. In a material with certain conductivity, σ , ohm's law exists as follows,

$$\mathbf{J} = \sigma \mathbf{E} \quad (2-11)$$

Therefore, the Maxwell's equation (2-4) will become,

$$\nabla \times \mathbf{H} = j\omega \mathbf{D} + \mathbf{J} \quad (2-12)$$

by replacing (2-9) and (2-11) in (2-12),

$$\begin{aligned} \nabla \times \mathbf{H} &= j\omega \epsilon \mathbf{E} + \sigma \mathbf{E} \\ &= j\omega \epsilon' \mathbf{E} + (\omega \epsilon'' + \sigma) \mathbf{E} \\ &= j\omega (\epsilon' - j\epsilon'' - j\frac{\sigma}{\omega}) \mathbf{E} \end{aligned} \quad (2-13)$$

where the loss due to imperfect dielectric materials (ϵ'') and limited conductivity of metals (σ) is considered. As a result, the term in (2-13) with imaginary multiplier $j(\omega \epsilon'' + \sigma)$ is contributing towards the total loss and the loss tangent is defined as,

$$\tan \delta = \frac{\omega \epsilon'' + \sigma}{\omega \epsilon'} \quad (2-14)$$

The materials operating in microwave regime are usually characterized by specifying their electric permittivity, $\epsilon = \epsilon_0 \epsilon_r$, and loss tangent, $\tan \delta$. Several efforts, detailed in next section, have been performed to suppress the dielectric loss and a few architectures are proposed

to suppress the conductor loss to decrease the overall RF loss of the systems which will be covered in Chapters 3, 4 and 6 of this dissertation.

Towards RF Loss Reduction

There are numerous efforts reported in the literature to suppress the loss mechanisms associated with the RF components including the substrate, conductor, and dielectric losses. Si, the dominant substrate material in micromachining RF MEMS and CMOS processes, is a conductive material which will allow the flowing of induced eddy currents that are wasted in terms of heat in the substrate and eventually decrease the performance of RF components and systems. In [7], a Si bulk micromachining is proposed where the Si substrate is completely etched to enhance the substrate loss. Also, in [8], a trench machining approach is proposed where trench islands are created on the conductive Si substrate to cut the conductive paths and reduce the substrate loss.

The conductor loss, one of the major loss sources associated with RF circuits and systems, is mostly influenced by the limited material conductivity and internally/externally induced losses and will grow as the frequency increases in result of the skin effect in which the conductor's effective cross section area decreases. Therefore, as the frequency increases satisfying the requirements for next-generation communication systems as discussed, the conductor loss will grow resulting in poor RF performance of the conductors. The larger conductor loss will also be significant in high speed digital circuits including analog-to-digital/digital-to-analog converters and processors which will lead to substantially large RC delays and limit the maximum operation frequency [6].

The skin effect and proximity effect introduce high RF losses resulting from the time-varying magnetic flux generated by the conductor itself or the neighboring conductor, respectively, where most current is confined in the outmost surface of the conductor thus

reducing the effective cross-section of the conductor and increasing the ohmic resistance. The losses can be partially alleviated by the macroscopic patterning of the conductors and different constructions (e.g. litz wire) in low frequencies while the skin effect demands more microscopic treatment as the frequency increases.

A planar type superlattice conductor architecture has been firstly reported in [3] for conductor loss reduction where metallic thin films with negative/positive permeability are proposed to cancel the eddy current inside the conductor and overpass the skin effect by driving the current through the volume of the conductor. Due to the negative permeability of the ferromagnetic materials above their ferromagnetic resonance frequency, the eddy currents will be reversely induced inside the ferromagnetic layers of the conductor resulting in cancellation of the overall eddy currents inside the conductor. The analytical and simulation results in [3] show the feasibility of the uniform distribution of current inside the conductor resulting in loss reduction in RF regime. An experimental demonstration of the conductor loss reduction has been reported in [9]-[12]. In [9] multi-layer Cu/CoZrNb with a thickness of 450 nm/15 nm has been reported where a thickness ratio of 30 is selected to target the conductor loss reduction in low frequencies where 8.7% loss reduction is reported at 6 GHz. In [10] and [11], one-turn spiral inductor made of Cu/NiFe layers with a thickness of 650 nm/40 nm are reported where a 40% loss reduction and improved Q-factor in 13 GHz is demonstrated.

Although the state-of-the-art planar superlattice conductors show an improvement in the conductor loss reduction in RF regime, their inefficient physical dimensions and their inherent planar shape will limit the maximum conductor loss reduction performance. The electromagnetic discontinuity at the edge of the conductor will introduce non-ideal field distribution coming from the finite lateral width and the fringing field at the edge of the microstrip or stripline type

conductor. In order to eliminate this disturbance, a superlattice film with an infinitive width is plausible, but may not be very practical. Therefore, the planar superlattice architecture is not fully taking advantage of the eddy current cancelling effect and a limited loss reduction is achieved. In this work, architectures are demonstrated to overcome such drawbacks of the planar superlattice conductors. A new type of multi-layer conductor, namely cylindrical radial superlattice (CRS) conductor shows inherently a closed and continuous boundary condition in an azimuthal direction and therefore is considered to be more appropriate for ECC and more effectively lowering the conductor loss. Also, a complete study on the physical dimensions of the conductor is made which will be used for designing high performance planar superlattice conductors and the results are extended to high Q inductors in K band.

The dielectric loss is another source of loss associated with RF circuits and systems inheriting from imperfect dielectric materials where part of the propagating electromagnetic energy is wasted as heat inside them. As a result, the development of high performance components with dielectric materials compatible with standard CMOS and MEMS fabrication processes is crucial. Several efforts have been reported to suppress the dielectric loss [17]-[21]. The dielectric loss would be reduced by locally removing the dielectric materials forming air-lifted architectures ([17]-[18]) or using very low loss dielectric materials [20]-[21]. In [17], the thick polymer processing technique is used to realize high quality air-lifted inductors operating in DC-10 GHz range in which the thick SU-8 is photo patterned and soft-baked to create a bridge structure followed by metallization of the polymer using electroplated Cu to fabricate the inductors. In [18], a four-pole band-pass filter for 60 GHz is introduced where micromachined polymer pillar structures are firstly fabricated. A metallic plate is then mounted on top of them to create a completely air-lifted structure. The measurement results show a band-pass filter with a

3dB BW at 60 GHz of 1.6 GHz and an insertion loss of 2.9 dB. In this work, dielectric materials with low tangent loss are used to realize passive components operating in RF regime ranging from 2.4 GHz to 60 GHz. The optimized fabrication techniques are presented to fabricate compact, high performance passive RF components. Also, a glass interposer layer is used as a low dielectric loss hosting medium for implementation of in-substrate passive components.

RF Loss Studies Using an Analytical Model for RF Inductors

In this section, the implementation of RF inductors in a silicon-based process, complementary metal oxide semiconductor (CMOS), is given. Although, the performance of the implemented inductors, in this section, is not impressive, they highlight the RF losses and provide guidelines for possible solutions for passives with minimal RF loss. Also, a modeling approach based on the equivalent lumped-element circuit model of an inductor is presented which describes the inductance and Q-factor performance versus frequency.

An inductor is an electrical component that stores magnetic energy. When the current flows in a conductor, a magnetic field is generated surrounding the conductor based on Ampere's law,

$$\nabla \times \mathbf{H} = \mathbf{J} \quad (2-15)$$

This process is reciprocal in a way that a current will be induced in a conductor while it is affected by an external magnetic field. As a result, a form of energy will be confined inside the magnetic field because when the flow of electrical current stops, the initially generated magnetic field will cause a current flow to be continued. The amount of inductance is then defined as how strong the inductor is able to store magnetic energy. Also, as extension of (2-6), the magnetization in a given material in a magnetic field of \mathbf{H} will be given by,

$$\mathbf{B} = \mu_0 \mu_r \mathbf{H} \quad (2-16)$$

where μ_r is the permeability of the material. As a result, using divergence, (2-1), and Faraday's law, (2-3), it would be possible to extract the flux linkage, Ψ , for a given surface area of S [22],

$$\Psi = \iint_S \mathbf{B} \cdot d\mathbf{S} \quad (2-17)$$

Assuming a constant and uniform distribution of flux density in a medium, a linear relationship of flux linkage and current will define inductance,

$$\Psi = LI \quad (2-18)$$

The quality factor (Q) in an inductor is a measure of how efficiently the inductor can store magnetic energy. It is defined as the amount of energy stored, E_{stored} , by an inductor divided by the amount of energy dissipated, $E_{dissipated}$, in each cycle,

$$Q = 2\pi \times \frac{E_{stored}}{E_{dissipated}} \quad (2-19)$$

As a result, Q-factor is a crucial parameter on the power consumption and overall efficiency of the RF systems employing inductors. To extract the Q-factor of an inductor versus frequency, a simple modelling has been performed which estimates the dependence of the Q-factor in different frequencies. The goal is to set the maximum value of an inductor's Q-factor near its operation frequencies.

Figure 2-1 depicts the equivalent circuit lumped-element model of the inductors assuming different types of structure. The inductors fabricated in a Si-based process such as in CMOS processes, will follow the model in Figure 2-1C where a conductive substrate gives rise to the total loss of inductor. For a simple inductor shown in Figure 2-1A, the Q-factor of the inductor could be written as,

$$Q = \frac{\omega L_{ind}}{R} \quad (2-20)$$

where L_{ind} and R_{ind} are the series inductance and resistance of the inductor. Based on (2-20), the Q-factor of the inductor will increase as the frequency increases since the frequency term is in the nominator. However, in actual inductors, the skin effect should be taken into account in which the resistive element of the inductor, in denominator, will also increase with the frequency rise,

$$Q_{ac+dc} = \frac{\omega L_{ind}}{R_{dc} + R_{ac}} \quad (2-21)$$

where R_{ac} represents the resistance of the inductor assuming the skin effect. The other important parameter affecting the Q-factor are the capacitive parasitics of the inductor which highly impact the high frequency performance of the inductors and are needed to be studied. As a result, the actual Q-factor of the inductor assumes the capacitive parasitics.

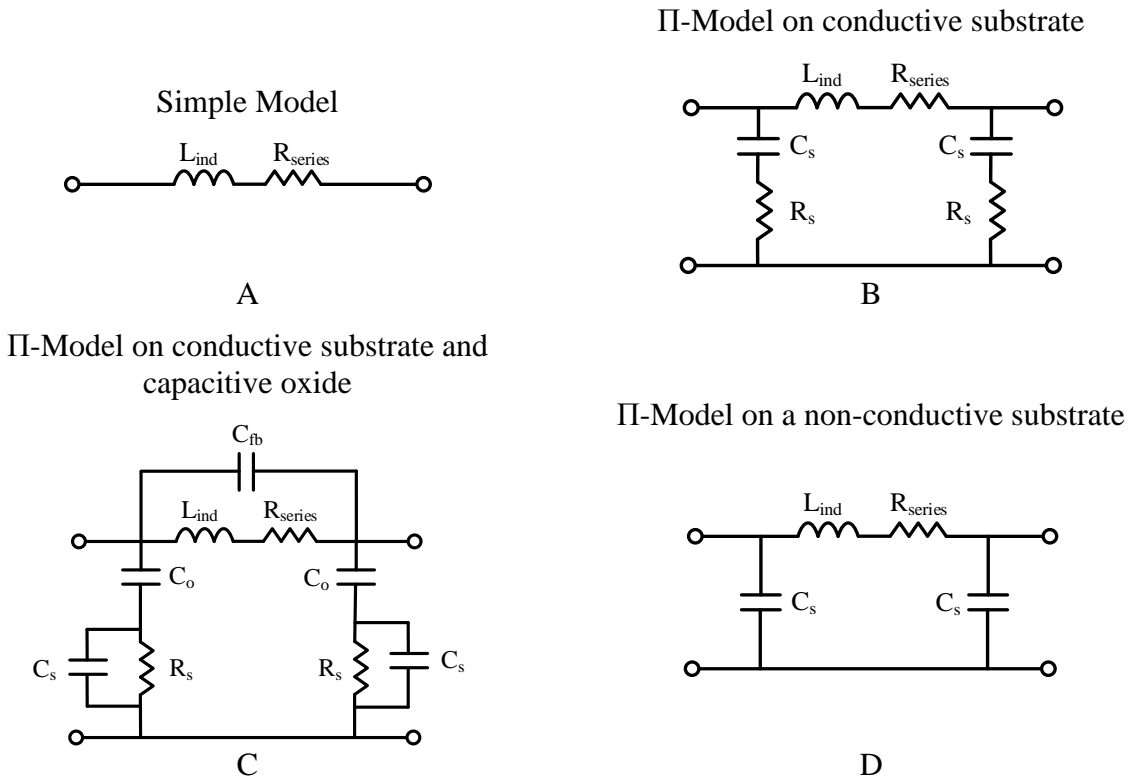


Figure 2-1. The equivalent circuit lumped-element models for integrated inductors. A) Simple one-port model, B) the π -model, C) the π -model assuming a conductive substrate, and D) the π -model with a non-conductive substrate.

In order to study the high frequency characteristics of the inductor using the Q-factor definition in (2-19), the model in Figure 2-1D including the parasitic capacitances will result in,

$$Q_{act} = \frac{\text{Im}\{Y_{21}\}}{\text{Re}\{Y_{21}\}} \quad (2-22)$$

where Q_{act} is the actual Q-factor of the inductor will all elements in Figure 2-1D and Y_{21} is the element of the 2×2 Y-parameters matrix of the two-port inductor. The resistive portion of the inductor are ignored for simplicity. By solving for the Y-parameters of the inductor and plugging in (2-22), Q_{act} will be given as,

$$Q_{act} = \frac{(1 - \omega^2 LC)\omega L - R^2 \omega C}{R(1 - \omega^2 LC) + RLC\omega^2} \quad (2-23)$$

in which $R = R_{dc} + R_{ac}$ and L and C are the inductance and shunt capacitance of the inductor model in Figure 2-1D. Based on the given discussion, R , L , and Q-factor are all frequency-dependent parameters and by plugging in the R (freq.) in (2-23), the Q-factor relaxation with frequency could be found. In this modelling approach, the analytical model in [23] is used to analytically simulate the inductors. The R_{ac} is affected by skin effect where the electromagnetic wave will decay through the volume of the conductor as shown in Figure 2-2.

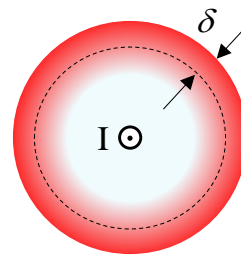


Figure 2-2. The demonstration of skin effect in a conductor handling ac current.

The skin depth, δ , is the distance where the magnitude of current drops by $1/e$,

$$\delta = \sqrt{\frac{2}{\omega \mu \sigma}} \quad (2-24)$$

where ω is the angular frequency, μ_r is the relative permeability of the conductor and σ is its conductivity. The R_{ac} of a solid conductor could be approximated by,

$$R_{ac} = R_{dc} \frac{\xi(\eta)}{2} \left[\frac{\sinh \xi(\eta) + \sin \xi(\eta)}{\cosh \xi(\eta) - \cos \xi(\eta)} \right] \quad (2-25)$$

where $\xi(\eta)$ is given by,

$$\xi(\eta) = d \sqrt{\pi} / (2\delta) \quad (2-26)$$

Also, it is known that the analytical inductance value is approximated by [23],

$$L = \frac{\mu_0 \mu_r N^2 w t_m}{l} \quad (2-27)$$

for an inductor using N number of turns and conductor of length l , and width w and thickness of t_m . By replacing (2-24) – (2-27) and the R_{ac} values into Q_{act} formula, (2-23), that would be possible to simulate the Q-factor of an inductor in high frequencies.

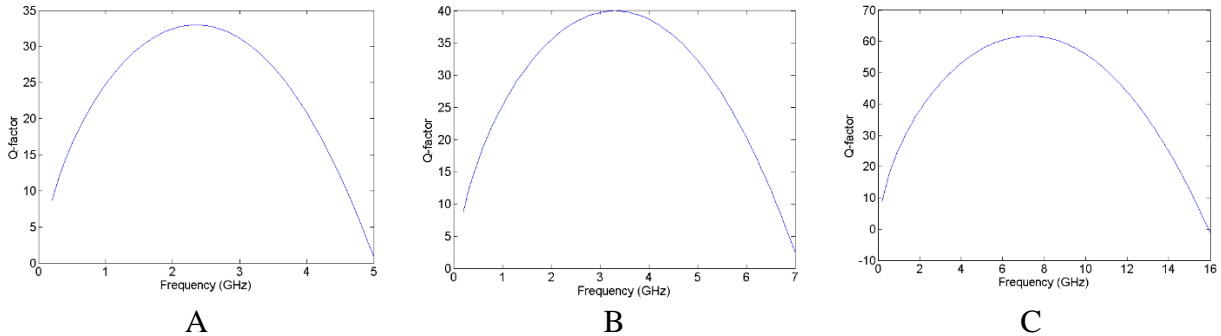


Figure 2-3. The simulation results of the Q-factor of a 1-nH inductor assuming a shunt parasitic capacitance of A) 1 pF, B) 0.5 pF, and C) 0.1 pF.

Figure 2-3A depicts the analytical simulation results using MATLAB for the Q-factor of a 1 nH inductor assuming a 1 pF shunt parasitic capacitance. In this simulation, a constant 1 pF parasitic capacitance is assumed to see the Q-factor behavior with respect to frequency. As shown, the Q-factor peaks at frequencies close to 2.5 GHz and decreases in higher frequencies in result of the parasitic capacitances and the also the skin effect and increased ohmic loss in higher

frequencies. Since the skin effect is an internal source of loss growing up with frequency for solid conductors, in order to realize inductors with improved Q-factor in higher frequencies, the only possible way is to decrease the shunt capacitive elements. As it is shown in Figure 2-3B and Figure 2-3C, by decreasing the parasitic capacitance to 0.5 pF and 0.1 pF, both the magnitude of the Q-factor increases and its peak value shifts to higher frequencies. However, in practical applications, the effects from neighboring conductors and conductive substrate, will result in higher parasitic capacitance lowering the Q-factor and shifting its peak point to lower frequencies. As a result, one feasible solution remains in microscopically modifying the conductors in order not to follow the skin effect theory to increase the Q-factor in higher operation frequencies as will be discussed in Chapters 3 and 4.

The First-Generation RF Inductors in CMOS Process

To experimentally highlight the effects of loss, the first-generation integrated inductors in this work are implemented in a standard 0.5 μm ONSemiconductor CMOS process with 3-metal and 2-poly (3M2P) layers. Full-wave simulations using ANSYS HFSS v. 14.0 are first conducted for the design of RF inductors where Figure 2-4 shows the 3D schematic view of the implemented inductors. A 300 μm Si substrate is used for the simulations and the top metal layer with a thickness of 700 nm is used as the actual metal of the inductors. Patterned ground strips (PGS) using metal 1 are used to reduce the cross talk between the inductor and the substrate and to cut the path of eddy currents in order to reduce the total loss of the inductors. Figure 2-4A shows a one-port inductor with $N = 10$ turns and Figure 2-4B shows the two-port inductor with $N = 3$ with different types of PGS's. Table 2-1 presents the summary of the dimensions of the inductors which are fabricated using the CMOS process. The width (W) is the width of the utilized conductor where space (S) is the distance between neighboring conductors. The D_{in} and D_{out} are the distances of the internal and outside of the spiral inductors.

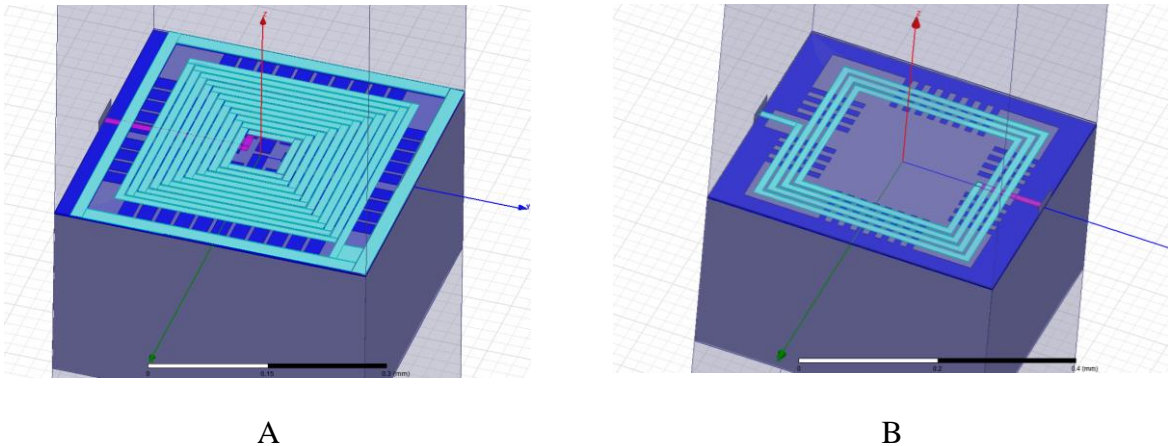


Figure 2-4. The 3D schematic view of the inductors in ANSYS HFSS v. 15.0. A) A 10-turn one-port inductor, B) a 3-turn two-port inductor.

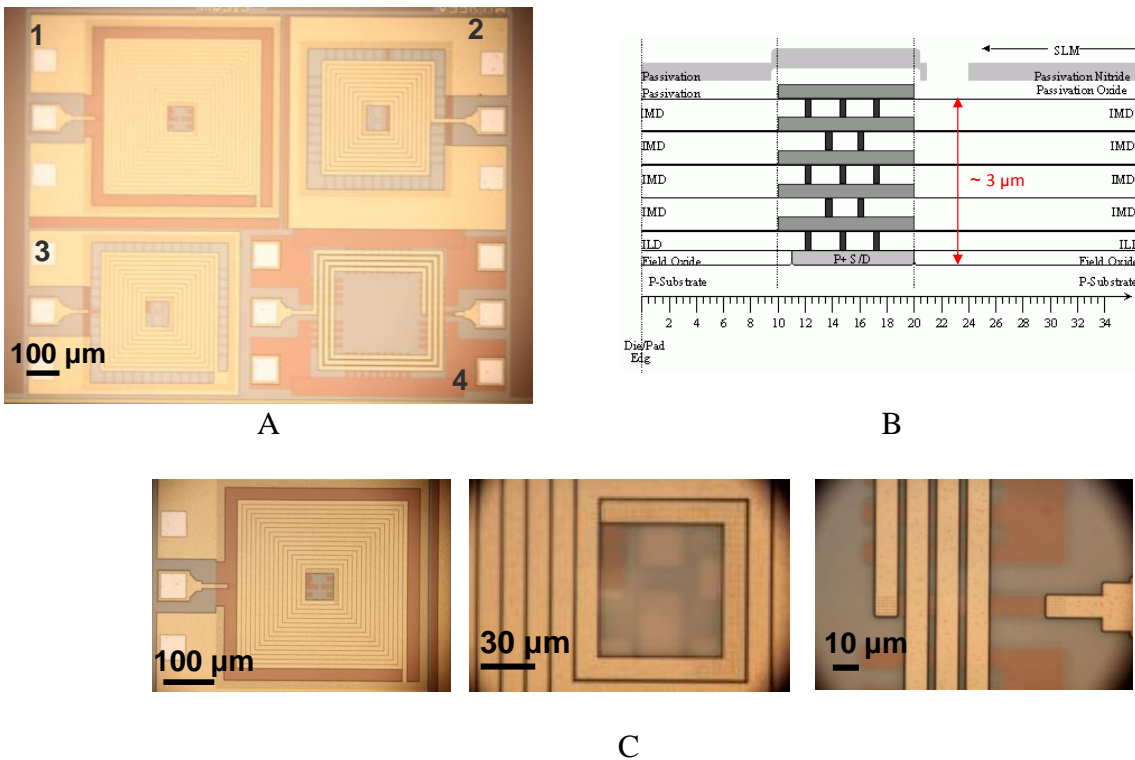


Figure 2-5. The optical micrographs of the implemented inductors in 0.5 μm CMOS process. A) The top view of the die consisting the library of inductors, B) the cross section schematic of the 3M2P 0.5 μm ONSemiconductor CMOS process, and C) the zoomed version view.

Figure 2-5 shows the optical micrographs of the top view of the library of inductors as their dimensions are tabulated in Table 2-1. Figure 2-5B shows the cross section view of the

CMOS inductors with 3M2P layers where a 3 μm silicon dioxide (SiO_2) layer is used as the passivation layer. The inductors use M3 as their actual metal because of having maximum thickness in this CMOS process and also maximum distance from Si substrate to reduce the losses. The ground-signal-ground feedings are used for microwave measurements where a vector network analyzer (VNA) N5227A (Agilent Inc.) is used for testing. Figure 2-5C shows the zoomed version of the optical photos where the input feeding, the top metal layer and PGS conductors, and the 2 μm gap between the metal layers are detailed.

Table 2-1. The summary of the CMOS implemented inductors in 0.5 μm CMOS process and their dimensions.

Inductor #	Inductance (nH)	# of turns	Width (μm)	Space (μm)	D_{in} (μm)	D_{out} (μm)
IND_1	53	15	9.9	1.2	69.4	400
IND_2	19.5	10	9.9	1.95	66.9	300
IND_3	19.5	10	9.9	1.95	66.9	300
IND_4	4.2	3	9.9	9.9	200	300

Figure 2-6 shows the comparison of the simulations and measurement results of the one-port RF inductor in 0.5 μm ONSemiconductor CMOS process with 10 number of layers where the Z_{11} parameter and the extracted inductance of the inductor are shown. The self-resonance frequency of the inductor is measured to be 1.8 GHz. Although a good agreement is achieved between the simulation and measurement results, the measured Q-factor of the inductor is close to 2 in frequencies near 1 GHz.

The main sources of loss are graphically shown in Figure 2-7 as red arrows and listed as follows,

- The conductor loss: even though the conductor is implemented using M3 (the thickest metal in this CMOS process), due to the limited conductivity of the conductors and the skin effect, portion of the electromagnetic (EM) energy is wasted in the conductors.
- The dielectric loss: because of using imperfect dielectric materials, part of the EM energy is wasted in terms of heat in the dielectric. Although SiO_2 is the dominant passivation layer due to its advantages in semiconductor fabrication technologies, it doesn't have a promising RF performance and adds to the loss.

- The substrate loss: due to the cross talk between the top conductors and the conductive substrate, portion of the EM energy is also wasted as eddy currents flowing inside the substrate, eventually converting to heat.
- The proximity effects: due to the existence of the nearby conductive materials, the eddy currents will be induced and dissipated in terms of heat.

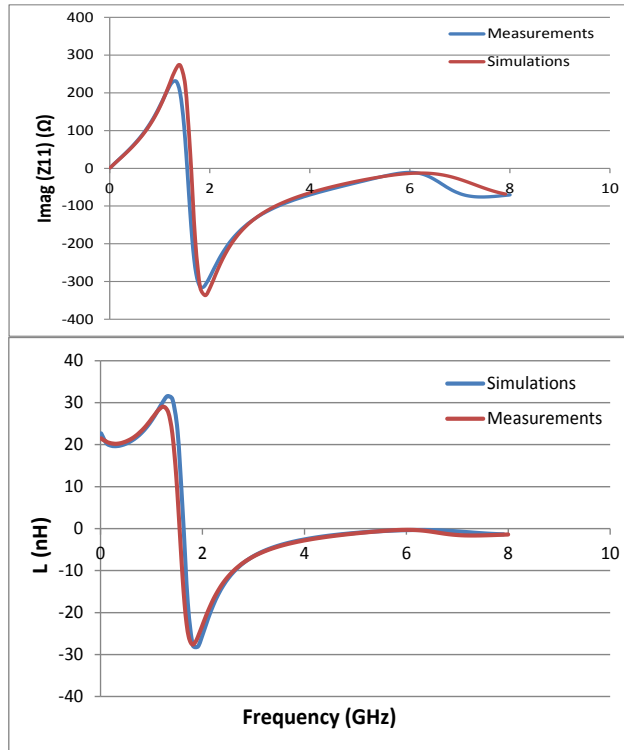


Figure 2-6. The comparison of the simulations and measurement results of the spiral inductor in 0.5 μm CMOS process with 10 number of turns.

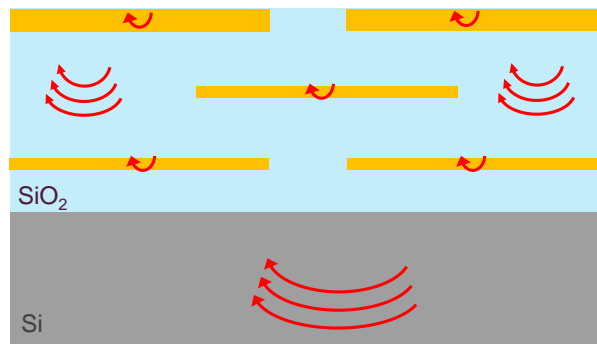


Figure 2-7. The main sources of RF loss reducing the Q-factor of the integrated inductors in 0.5 μm CMOS process using the cross section view.

In order to decrease the total loss of the passive components as in the case of inductors discussed above, one might look for solutions to decrease each individual parameter introducing

the loss. The proposed solutions in this work will be discussed in chapters 3, 4, 6, and 7 in which architectures to suppress the conductor losses, the dielectric losses, and related packaging and integration will be presented.

The Conductor Loss and Ohmic Loss Reduction in Microwave Regime

The conductor loss is associated with good conductors but not perfect conductors which are practically used in circuits and systems including the most common manufacturing metals given in Table 3-1. By assuming an $e^{j\omega t}$ time dependence, the Maxwell's equations given in (2-1) to (2-4) could be rewritten as,

$$\nabla \cdot \mathbf{B} = 0 \quad (2-28)$$

$$\nabla \cdot \mathbf{D} = \rho \quad (2-29)$$

$$\nabla \times \mathbf{E} = -j\omega \mathbf{B} \quad (2-30)$$

$$\nabla \times \mathbf{H} = j\omega \mathbf{D} + \mathbf{J} \quad (2-31)$$

By considering the effect of a lossy conductive medium with a limited conductivity of σ , the Helmholtz equations in phasor form could be written as,

$$\nabla \times \mathbf{E} = -j\omega \mu \mathbf{H} \quad (2-32)$$

$$\nabla \times \mathbf{H} = j\omega \epsilon \mathbf{E} + \sigma \mathbf{E} \quad (2-33)$$

which has two equations for two unknowns, \mathbf{E} and \mathbf{H} to be solved for the medium with given properties. By replacing (2-32) in (2-33) one could work out to get,

$$\nabla^2 \mathbf{E} + \omega^2 \mu \epsilon (1 - j \frac{\sigma}{\omega \epsilon}) \mathbf{E} = 0 \quad (2-34)$$

where,

$$\gamma = \alpha + j\beta = j\omega \sqrt{\mu \epsilon} \sqrt{1 - j \frac{\sigma}{\omega \epsilon}} \quad (2-35)$$

is considered as the complex propagation constant where \mathbf{E} field in (2-34) could be solved assuming it has an x component with variations in z ,

$$\mathbf{E}_x(z) = \mathbf{E}^+ e^{-\gamma z} + \mathbf{E}^- e^{\gamma z} \quad (2-36)$$

$$e^{-\gamma z} = e^{-\alpha z} e^{-j\beta z} \quad (2-37)$$

A good conductor is defined as the one having a conductivity condition of $\sigma \gg \omega \epsilon$ where most conductors including the ones tabulated in Table 3-1 are categorized as good conductors. Therefore, (2-35) could be approximated as,

$$\gamma = \alpha + j\beta \approx j\omega \sqrt{\mu \epsilon} \sqrt{\frac{\sigma}{j\omega \epsilon}} = (1+j) \sqrt{\frac{\omega \mu \sigma}{2}} \quad (2-38)$$

where skin depth or characteristic depth of penetration is given as,

$$\delta = \frac{1}{\alpha} = \sqrt{\frac{2}{\omega \mu_0 \mu_r \sigma}} \quad (2-39)$$

where $\mu_0 = 4\pi \times 10^{-7}$ Henry/m is the permeability of free space and μ_r is the relative permeability of the medium. The skin depth equation, (2-39), implies that amplitudes of the fields penetrating inside the conductors will decay by an amount of $1/e = 36.8\%$ since $e^{-\alpha z} = e^{-\alpha \delta} = e^{-1}$ which is called the skin effect. The unavoidable skin effect in RF frequencies will highly contribute towards the total loss of the circuits and systems operating in RF and decreases the system's efficiency and passive components' quality factor. In result of the skin effect, the current will be confined in the outmost region of a conductor and the effective cross section area carrying current will reduced and decreases as frequency increases (2-39). Therefore, the ohmic resistance in RF regime will continuously grow as the frequency increases, by a factor of \sqrt{freq} . ultimately degrading the performance of the RF components. This is critically important

in design of next-generation RF circuits and systems where the operation frequency tends to increase to help lift the heavy traffic in lower frequency bands.

To overpass the skin effect and remove the \sqrt{freq} . relationship of ohmic resistance and realize conductors having minimal ohmic loss in higher frequencies, a planar multilayer conductor is proposed firstly in[3] where utilization of stacked ferromagnetic/nonferromagnetic thin films is proposed to set the μ_r in skin depth equation, (2-39) to zero, resulting in,

$$\delta = \sqrt{\frac{2}{\omega\mu_0\mu_r\sigma}} \approx \infty \text{ for } \mu_r = 0 \quad (2-40)$$

A skin depth of infinity implies current penetrating through the volume of the conductor and increased cross section of the current flow like a DC fashion. This will result in a decrease in the ohmic loss of the conductor for the frequency range where μ_r approaches zero and the skin depth goes to infinity. Figure 2-8 shows the planar superlattice conductor where the high frequency current flow is assumed in y direction and the effective permeability of the stacked layers is given as,

$$\mu_{eff} = \frac{\mu_N t_N + \mu_F t_F}{t_N + t_F} \quad (2-41)$$

where μ_N , μ_F , t_N and t_F are the magnetic permeability of the non-ferromagnetic layer, the magnetic permeability of the ferromagnetic layer, the thickness of the non-ferromagnetic layer, and the thickness of the ferromagnetic layer, respectively.

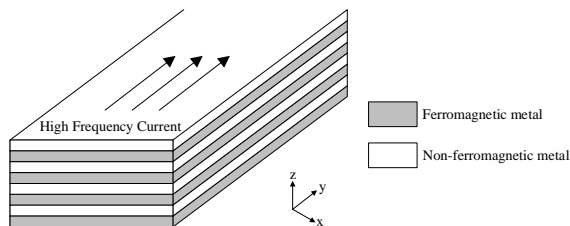


Figure 2-8. The planar superlattice conductors with alternating ferromagnetic/non-ferromagnetic thin films.

Due to the negative permeability of the ferromagnetic thin films in the microwave operation frequencies where ohmic loss reduction is intended, assuming $\mu_F < 0$ and $\mu_N = 1$ (for a non-magnetic material), by properly designing the multi-layer structure,

$$\mu_{eff} \approx 0 \text{ if } |\mu_F| = \text{thickness ratio} = \frac{t_N}{t_F} \quad (2-42)$$

Figure 2-9 shows the simulation results of the extracted ohmic resistances of the single-layer (solid) and multi-layer (superlattice) conductors in microwave regime using ANSYS HFSS v. 15.0. As expected by skin depth equation, (2-39), the resistance of the solid core conductors will increase by a factor of \sqrt{freq} as frequency increases; however, the resistance of the multi-layer conductor will have a minimum valley point for the frequency range where (2-42) is valid which is not dominated by the skin effect and is selectable by modifying the thickness ratio.

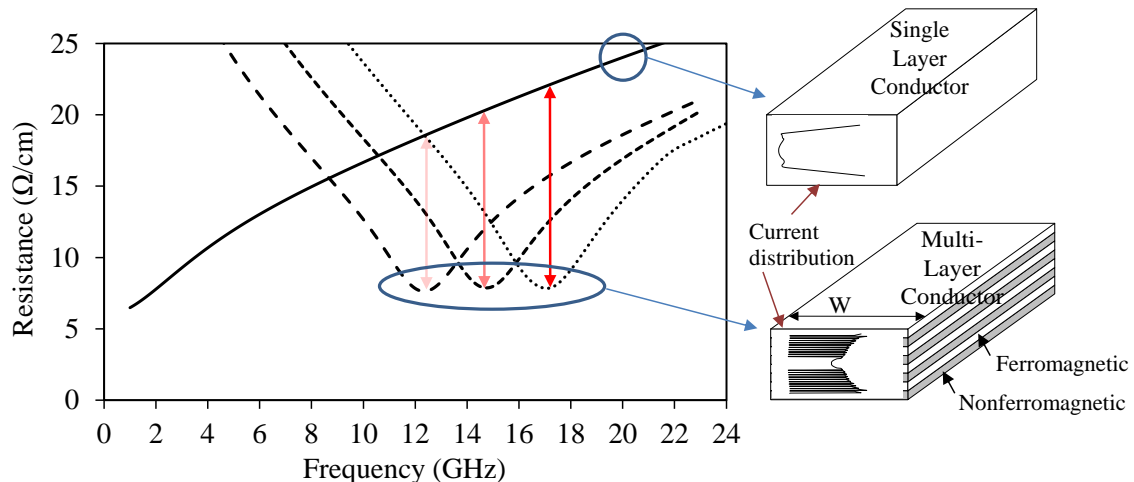


Figure 2-9. The comparison between the ohmic resistances of a single-layer (solid) conductor vs. a multi-layer (superlattice) conductor in microwave regime. The insets show the schematic of the conductors with the resulting current distribution in their cross section.

The extracted current distribution is depicted in the insets in Figure 2-9. For a single-core conductor, the current will be damped while penetrating through the volume of the conductor resulting in high resistive loss due to low effective cross section area. For the multi-layer

conductor, the current will be distributed uniformly in a multi-layer conductor and the whole cross section of the conductor will be used for current flow in the operation frequency. Also, it would be possible to tune the minimum resistance point of a multi-layer conductor (Figure 2-9) by changing the t_N / t_F ratio, independent of frequency as far as it is below the anti-resonance frequency (FAR) of the ferromagnetic material. This resistance reduction effect is more contrasted in the higher frequency where there is a bigger gap between the resistance of the multi-layer conductor and the conventional single-layer conductor highlighted in Figure 2-9.

Ferromagnetic Materials

Ferromagnetic materials are characterized as materials having a hysteretic response to an applied magnetic field in which their molecules will become magnetic dipoles and when the magnetic field is brought back to zero; they will have a non-zero remanent magnetization (\mathbf{M}_r).

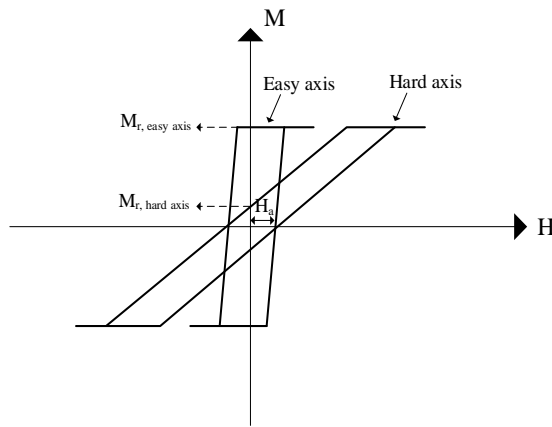


Figure 2-10. The typical hysteresis loop of a ferromagnetic material where the easy and hard axes are shown.

The saturation magnetization (\mathbf{M}_s) is the maximum amount of magnetization a ferromagnetic material could reach which is a function of type of the material. Coercivity (\mathbf{H}_c) is defined as the amount of magnetic field required to switch the orientation of magnetization (Figure 2-10). The coercivity is structure-sensitive and is a function of physical properties like thickness and geometrical dimensions, grain size and crystalline structure, film stress, etc.

Ferromagnetic materials are classified in two main categories of soft and hard magnetic materials. The soft magnetic materials will be easily magnetized and typically have a low coercivity value whereas the hard magnetic materials typically have a high coercivity value and are used as permanent magnets to store magnetic energy. Over the past few decades, there has been a considerable amount of research conducted on the modelling, characterization and synthesis of ferromagnetic materials due to their wide range of applications in telecommunication and wireless systems [26], power inductors and transformers [27], sensing applications [28], microwave absorbers [29], and low loss conductors [13]. Ferromagnetic materials, while deposited as thin films, have extremely dynamic frequency-dependent properties in frequencies ranging from DC to K-band (18–26 GHz). Figure 2-11 shows the real and imaginary parts of permeability and some of the RF applications of ferromagnetic materials as thin films in those frequencies.

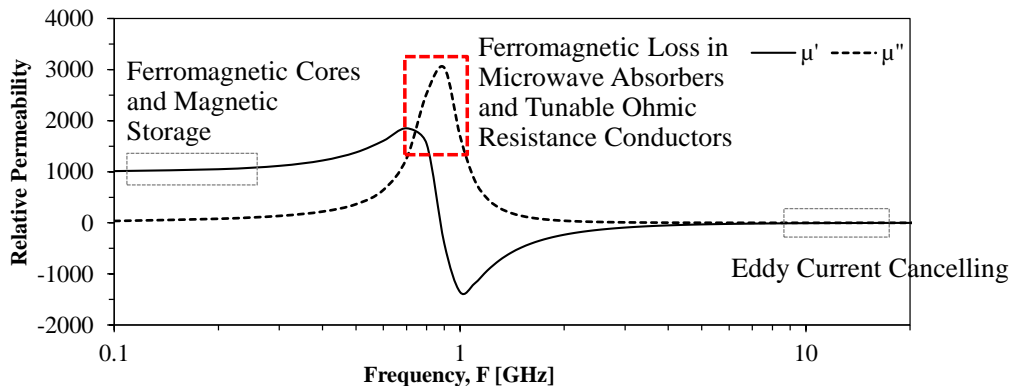


Figure 2-11. The RF applications of ferromagnetic materials as thin films.

Below the ferromagnetic resonance frequency (f_{FMR}), where the real part of magnetic permeability (μ_r) is high and imaginary portion indicating magnetic losses is low, ferromagnetic materials are most commonly used as the magnetic cores of the inductors to enhance the inductance and quality factor and improve the inductance density by storing the magnetic energy in radio frequency (RF) regime in MHz [30] and GHz [31] frequency ranges for a given wide

frequency spectrum. In frequencies much larger than f_{FMR} where the real part of the ferromagnetic materials is negative, they could be used for cancelling the self-generated eddy currents inside the conductor and improve the conductor loss in those frequency ranges. Right at f_{FMR} , the magnetic losses of a ferromagnetic material maximize offering a new application for ferromagnetic materials where a thin layer of ferromagnetic film could be used to transform the incident electromagnetic (EM) wave into heat. This narrow-band frequency range compared to wide-band lower frequency ranges $f \ll f_{FMR}$ (as the magnetic cores) or higher frequency ranges $f \gg f_{FMR}$ (low loss conductors), has not been much studied and investigated before. However, the naturally high amount of imaginary part of μ_r near f_{FMR} , being intrinsically narrow-band or frequency selective, and the ability to be widely tuned in frequency using external magnetic fields, drive the idea to use these materials in variable and tunable microwave components. In this work, we introduce a new application for ferromagnetic materials which utilizes the mentioned unique properties of those materials near f_{FMR} frequencies where the increased loss enables the realization of variable and tunable conductors in GHz frequency ranges.

The relative permeability of a ferromagnetic material is a function of frequency,

$$\mu_r(f) = \mu'_r(f) - j\mu''_r(f) \quad (2-43)$$

where the in-plane permeability of a ferromagnetic material is given by,

$$\mu_r(f) = \frac{\omega_{AR}^2 - \omega^2}{\omega_{FMR}^2 - \omega^2} \quad (2-44)$$

in which (ω_{FMR}) is the ferromagnetic resonance frequency above which the real part of μ_r becomes negative until the anti-resonance frequency (ω_{AR}) where the real part of permeability approaches zero. Also,

$$\omega_{FMR} = \sqrt{\omega_H(\omega_H + \omega_M)} \quad (2-45)$$

$$\omega_{AR} = \omega_H + \omega_M \quad (2-46)$$

in which,

$$\omega_H = \gamma H_a + j\alpha\omega \quad (2-47)$$

$$\omega_M = \gamma M_s \quad (2-48)$$

where γ is the gyromagnetic ratio, α is the Gilbert damping parameter, M_s is the magnetic saturation, and H_a is the anisotropy field. Also from (2-45), and (2-47)-(2-48),

$$f_{FMR} = \frac{\gamma}{2\pi} \sqrt{4\pi M_s H_a} \quad (2-49)$$

which is an important result relating the ferromagnetic resonance frequency to fundamental magnetic properties of a ferromagnetic material, the saturation magnetization, $4\pi M_s$, and anisotropy field, H_a .

The dynamic frequency response of the ferromagnetic thin film has been investigated theoretically [4] and experimentally[5] in a planar coordinating system. The complex permeability spectrum of an in-plane magnetized thin film can be calculated by the Landau-Lifshitz-Gilbert (LLG) equation,

$$\mu_r = \left\{ 1 + \gamma^2 4\pi M_s + \frac{[H_{Kp} - H_{Ku} + 4\pi M_s + j\omega\alpha/\gamma]}{\gamma^2 H_{Kp}[H_{Kp} - H_{Ku} + 4\pi M_s] - \omega^2 + j\omega\alpha\gamma[2H_{Kp} - H_{Ku} + 4\pi M_s]} \right\} \frac{\tanh[(1+j)t/(2\delta)]}{(1+j)t/(2\delta)} \quad (2-50)$$

where H_{Kp} is the in-plane anisotropy field, H_{Ku} is the out-of-plane anisotropy field, γ is the gyromagnetic ratio, α is the Gilbert damping parameter, t is the thickness of the thin film, ω is the angular frequency, σ is the electric conductivity of the magnetic thin film, and δ is the equation for the skin depth.

In most real application where application of an external magnetic field is not feasible, the in-plane anisotropy field is a function of internal magnetocrystallinity and demagnetizing fields leading to shape anisotropy for thin film applications. For most soft magnetic materials,

where $\omega_M \gg \omega_H$ and $\omega_{AR} \gg \omega_{FMR}$, the μ_r in (2-44) is negative for a broad frequency range of $\omega_{AR} < \omega < \omega_{FMR}$.

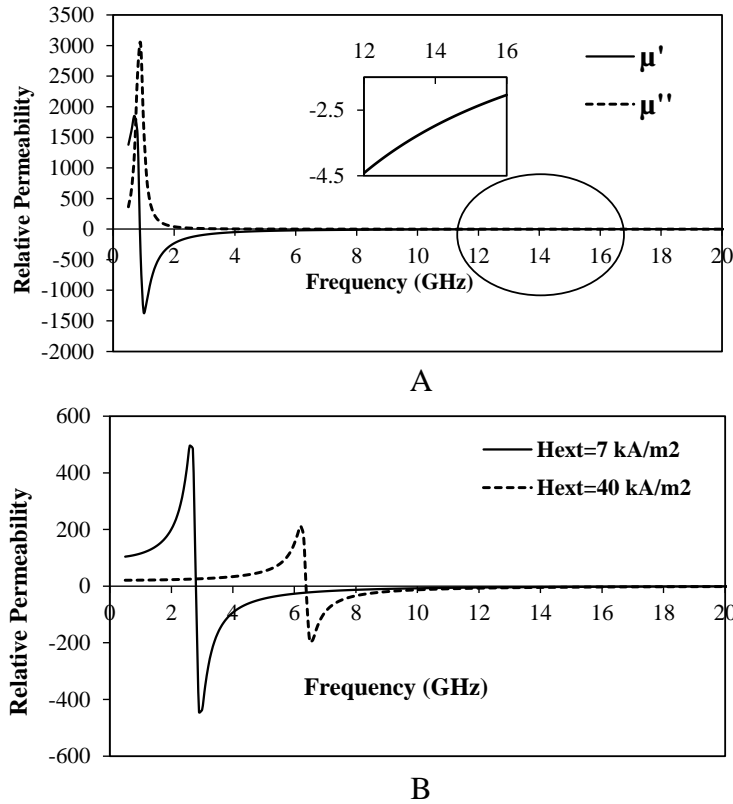


Figure 2-12. The calculated permeability values. A) Ni₈₀Fe₂₀ assuming no external magnetic field. The inset shows the real part, μ' , for the frequency between 12 to 16 GHz, B) the calculated real part of the permeability for different external magnetic fields.

Permalloy (Ni₈₀Fe₂₀) is one of the most commonly studied soft magnetic materials.

Figure 2-12A shows the calculated permeability of the Ni₈₀Fe₂₀ using the LLG equation where $M_s = 10000$ G = 1 T is assumed as the magnetic saturation, $H_{Kp} = 10$ Oe the in-plane anisotropy field, $H_{Ku} = 0$ Oe the out-of-plane anisotropic field, $\gamma = 1.75 \times 10^7$ s⁻¹Oe⁻¹ the gyromagnetic ratio, $\alpha = 0.01$ the Gilbert damping parameter, and t the typical thickness of the thin film. The skin depth, δ , is calculated by using the electrical conductivity of Ni₈₀Fe₂₀ and copper where $\sigma_{\text{Ni80Fe20}} = 6 \times 10^6$ S/m and $\sigma_{\text{Cu}} = 5.8 \times 10^7$ S/m, respectively. The ferromagnetic resonance frequency of Ni₈₀Fe₂₀ thin film, $f_{MR} \approx 900$ MHz and the anti-

resonance frequency is $f_{AR} \approx 28$ GHz. Figure 2-12B shows the tunability of the permeability of the ferromagnetic materials by using an external magnetic field. The f_{MR} frequency shifts to higher frequencies as the external magnetic field increases. As a result, by deposition of thin ferromagnetic layers with dynamic response as in LLG, that could be used as conductor to realize passive components with extraordinary performance, that couldn't be achieved by conventional conductors, as we call them "metaconductors". However, since the ferromagnetic materials have much lower conductivity compared to commonly-used high performance conductor materials like copper or silver, they could not be practically used as the solid conductor in RF components because of high conductor losses. In this work, we propose combining the ferromagnetic materials with ultra-thin thicknesses with the other non-ferromagnetic excellent conductors in a multi-layer nano-superlattice architecture. This will let us exploit those aforementioned dynamic properties of the ferromagnetic materials and build tunable RF components with new features and extra capabilities.

As mentioned before, ferromagnetic materials are often used as magnetic cores in order to enhance the inductance and increase the scalability of inductors by increasing the inductance per area term. For the aforementioned purpose, they are to be operated below their ferromagnetic resonance frequency (f_{MR}) where they have a high permeability value.

Ferromagnetic materials could be operated between the ferromagnetic resonance frequency (f_{MR}) and the anti-resonance frequency (f_{AR}) where the real part of the permeability, μ' , is negative. Therefore, they could be used as eddy current cancelling (ECC) conductors and the t_N/t_F is an important design parameter and by properly choosing the thickness ratio based on (2-42), it would be possible to make the effective magnetic permeability close to zero and enlarge the skin depth, resulting in the reduction of the conduction loss in the frequency range of interest.

Summary

In this chapter, a summary of the losses associated with the RF circuits and systems is given. RF inductors implemented in a CMOS process are used as a platform to identify the RF losses and to provide guidelines for realization of RF passives with reduced loss. Conductor losses, dielectric losses and related substrate loss are recognized as the major loss sources. At last, an introduction to the ferromagnetic materials and their characteristics in RF regime is made; since they are used as the structural material to fabricate RF passives with extraordinary characteristics like low loss conductors and magnetic field effect transconductors.

CHAPTER 3

LOW LOSS RADIAL CONDUCTORS FOR RF COMPONENTS

In the monolithic integration of giga-scale chips, where signal integrity including RC delay issues signifies, high performance conductors, transmission lines and interconnects are strongly demanded, which prompts development of high performance and low loss conductors in the RF regime. Table 3-1 tabulates the most common metals which are used by industrial and scientific research works and gives a comparison on their electrical and mechanical properties. Copper is the selected metal by most manufacturing processes to be widely used as a low loss conductor in many passive devices due to its high conductivity, ease of deposition with thicknesses ranging from nanometer to several microns, and moderate cost. The conductivity of copper is only 5% smaller than that of the silver, the highest conductive metal existing in nature. However, the advantages of using copper such as its high conductivity, might not be as beneficial in devices operating in radio frequency (RF) range due to the skin effect and other mentioned losses increasing its conductor loss.

Table 3-1. The comparison of common manufacturing metals and their electrical/mechanical properties.

Metal	Bulk Conductivity at 20°C (S/m)	Thermal Conductivity at 330 K (W.m ⁻¹ .K ⁻¹)	Young's Modulus (GPa)	Temperature Coefficient (K ⁻¹)
Silver	6.3×10^7	429	83	0.0038
Copper	5.96×10^7	401	130	0.003862
Gold	4.1×10^7	318	78	0.0034
Nickel	1.43×10^7	91	200	0.006

In this chapter, radial conductor architectures for conductor loss reduction in RF regime and their comparison and analysis are presented and the effects of the physical dimensions and the ferromagnetic materials will be discussed followed by experimental verification. The finite-element method (FEM) simulations are used for evaluating the parametric effects on the structures which are used for conductor loss reduction in RF.

The Proposed Cylindrical Radial Superlattice Conductor Architecture

A planar type superlattice conductor architecture has been previously reported for conductor loss reduction where metallic thin films with negative/positive permeability are used to drive the current through the volume of the conductor and overpass the skin effect. However, the planar superlattice conductors have electromagnetic discontinuity at the edge of the conductor which will introduce non-ideal field distribution coming from the finite lateral width and the fringing field at the edge of the microstrip or stripline type conductor. In order to eliminate this disturbance, a superlattice film with an infinitive width is plausible, but may not be very practical. Therefore, the planar superlative architecture is not fully taking advantage of the eddy current cancelling effect and a limited loss reduction is achieved. This section entails the proposed cylindrical radial superlattice (CRS) conductors that are proposed as the lowest loss conductors for circuits and systems operating in RF frequencies. The CRS conductor is demonstrated to overcome such drawbacks of the planar superlattice conductors, where a CRS conductor shows inherently a closed and continuous boundary condition in an azimuthal direction and therefore is considered to be more appropriate for ohmic loss reduction and more effectively lowering the conductor loss.

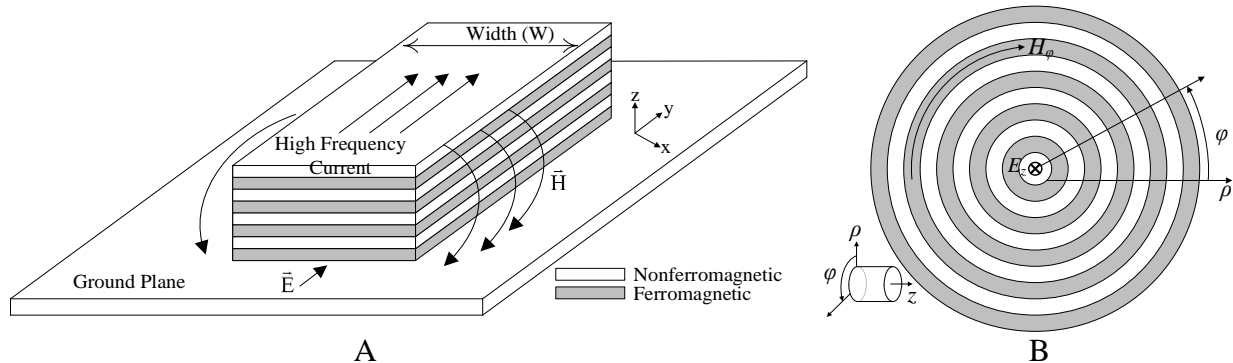


Figure 3-1. The schematic of superlattice conductor unit cells. A) The planar, B) the cylindrical radial superlattice conductor. The t_N and t_F are the thickness of the nonferromagnetic and ferromagnetic thin film layers, respectively.

Figure 3-1A shows the planar superlattice conductor where the t_N and t_F denote the thicknesses of the non-ferromagnetic and ferromagnetic thin film layers, respectively. While uniform field distributions are assumed inside a segment of the conductor (as shown), the field distribution will be disturbed by the fringing effect at the edges of the planar conductor and the eddy current cancelling will not be effective in those regions. Figure 3-1B shows the proposed cylindrical radial superlattice conductor (CRS) where the intrinsic radial shape of the conductor will offer a suitable platform for uniform field distribution without any discontinuity and therefore; an enhanced ohmic loss reduction effect without dependency on the dimensions of the conductor.

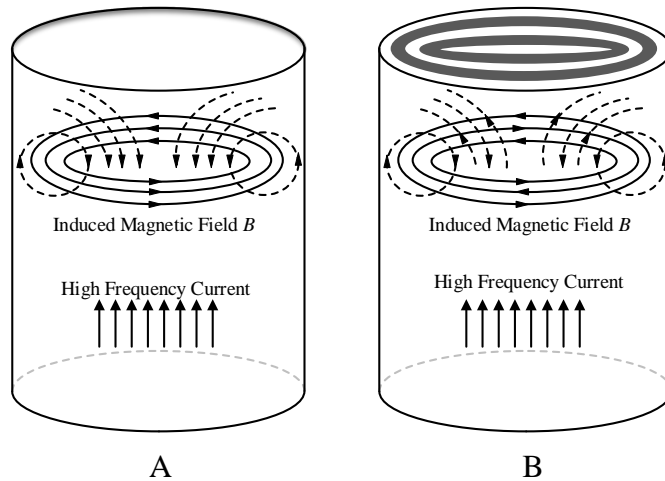


Figure 3-2. The illustration of eddy currents in a radial conductor carrying high frequency current using A) a solid conductor where generated eddy currents (dashed line) will cancel out the actual current in the middle of the conductor, and B) a CRS conductor where the ECC effect occurs and the current will be driven throughout the volume of the conductor decreasing the ohmic loss in the target frequency range. The white and gray colors show the nonferromagnetic, ferromagnetic metal layers, respectively.

Figure 3-2 illustrates the generated magnetic fields inside the regular solid core and the CRS conductors. In result of the RF current flowing which is alternating and high frequency, an alternating magnetic flux, \mathbf{B} , will be generated in both conductors based on Faraday's law. Because the generated magnetic flux, \mathbf{B} , is itself alternating, it will induce another set of eddy currents based on Ampere's law which will flow inside the conductor and in the opposite

direction of the actual current which will result in the skin effect, or the current will be confined in the outmost region of the conductor (Figure 3-2A)). Due to the negative permeability of ferromagnetic materials and based on (2-6), the generated magnetic fields inside the CRS conductor in ferromagnetic regions will be reversely induced and therefore the eddy currents will be cancelled inside the conductor shown in Figure 3-2B. Therefore, in the design frequency band, the high frequency current will be driven through the volume of the conductor similar to DC fashion; decreasing the ohmic loss in GHz range.

Simulations and Modeling of the CRS Unit Cell

Electromagnetic (EM) full wave simulations have been performed to examine the proposed CRS conductor using high frequency structure simulator (HFSS v. 15.0, ANSYS Inc.). Due to the utilization of very thin nano-layers as the multi-layer conductor, it is not feasible to simulate a large structure; i.e. in mm-range, and numerical finite-element-method (FEM) simulators won't be able to handle the model because of the high aspect ratio. As a result, a unit cell consisting of 10 μm -length of the conductors are simulated to verify the theory and the results are extended to design the superlattice conductors with reduced ohmic loss in microwave range.

Figure 3-3A depicts the simulation model which is used in ANSYS HFSS for CRS conductors. The CRS conductor consists of a solid core conductor covered by nanoscale multiple superlattice structures (Figure 3-4B) where a ground plane is used underneath the structure to allow propagation of transverse electromagnetic (TEM) waves. Note that an air dielectric layer is used between the CRS conductor and the ground layer to eliminate the contribution of the dielectric loss in analysis. The lumped element equivalent circuit model, as shown in Figure 3-3B, is used to extract the conduction resistance and inductance of the conductor's unit cell by assuming the series resistance and inductance values.

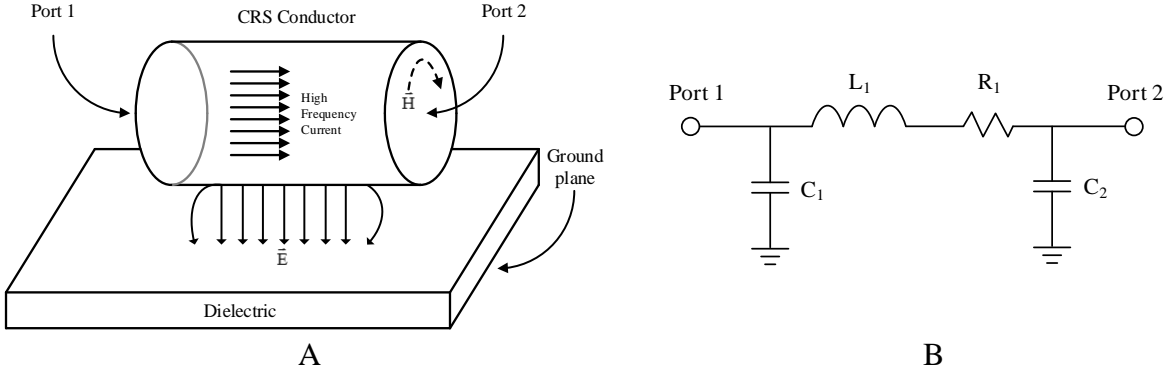


Figure 3-3. The simulation models. A) The two-port CRS conductor under study, B) the equivalent lumped element circuit model of the CRS conductor.

A unit cell of the CRS conductor with a length of 10 μm and 16 layers of Cu/Ni₈₀Fe₂₀ radial superlattice has been simulated for the extraction of equivalent parameters of resistance, inductance, and capacitance. The results are compared with those of the solid Cu reference conductor with the same dimension such as the conductor diameter and the length. In the equivalent circuit model of the two-port CRS conductor in Figure 3-3B, L₁ and R₁ are the series inductance and resistance between port 1 and port 2 and C₁ and C₂ are the capacitances between the top conductor and ground at each port. By using the Y-parameters in the 2-port network, the value of the equivalent circuit elements can be extracted,

$$Re[Y_{21}] = \frac{-R_1}{R_1^2 + \omega^2 L_1^2} \quad (3-1)$$

$$Im[Y_{21}] = \frac{\omega L_1}{R_1^2 + \omega^2 L_1^2} \quad (3-2)$$

By substituting (3-1) in (3-2), the L₁ and R₁ values could be calculated as in (3-3) and (3-4). For the frequency range above 0.1 GHz, (3-4) is used for the calculation of loss. As there is no dielectric layer surrounding the conductor introducing dielectric loss, R₁ is mainly attributed to the conductor loss.

$$L_1 = \frac{Im[Y_{21}]}{\omega[(Re[Y_{21}])^2 + (Im[Y_{21}])^2]} \quad (3-3)$$

$$R_1 = \frac{(-Re[Y_{21}])^{-1} \pm \sqrt{(Re[Y_{21}])^{-2} - 4\omega^2 L_1^2}}{2} \quad (3-4)$$

Figure 3-4A shows the simulated resistance spectra of the 16-layer CRS conductor in comparison with a reference Cu conductor. The CRS conductor consists of alternating 125 nm-thick Cu and 50 nm-thick Ni₈₀Fe₂₀ layers with a thickness ratio of 2.5:1. The resistance of the CRS conductor is lower than that of the Cu counterpart from 10 GHz and the lowest resistance is obtained at 15 GHz, where almost three times resistance reduction is achieved compared with the Cu counterpart. It should be mentioned that in each layer either Cu or Ni₈₀Fe₂₀ the following criteria are used for design: 1) the maximum thickness of each layer must be smaller than the skin depth of the material at the design frequency to suppress self-confined eddy current paths, 2) the thickness ratio of |Cu/Ni₈₀Fe₂₀| closely equals to the permeability ratio of |Ni₈₀Fe₂₀/Cu| at the design frequency.

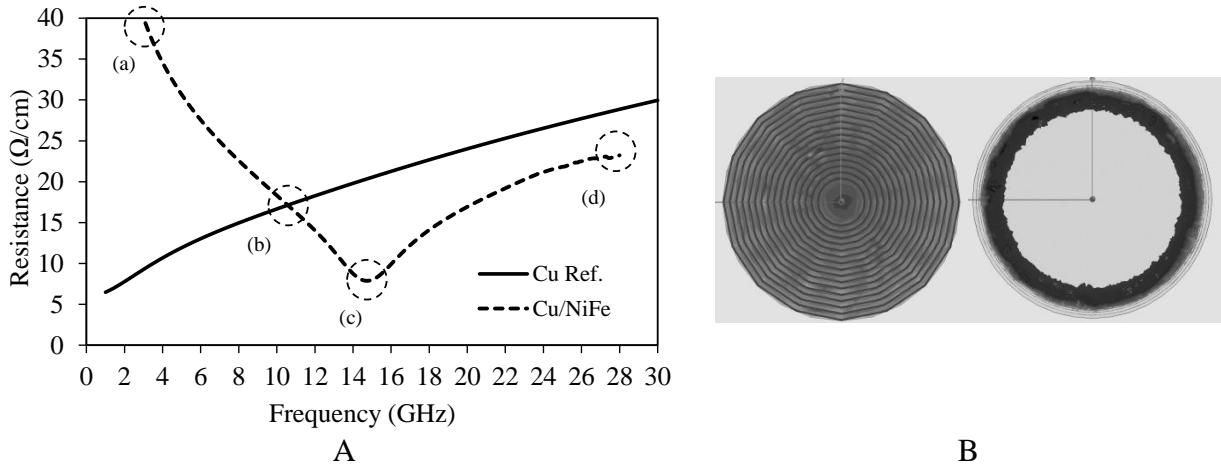


Figure 3-4. The resistance of a CRS conductor. A) With 16 layers of 125 nm-thick Cu and 50 nm-thick Ni₈₀Fe₂₀ (dotted line) and a solid Cu reference conductor (solid line) as a function of frequency. The (a), (b), (c), and (d) points are corresponding to the frequencies of 6 GHz, 10 GHz, 15 GHz, and 25 GHz in Figure 3-5, B) Simulated current distribution at the cross-section area of the CRS conductor (lower left) and the solid conductor (lower right) is shown.

The extracted frequency-dependent permeability in Figure 2-12 are used as the permeability for Ni₈₀Fe₂₀ which are fed to ANSYS HFSS for simulations. As the ferromagnetic

resonance frequency of Ni₈₀Fe₂₀ occurs at around 900 MHz, the resistance value on or right below and above the resonance frequency is prohibitively high because of high magnetic permeability and magnetic loss factor which is not the region of our interest and is skipped in analysis. Figure 3-4 shows the resistance of the CRS conductor between 4 GHz and 28 GHz. Simulated current distribution at each point of (a), (b), (c), and (d) is plotted in Figure 3-5. The uniform current distribution at 15 GHz is shown in Figure 3-5C.

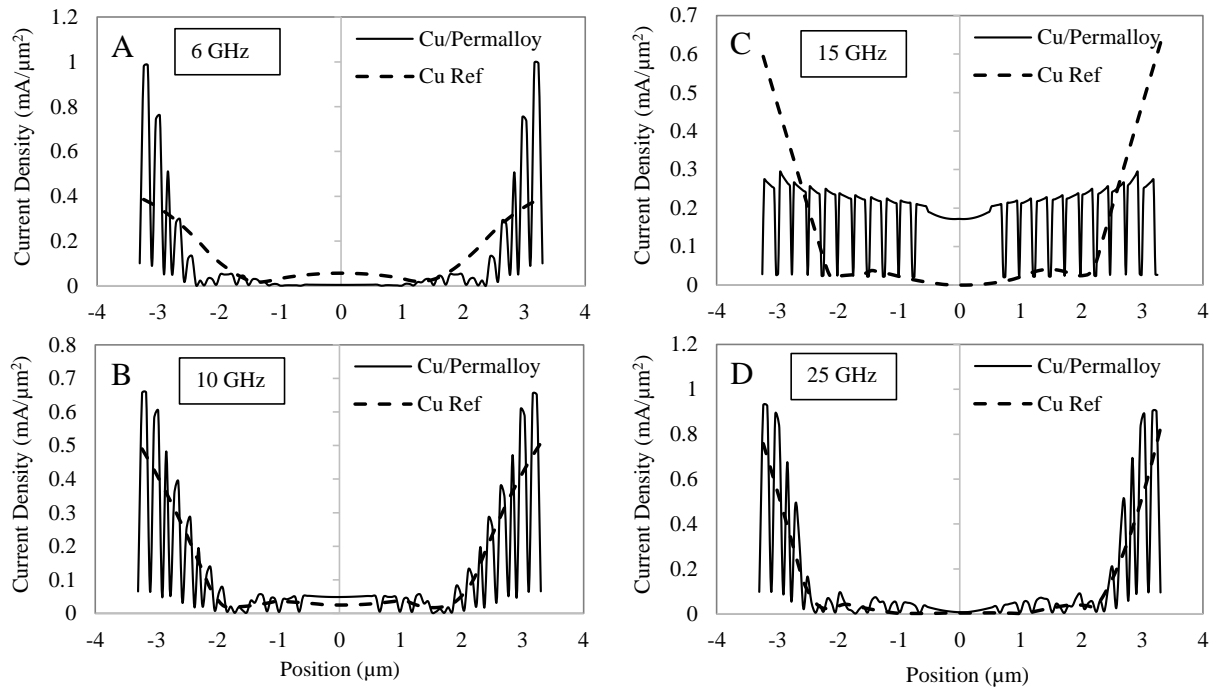


Figure 3-5. Current distribution of the 16-layer Cu/Ni₈₀Fe₂₀ CRS conductor (solid lines) with 125 nm Cu and 50 nm Ni₈₀Fe₂₀ and its solid Cu reference (dashed lines) at the frequencies: A) 6 GHz, B) 10 GHz, C) 15 GHz, and D) 25 GHz.

Between the frequency range of 4 GHz and 15 GHz, where the permeability of Ni₈₀Fe₂₀ increases from around -90 to -2.5, the resistance starts to decline steadily where it falls below the resistance of the solid Cu conductor at 10 GHz. Since the eddy current canceling effect begins in this frequency range, the resultant resistance does not go up as the frequency rises. At 15 GHz, the effective permeability of the CRS conductor becomes zero and the eddy currents from Cu layers and Ni₈₀Fe₂₀ layers cancel each other resulting in a more uniform current distribution and

the resistance reaches the minimum point. At this frequency, the thicknesses ratio of each layer is reciprocal to that of the permeability ratio.

Beyond 15 GHz, the eddy current canceling effect may be diminished, due to the continuously increasing permeability of Ni₈₀Fe₂₀ and the skin depth decreases again. Therefore, the resistance recovers to its ordinary value. According to the LLG equation (2-50), the permeability zero point of the Ni₈₀Fe₂₀, e.g. the anti-resonance frequency (f_{AR}) is approximately 28 GHz. The extracted current distribution at 25 GHz is shown in Figure 3-5D. Beyond 28 GHz, the effective permeability becomes positive again and the resistance increase follows the trend of \sqrt{f} .

The Effect of Layer Thickness on Resistance Spectra

The thickness of the individual layer has a great impact on the ECC effect as a detailed analysis will be given later in this chapter. Generally, the smaller the thickness of each layer, the lower resistance of the CRS conductor can be achieved. In order to investigate the relationship between the layer thickness and the resistance spectrum, the CRS conductors have been simulated with the different total number of layers while keeping the same total conductor radius dimension and thickness ratio (Cu/ Ni₈₀Fe₂₀: 4/1). The conductors with the same total thickness of 6 μ m and the same thickness ratio but different individual layers' thicknesses are used as follows: 1) N=8 layers with t_{Cu}=600 nm/ t_{NiFe}= 150 nm; 2) N=12 layers with t_{Cu}=400 nm/ t_{NiFe}= 100 nm; and 3) N=24 layers with t_{Cu}=200 nm/ t_{NiFe}=50 nm. As illustrated in Figure 3-6, the resistance at 13 GHz decreases as the number of layers is increased where a reduction of close to 4 times compared to reference Cu conductors occurs at 13 GHz when 24 layers of Cu/Ni₈₀Fe₂₀ layers are used. As mentioned previously, a multi-layer superlattice conductor with the thinner metal layers has a better ECC effect and is more appropriate for ohmic loss reduction. However,

the thinner the metal layers, the harder is the fabrication to achieve uniform layers, especially, for the cylindrical shape conductors.

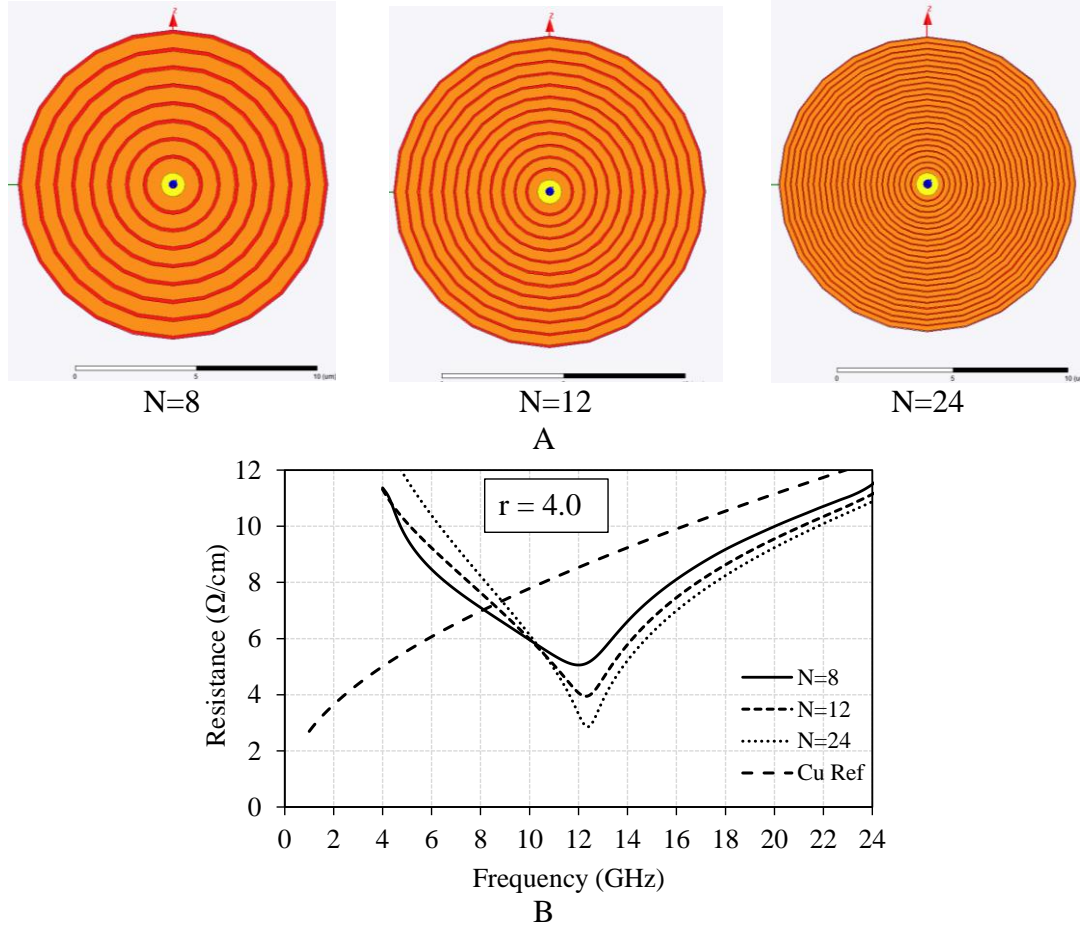


Figure 3-6. The conductors with different number of layers. A) The schematic view, B) the resistance spectra of CRS conductors with the different number of layers, with the same total diameter dimension and the same thickness ratio of Cu/ Ni₈₀Fe₂₀ of 4:1.

Figure 3-7 depicts the tunability of the CRS conductors where the minimum resistance point is shifted based on the design parameter of Cu/Ni₈₀Fe₂₀ ratio. For different thickness ratios, the frequency in which the thickness ratio is equal to $|\mu_r|$ is different and the minimum ohmic loss is different. Three different minimal frequencies of 12, 15, and 18 GHz are showed in Figure 3-7 with a thickness ratio of 4, 2.5, and 1.6, respectively. The simulation results in Figure 3-7 might not reflect an actual CRS conductor since they are done using a unit cell structure; however, the tunability of the conductor by modifying the thickness ratio is demonstrated.

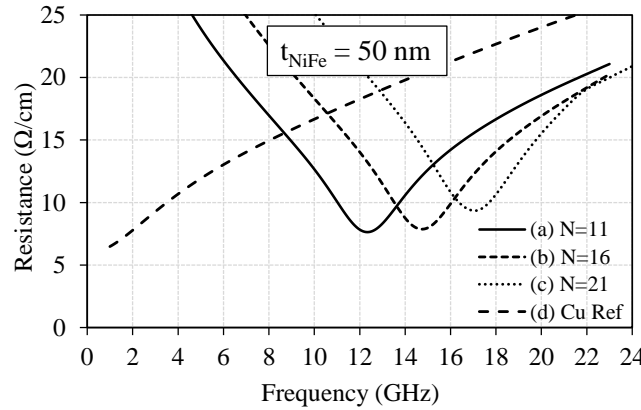


Figure 3-7. Resistance spectra of CRS conductors with the different thickness ratio of $\text{Cu}/\text{Ni}_{80}\text{Fe}_{20}$ and the same total diameter dimension: (a) 200/50 nm with $N=11$, (b) 125/50 nm with $N=16$, (c) 80/50 nm with $N=21$, and (d) reference solid Cu conductor.

In order to make the fabrication feasible, a gold wire-bonded structure will be used to realize CRS conductors. As a result, a set of simulations are also done based on a gold core coated with multi-layer structure consisting of $\text{Cu}/\text{Ni}_{80}\text{Fe}_{20}$ layers (Figure 3-8B). Figure 3-8A shows the simulation results where a $\text{Cu}/\text{Ni}_{80}\text{Fe}_{20}$ ratio of 2.5:1 with a $\text{Cu}/\text{Ni}_{80}\text{Fe}_{20}$ thickness of 400 nm/160 nm is used. At 15 GHz, a resistance reduction ratio of 2 compared to the reference Cu conductor has been achieved for the given conductor.

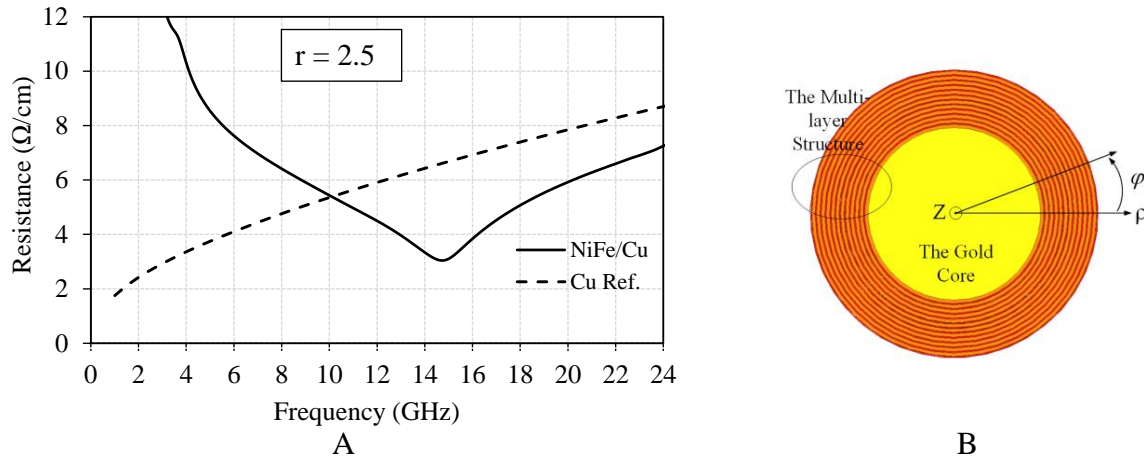


Figure 3-8. The resistance spectra of a CRS conductor. A) With 16 layers of 400 nm-thick Cu and 160 nm-thick $\text{Ni}_{80}\text{Fe}_{20}$ and a ratio of 2.5:1 vs. its solid Cu reference (solid line), B) the cross section of the simulated CSR structure with a gold core in ANSYS HFSS.

The Radial Inductors Using the CRS Conductors

The simulations of the CRS unit cell were provided in last section. In order to practically verify them, a structure which is fully radial is required as the core so that the multi-layer ferromagnetic/non-ferromagnetic layers could be deposited on it to achieve the CRS conductor architecture. As a result, another requirement of the structure is its uniformity so the upcoming layers with nm-range thicknesses could be uniformly deposited. In this work, a gold wire-bonded structure (inset in Figure 3-9A) is selected as a candidate that has the requirements of being radial and uniform and is used to verify the performance of the CRS conductor.

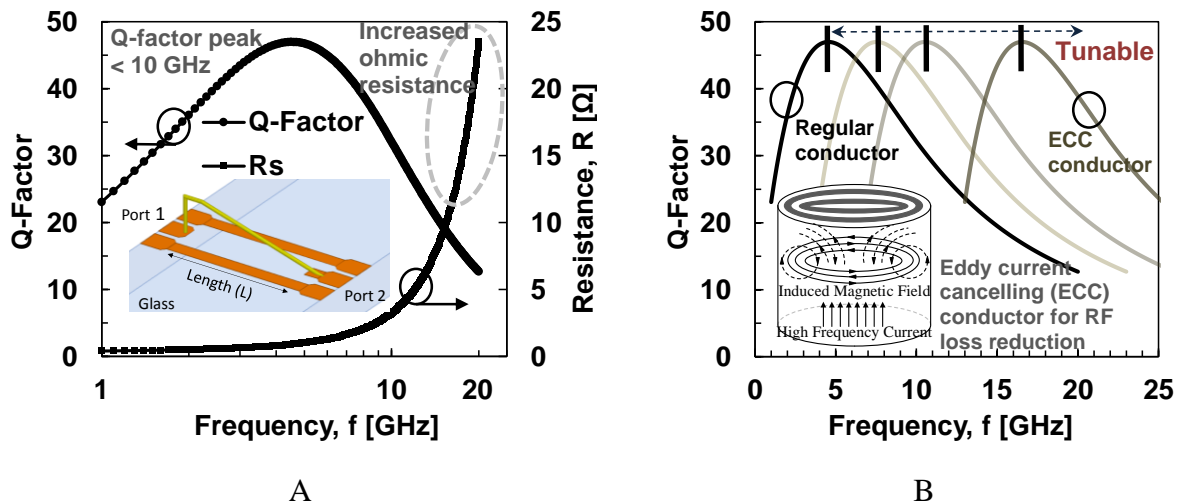


Figure 3-9. The simulation results of the air-lifted radial inductors. A) Inductor's series resistance and Q-factor versus frequency with $L = 2$ mm, where the inset shows the schematic of the two-port air-lifted inductor, B) the tunability of the Q-factor peak point in ECC conductors versus operation frequencies. The white/gray colors in the inset show the Cu/NiFe films where the reverse direction of generated eddy currents in NiFe causes the ECC phenomenon.

Figure 3-9A shows the simulation results of a two-port air-lifted radial inductor with a diameter of 25 μm on the glass substrate with coplanar waveguide (CPW) feedings with a length of 2 mm and inductance of 1.9 nH, using ANSYS HFSS v. 15.0. Due to the increased ohmic resistance of the inductor in higher frequencies in result of skin effect, the simulated peak point

of the Q-factor occurs below 10 GHz. Therefore, realization of passive components with high performance in higher frequencies such as K-band, is of great challenge.

Although the substrate losses will be the dominant loss mechanism minimizing the performance of RF passives in high frequencies, with the numerous works reported to suppress the substrate losses [8], [19] or with the growth of interposer technologies [46], passive components could be completely fabricated on a dielectric substrate. As a result, minimizing the conductor losses will highly improve the efficiency of the RF systems operating in higher frequencies and will be the key solution to shift the Q-factor maximum point to higher operation frequencies. This is more prominent when considering the trend in the operation frequency of the RF circuits and systems which is towards higher frequencies due to the heavy traffic in lower frequency bands and miniaturization purposes. This effect is shown in Figure 3-9B where using a multi-layer non-ferromagnetic / ferromagnetic superlattice conductor, the generated eddy currents inside conductor layers cancel each other out due to the negative permeability of the ferromagnetic layers. As a result, the conductor loss will be minimized in the frequency range of interest not driven by skin effect and utilization of the eddy current cancelling (ECC) conductors would allow implementation of passive components with high performance in high frequencies.

The CRS Conductors Using Electrodeposition

The proposed CRS conductors have been micromachined to experimentally examine their performance. For the implementation of a CRS conductor, multiple thin layers of Cu and Ni₈₀Fe₂₀ have been deposited alternately to the thickness as designed around a cylindrical conductor made of gold with a diameter of 25 μm. The cylindrical gold conductor core, i.e. a gold bonding wire, has been prepared with a commercial wire bonder (Kulicke and Soffa Industries, Inc.) which provides the platform to fabricate the CRS architecture.

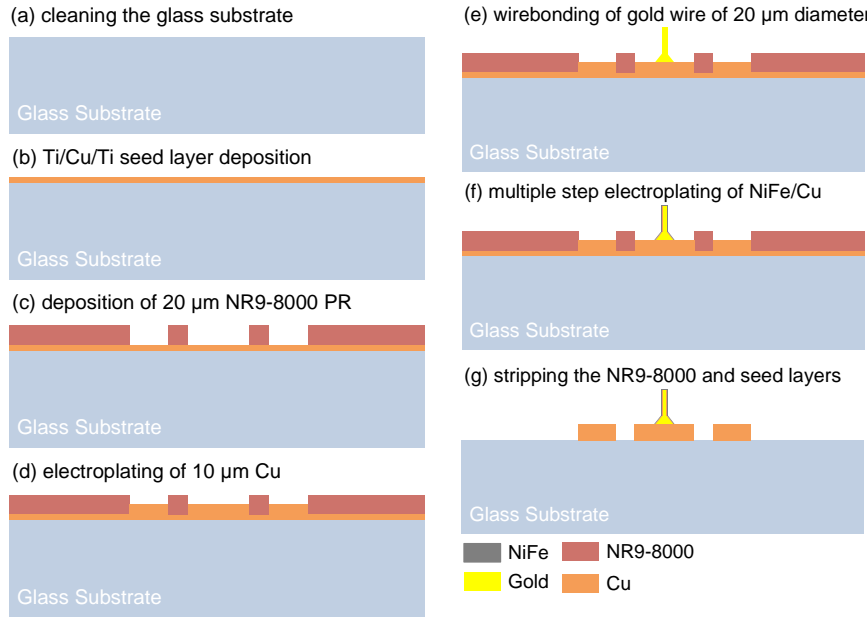


Figure 3-10. The microfabrication process steps for the CRS conductors made of Cu/NiFe layers using a gold conductor core.

Also, since the gold wire is conductive, there will be no need for a seed layer on the radial conductor which makes the fabrication a lot easier and more efficient. Figure 3-10 shows the microfabrication process steps for the CRS conductors made of Cu/NiFe layers using a gold conductor core [47]. The seed layers (Ti/Cu/Ti) are deposited on a clean glass wafer and the pads with CPW input probe are made of 10 μm electroplated copper. Immediately after the electroplating in step (d), the gold wire bonding has been performed to increase the yield of the wire bonding before the copper gets oxidized. After the production of a natural oxide on the copper pads in room temperature, the gold wire will not bond on them. The radial inductors with different pad sizes and lengths are fabricated as shown in Figure 3-11A. The 2-inch substrate containing the devices will go through the multi-step electroplating to realize the CRS conductors. Table 3-2 shows the composition and conditions of the in-house electrolyte bath used for electrodeposition of Ni₈₀Fe₂₀. Although the fluctuation of thickness is higher in electrodeposition compared to other methods of deposition including sputtering and evaporation,

there are methods to control the thickness and enhance the thickness uniformity of electrodeposited conductors [24]-[25]. Figure 3-11B shows the top view of the device after deposition of NiFe/Cu thin films which shows a clear color difference between two. The devices are finally released by removing the NR9-8000P electroplating photoresist followed by removal of the seed layers.

Table 3-2. The composition of the utilized $\text{Ni}_{80}\text{Fe}_{20}$ electrolyte.

Compound	Concentration (g/L)
Nickel Sulfate - $\text{NiSO}_4\cdot(\text{H}_2\text{O})_6$	40
Iron Sulfate - $\text{Fe}_2(\text{SO}_4)_3$	8
Nickel Chloride - $\text{NiCl}_2\cdot(\text{H}_2\text{O})_6$	5
Boric Acid – H_3BO_3	25
Saccharin - $\text{C}_7\text{H}_5\text{NO}_3\text{S}$	3
pH level	4
Temperature	24° C

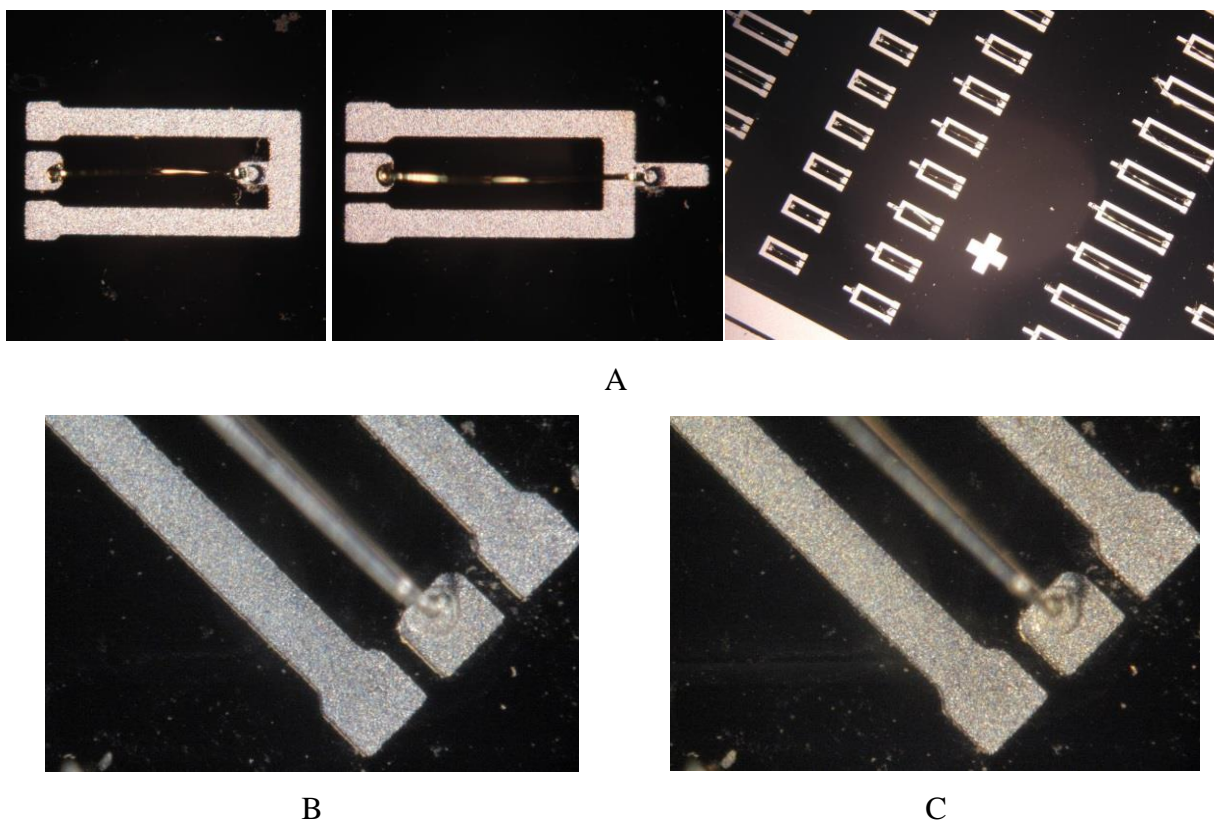


Figure 3-11. The optical micrographs of the fabricated radial inductors with different shapes. A) Prior to multi-step electroplating, B) after deposition of 160 nm NiFe, C) after deposition of 400 nm Cu.

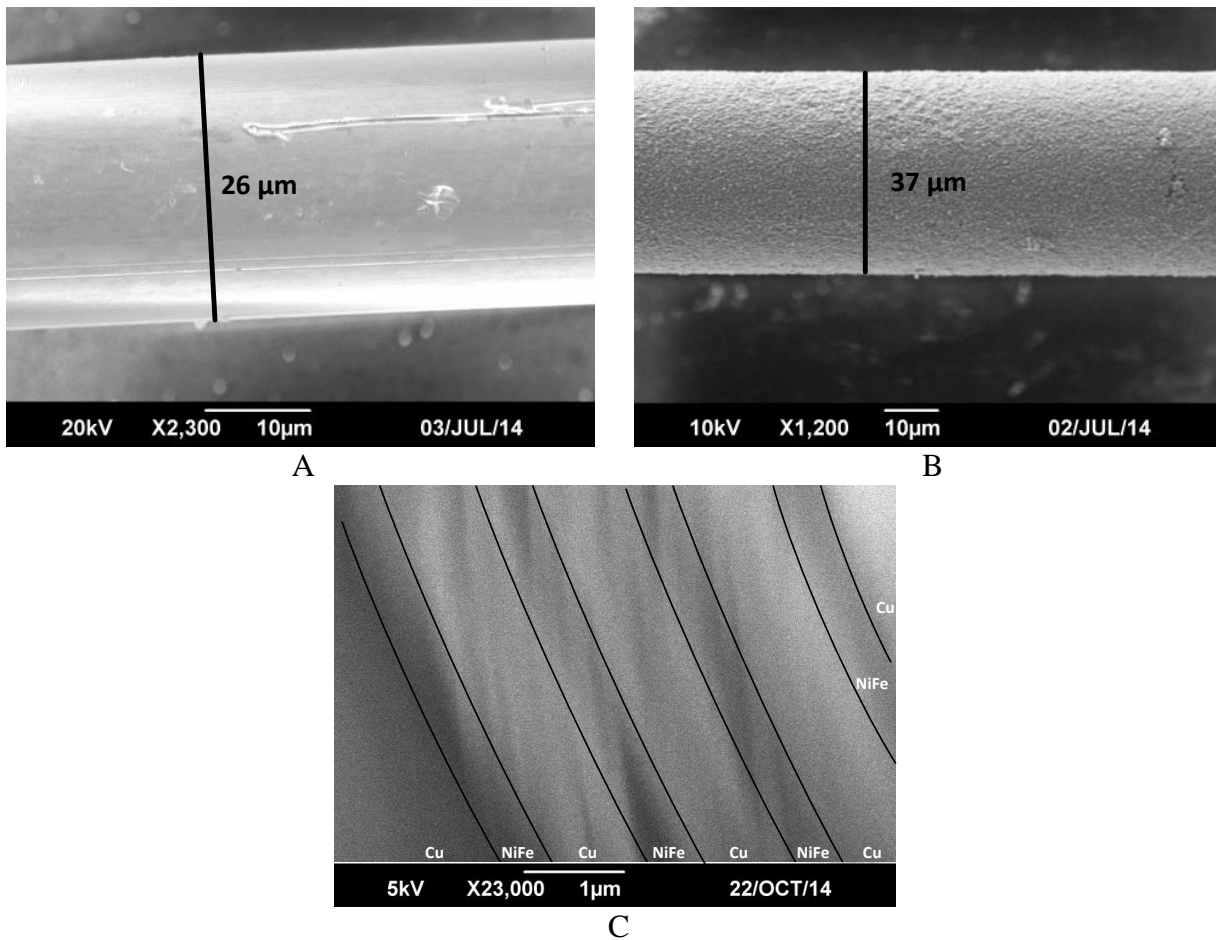


Figure 3-12. The SEM micrograph of the gold wire. A) Prior to electroplating process, B) after 21 layers of $\text{Ni}_{80}\text{Fe}_{20}/\text{Cu}$ (160 nm/400 nm) electroplating, and C) cross section view of the CRS conductors in SEM.

Figure 3-12 shows the scanning electron microscopy (SEM) micrographs of the wire bonded structure before and after electroplating processes consisting of a conformal deposition of 21 layers of $\text{Ni}_{80}\text{Fe}_{20}/\text{Cu}$ (160 nm/400 nm) layers. In order to see each individual layer, SEM pictures have been taken (Figure 3-12C). The conductors' cross sections are cut by using a laser machine and immersed inside a polymer to get stabilized. The polymer containing the cross section cut of the conductors has been polished using several fine polishing pads to view the cross section. Due to the method of taking cross section view images, portion of the polymer stays on the cross section which deteriorate the quality of the images. However, the routings of the deposited metal thin films could be recognized in SEM. Figure 3-13 shows the SEM images

of the fabricated air-lifted inductors using CRS conductors. The equivalent circuit model is the same as one in Figure 3-3B while port 2 is grounded. The air-lifted architecture of these conductors will help reduce the dielectric loss and study on their conductor loss. Nanoscopic thin films are then deposited using electroplating as the conformal and uniform coating method for these radial-shape conductors.

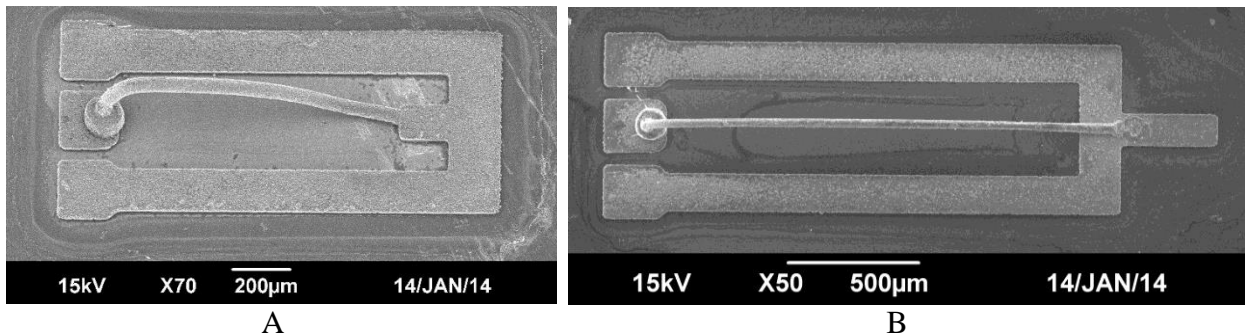


Figure 3-13. The SEM of the air-lifted radial inductors with A) L=0.5mm, and B) L=1.5mm.

The air-lifted inductor has been characterized using a vector network analyzer (E5071C, Agilent Inc.) after standard short-open-load one-port calibration between 1 and 20 GHz. The high frequency (GHz range) measurements have been performed in 1~ 20 GHz range while microwave performance in the Ku-band (12 ~ 18 GHz) is detailed. Figure 3-14A shows the measured resistance of the air-lifted inductor made of the CRS conductors with 1.5 mm length (Figure 3-13B) as a function of frequency. Due to the higher resistance (R_1) of the CRS conductors in low frequency region ($f < 10$ GHz in Figure 3-4A), the Q-factor ($\equiv \omega L/R$) of the reference Cu conductor is higher compared to that of the CRS conductors. However, when the frequency reaches 10 GHz and goes above, as predicted in Figure 3-4A, the resistance of the CRS conductors starts falling below that of the reference conductor and the Q-factor of the CRS conductors is higher while it reaches a peak value of 45 at 18 GHz. Figure 3-14B shows the

extracted Q-factor and inductance of the fabricated CRS conductor and the reference Cu conductor.

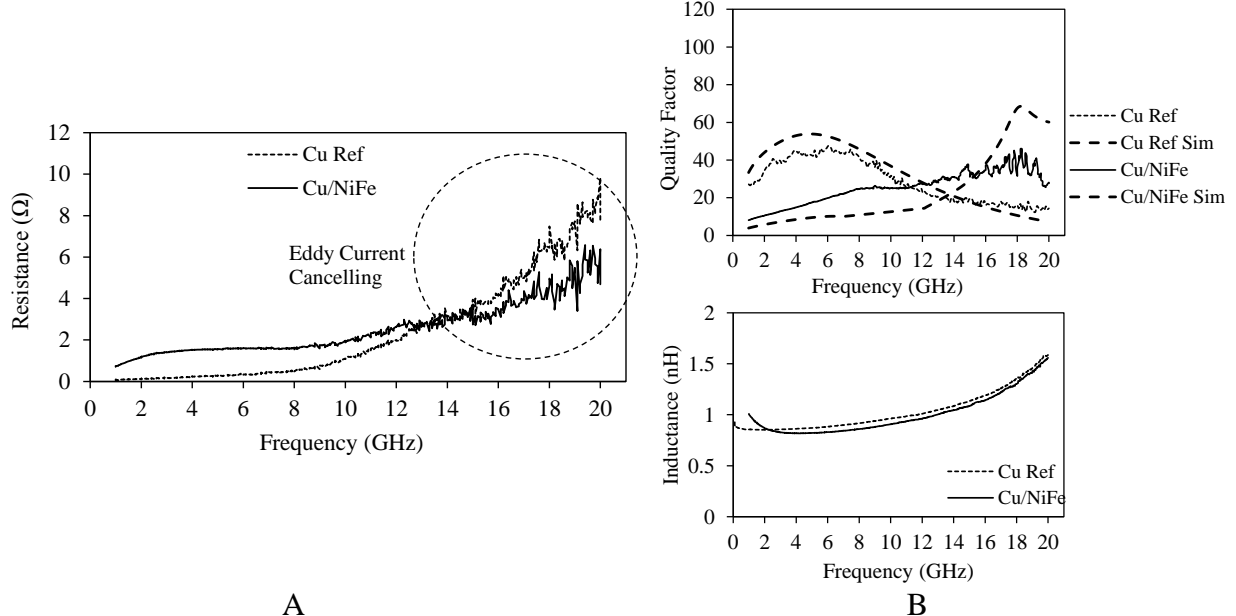


Figure 3-14. The measurement results of the A) extracted inductance and resistance of the CRS conductor compared to the reference solid Cu conductor, and B) quality factor and inductance of the 1-mm long CRS conductor based inductor with $t_{\text{NiFe}} = 160 \text{ nm}$, $t_{\text{Cu}} = 400 \text{ nm}$.

Due to the very high aspect ratio of the structure, namely, the ratio between the inductor's length to the thickness of each individual layer, our finite-element modelling software will not be able to simulate the whole structure at once. Therefore, a unit cell of $10 \mu\text{m}$ length has been simulated as a subcircuit, which is further cascaded to the length of the inductor to extract the lumped element parameters and the Q-factor of the air-lifted half-turn Cu/Ni₈₀Fe₂₀ inductor. The simulation results of the CRS and reference Cu conductors are also depicted in Figure 3-14B. First, the measurement result of the Q-factor for the reference Cu conductor is slightly lower than that of the simulation which is attributed to fabrication imperfection and surface roughness in the real conductor, while the overall trend of the Q-factor from measurement follows well that of the simulation. For the CRS conductors, the Q-factor in measurement peaks at a frequency close to the simulation results, while the Q-factor of the measurement is higher in the low frequency

range ($f < 14$ GHz). This is attributed to the fact that the actual permeability of the Ni₈₀Fe₂₀ thin films is not as high as assumed in the simulations.

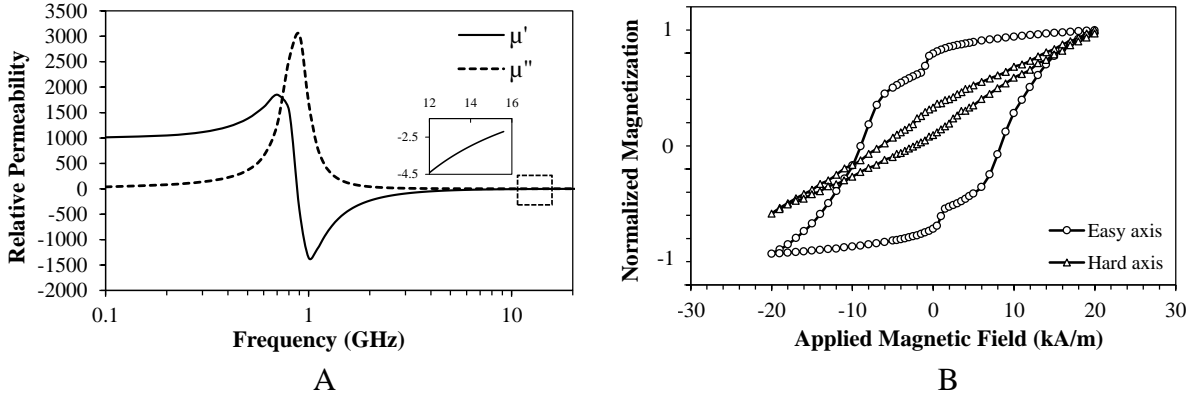


Figure 3-15. The estimated real part (solid line) and imaginary part (dashed line) of A) the permeability spectra of a Ni₈₀Fe₂₀ thin film in the frequency range of 0 to 20 GHz. At 15 GHz, the real part of the permeability is -2.5, B) the magnetic hysteresis loop measurements of the multilayer Cu/Ni₈₀Fe₂₀ thin films which are used in this work.

As a result, the resistance of the Cu/Ni₈₀Fe₂₀ inductor will be lower in the fabricated one which accounts for the higher Q-factor in low frequency region ($f < 14$ GHz). Also, fabrication defects such as the non-uniformity of the plated nanolayers, the surface roughness, in some portion of the overall conductor structure will result in mismatches. This may be favorably utilized for broad band high Q applications operating in Ku-band as the phenomenon is fully understood. Figure 3-15 shows the utilized permeability data for simulations and the ferromagnetic material characterization from vibrating sample magnetometer (VSM) measurements (ADE Technologies EV9 with a maximum applied field of ± 1800 kA m⁻¹). Figure 3-16 shows the measurement results of the implemented CRS inductors with 0.5 mm length (Figure 3-13A) where regular wire inductors are also measured as control devices for comparison [48]. As predicted in Figure 2-9, the RF resistance of the single layer copper constantly increases with frequency due to the skin effect while that of the CRS conductor is higher in the low frequency range but starts to fall below that of the regular wire conductor at the

frequency range between 10-24 GHz. Therefore, the presented CRS conductors could be exploited as low loss conductors for RF passive components including interconnects, transmission lines, inductors, etc. in higher frequencies where regular conductors have a high loss and low Q-factor.

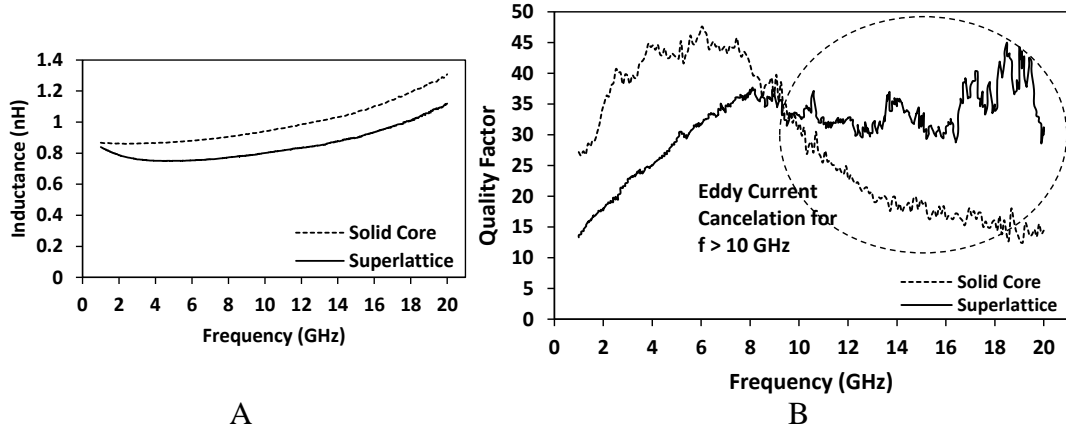


Figure 3-16. The measurement results of the 1 mm long CRS and regular wire inductors, A) the measured inductance, and B) the measured Q-factor.

A comparison of the reported inductors consisting of multilayer structures for ohmic loss reduction in literature and this work is given in Table 3-3.

Table 3-3. Comparison of the state-of-the-art inductors with multilayer conductors.

Reference	Structure	Inductance (nH)	Q-factor
[9]	Cu/CoZrNb	1.5	20 @ 6 GHz
[10]	Cu/NiFe	1.5	21 @ 15 GHz
[12]	Cu/CoZrNb	1.4	20 @ 10 GHz
This work [13]	Radial Cu/NiFe	1.4	45 @ 18 GHz

The CRS Conductors Using Physical Vapor Deposition

In previous section, CRS conductors using electrodeposition are reported where the proposed conformal method for deposition of Cu/NiFe nano-layers enables the fabrication of full CRS conductors with improved conductor loss in higher frequencies. However, the surface roughness resulting from electrodeposition and the minimum possible thickness will limit the conductor loss reduction offered by those conductors. Also, the full superlattice structure with uniform radial shape will result in a higher resistance in lower frequencies (< 10 GHz) while the

conductor loss reduction in higher frequencies in K-band is observed. In this section, sputtering method has been used for implementation of the state-of-the-art air-lifted radio frequency (RF) inductors made of hybrid cylindrical radial superlattice (*h*-CRS) conductors with a gold core featuring ultra-high quality factor (Q-factor) in ultra-wideband (UWB) and K-bands. A CRS conductor is made of paired Cu/NiFe layers with a thickness of each pair of 150 nm/25 nm, respectively, using a DC/RF sputtering thin film deposition process. The negative permeability of NiFe thin films above their ferromagnetic resonance frequency is used to cancel the eddy currents inside conductors and reduce the conductor loss in Ku and K-bands. The directional thin film deposition aspect of the used fabrication method for the CRS conductors results in a hybrid conductor structure comprising both solid and multi-layer superlattice parts leading to dual-band high-Q characteristics in UWB and K bands. The intrinsic radial shape of the utilized CRS conductors with the uniform and closed boundaries make them superior for the super compact RF low loss conductors. In result of using CRS conductors with ultra-thin layers and the air-lifted structure with suppressed dielectric losses, a record-breaking Q-factor of greater than 80 at 20 GHz is achieved for 1.8 nH inductors.

Analysis and Design

The full CRS conductor in Figure 3-17A will offer a suitable platform for uniform field distribution without any discontinuity because of having inherently radial shape. Therefore, an enhanced eddy current cancelling (ECC) effect without much dependency on the conductor's lateral dimensions is achieved unlike planar superlattice conductors which have discontinuity at the edges and limited ECC effects. Figure 3-17B shows the proposed conductor in which conductor loss suppression is controlled by both the CRS structure in higher frequency bands and the solid structure in lower frequency bands. Therefore, a dual-band increased Q-factor is achievable using the proposed structure as shown in Figure 3-18. The first band residing in the

ultra-wide-band spectrum (UWB, 3.1 – 10.6 GHz) is attributed to the lower solid conductor part of and the second band residing in K-band (18 – 27 GHz) results from the upper superlattice structure with controlled ohmic loss reduction.

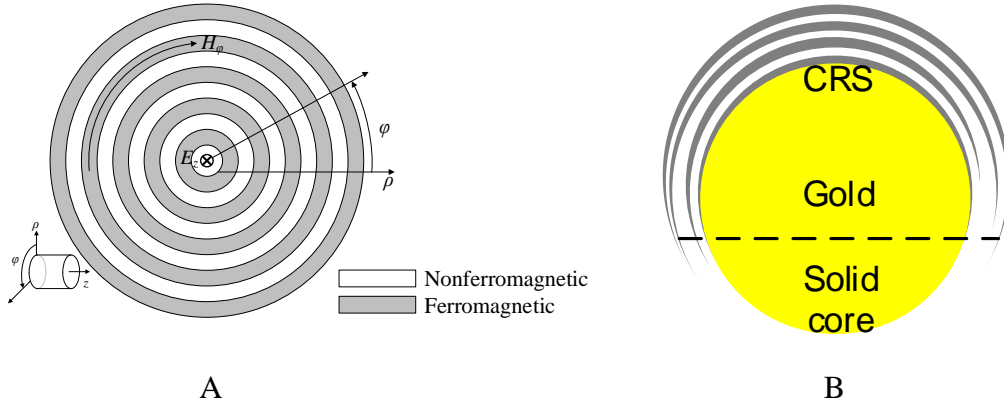


Figure 3-17. The cylindrical radial superlattice conductors. A) Full CRS conductor, B) the proposed hybrid cylindrical radial superlattice (*h*-CRS) conductor. Gray and white colors denote the ferromagnetic and non-ferromagnetic thin films, respectively

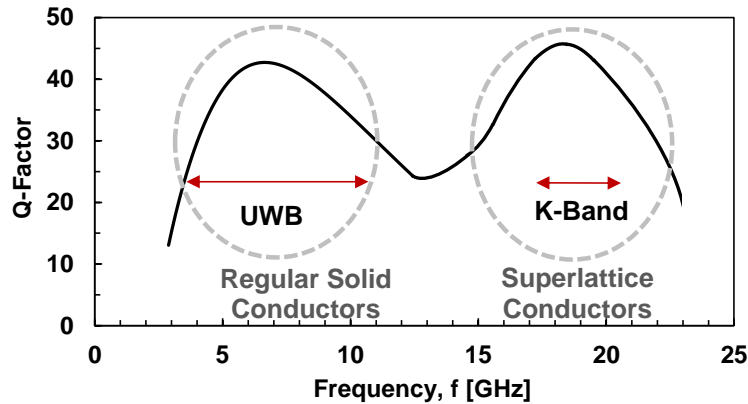


Figure 3-18. The concept of the dual-band improved Q-factor using a hybrid conductor consisting of the lower regular solid conductor for the first band and the upper superlattice conductor for the higher band.

Figure 3-19A shows the simulation results of the extracted ohmic resistance of conductors' unit cell using ANSYS HFSS v. 15.0. The permeability values of NiFe shown in Figure 2-12A are used for this simulation. The ohmic resistance of the conductors (i), (ii), and (iii) in Figure 3-19B which are full CRS, solid Cu with gold core, and half CRS, respectively, are simulated. At $f = 14$ GHz, the Cu/NiFe thickness ratio approaches the $|\mu_{\text{NiFe}}|$ ($| -6 |$ in 14 GHz)

resulting in minimum ohmic resistance versus frequency. Although the full CRS conductor ((i) in Figure 3-19B) has a lower RF resistance compared to half CRS conductor, its resistance in below 10 GHz band is higher than reference Cu and half CRS conductors because of utilization of NiFe which has a high permeability and lower conductivity than Cu. The proposed half CRS conductor ((iii) in Figure 3-19B) shows slightly higher resistance at 14 GHz compared to full CRS structure, however, the simulations show that its resistance in below 10 GHz frequencies is lower than full CRS conductors which results in overall lower resistance operation in wider-band. The conductor structure (iv) in Figure 3-19B is the estimated half CRS conductor after fabrication, although, the approximated model (iii) in Figure 3-19B is used for simulations.

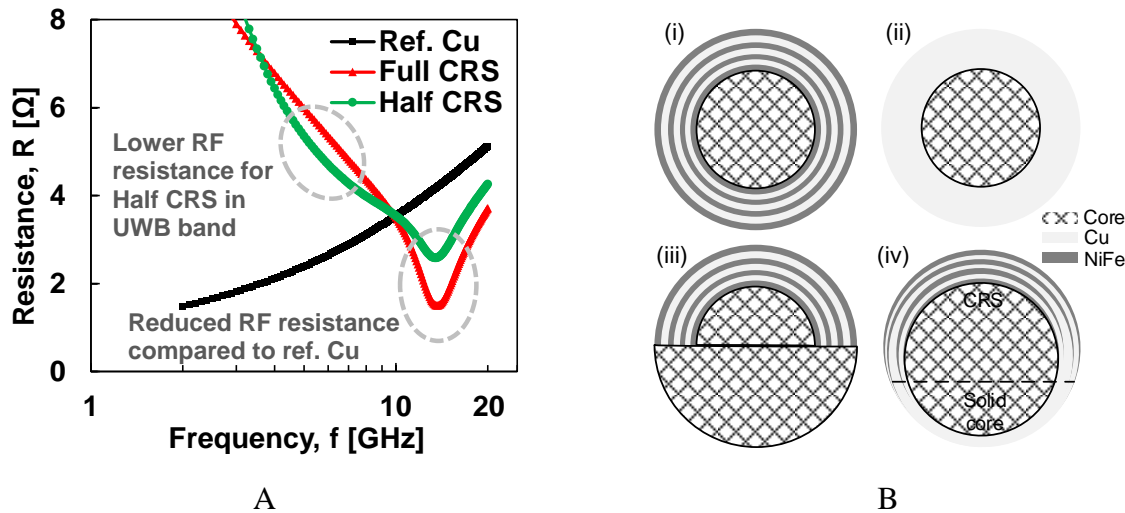


Figure 3-19. The comparison of the CRS conductors. A) The simulation results of the RF resistance of conductor's unit-cell comparing a full CRS, half CRS and reference Cu conductors with Cu/NiFe (150nm/25nm) layers, B) the schematic of the CRS conductors (i) full CRS, (ii) reference Cu with core, (iii) half CRS rough model, and (iv) approximated half CRS

Microfabrication and Measurement Results

For experimental verification, two-port air-lifted inductors (as in inset of Figure 3-9A) using the mentioned CRS conductor are fabricated. Magnetic and RF characterizations are performed. A 25 μm diameter radial gold wire is used which provides the cylindrical radial

platform required for the implementation of the CRS conductor. The gold wire-bonded structure has showed to be fully radial in micron scale with excellent surface uniformity suitable for the deposition of nano-superlattice structures where wirebonding is performed using Hybond wirebonder tool (522A-40, Hybond Inc.). Figure 3-20 shows the fabrication process.

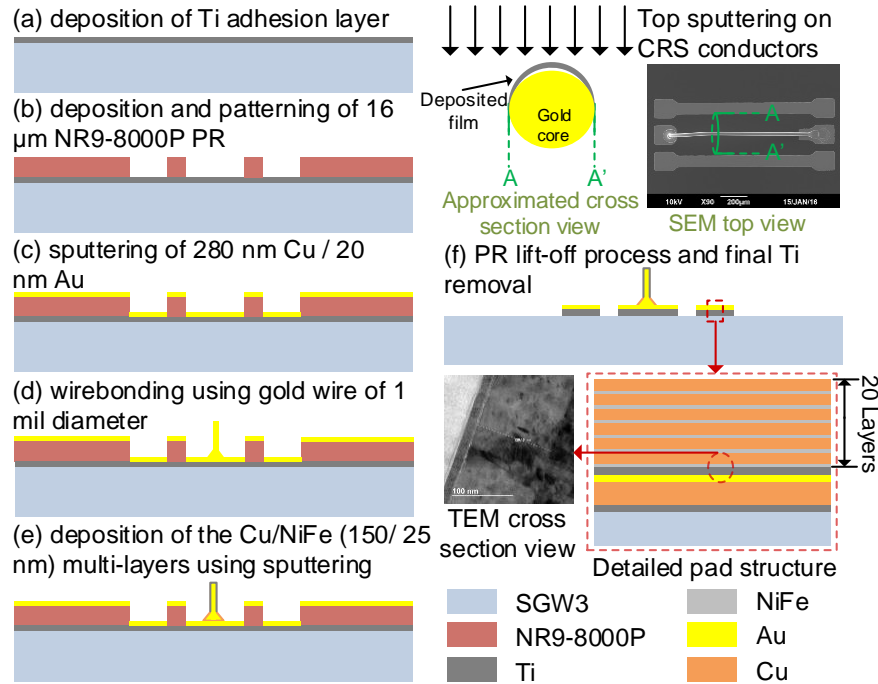


Figure 3-20. The fabrication process for CRS inductors utilizing Cu/NiFe conductors. The insets show the schematic of the directional sputtering and the detailed TEM cross section view of multiple metallic stacked thin films making the pads.

A super-uniform low loss glass substrate (SGW3, Corning Incorporated, $\epsilon_r = 5.8$, $\tan \delta = 0.0042$) with a thickness of 300 μm and a surface roughness of less than 1.0 nm is used. A 20 nm-thick gold as the top layer of the pad is used to improve the connectivity of gold wire to the signal pads since multiple metal sputtering steps are performed after wirebonding. The detailed structure of the pads are shown as inset in Figure 3-20 where two titanium (Ti) adhesion layers are used for improving the adhesion of Cu to the glass substrate and gold to the upcoming Cu/NiFe paired layers using DC/RF sputtering (CMS-18, Kurt J. Lesker Inc.) followed by the

transmission electron microscopy (TEM) image of the stacked metal layers. The directional thin film deposition feature of the sputtering technique on top of the horizontal gold wire-bonded structures will result in a shadowing effect that mimics the approximated model shown in Figure 3-17B.

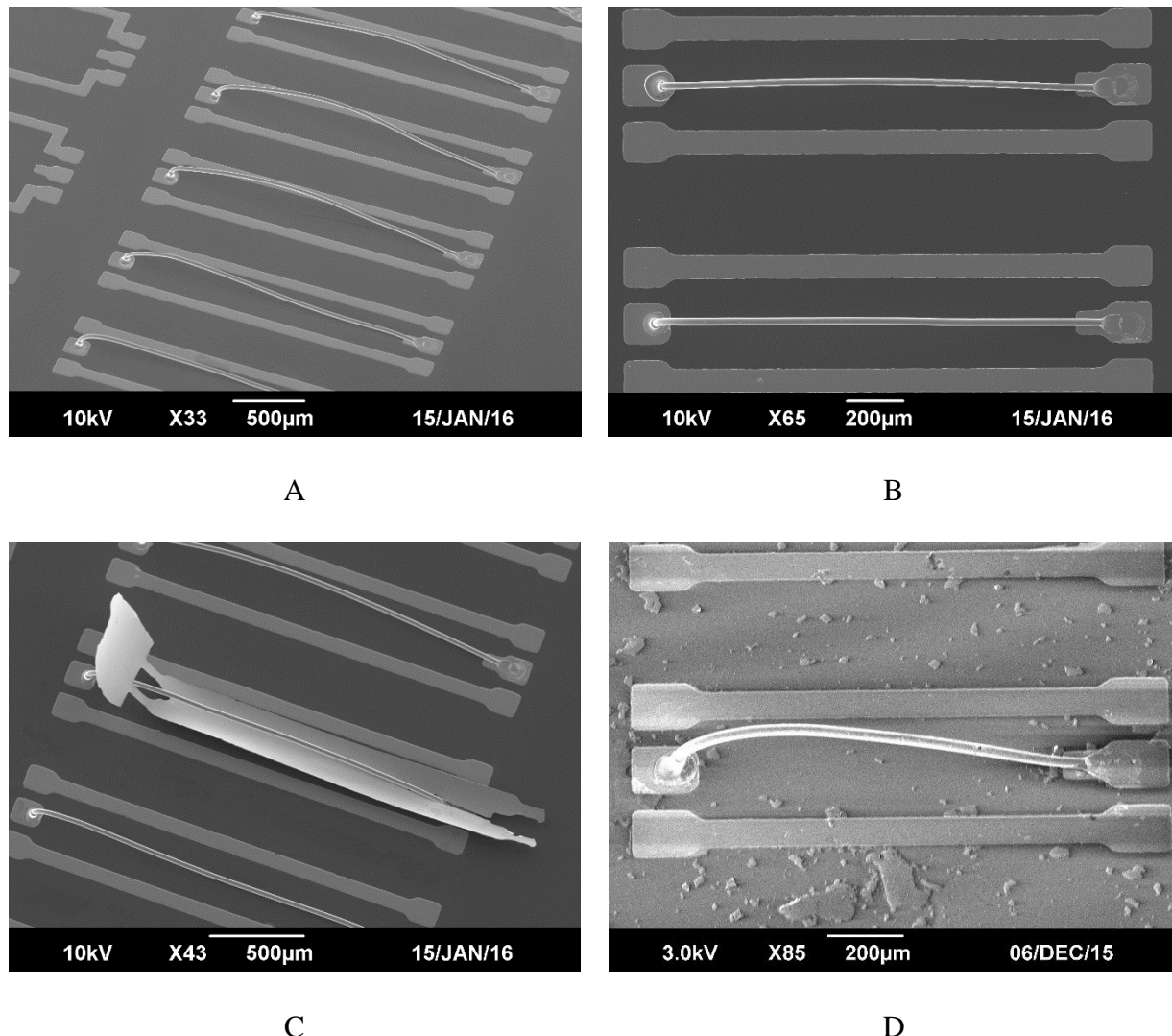


Figure 3-21. The SEM micrographs of the two-port inductors using Cu/NiFe nano-superlattice conductor architecture with $L = 2$ mm. A) Side view of the series of inductors, B) top view, C) an example of a failed device where lift-off process was unsuccessful, D) an example of a device where cleaning process was incomplete.

Figure 3-21 shows the scanning electron microscope (SEM) images of the fabricated inductors with different lengths where Figure 3-21A and Figure 3-21B show the side and top

views of the two-port inductors using the *h*-CRS structure. 10 layers of Cu/NiFe conductors with a thickness of 360 nm/30 nm totaling a 3.9 μm are used where the lift-off photoresist of 17 μm is used. Although the lift-off process was successful, due to the relatively high thickness of deposited film, some of the devices were failed and the upcoming film was not completely delaminated (Figure 3-21C). Also, the devices need to be fully cleaned after step (f) in Figure 3-20 to ensure getting rid of all particles where Acetone/Methanol/Isopropyl Alcohol in sequence followed by ultrasonic bath are used in Figure 3-21A to C and Figure 3-21D shows a substrate with incomplete cleaning.

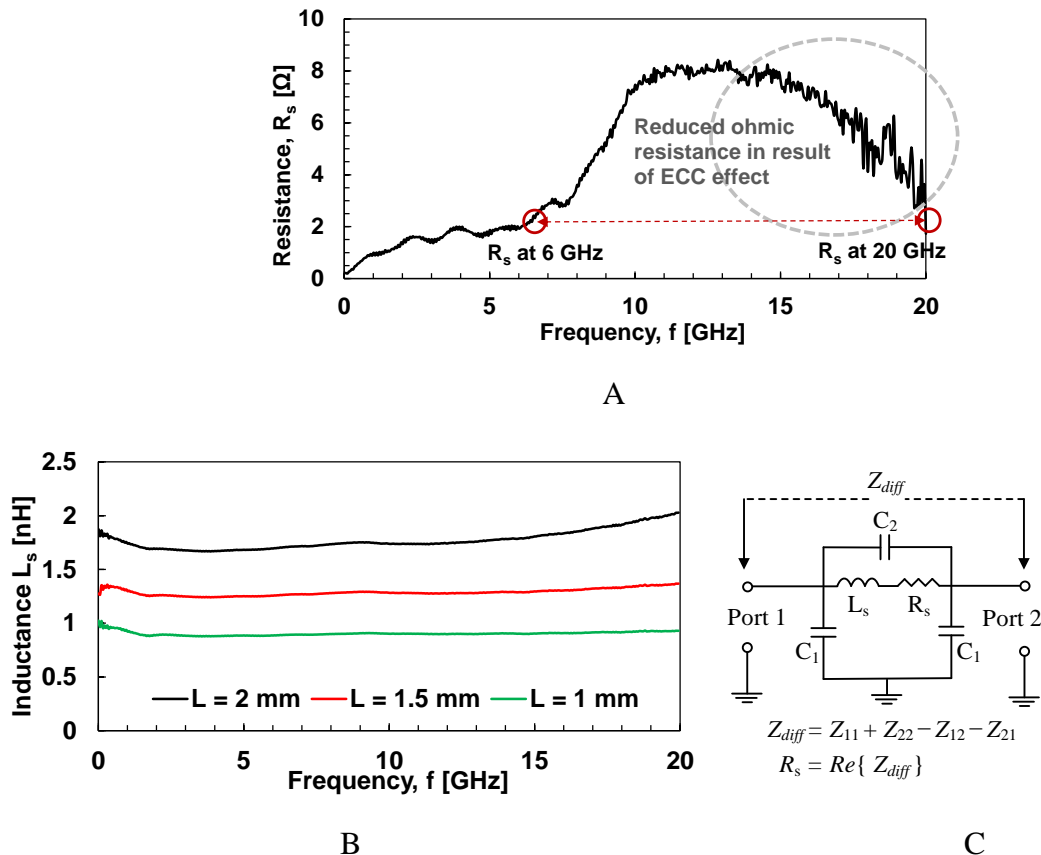


Figure 3-22. The measurement results of the *h*-CRS inductor. A) Measured series resistance of the Cu/NiFe hybrid nano-superlattice inductors with $L = 2 \text{ mm}$, B) the extracted inductance values for inductors of different lengths, and C) the PI-type lumped-element equivalent circuit model.

The RF measurements have been performed using a vector network analyzer (E5071C, Agilent Inc.) after standard short-open-load-through (SOLT) two-port calibration between 10 MHz and 20 GHz. A Cascade Microtech probe station with ground-signal-ground (GSG) probes (150 μ m pitch) is used for testing. Figure 3-22 shows the measured resistance and inductance of the inductors by considering a PI-type lumped-element equivalent circuit (Figure 3-22C).

The extracted resistance of the inductors will increase as the frequency increases in frequencies lower than 10 GHz as a result of the solid conductor architecture. However, in frequencies higher than 10 GHz, when the $|\mu_{r, NiFe}|$ approaches the Cu/NiFe thickness ratio, the ECC effect of the nano-superlattice structure will come into effect and reduce the AC resistance of the inductor. The inductor's ohmic resistance value at 20 GHz approaches the resistance value at 6 GHz. The extracted inductance values of the inductors with different lengths are shown in Figure 3-22B with relatively constant inductance values up to 20 GHz. The CRS radial inductors are designed to have small parasitics and a self-resonance frequency of higher than 30 GHz, which make them suitable for conductor loss reduction studies.

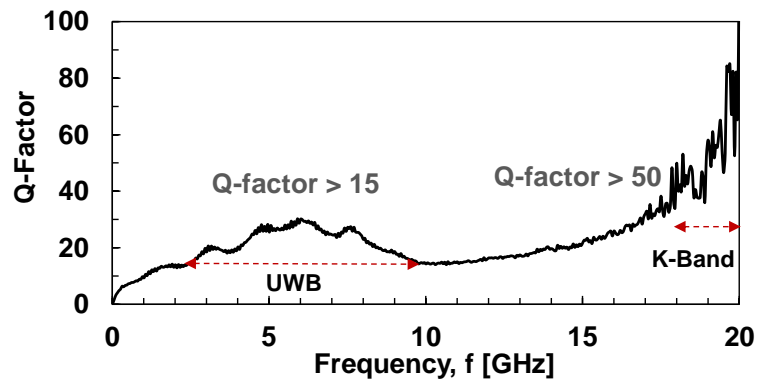


Figure 3-23. The measured Q-factor of the fabricated air-lifted *h*-CRS conductor-based inductor with L = 2 mm.

Figure 3-23 shows the extracted Q-factor of the inductors with L = 2 mm made of Cu/NiFe *h*-CRS structure. The first Q-factor peak point of 30 is achieved at 6 GHz similar to

regular solid-core inductors (in Figure 3-9A) where the Q-factor larger than 15 is achieved for the UWB band. Meantime, since the inductors have reduced resistance in higher frequencies as a result of using the Cu/NiFe nano-superlattice architecture, and the similar resistance value in K-band as the one in UWB band, the resultant Q-factor is significantly high. A Q-factor of larger than 50 is achieved in K-band and moreover the record-breaking Q-factor of 80 for the 1.8 nH inductor is achieved at 20 GHz.

The air-lifted inductors with Q-factor peaks at UWB and K-bands are therefore demonstrated benefiting from the solid and superlattice portions in both bands. The sputtering thin film deposition method has showed to be a reliable and efficient method of fabrication for the proposed *h*-CRS structure.

Summary

Cylindrical radial superlattice (CRS) conductors are proposed for RF conductor loss reduction. Due to the limitations of the planar-type superlattice conductors, namely, the fringing fields at the edges of the conductor, the eddy current cancelling (ECC) effect is not effective in those regions and as a result, the loss reduction is limited. The CRS conductors, however, will have an inherently radial shape, suitable for ECC conductors with minimal conductor loss. Analytical simulations of the unit cell show an improved ECC effect for CRS conductors compared to their planar counterparts. The RF inductors made of CRS conductors using electrodeposited Cu/NiFe are demonstrated and experimentally verified. Also, a PVD method of fabrication has been used for realization of hybrid CRS conductors (*h*-CRS) in which an improved Q-factor for an inductor in a double band of SWB and K-band is achieved.

CHAPTER 4

LOW LOSS PLANAR CONDUCTORS FOR RF COMPONENTS

Although, cylindrical radial superlattice conductors presented in previous chapter have superior performance over their planar counterparts in terms of RF loss reduction, the planar superlattice conductors are still demanded in most applications where a planar conductor is used including CMOS and RF MEMS where integration of a cylindrical conductor is not feasible or is difficult and might not be compatible with standard microfabrication processes. Therefore, studying the planar superlattice conductors as low loss conductors and presenting high performance components utilizing the planar superlattice conductors is critical.

In the remaining sections of this chapter, the analysis of the physical dimensions of a planar superlattice conductor will be given followed by experimental demonstration of high quality inductors and transmission lines employing the proposed planar conductors.

Study on Width and Thickness of the Planar Superlattice Conductors

The physical dimensions of the superlattice conductors will have a huge effect on its ohmic loss reduction performance. As discussed previously, the thickness of each individual layer will have an effect of overall performance. Therefore, studying its physical dimensions will help designing the more efficient superlattice conductors for RF loss reduction. In this section, a detailed analysis is given on the effect of the width and thickness of planar superlattice conductors for ohmic loss reduction in radio frequencies (RF) of K and Ka bands and the design constraints towards the high performance multi-layer superlattice conductors are discussed. Also, for the first time, Cu/Ni, an abundant material pair, has been used where Ni has a high contrast between its in-plane and out-of-plane coercivity suitable for the thin film superlattice ECC conductors. Finally, the high performance transmission lines and interconnects are fabricated and characterized for the proof of concept.

Analysis and Simulation Results

Figure 4-1A shows the schematic view of a CPW transmission line employing the proposed multi-layer superlattice conductor and Figure 4-1B depicts the cross section of the conductor in the Cartesian coordinate system where the ferromagnetic thin films with negative permeability in a GHz range of interest are used to cancel the eddy currents due to the nonferromagnetic material with positive permeability ($\mu_N \approx 1$), resulting in suppression of the skin effect and low ohmic loss.

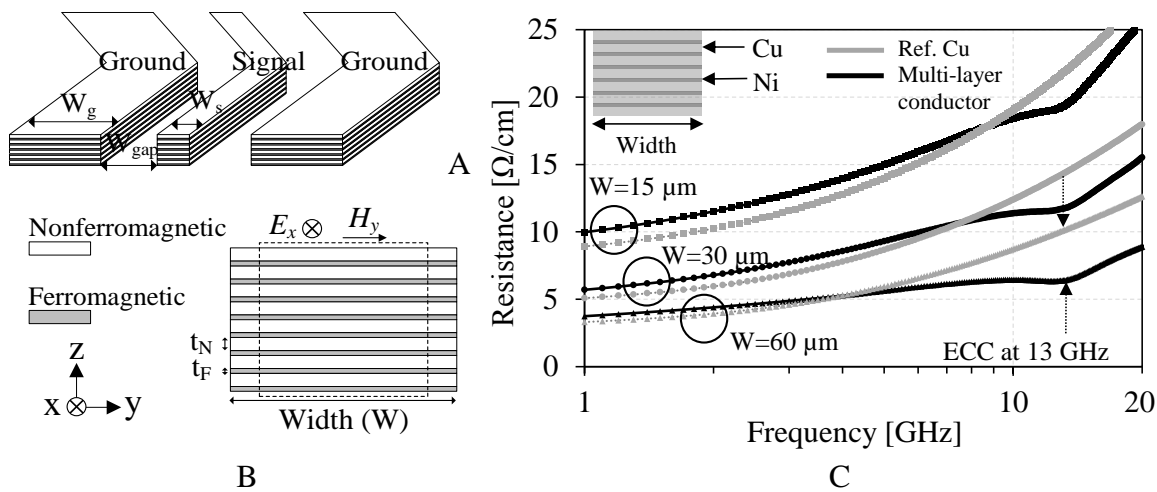


Figure 4-1. The schematic of the coplanar waveguide (CPW) transmission line A) Employing the planar multi-layer conductor architecture, B) planar superlattice conductor cross section, and C) simulation results of a unit-cell of the multi-layer conductors with different widths and a given thickness of $t_{\text{Cu}} = 150 \text{ nm}$, $t_{\text{Ni}} = 25 \text{ nm}$ showing the resistance spectra vs. frequency in the microwave region. t_N and t_F denote the thickness of the nonferromagnetic and ferromagnetic thin film layers, respectively.

While uniform field distributions are assumed inside a segment of the conductor (as shown), the field distribution will be disturbed by the fringing effect at the edges of the planar conductor and the eddy current cancelling will not be effective in those regions. By using a wider conductor, the relative contribution of the edges will be lowered. The full-wave simulations using a high frequency structure simulator (HFSS, v. 15.0, ANSYS Inc.) have been performed to study the dimension effects of the multi-layer conductors. The bold lines in Figure 4-1C show

the resistance of the multi-layer conductors where the gray lines show the corresponding reference solid Cu conductors for 3 conductor widths of $W = 15, 30$, and $60 \mu\text{m}$. The percentage of loss reduction is the difference between the RF resistance of the multi-layer and the reference solid conductors divided by the resistance of the reference conductor in percent. For $W = 60 \mu\text{m}$, more than 50% loss reduction has been achieved where the loss reduction percentage will be diminished for conductors with smaller width. For conductors wider than $60 \mu\text{m}$, the loss reduction percentage will not depend much on the conductor's width and the effect of fringing fields would be ignorable and dominated by other design parameters for the multi-layer conductor.

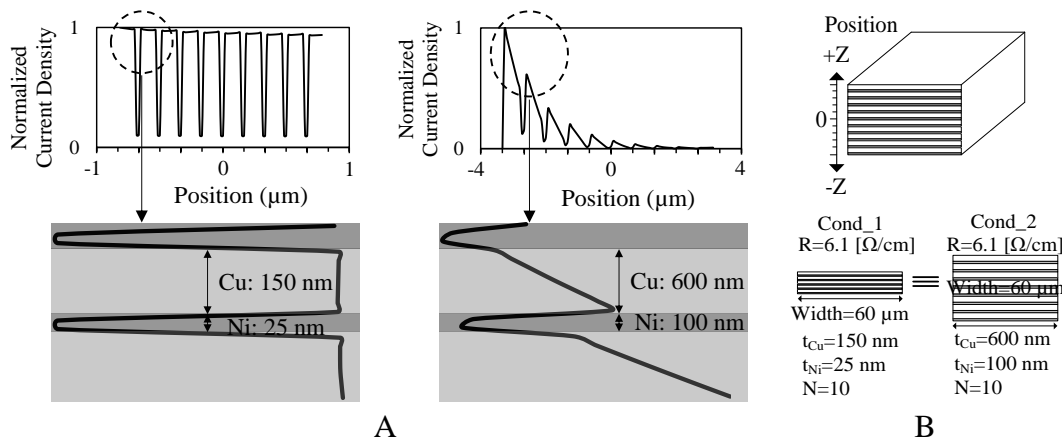


Figure 4-2. The current distribution into the volume of the conductors. A) At an ECC frequency of 13 GHz, B) comparison of two multi-layer conductors with the same thickness ratio of $t_{\text{Cu}}/t_{\text{Ni}} = 6$ (same ECC operation frequency) but different film thicknesses.

Another parameter affecting the performance of the multi-layer conductors is the thickness of the individual thin films. Figure 4-2B depicts two conductors (Cond_1: $t_{\text{Cu}}= 150 \text{ nm}$, $t_{\text{Ni}}= 25 \text{ nm}$, and Cond_2: $t_{\text{Cu}}= 600 \text{ nm}$, $t_{\text{Ni}}= 100 \text{ nm}$) with 10 alternating layers of Cu/Ni and Figure 4-2A shows the extracted current distribution through them. For Cond_1 (total conductor thickness of 1.75 μm), the current will be fully uniform inside the conductor with a good microscopic ECC effect. For Cond_2 (total conductor thickness of 7 μm), there exists the ECC effect and ohmic loss reduction compared to its solid reference counterpart at the same operation

frequency of 13 GHz; however, it is limited because the current is quickly degraded in the Cu layers thicker than its skin depth and the ECC effect is not fully exploited. Therefore, Cond_1 shows the similar RF resistance value as Cond_2, however, with more than 4 times smaller thickness, revealing 75% conductor volume reduction effect.

The other way of comparing Cond_1 with Cond_2 is to compare the percentage of ohmic loss reduction of each conductor with respect to its solid reference Cu counterpart. This will give a fair comparison as the comparing conductors have the same cross section area with the reference conductor. The HFSS simulation results with appropriate mesh sizing shows that Cond_1 will provide a better loss reduction percentage due to its thinner metal lines and a more uniform current distribution through its thickness. This eventually results in utilizing the maximized conductor's volume and most benefitting from the eddy current cancelling effect (ECC) of the multi-layer conductors.

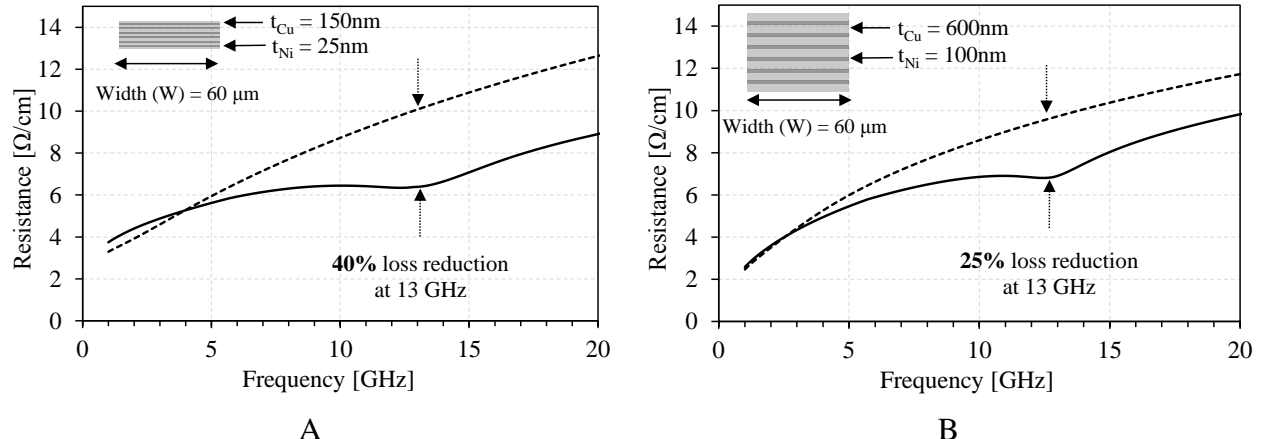


Figure 4-3. The simulation results of the RF ohmic resistance of two conductor unit cells, A) Cond_1 $t_{Cu} = 150\text{ nm}$, $t_{Ni} = 25\text{ nm}$, and B) Cond_2: $t_{Cu} = 600\text{ nm}$, $t_{Ni} = 100\text{ nm}$. The dashed line shows the resistance of the reference copper conductor with the same thickness as its respective multi-layer conductors.

Fabrication and Experimental Results

High performance transmission lines and interconnects are fabricated using the proposed multi-layer superlattice conductors to experimentally verify their performance followed by

magnetic and RF characterizations. A low-loss glass substrate coated with a 30 μm thick Benzocyclobutene (BCB, Cyclotene 4026-46; Dow Chemical, $\epsilon_r = 2.65$, $\tan \delta = 0.02$) is used as the low dielectric loss medium with highly uniform surface for device implementation. 10 layers of Cu/Ni (150 nm/25 nm) thin films are alternately deposited by DC/RF sputtering (Kurt J. Lesker CMS-18) and final devices are released using a lift-off process. Figure 4-4A shows the fabrication process flow and Figure 4-4B shows the integrated transmission lines with various dimensions and shapes with CPW probing pads as feedings.

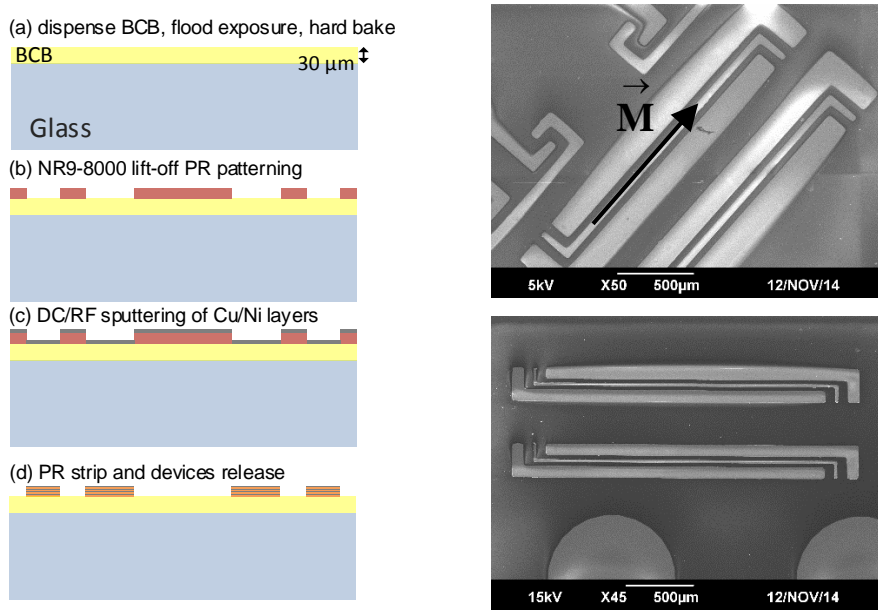


Figure 4-4. The planar transmission lines using optimized superlattice conductors. A) The fabrication process B) the SEM micrographs of the fabricated transmission lines and interconnects where M shows the direction of magnetization.

The magnetic characterization of the multi-layer Cu/Ni conductors with a dimension of 3 mm \times 3 mm shows an in-plane anisotropy field of 150 Oe, an out-of-plane anisotropy field of less than 5 Oe, and a magnetization saturation of 0.4 T from vibrating sample magnetometer VSM) measurements (ADE Technologies EV9 with a maximum applied field of $\pm 1800 \text{ kA m}^{-1}$) (Figure 4-5). This large contrast between the in-plane and out-of-plane anisotropy field of Ni

allows implementing self-magnetic-biased wider conductors without any distortion of magnetic alignment on the easy axis.

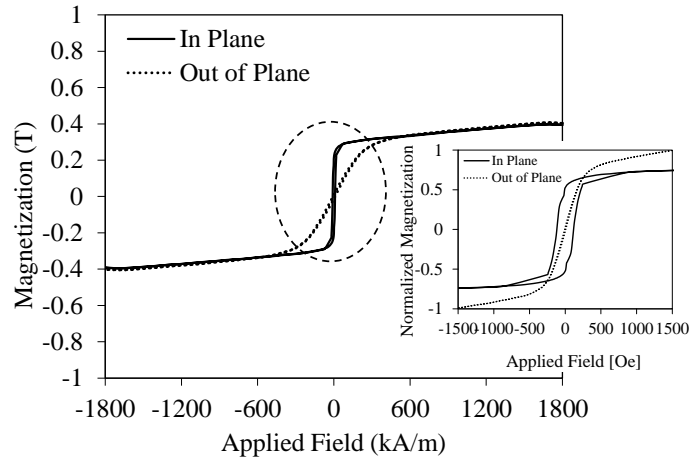


Figure 4-5. The magnetic characterization measurement results of 10 layers of Cu/Ni (150nm/30nm).

The RF measurements have been performed using a vector network analyzer (E5071C, Agilent Inc.) after standard short-open-load-through (SOLT) two-port calibration between 10 MHz and 20 GHz. The resistance of the lines is extracted from the two-port differential scattering parameters (Figure 4-6A). The contact resistance of the measurement probes (Figure 4-6B) are calculated as the difference between the minimum measured frequency (10 MHz) and the DC resistance of the conductor to be 1.2Ω , which has been deducted from the measured resistance raw data.

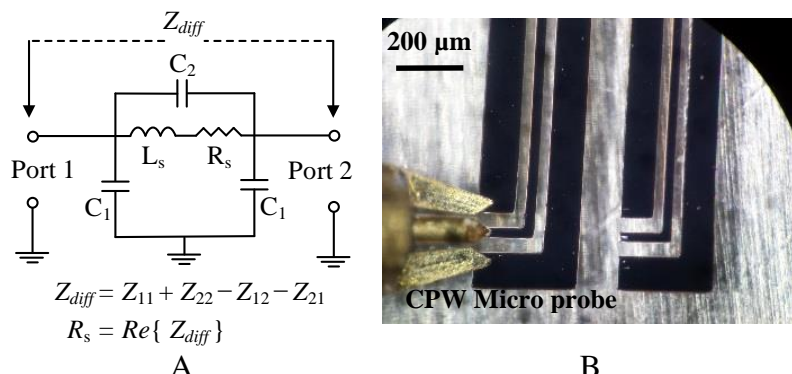


Figure 4-6. The two-port planar transmission lines. A) Schematic of the ohmic resistance extraction method, B) the device under test.

Figure 4-6B shows the micrograph of the CPW microprobes, ground-signal-ground (GSG) with 150 μm pitch, landed on the devices under test and Figure 4-7A shows the measurement results of the transmission lines with $W= 60 \mu\text{m}$ where the comparisons with the corresponding reference Cu conductors are made. The extracted ohmic resistance of the transmission line with reduced RF loss is shown in green.

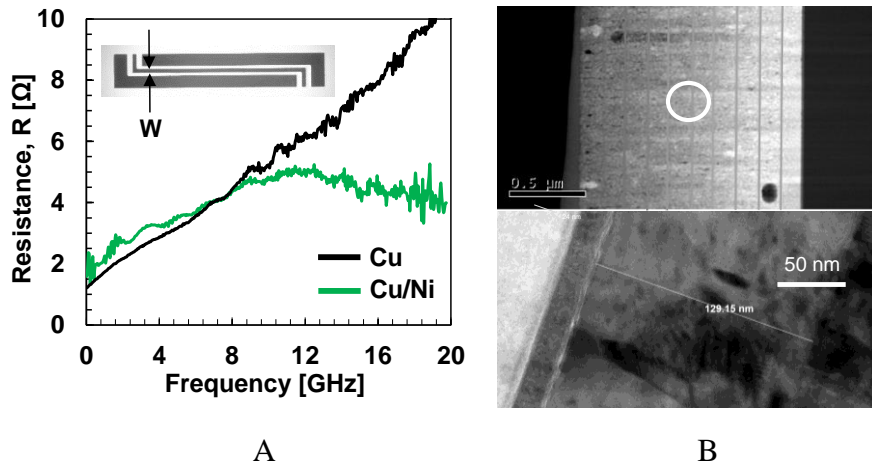


Figure 4-7. The measurement results of the fabricated transmission line with $W=60 \mu\text{m}$. A) The extracted ohmic resistance and the corresponding solid reference Cu conductor, B) the TEM micrographs of the nano-machined conductor's cross sectional view where the Cu/Ni multi-layer structure is shown.

For frequencies above 10 GHz up to 20 GHz, the resistance of the multi-layer CPW lines falls below the resistance of the reference Cu conductors due to the ECC effect. At frequencies above 13 GHz, there is some deviation between the measurement and simulation results. The magnetic permeability value of Ni used for the simulation is extracted from the LLG equation. It is speculated that the magnetic permeability of Ni does not accurately represent the real permeability of Ni in 13 to 20 GHz, where the magnitude of the relative magnetic permeability is much smaller than unity. This effect has been favorably used for conductors with reduced RF loss in a wider frequency range than initially designed. Figure 4-7B shows the transmission

electron microscope (TEM) micrographs of the conductor's cross sectional view where nm-range Cu/Ni multi-layer conductors are shown.

Figure 4-8 shows the measurement results of three conductors with widths of $W=30$, 50 , and $60 \mu\text{m}$ where all measurement results show a resistance drop for frequencies above 10 GHz . The extracted resistance of the control conductor made of solid Cu with $W=30 \mu\text{m}$ has also been shown in Figure 4-8. The resistance of the lines is extracted from the two-port scattering parameters (Figure 4-6A). At frequencies above 13 GHz , there might be some discrepancy between the measurement and simulation results mainly attributed to fabrication imperfection and tolerance.

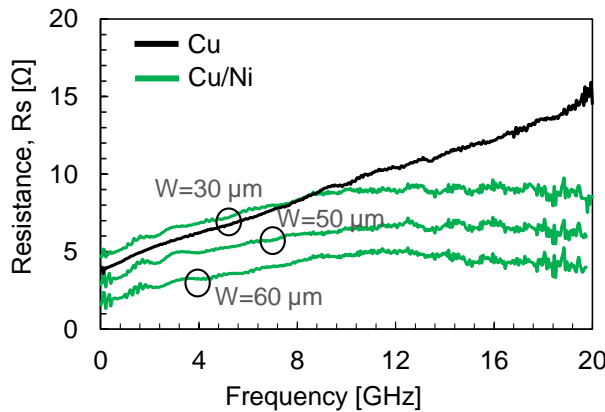


Figure 4-8. The measurement results of the CPW transmission lines with $W=30$, 50 , and $60 \mu\text{m}$. The black dashed lines show the corresponding reference Cu conductor with $W=30 \mu\text{m}$.

Table 4-1 summarizes the comparison of the state-of-the-art conductors that utilize various ferromagnetic materials in a multi-layer structure to reduce the RF conductor loss. The utilized figure of merit is defined as frequency / (normalized resistance \times cross section area), where normalized resistance is the resistance of the conductor divided by its length, the cross section area ($= t \times w$) with "t" the total thickness of the conductor and "w" its width. The conductors with the thickness in the order of one skin depth at the operation frequencies will be

limited by the self-confined eddy currents and current penetration through the volume of the conductor will be exponentially vanished beyond one skin depth. As a result, the maximum loss reduction percentage and the highest FoM are achieved using the proposed Cu/Ni multi-layer conductors with wider and thinner films. In overall, the proposed conductor could be exploited for next generation RF circuits and systems in the K and Ka bands.

Table 4-1. The state-of-the-art comparison of multi-layer conductors.

Reference	Multilayer Structure Material / (nm)	Width (μm)	Thickness (μm)	% of loss Reduction	FoM (GHz / $\Omega \cdot \mu\text{m}$)
[9]	Cu/CoZrNb	750/25	12	7.9	20
[10]	Cu/NiFe	650/40	30	8.3	36
[11]	Cu/NiFe	300/100	90	6.7	40
This Work [14]	Cu/Ni	150/25	60	1.7	68.6

Planar Superlattice Conductors Using Cu/Ni Multi-Layer Structure

In this section, ultra-high quality factor (Q-factor) integrated inductors in K-band are reported where the proposed Cu/Ni nano-superlattice conductor in previous section with the optimized dimensions, is used for the conductor instead of a conventional thick single-layer Cu or Ag film. The inductors are nanomachined and measurement results show the highest Q-factor of an on-wafer K-band inductor reported to the best of the authors' knowledge.

Inductor Design

Figure 4-9A depicts the schematic of the proposed inductor where the inductance is taken differentially from the two-port coplanar waveguide (CPW) feedings and 10 layers of thin Cu/Ni providing a low conductor loss medium are used as the conductor. Also, a 30 μm thick Benzocyclobutene (BCB, Cyclotene 4026-46; Dow Chemical, $\epsilon_r = 2.65$, $\tan \delta = 0.02$) is used as the low dielectric loss and uniform hosting medium to improve the overall Q-factor. The inductor's dimensions are chosen to have minimal parasitic gap capacitance and a high self-resonance frequency (> 30 GHz) to study the inductor performance in K-band. Figure 4-9B

depicts the fabrication process flow which is done using DC/RF sputtering (Kurt J. Lesker CMS-18) of Cu/Ni thin films on a glass wafer coated with hard-baked BCB and lift-off processes.

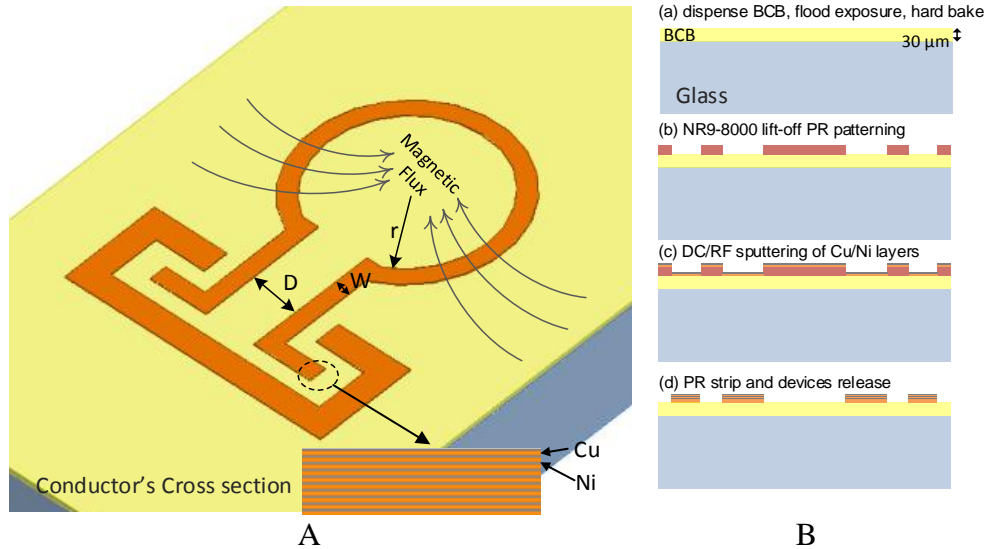


Figure 4-9. The two-port planar inductor. A) The schematic of the inductor and its cross section with $r = 400 \mu\text{m}$, $D = 280 \mu\text{m}$, and $W = 60 \mu\text{m}$, B) the fabrication process.

Fabrication and Experimental Results

The proposed high performance inductors with the multi-layer conductor architecture have been fabricated and magnetic and RF characterizations are performed. Figure 4-10 shows the integrated planar inductors with various dimensions and shapes with the coplanar waveguide (CPW) probing pads. The conductor consists of 10 layers of alternating Cu/Ni layers with 150 nm/25 nm thicknesses, respectively, and with different widths of the signal line. The thickness of Ni has been chosen small as it has much smaller conductivity compared to Cu and to keep the majority of current in Cu layers. As the width of the conductor increases, the relative contribution of the edge portion to the overall ECC effect is small and the resultant ohmic loss suppression effect is much apparent. Also, Ni has been chosen as the ferromagnetic material due to its high in-plane anisotropy field.

The RF measurements have been performed using a vector network analyzer (E5071C, Agilent Inc.) after standard short-open-load-through (SOLT) two-port calibration between 10

MHz and 20 GHz. A Cascade Microtech probe station with ground-signal-ground (GSG) probes (150 μ m pitch) are used for testing.

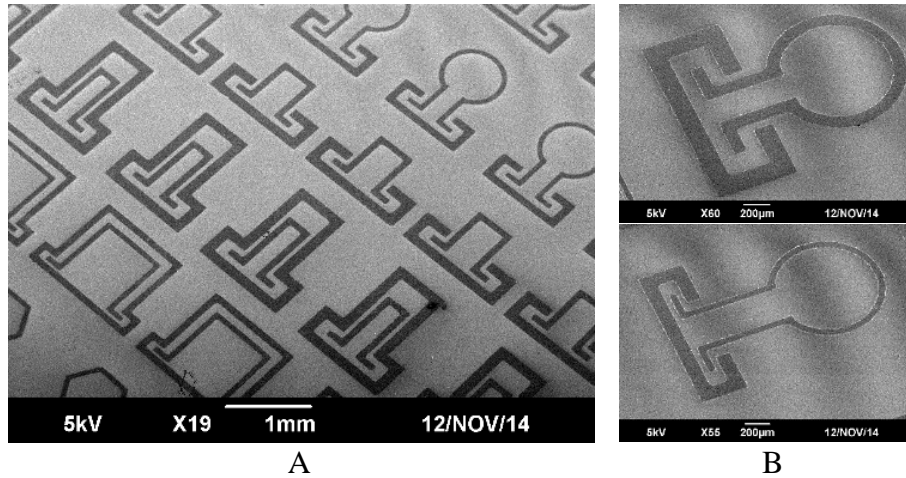


Figure 4-10. The SEM micrographs. A) The series of the fabricated high performance inductors with various dimensions and shapes using low loss multi-layer conductor, B) with different widths of the signal line.

Figure 4-11 shows the measured resistance and inductance of the inductors by considering a PI-type lumped-element equivalent circuit. In order to make a comparison, the conductor made of single layer Cu with the same thickness of 1.7 μ m has been fabricated. Several de-embedding pads are placed on the substrate to take out the series and parallel parasitic effects. Also, the contact resistances of the measurement probes are calculated as the difference between the minimum measured frequency (10 MHz) and the DC resistance of the conductor to be 1.2 Ω which is subtracted from the measured resistance raw data. In low frequency region, the resistance of the multi-layer conductor is slightly higher than that of the reference Cu conductor because of using ferromagnetic material which has higher permeability than Cu with a relative magnetic permeability of 1 and therefore having a smaller skin depth (2-40) and higher resistance. For frequencies above 10 GHz up to 20 GHz, the resistance of the multi-layer inductors gets almost constant and doesn't increase with frequency as a result of the ECC effect

inside the conductor and falls below the resistance of the reference Cu conductors. A maximum 65% of loss reduction has been achieved at 20 GHz.

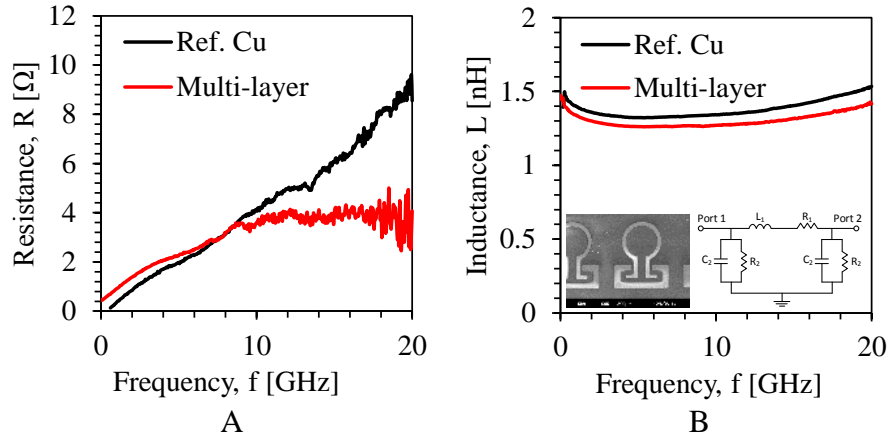


Figure 4-11. The measurement results. A) The measured series resistance and B) inductance of the multi-layer and reference Cu inductors.

Figure 4-12 shows the measured Q-factor of the fabricated inductors. The multilayer inductors show a three times higher Q-factor for the K-band frequency range of 18-20 GHz [15].

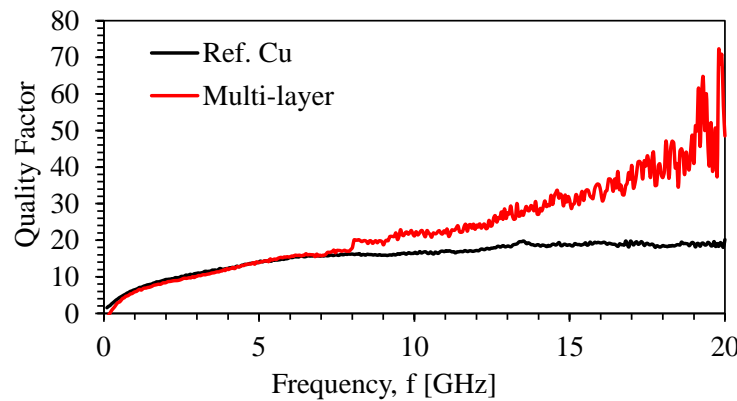


Figure 4-12. The measured Q-factor of the fabricated planar inductors made of multi-layer and reference Cu versus frequency.

Cu/Ni Multi-Layer Devices with Magnetic Alignments

In the previous section, high quality inductors based on self-biased magnetic films are presented. Due to the very high aspect ratio of the deposited film, namely, the area of the film with respect to its thickness, the magnetic alignments will be based on shape anisotropy and will be in-plane in the direction of deposited films. In this section, magnetic field alignment will be

performed after deposition of magnetic films and also, in-situ measurements will be performed by applying an external magnetic field to the devices under test.

Figure 4-13 shows the measurement results of the inductors made of Cu/Ni multi-layer structure after magnetic alignments. The inductors are magnetically treated by an external DC magnetic field prior to measurements. The results of the extracted resistance show a clear drop above 17 GHz due to the eddy current cancelling effect whereas the measurement results of the reference copper show an increasing as frequency increases due to the skin effect. A record breaking Q-factor of 70 at 20 GHz is achieved for the inductor.

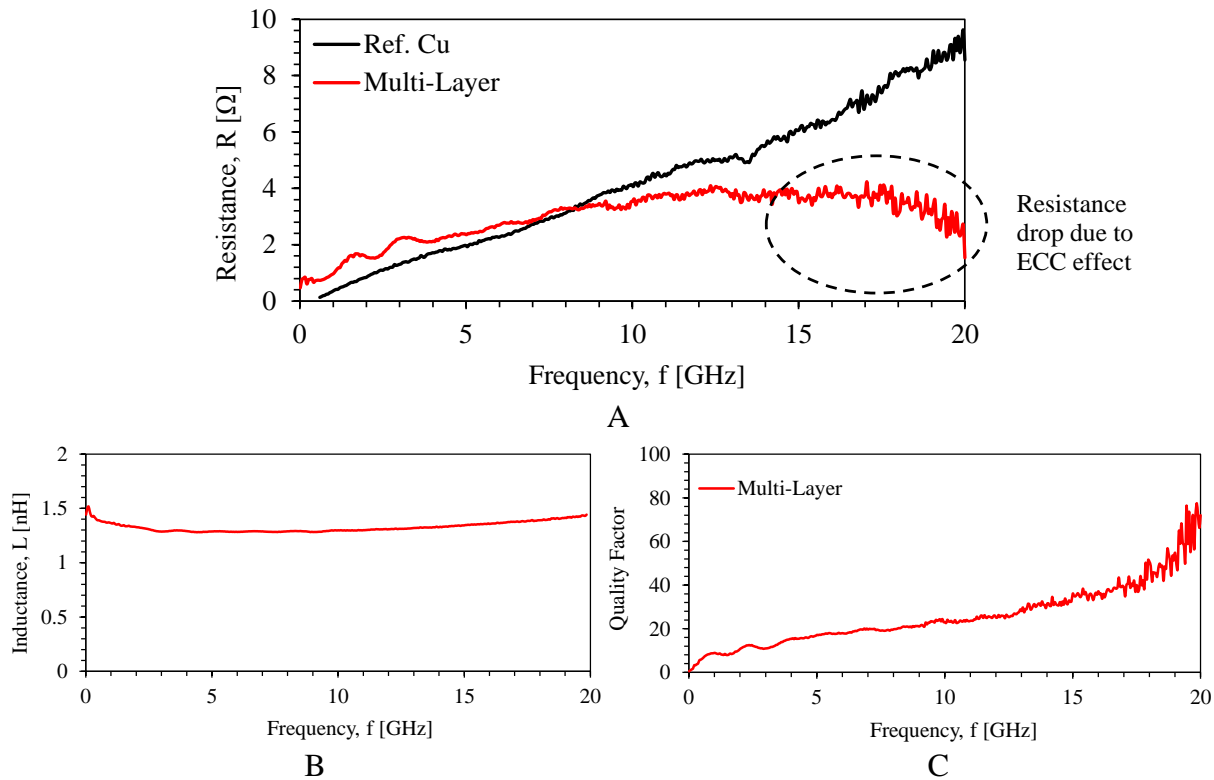


Figure 4-13. The measurement results of the series resistance of the inductor after magnetic alignment of Ni films. A) Measured series resistance, B) inductance, and C) Q-factor.

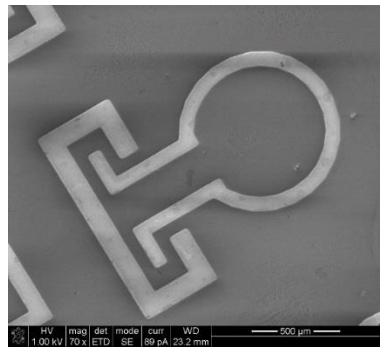
Planar Superlattice Conductors Using Cu/NiFe Multi-Layer Structure

In this section, the design and fabrication of various RF components including the transmission lines and inductors using Cu/NiFe conductor are reported. Cu/NiFe conductors are

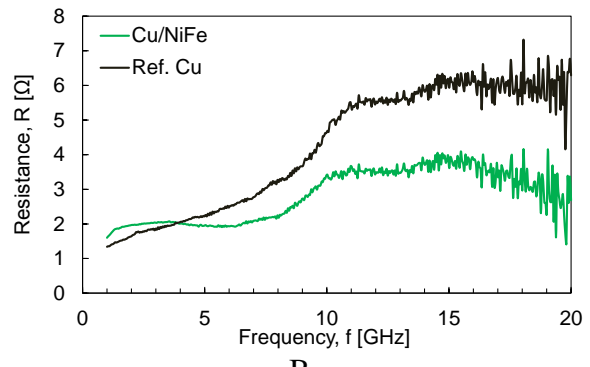
used as the multi-layer conductor architecture where NiFe with much higher permeability compared to Ni has been used as the ferromagnetic material adding to the features of the Cu/NiFe multi-layer conductor since much higher resistance in lower frequency bands will be achievable. In order to increase the integrability of the devices, a super-uniform glass substrate from Corning Incorporated, SGW3 [50]. Also, the effects of number of layers and substrate effects will be experimentally studied.

Figure 4-14A shows SEM micrograph of the two-port inductor with Cu/NiFe and a thickness of 360 nm/30 nm on Corning glass substrate. The same devices are fabricated using sputtered Cu as control devices for comparing the extracted ohmic resistances. Figure 4-14B shows the measured resistance of the inductors where a reduction of ohmic resistance in high frequencies is observed for the device using Cu/NiFe conductors.

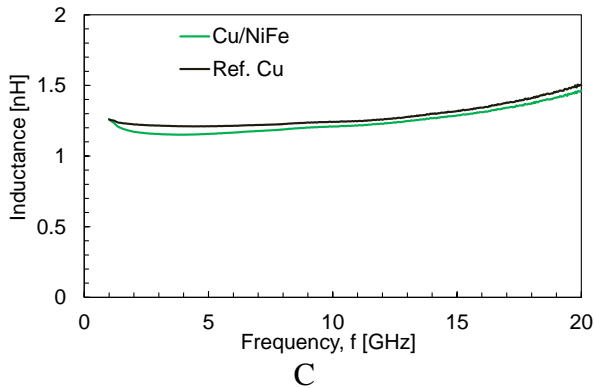
Figure 4-15 shows the devices made of Cu/NiFe conductors where a thickness of 180 nm/30 nm is used. Two devices with the same structure however different substrates (different surface roughness) are used highlighting the effects of surface roughness as well as tangent loss. The Corning glass substrates ($\epsilon_r = 5.8$, $\tan \delta = 0.0042$ in Table 6-1) and a Soda-Lime glass with a thickness of 1.5 mm ($\epsilon_r = 6.0$, $\tan \delta = 0.02$) are used. Corning glass is superior in terms of both surface roughness and the dielectric tangent loss. Also, for each of the substrates a reference device using Cu has been used for comparison. For the Soda-Lime substrate, even though the extracted resistance of the Cu/NiFe remains lower than that of the reference Cu, both of the resistance curves increase as the frequency increases because the substrate loss in the K-band regime remains dominant. However, for the Corning glass substrate with much lower dielectric loss, the extracted resistance of the Cu/NiFe devices remains lower than that of the reference Cu one and doesn't increase with frequency due to conductor loss suppression effects.



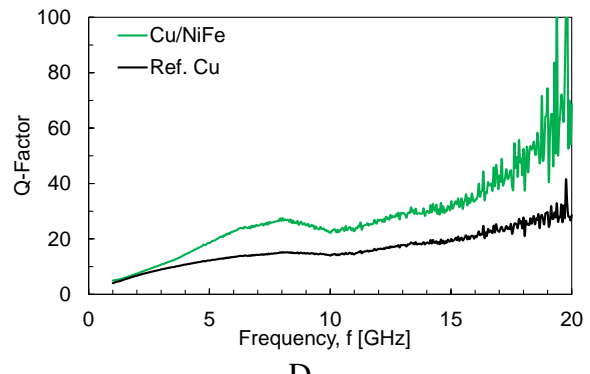
A



B

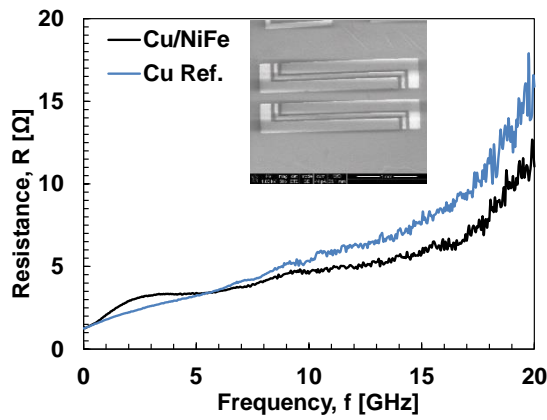


C

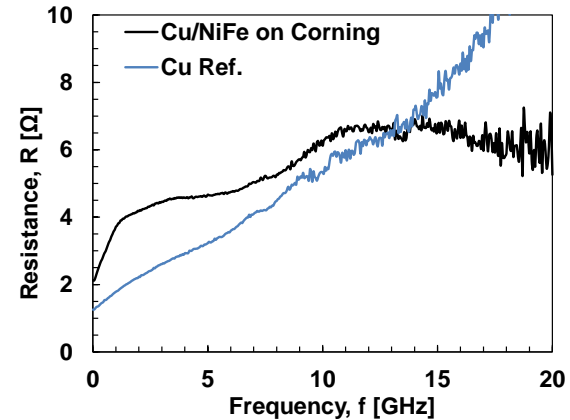


D

Figure 4-14. The fabricated inductor using Cu/NiFe (360 nm/30 nm) on Corning glass substrate. A) The SEM micrograph of the device, B) the extracted ohmic resistance, C) the extracted inductance, and D) the extracted Q-factor.



A



B

Figure 4-15. The effect of number of substrate on the extracted ohmic resistance. A) The SEM micrograph of the fabricated CPW transmission line, B) the extracted ohmic resistance.

Summary

In this Chapter, the effects of the width and thickness of the planar type nano-superlattice conductors have been studied for more effective eddy current cancelling. Pure Ni has been used as an appropriate ferromagnetic material to realize high performance multi-layer superlattice conductors. A large loss reduction percentage and the highest FoM have been achieved using the proposed Cu/Ni multi-layer conductors with wider and thinner films. Also, two-port RF inductors with improved Q-factor in K-band using the proposed conductor architecture have been experimentally demonstrated. BCB and Corning glass wafers have been used as the substrate and the effects of the substrate on the loss reduction has been shown. The proposed conductors could be exploited for next generation high performance RF circuits and systems in the Ku, K, and Ka bands.

CHAPTER 5

MAGNETIC FIELD EFFECT TRANSCONDUCTORS

In this chapter, the design, fabrication and experimental demonstration of magnetically-driven tunable ohmic resistance conductors in RF regime are presented. These conductors are made of alternating non-ferromagnetic / ferromagnetic thin films (Cu/NiFe in this case) which use the ferromagnetic resonance phenomenon as the loss mechanism and have a high loss near the ferromagnetic resonance frequency which could be tuned to the frequency of interest while having low loss in other frequencies. The tunability of the conductors are examined by applying an external magnetic field. The thickness ratio of the Cu/NiFe layer is used as the controlling parameter for the maximum amount of loss. We call these conductors, magnetic field effect transconductors (M-FET's), since they use a magnetic field effect and have tunable ohmic resistance with respect to frequency.

An introduction of the theory and the electron spin torque transfer of the magnetic materials will be firstly given. The spin torque transfer is used as the loss mechanism for realization of the tunable nano-superlattice conductors. Then, the design of the conductors using the microscopic current control will be discussed. A comprehensive material characterization including the magnetic and physical characterizations will be provided. Finally, the microfabrication of the conductors and the measurement results will be reported.

Theory

Before introducing the operation principle of M-FETs, a theoretical background regarding the loss mechanism of the ferromagnetic materials is provided to understand the concept of M-FETs. The author believes that this knowledge is highly required since the magnetic loss of the ferromagnetic materials in high frequencies is the main mechanism of operation of M-FETs.

The precise mechanisms of interaction between the magnetic moments in a ferromagnetic material are very complex to model. When a magnetic field is applied to a ferromagnetic material, the magnetic moments tend to move themselves in the direction of the applied magnetic field to reduce their magnetostatic energy. Landau-Lifshitz were the scientists that proposed a dynamic mathematical model to study the movements of the magnetic moments in a time domain. In result of their research, the magnetic movement of a magnetic moment under an external magnetic field is described as,

$$\frac{d\vec{M}}{dt} = -\mu_0 \gamma \vec{M} \times \vec{H}_{ext} \quad (5-1)$$

where \mathbf{M} is the magnetic moment, μ_0 is the permeability of air, γ is the gyromagnetic ratio, and \mathbf{H} is the applied magnetic field. Gyromagnetic ratio is the ratio of the magnetic dipole moment to angular moment of any particle (like an electron). A self-rotating electron has a distinct gyromagnetic ratio which could be calculated using,

$$\gamma = g_e \frac{|-e|}{2m_e} \quad (5-2)$$

in which g_e is a dimensionless factor which could be calculated. Because the mechanism of movements of magnetic moments, the alignment processes, are dissipative, Gilbert has added a dissipative term to (5-1), giving the Landau-Lifshitz-Gilbert (LLG) equation as,

$$\frac{d\vec{M}}{dt} = -\mu_0 \gamma \vec{M} \times \vec{H}_{ext} + \frac{\alpha}{M_s} (\vec{M} \times \frac{d\vec{M}}{dt}) \quad (5-3)$$

in which α is the Gilbert damping constant. The Gilbert damping constant is actually not quite constant and depends on the applied magnetic field and frequency of movement. The LLG equation in (5-3) describes the damped movement of a magnetic moment under an applied magnetic field as shown in Figure 5-1 where \mathbf{H} shows the direction of magnetic field. When an alternating magnetic field, like an electromagnetic H field, is applied perpendicular to a DC

magnetic field, the magnetic moment will have a damped movement, the so called precessing movement, trying to align itself to the external magnetic field. When the frequency of the precessing movement of magnetic moment approaches the frequency of the electromagnetic field, the ferromagnetic resonance occurs and the ferromagnetic material will have maximum energy absorption.

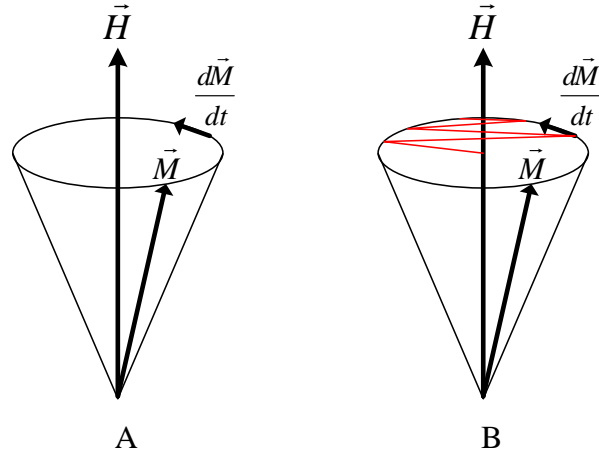


Figure 5-1. The illustration of the movement of a magnetic moment under an applied magnetic field. A) Without damping with Larmor frequency, B) precessing damped movement of the magnetic moment trying to align to external magnetic field.

The ferromagnetic resonance frequency is a function of external DC magnetic field strength and described by Kittel formula,

$$f_{FMR} = \frac{\gamma}{2\pi\mu_0} \sqrt{(\vec{H}_{ext} + \mu_0 \vec{H}_{Kp})(\vec{H}_{ext} + \mu_0 \vec{H}_{Kp} + \mu_0 M_s)} \quad (5-4)$$

in which γ is the gyromagnetic ratio, μ_0 is the permeability of air, H_{ext} is the external applied magnetic field, H_{Kp} is the anisotropy field of the ferromagnetic material, and M_s is its magnetization saturation. This spin torque transfer and loss mechanism phenomenon and the ability to be tunable upon an external magnetic field is used in this work to realize magnetic field effect transconductors.

Design and Analysis

In this section, the design and a theoretical background of the proposed tunable nano-superlattice conductors will be provided. It is known that semiconductors are type of materials which are dominating the electronics industry out of which transistors as the devices with tunable conductivity are made. The main difference of a semiconductor material like silicon with a conductor such as copper is that silicon could be doped to change its conductivity using external materials. The doping process in a semiconductor acts similar to a knob by changing it, or changing the dosage of impurity, enables a conductivity modification inheriting from the variation of concentration of electrons in conduction band or holes in valence band. However, a pure conductor like copper has a fixed conductivity which will not change real-time by an external stimulator. In this chapter, we are proposing a new type of conductor which has a tunable conductivity upon applying an external magnetic field. Similar to regular field-effect transistors (FET's) which could have a tunable conductivity using an external electric field, the proposed magnetic field effect transconductors (M-FET's) also have a tunable conductivity with an exception of using actual electrical conductors instead of semiconductors. The advantages of M-FET's compared to conventional FET's is the fact that they could be used for higher speed and higher frequency applications, are easier to fabricate as do not require a complex doping control, and could be used in passive RF components such as tunable transmission lines, metamaterials, microwave absorbers, and etc.

The main idea is using metals as conductors which satisfy two requirements: 1) they must have a frequency-dependent property like ferromagnetic materials with permeability vs. frequency as described by LLG, 2) their thickness should be a few times smaller than the skin depth in the frequency of operation. As a result, a microscopic modification of current inside a conductor is feasible resulting in a tunable conductor in microwave regime.

Skin Depth in Ferromagnetic Materials and μ_r -Frequency Relationship

Most components operating in RF regime use conductors with high electrical conductivity such as silver (Ag), copper (Cu), gold (Au) or aluminum (Al) to minimize the ohmic conductor losses and maximize overall system's efficiency. However, in RF region, electrical resistance is mainly limited by the skin effect and as explained in Chapter 2, in higher operation frequencies, the current will be confined in the outmost region of the conductors which is unavoidable in those frequencies. The magnitude of current will decrease by a factor of $1/e$ in one skin depth,

$$\delta = \sqrt{\frac{\rho}{\pi f_{operation} \mu_r \mu_0}} \quad (5-5)$$

in which ρ is the resistivity of the conductor, μ_0 is the permeability of air and μ_r is the relative permeability of the conductor material. Table 5-1 tabulates the skin depth values in μm for some common conductors ($\mu_r = 600$ for Ni is assumed) in different frequencies which shows that skin depth becomes smaller as the frequency increases in operation frequencies such as in K-band.

Table 5-1. The skin depth, δ , comparison in different frequencies. The units are in [μm].

Conductor/Frequency	1 GHz	10 GHz	20 GHz
Copper (Cu)	2.06	0.652	0.461
Silver (Ag)	2	0.634	0.448
Nickel (Ni)	0.17	0.054	0.038

Based on the skin effect theory, the ohmic loss of the conductors at higher frequencies are governed by the resistivity (ρ) and the skin depth. The other parameter in (5-5), to be exploited in this work, which could be used to change the skin depth and the resulting ohmic resistance of the conductor is the permeability of the conductor, μ_r . For non-ferromagnetic conductors, $\mu_r = 1$ and the ohmic resistance of the conductors will constantly increase by a \sqrt{freq} relation. As a result, since $\approx 99\%$ of the current will be confined in a distance 5 times of the skin depth of the

conductor in the operation frequencies, by realizing conductive layers with thicknesses a few times smaller than the skin depth in nano-meter range, that would be possible to microscopically modify the current flow and the ohmic resistance of the conductor could be controlled versus frequency. Although, the given parameters in (5-5) are non-controllable and fixed by the intrinsic properties of the material, the μ_r in a ferromagnetic material is variable and tunable versus external applied magnetic field based on Landau-Lifshitz-Gilbert (LLG) theory.

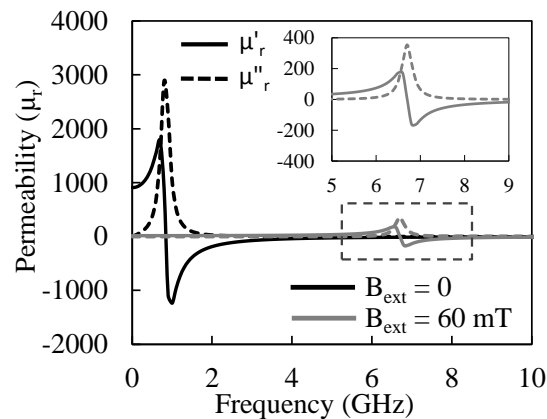


Figure 5-2. The theoretical permeability spectra of a Ni₈₀Fe₂₀ thin film with a thickness of 30 nm before and after application of an external magnetic flux of 60 mT.

Figure 5-2 shows the real and imaginary parts of the permeability of a Ni₈₀Fe₂₀ thin film with a thickness of 30 nm before and after applying an external magnetic flux of 60 mT towards its easy axis. Near resonance frequency (f_{FMR}) where the real part of μ_r becomes negative, the imaginary part representing the magnetic losses is maximized. As a result, the ferromagnetic material will have maximum magnetic loss near those frequencies. Also, since the f_{FMR} frequency is tunable versus an applied magnetic field, the resulting magnetic loss of the ferromagnetic material will also be tunable.

M-FET Conductor Architecture

Even though the μ_r in a ferromagnetic material could be externally manipulated to have a tunable magnetic loss and resulting ohmic loss if used as a conductor, ferromagnetic materials

are typically not considered as good conductors compared to excellent conductors such as copper or silver that are used most widely in microwave components. Therefore, a solid ferromagnetic conductor is not considered as a good conductor and cannot be used as a wide-range tunable conductor. In this work, an electrical conductor with a magnetic field dependent conductance change is presented, where the conductor consists of multiple pairs of nanoscopic non-ferromagnetic (Copper, Cu) and ferromagnetic (Permalloy, Ni₈₀Fe₂₀) metals, where each Cu/Ni₈₀Fe₂₀ superlattice conductor pair has a thickness of 150 nm/25 nm or 180 nm/60 nm. The thin Ni₈₀Fe₂₀ conductor with a thickness of 30 – 60 nm and a width of 60 μm shows large shape anisotropy and presents its ferromagnetic resonance in the microwave range according to the LLG equation.

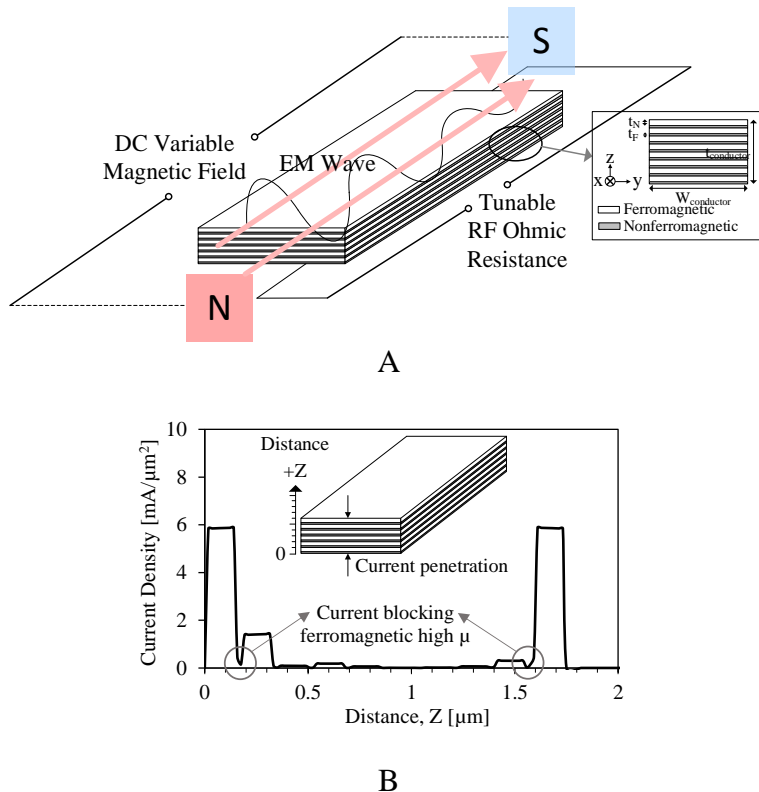


Figure 5-3. The proposed magnetically tunable superlattice conductor. A) The schematic of the conductor under an applied DC magnetic field, B) the distribution of the current density through the volume of the conductor at f_{FMR} frequency for Cu/Ni₈₀Fe₂₀ (150 nm/25 nm) totaling a 1.75 μm -thick conductor.

Figure 5-3A shows the proposed M-FET where the schematic of the proposed tunable conductors made of 20 Cu/Ni₈₀Fe₂₀ layers with a thickness of 180 nm/30 nm, respectively, totaling a conductor of 2.1 μm thickness. The 30 nm-thick Ni₈₀Fe₂₀ layers in between the sandwich Cu layers are used to control the ohmic resistance of the total conductor near f_{FMR} frequency. However, due to employment of ultra-thin ferromagnetic layers, the majority of conductor is made of a highly conductive metal (Cu in this work) leading to an improved selectivity. The proposed unique conductor architecture operates as an actual conductor propagating EM waves and not as a reflector and the ohmic resistance tunability occurs in the direction of propagation. A variable DC magnetic field (Figure 5-3A) is used to tune the f_{FMR} and ohmic resistance peak point versus frequency.

In order to make the conductor frequency selective, a conductor having a low ohmic resistance in all frequencies except a high resistance in a narrow tunable frequency band is intended. The thickness of the Cu layers are chosen to be 6 times more than Ni₈₀Fe₂₀ layers, overall consisting $\approx 85\%$ of the conductor's volume to make the conductor have high resistance only in the vicinity of f_{FMR} where $\mu_r'' \gg 1$ with high magnetic losses and low resistance in other frequencies. Figure 5-3B depicts the finite-element-method (FEM) simulation results of the proposed conductor using ANSYS HFSS v. 15.0 where it shows ferromagnetic layers successfully modify the electromagnetic wave penetration through the conductor in a frequency-selective manner.

Tunability Using an External DC Magnetic Field

Upon applying an external DC magnetic field in the direction of electromagnetic (EM) wave propagation, the magnetic torque of Ni₈₀Fe₂₀ is aligned with the magnetic field of the EM wave, causing the EM energy to be transferred to the spin torque and dissipated as heat, resulting

in the decrease of electrical conductance. With a magnetic flux of 0 and 60 mT, the ferromagnetic resonance frequency changes from 900 MHz to 7 GHz (700 % frequency tunability) and so is the maximum electrical resistance point (Figure 5-4A). The Kittel equation [32] predicts the increase of the ferromagnetic resonance frequency as a function of the external magnetic field strength,

$$f_{FMR} = \frac{\gamma}{2\pi\mu_0} \sqrt{(\vec{H}_{ext} + \mu_0 \vec{H}_{Kp})(\vec{H}_{ext} + \mu_0 \vec{H}_{Kp} + \mu_0 M_s)} \quad (5-6)$$

in which γ is the gyromagnetic ratio, μ_0 is the permeability of air, H_{ext} is the external applied magnetic field, H_{Kp} is the anisotropy field of the ferromagnetic material, and M_s is its magnetization saturation. Meantime, more magnetic dipoles are aligned with the DC magnetic field and the magnitude of the imaginary part of magnetic permeability (μ''), which is indication of the magnetic loss, decreases.

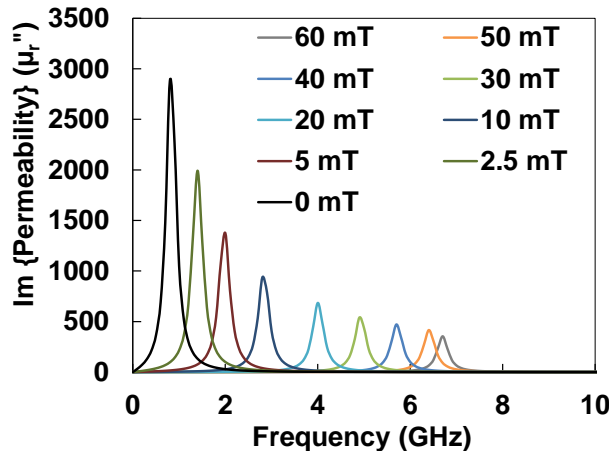


Figure 5-4. The imaginary part of permeability expected by Kittel formula where the peak point values of the permeability versus operation frequency are shown.

Comparison of M-FET and MOSFET

The proposed M-FET conductor architecture utilizes very thin ferromagnetic layers to microscopically modify the current flow in a conductor and the resulting ohmic resistance of it. The spin torque transfer from electromagnetic wave to the magnetic moment which has

maximum loss near f_{FMR} frequency has been used as the loss mechanism to increase the ohmic loss near ferromagnetic resonance. Near f_{FMR} , the magnetic loss of the ferromagnetic material is maximum which will affect the current flow in neighboring non-ferromagnetic layers and eventually increases ohmic loss in a frequency-selective manner. The main parameter that makes the ohmic resistance of the conductors tunable versus frequency is the amount or volume of the ferromagnetic material (with respect to the non-ferromagnetic material) which affects the neighboring non-ferromagnetic conductors. As a result, by increasing the volume, in other words, by modifying the thickness ration of the non-ferromagnetic / ferromagnetic conductors, the absolute value of the resulting ohmic loss of the conductors will be modified. This is the dual of doping in semiconductor technology where by controlling the level of doping, that would be possible to change the conductivity of the semiconductor.

In a MOSFET transistor, electric field (E-field) is used for biasing and controlling the resistive channel and resulting ohmic resistance of the channel. However, in M-FETs, a magnetic field is used to change the ohmic resistance while operating in a single frequency or the peak point of the resistance in different frequencies.

Figure 5-5 shows the comparison of the regular metal-oxide semiconductor field-effect transistor (MOSFET) with respect to proposed M-FET. In conventional MOSFET transistors, a DC electric field (E-field) is applied which enables creation of a channel below the gate oxide inside the substrate where the conductivity of the channel is tunable upon applied electric field. However, the proposed M-FET utilizes a magnetic field (H-field) in the longitudinal direction parallel to the conductor's length and perpendicular to the electromagnetic H-field. Since the conductor in M-FET is made of alternating non-ferromagnetic / ferromagnetic layers with thicknesses much smaller than the skin depth, the applied DC H-field will affect the

ferromagnetic layers which have maximum loss near their ferromagnetic resonance frequency (f_{FMR}). Since f_{FMR} is tunable by applying an H-field, the resulting multi-layer conductor will have a tunable ohmic loss versus frequency.

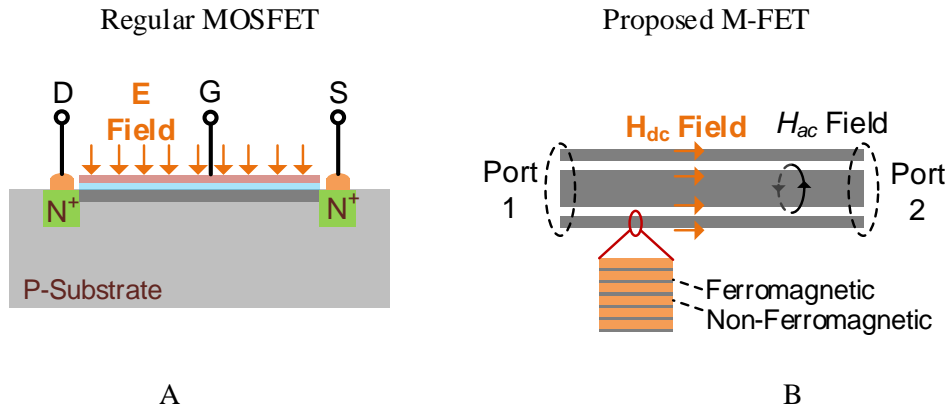


Figure 5-5. The schematics comparing the regular FET and the proposed M-FET. A) The cross section view of the regular FET transistors working based on an applied E-field, B) the proposed M-FET where an H-field is applied for realization of tunable nano-superlattice conductors.

Table 5-2. The comparison of the MOSFET and the proposed M-FET.

Parameter/Structure	MOSFET	Proposed M-FET
Material	Semiconductor	Electrical conductor
Conductivity change	Semiconductor doping	Non-ferromagnetic / ferromagnetic thickness ratio
Bias	Electric field	Magnetic field
Carriers	Electrons and holes	Electrons

Table 5-2 shows the comparison of the principles of operation of the regular MOSFET and the M-FET which is proposed in this work. The main difference is the fact that M-FET uses conductors only for realization of a tunable ohmic resistance with electrons as carriers; however, MOSFETs uses a semiconductor and the electron/hole pair carriers with a completely different theory of operation.

Material Characterizations

In this section, a comprehensive material characterization of the ferromagnetic materials employed in this work are provided to extract their dynamic frequency response and the related

design procedure for passive microwave components' implementation. As shown in Figure 2-5, a B-H loop is used to characterize the properties of a ferromagnetic material by representing its magnetization saturation and coercivity field. The magnetization saturation (M_s) occurs when almost all of the magnetic moments in a ferromagnetic material are magnetized in parallel to the applied magnetic field. M_s is a function of the material and not the physical shape of the ferromagnetic material like if it is a bulk material or thin film. Coercivity field (H_c) is the amount of magnetic field which is required to reverse the magnetization in a ferromagnetic material. Unlike M_s , coercivity is highly dependent on the physical properties of the material. Coercivity is a function of general shape of the material such as its thickness in the case of thin films, the crystalline structure, grain size, and the film stress. Therefore, when ferromagnetic materials are sandwiched between other layers, their coercivity changes due to a different amount of film stress.

When ferromagnetic materials are deposited with very small thicknesses in the nanometer range, their magnetic properties highly change. As a result, the characterization of these materials with different thicknesses will help understand their properties for the given thicknesses. Pure Ni and Ni₈₀Fe₂₀ are among the most commonly studied ferromagnetic materials which are also used in this work. Figure 5-6 shows the measurement results of the B-H characteristic loops of a single layer Ni thin film with thicknesses of 15, 30, 60, and 200 nm. The Ni thin films are deposited using RF sputtering (Kurt J. Lesker CMS-18) on the (100) Si substrate and later 3 mm × 3 mm samples are prepared for measurements. The vibrating sample magnetometer (VSM) has been used (ADE Technologies EV9 with a maximum applied field of $\pm 1800 \text{ kA m}^{-1}$) to measure the B-H loops. The horizontal axis shows the applied H-field in Oersted (Oe) and the vertical axis shows the magnetization in Tesla (T). A magnetization

saturation of 0.5 T has been recorded for the Ni thin films independent of their thicknesses. For the given thickness of 15 nm and 30 nm, not much difference has been observed for the measured coercivities; however, increasing the thickness of Ni will increase the coercivity. A maximum coercivity of 350 Oe has been measured for Ni with a thickness of 60 nm.

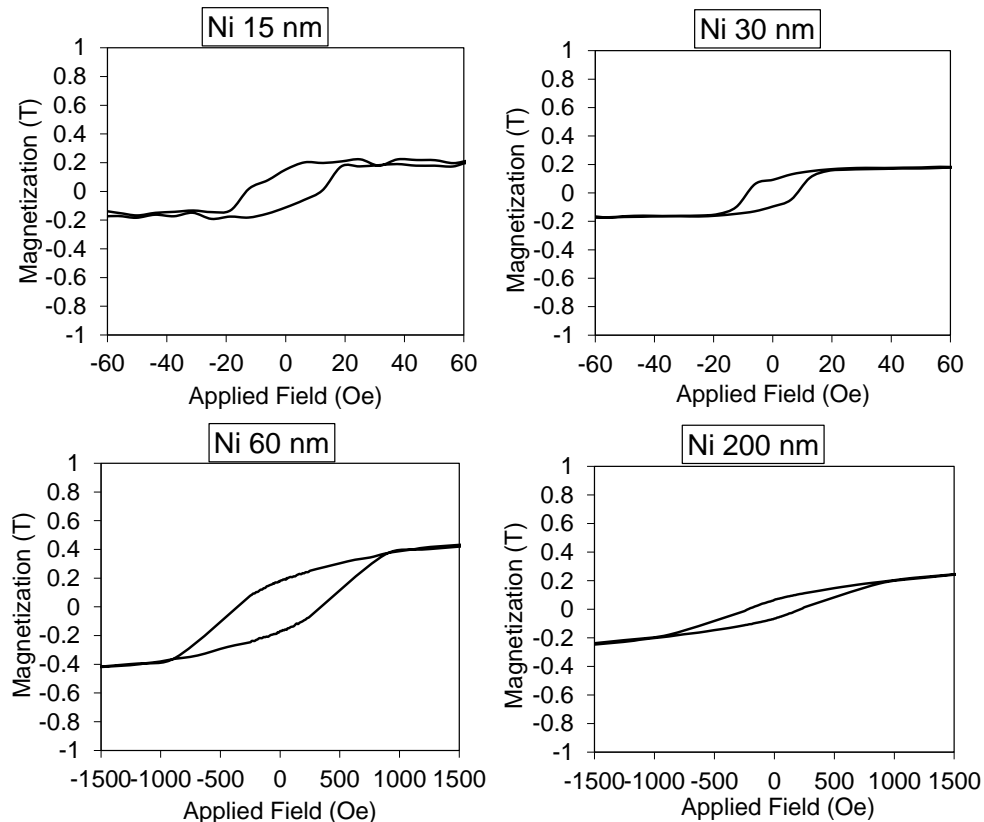


Figure 5-6. The measurement results of B-H loops of a single layer Ni thin film with different thicknesses.

The Cu/Ni multi-layer structure are also deposited using DC/RF sputtering (Kurt J. Lesker CMS-18) on the (100) Si substrate and magnetic characterizations have been performed due to their wide range of applications in low loss conductors as explained in Chapter 4 and M-FET's that will be explained in this Chapter. Cu is used for the non-ferromagnetic material because of having a high electrical conductivity. The stress between the layers in a Cu/Ni structure is the dominant factor changing the coercivity fields. Figure 5-7 shows the B-H loop

measurements which have been performed for the Cu/Ni conductors with the same Ni thickness but a different total number of layers. The 10 layer Cu/Ni structure has recorded a coercivity field of 120 Oe while the 3 layer Cu/Ni structure shows a coercivity field of 114 Oe which is expected since 10 layer sample has a higher stress than the 3 layer sample. Compared to a single layer Ni with 30 nm thickness with a coercivity of 15 Oe, the Cu/Ni samples show a considerable increase in the coercivity field up to 120 Oe. The utilized substrate for all measured samples was Si (100) which were all cut in a square shape close to 3 mm × 3 mm. Figure 5-8 shows the comparison of measured coercivity fields of Ni ferromagnetic thin films with different deposition thicknesses.

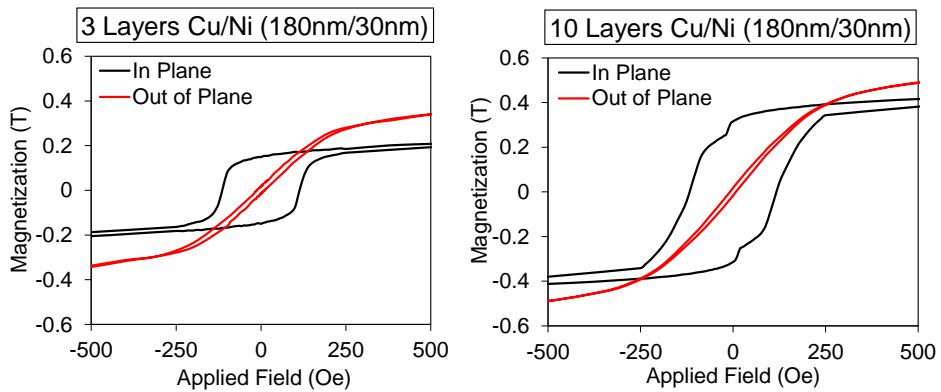


Figure 5-7. The B-H loop measurement results of the Cu/Ni multi-layer conductors.

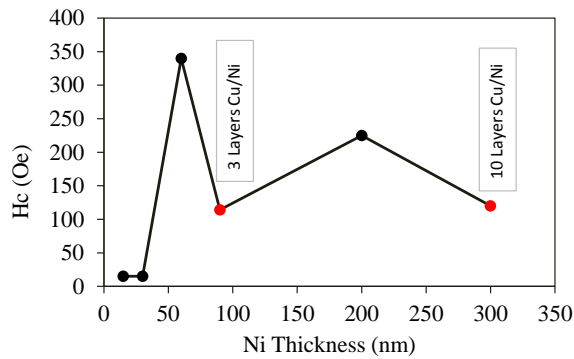


Figure 5-8. The comparison of measured coercivity fields of Ni ferromagnetic thin films with different deposition thicknesses.

Permalloy ($\text{Ni}_{80}\text{Fe}_{20}$) is another ferromagnetic material which has been widely used in this study. The Cu/NiFe conductors have been used in Chapter 4 for planar low loss conductors and are used in this Chapter for realization of M-FETs. Figure 5-9 shows the B-H loop measurement results of the Cu/NiFe conductors with a thickness of 180 nm/30 nm with 10 and 15 paired layers. One could observe that the coercivity of NiFe films is much smaller than Ni films. A coercivity of 5 Oe has been measured for 10 layers of Cu/NiFe while a coercivity of 9 Oe is measured for 15 layers of Cu/NiFe.

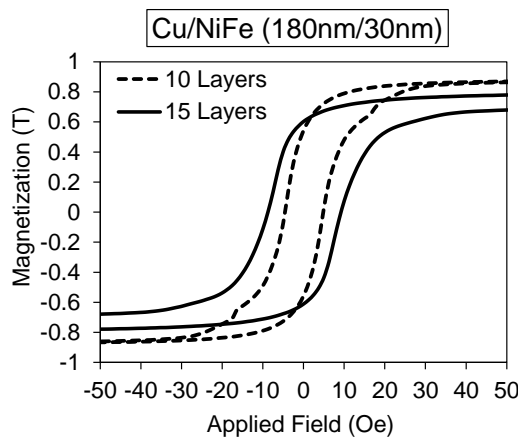


Figure 5-9. The B-H loop measurement results of Cu/NiFe conductors of 10 and 15 layers.

One important conclusion that could be conducted comparing Ni and NiFe is the fact that increasing the stress of the films has a much higher impact on NiFe films than Ni films. The coercivity in the Ni films is highly dependent on the thickness of Ni and less dependent on the stress of the films. Increasing the number of Cu/Ni layers from 3 to 10 paired layers has only increased the coercivity from 114 Oe to 120 Oe while 15 layers of Cu/NiFe has almost 80% increased coercivity compared to 10 layers Cu/NiFe from 5 to 9 Oe (Figure 5-9). Figure 5-10 shows the comparison of Cu/Ni and Cu/NiFe conductor samples with the same structures (10 paired layers and the thicknesses of 180 nm/30 nm). As it is seen, Cu/Ni samples have much

higher coercivity compared to Cu/NiFe samples (120 Oe compared to 5 Oe) while having almost half magnetization saturation (0.5 T compared to 0.9 T).

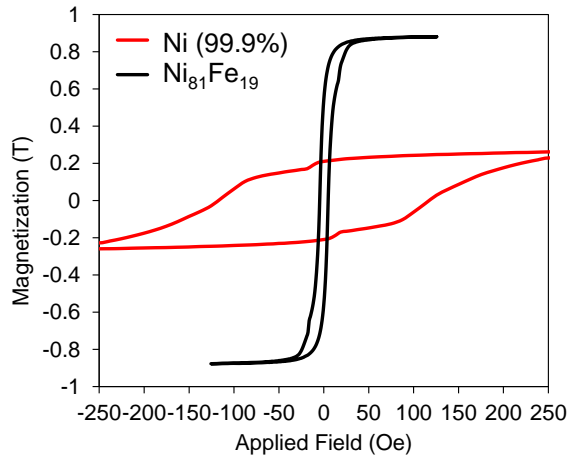


Figure 5-10. The comparison of Cu/Ni and Cu/NiFe conductor samples with 10 number of layers and the same thicknesses of 180 nm/30 nm.

Other combinations of Cu/NiFe have also been magnetically characterized as they are used in this Chapter for realization of M-FETs with different amounts of maximum ohmic loss at ferromagnetic resonance.

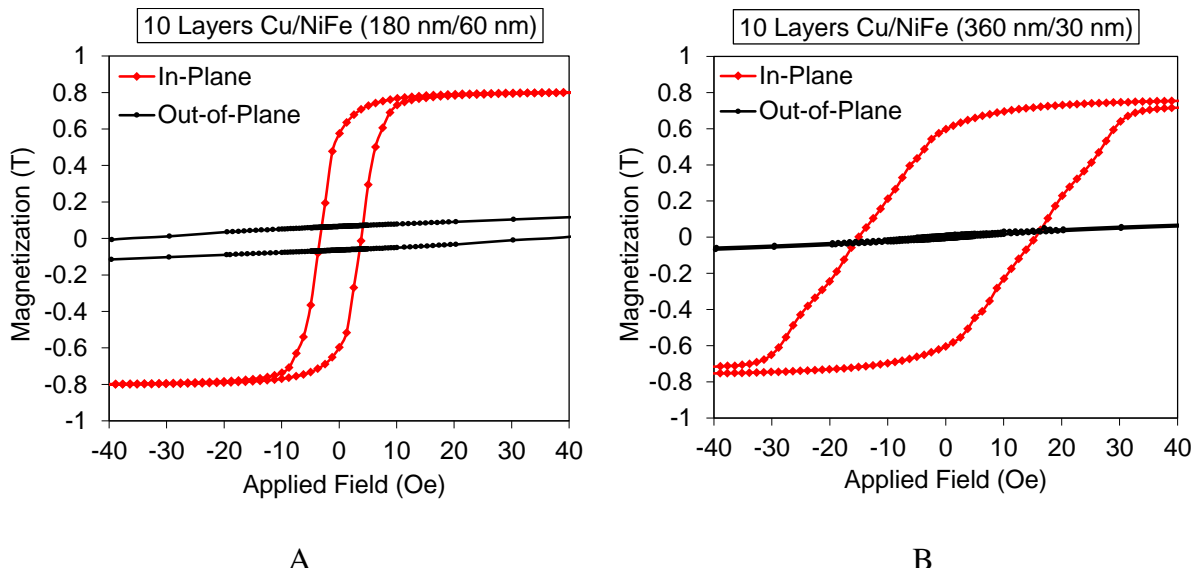


Figure 5-11. The B-H loop measurement results of the Cu/NiFe samples. A) 10 layers with Cu/NiFe of 180 nm/60 nm, B) 10 layers with Cu/NiFe of 360 nm/30 nm.

Figure 5-11 shows the magnetic characterization of Cu/NiFe samples which are deposited on a Si substrate using the PVD method explained before. Due to the relatively small coercivity of NiFe, the coercivity of the Cu/NiFe samples will be highly dependent on the stress of the film. The 10 layers 360 nm /30 nm with higher stress compared to 10 layers 180 nm /30 nm and 10 layers 180 nm /60 nm, has a higher coercivity field of 15 Oe compared to 5 to 6 Oe for other two samples.

Effect of Ferromagnetic Material on Resonance Frequency Tunability

The B-H loop measurements performed in previous section will be used to extract important information regarding the ferromagnetic material which could be used to predict their performance as will be used in this work to extract their dynamic response. The dynamic frequency response of ferromagnetic thin films with uniaxial anisotropy is given by LLG equation and can be extracted using magnetic properties of the materials. The magnetization saturation, the in-plane and out-of-plane anisotropy fields are directly read from the B-H characteristic loops using VSM measurements to see the frequency response of the permeability including the ferromagnetic resonance and the amplitude of the real and imaginary parts of permeability.

Ni and Permalloy ($\text{Ni}_{80}\text{Fe}_{20}$) are well-known ferromagnetic materials while their properties in RF are quite different from each other and could be used for different applications as explained in the following. Figure 5-12 shows the magnetic characterization B-H loops for Cu/Ni and Cu/NiFe samples using VSM measurements followed by their estimated frequency-dependent permeability graphs using the LLG dynamic model. Two significant differences comparing Ni and NiFe are observed: (1) the in-plane anisotropy, and (2) the relative permeability values. The ferromagnetic resonance frequency (f_{FMR}) is the frequency where the real part of permeability becomes zero and the imaginary part is maximized. Since the in-plane

anisotropy field of Ni (120 Oe) is much larger than that of the NiFe (5 Oe), it is much less dependent on an external magnetic field, i.e. the f_{FMR} shifts from 3 GHz to 5 GHz for Ni while from 900 MHz to 7 GHz for NiFe upon an external magnetic flux of 60 mT. This contrasts the magnetic tuning capability of NiFe compared to Ni which will be exploited in this work. Also, much higher values of the imaginary part of NiFe compared to Ni, representing magnetic losses, will be used. These two effects are favorably used in designing different applications such as low loss conductors using Cu/Ni and magnetically-tunable conductors using Cu/NiFe.

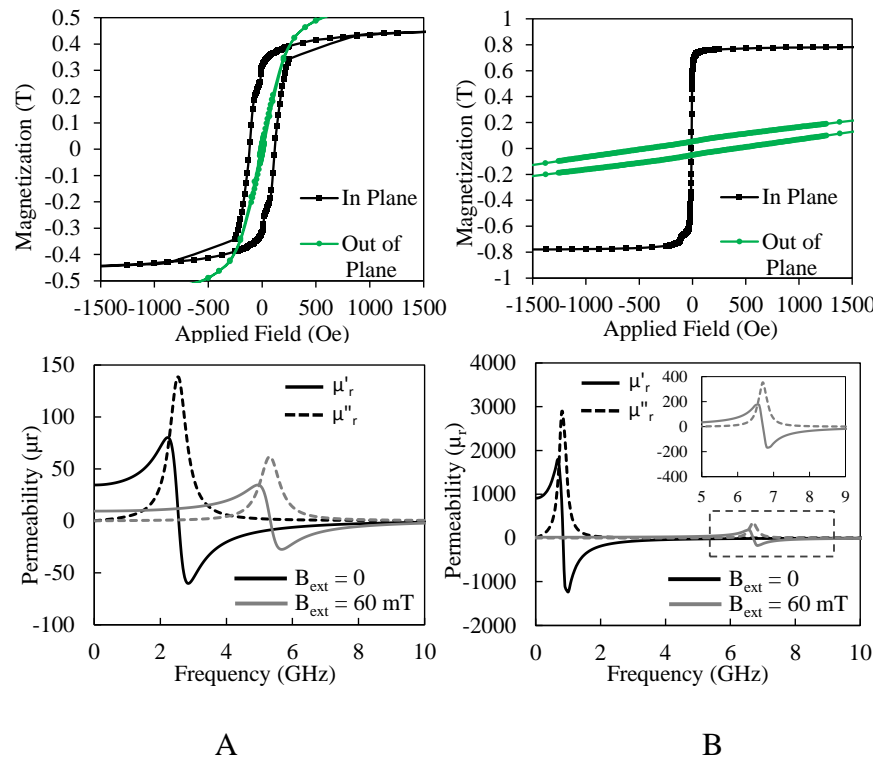


Figure 5-12. The magnetic characterization B-H loops (upper) and theoretical permeability spectra (lower). A) Cu/Ni and B) Cu/Ni₈₀Fe₂₀ thin films. The real and imaginary parts of the permeability $\mu_r = \mu_r' - j\mu_r''$ are shown using solid and dashed lines, respectively, in the frequency range of 0 to 10 GHz where the black and gray lines indicate applied magnetic flux of 0 and 60 mT, respectively

Table 5-3 shows the summary of the magnetic properties of Ni and NiFe which are used in this work. The magnetization saturation and in-plane anisotropy field values are directly read from B-H loop measurements and other parameters are borrowed from literature.

Table 5-3. Comparison of the material properties of pure Ni and Ni₈₀Fe₂₀.

Material/Property	Ni (99.99%)	Ni ₈₀ Fe ₂₀
Magnetization saturation (T)	0.5	0.9
In-plane anisotropy field (Oe)	145	5
Gilbert damping ratio [33]	0.04	0.01
Electrical conductivity (S/m)	1.43×10 ⁷	6×10 ⁶
f _{FMR} (MHz)	3000	900

Physical Characterizations

After performing the magnetic characterizations, the physical characterizations are to be performed to see how physically the layers are deposited on top of each other. Since the layers are very thin in the range of nano meter (nm), the roughness of the substrate will have and important effect on the performance of final machined devices. Also, the intermediate effects between the layers and the possible diffusion of the nano-layers with different materials should be physically observed. At last, the effect of substrate will be seen by looking at the multi-layer conductors deposited on top of different types of substrates.

The physical structure of the deposited layers are first milled using a Focused Ion Beam (FIB) tool (Dual-Beam Strata DB235) with gallium metal ion beam source for nanoscale cutting. The cross section view of the conductors are then detected using both scanning electron microscopy (SEM) and transmission electron microscopy (TEM) imaging. Figure 5-13 shows the TEM image results (2010F JEOL USA, Inc.) of the conductors' cross section views on Si and glass substrates. Figure 5-13A and Figure 5-13B show the Cu/NiFe 180 nm/30 nm conductors on Si and Corning glass substrates, respectively. The thin NiFe layers are recognizable in gray color in between the Cu layers. Figure 5-13C shows the Cu/NiFe 180 nm/60 nm conductor where the NiFe layers are quite visible having almost one third thickness of the Cu nano layers. Although the silicon substrates are polished to a high level of smoothness, the glass substrates used in this

work are also highly uniform and the TEM images show no sensible difference comparing these two substrates.

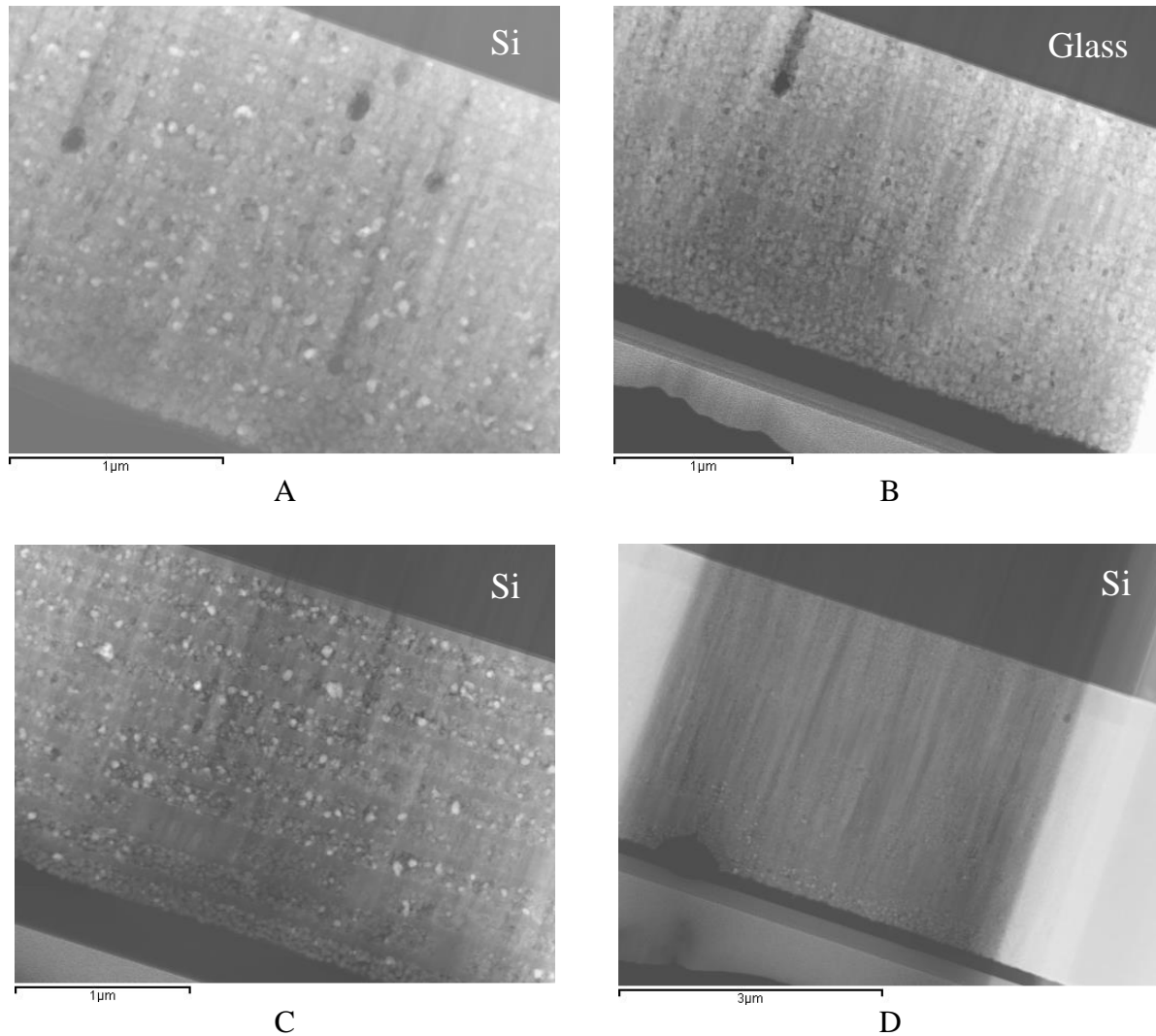


Figure 5-13. The TEM micrographs of the cross section view of the deposited multi-layer conductors. A) Cu/NiFe of 180 nm/30 nm on (100) Si substrate, B) Cu/NiFe of 180 nm/30 nm on SGW3 Corning glass substrate, C) Cu/NiFe of 180 nm/60 nm on (100) Si substrate, and D) Cu/NiFe of 360 nm/30 nm on (100) Si substrate.

Figure 5-14 shows the zoomed in version of the Cu/NiFe of 180 nm/30 nm conductor sample on SGW3 Corning glass substrate where the nano layers of the titanium (Ti) adhesion promoter and the Cu and NiFe are indicated. Figure 5-14B shows the roughness of the glass substrate which is duplicated to the upcoming nano layers giving rise to the RF loss. Another

effect than could be observed from the TEM image is the diffusion of the layers which takes place at the interface between them. This will create a mixture of Cu and NiFe in those regions deviating from the ideal case of perfect layers on top of each other which reduces the performance of the RF devices. In the case of low loss conductors in Chapter 4, this effect will be reflected in terms of the limited RF resistance reduction extracted from the transmission lines and inductors diminishing the maximum conductor loss reduction. This could be solved by using an extra ultra-thin neutral conductive metal like Rubidium (Rb) in between the layers to reduce diffusion which is currently being investigated.

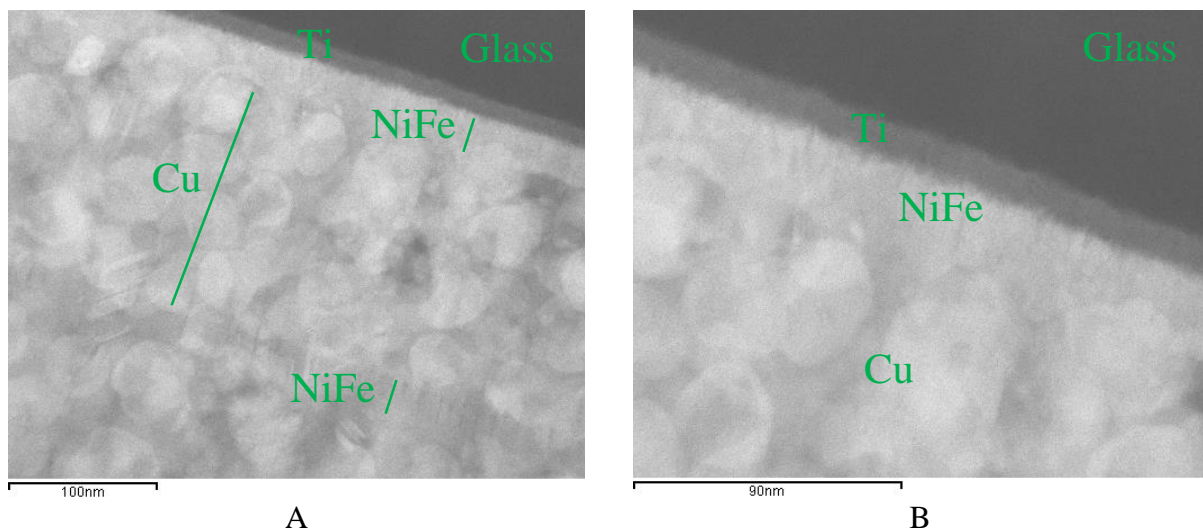


Figure 5-14. The zoomed in version of the Cu/NiFe of 180 nm/30 nm conductor sample on SGW3 Corning glass substrate.

Further material characterization is performed using energy dispersive X-ray spectroscopy (EDX) on the cross section of the conductors to map the material through the conductor. The EDX is performed using an electron beam size of 0.5 nm diameter (TEM tool, 2010F JEOL USA, Inc.). Figure 5-15 shows the EDX results of the conductor's cross section which shows the Cu (blue), Ni (green), and Fe (red) peaks alternating through the conductor's cross section. The nickel and iron peaks occur on the same position since an alloy material

(Permalloy) is used for deposition of the ferromagnetic material; however, the copper peaks are on the alternative positions periodically repeating through the conductor's cross section.

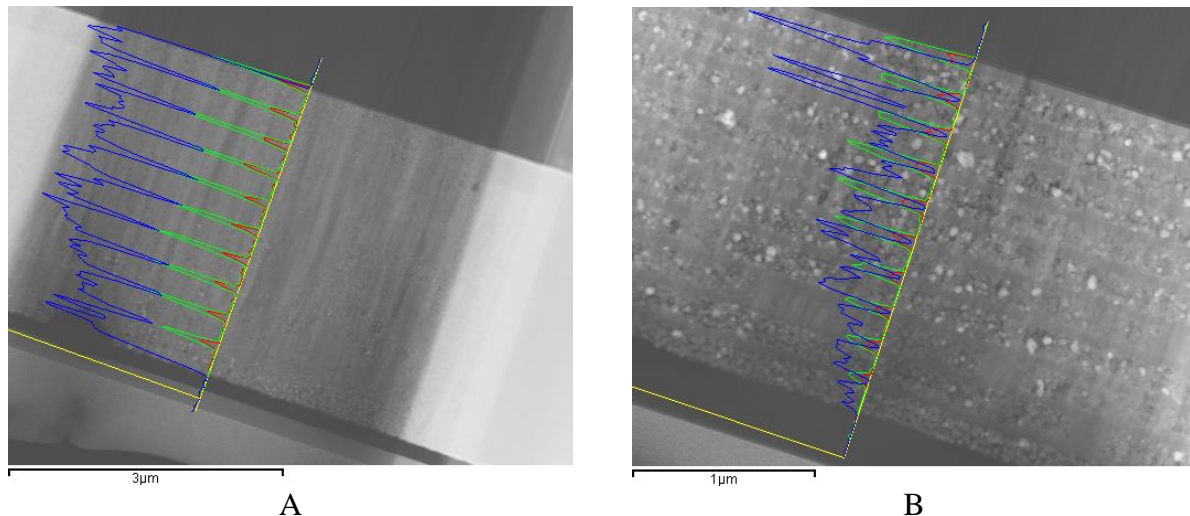


Figure 5-15. The EDX characterization results of Cu/NiFe. A) Conductor of 360 nm/30 nm thickness, B) conductor of 180 nm/60 nm thickness.

Fabrication and Experimental Results

The coplanar waveguide (CPW) transmission lines are used as the conductor to implement the proposed M-FETs structures. The requirement of the M-FET realization is generation of an alternating magnetic field which is perpendicular to a DC magnetic field to be able to perform the so called spin torque transfer from electromagnetic wave to the magnetic moment of the ferromagnetic material. The proposed nano-superlattice conductors are fabricated in order to experimentally demonstrate the tunable conductor concept. Since the deposited metal layers are very thin, a super-uniform low loss glass substrate (SGW3, Corning Incorporated, $\epsilon_r = 5.8$, $\tan \delta = 0.0042$) with a thickness of 300 μm and a coefficient of thermal expansion (CTE) of $31.7 \times 10^{-7} / ^\circ\text{C}$ and a surface roughness of less than 1.0 nm is used. Coplanar waveguide (CPW) transmission lines employing the planar multi-layer metaconductor architecture are nano-machined and RF characterizations have been performed. Two different methods have been investigated for the fabrication of the transmission line M-FETs shown in Figure 5-16. In the

first method, the Cu/Ni and Cu/NiFe thin films are alternately deposited by DC/RF sputtering (CMS-18, Kurt J. Lesker, Inc.) and final devices are patterned using a lift-off process (Figure 5-16A). The resulting pattern will depend on the resolution of lift-off photoresist (NR9-8000P Futurrex Inc.). Since the utilized PVD film deposition method has a good coverage, a slightly over developed photoresist is used in this work to ensure a successful lift-off process of the relatively thick films such as deposition of Cu/NiFe conductors of 360 nm/30 nm, with a total thickness of 3.9 μ m. Using the second method in Figure 5-16B, a mixture of acetic acid, nitric acid, sulfuric acid, and DI water has been used as the etchant with a composition of CH_3COOH : HNO_3 : H_2SO_4 : $\text{H}_2\text{O} = 2: 2: 1: 8$.

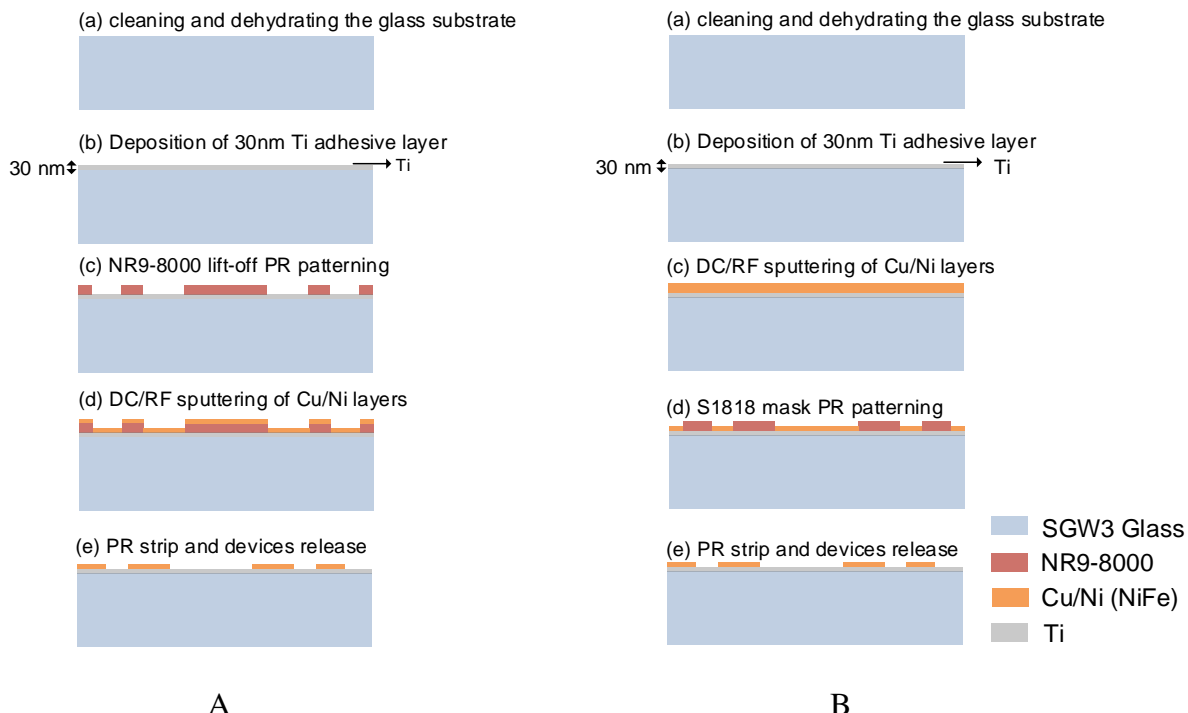


Figure 5-16. The microfabrication process of the M-FETs. A) Method I using lift-off process, B) method II using wet etching process.

The utilized etchant is able to etch both Cu and Ni/NiFe simultaneously. The photolithography in method II is performed after the deposition of film and prior to wet etching.

As a result, since the wet etching is an anisotropic process, the main disadvantage of this method is the undercut which is made after patterning the final devices reducing the dimensions of them.

Figure 5-17 shows the optical micrographs of the fabricated M-FETs using the lift-off and process. In order to achieve a successful lift-off, the NR9-8000P photoresist is slightly overdeveloped to create an undercut as shown in Figure 5-17B to ensure a successful lift-off process.

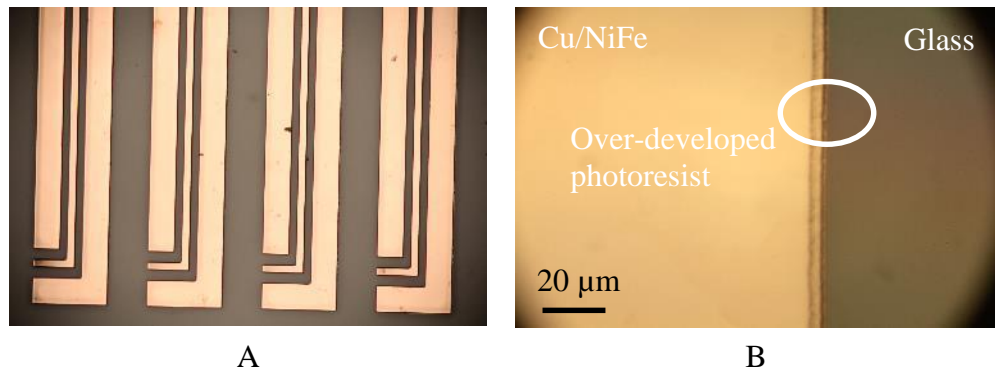


Figure 5-17. The optical micrographs of the fabricated M-FETs. A) The devices which are made using a lift-off process, B) the edge of the conductor using the over-developed photoresist after the lift-off process.

Figure 5-18 shows the scanning electron microscopy (SEM) micrographs of the fabricated transmission lines with the signal line width, $W = 60 \mu\text{m}$ and $30 \mu\text{m}$ and the detailed view of conductor's feeding line with 90° rotated angle.

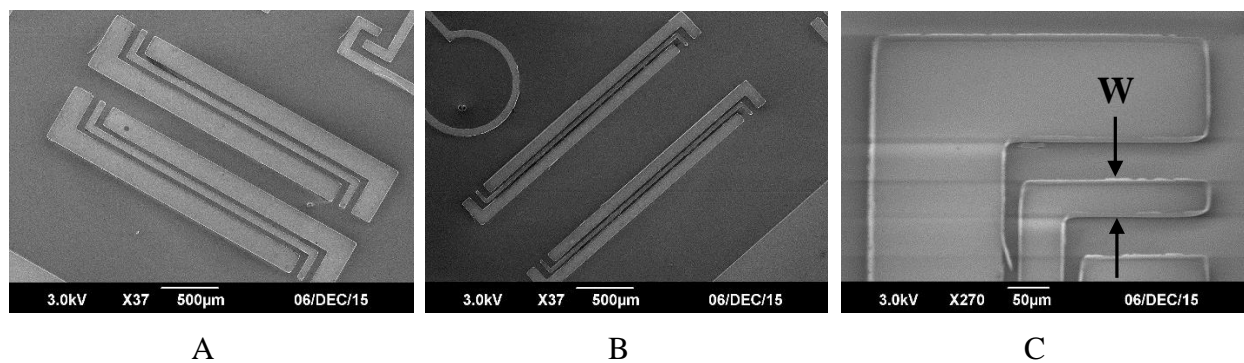


Figure 5-18. The SEM micrographs of the fabricated transmission lines with a length of 2.0 mm. A) Width, $W = 60 \mu\text{m}$, B) $W = 30 \mu\text{m}$, and C) the detailed view of conductor's feeding line with 90° rotated angle.

RF Measurements

RF measurements have been performed using a vector network analyzer (E5071, Agilent Inc.) after standard short-open-load-through (SOLT) two-port calibration between 10 MHz and 20 GHz. A Cascade Microtech probe station with ground-signal-ground (GSG) probes (150 μm pitch) are used for testing. Several de-embedding pads are placed on the substrate to take out the series and parallel parasitic effects. Figure 5-19 shows the utilized test setup for RF measurements of the M-FET conductors using VNA. A variable DC magnetic field is applied through the length of the conductors and the two-port RF measurements have been performed. The PI-type lumped-element equivalent circuits are used as in inset of Figure 4-11B for extraction of the ohmic resistance of the M-FETs.

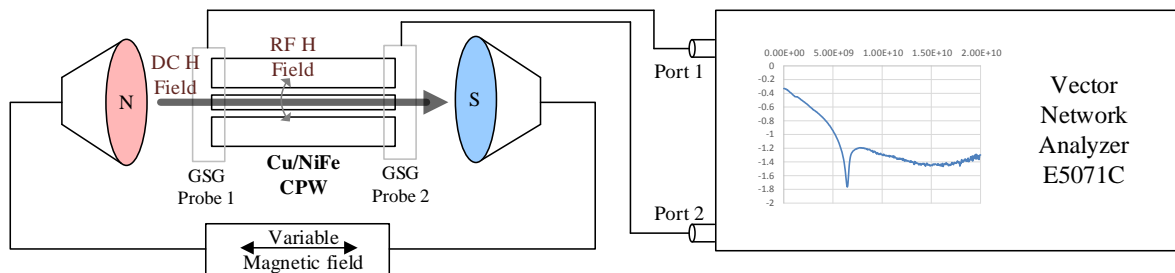


Figure 5-19. The test setup for RF measurements of M-FETs using VNA.

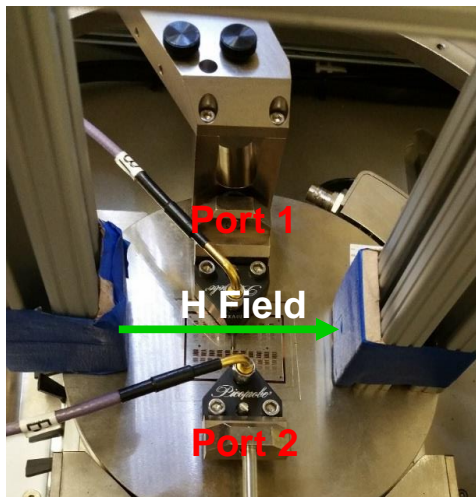


Figure 5-20. The actual measurement platform and device-under-test (DUT) under an applied DC magnetic field.

Figure 5-20 shows the actual measurement platform where the two-port RF measurements are being performed for the device-under-test (DUT) and the NdFeB permanent magnets [34] in a variable magnetic setup are used. Two ports of the CPW transmission lines are 90° rotated in order to make it feasible to establish the magnetic field while devices are being tested.

The Effect of Ferromagnetic Material

The first parameter to be investigated for the implementation of the M-FET devices is the ferromagnetic material. A ferromagnetic material highly responsive to a DC magnetic field with high values of imaginary part of permeability is interested. In result of that, a tunable conductor having high ohmic resistance near ferromagnetic resonance could be realized.

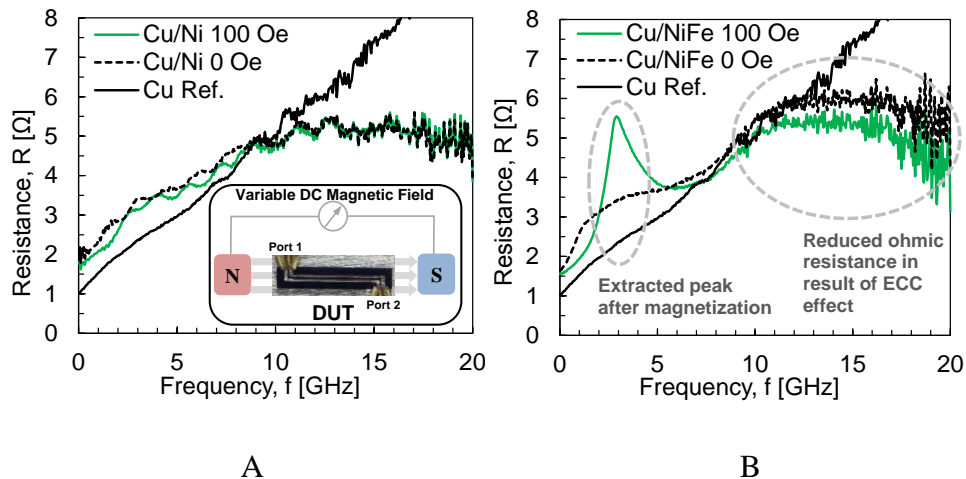


Figure 5-21. The measured extracted resistance of the transmission lines before and after DC magnetic field of 0 and 100 Oe. A) Cu/Ni conductor, and B) Cu/NiFe conductor.

The main two differences comparing Cu/Ni and Cu/NiFe conductors mentioned earlier in this Chapter are the peak value of imaginary part of permeability and the tunability of the ferromagnetic materials under an applied DC magnetic field. Since Ni has a much higher in-plane anisotropy, it will be much less dependent to an applied magnetic field and therefore, the resulting Cu/Ni M-FET. Also, due to the much smaller permeability, the amount of loss

associated with Ni is much less compared to NiFe and as a result, the peak resistance of the Cu/Ni conductor is expected to be much less compared to Cu/NiFe.

Figure 5-21 shows the measured resistances of the transmission lines made of Cu/NiFe and Cu/Ni by considering a PI-type lumped-element equivalent circuit before and after application of an external magnetic field. The Cu/Ni and Cu/NiFe transmission lines have the same thicknesses of 150 nm/25 nm the reference solid Cu with the same total thickness of 1.75 μm for all three conductors. Several de-embedding pads are placed on the substrate to take out the series and parallel parasitic effects. The inset in Figure 5-21B shows the schematic of the applied magnetic field on the devices under test. A DC magnetic field of 100 Oe has applied for both conductors in Figure 5-21.

At frequencies below 10 GHz, for Cu/Ni conductors shown in Figure 5-21A, in frequencies near f_{FMR} at an external magnetic field of 100 Oe, due to the relatively high in-plane anisotropy field of the Ni films, the peak of the permeability shown in Figure 5-21A doesn't get much affected and a slight increased ohmic resistance is observed. However, for Cu/NiFe conductors shown in Figure 5-21B, the f_{FMR} frequency shifts from 900 MHz to 3 GHz at an external magnetic field of 100 Oe and a maximum peak ohmic resistance occurs at 3 GHz. As mentioned earlier, the tunability and much higher permeability of NiFe thin films theoretically will allow us realize transmission lines with highly increased ohmic resistance near f_{FMR} and highly tunable with respect to external magnetic field. Experimentally verified in this section, $\text{Ni}_{80}\text{Fe}_{20}$ thin films have proven to have superior performance in realizing tunable ohmic resistance in nano-superlattice conductors which are magnetically-driven. At frequencies above 10 GHz, when $|\mu'_{r, \text{Ni}}|$ approaches the Cu/Ni thickness ratio of 6, the effective resistance of the

conductors made of Cu/Ni decreases and falls below that of the reference Cu conductors, suitable for RF devices in Ku and K bands.

Measurement Results

Cu/NiFe has been chosen for the implementation of the proposed M-FET devices. The Cu/NiFe structures with the thickness of 150 nm/25 nm are fabricated using the same fabrication process (lift-off approach) shown in Figure 5-16A. Figure 5-22 shows the measurement results of the Cu/NiFe transmission lines (150 nm/25 nm) under various magnetic fields applied along their easy axes with the same total thickness of 1.75 μm . For the sake of comparison, the measurement results of the transmission lines made of solid Cu with the same thickness of 1.75 μm have been included. Due to the spin torque transfer phenomenon explained earlier in this Chapter, the loss mechanism occurs at resonance when the frequency of the electromagnetic wave approaches the frequency of the precessional movement of the magnetic moment \mathbf{M} . Figure 5-23 shows the peak envelope of the imaginary part of permeability together with the normalized tangent loss of the ferromagnetic films versus applied magnetic field. The increase of the ferromagnetic resonance frequency as a function of the external magnetic field strength is observed. More magnetic dipoles are aligned with the DC magnetic field and the magnitude of the imaginary part of magnetic permeability (μ''), which is indication of the magnetic loss, decreases. The tangent loss is defined as the multiplication of the absolute value of $|\mu''_{r, \text{NiFe}}|$ by its resonance frequency. Although the peak of the $|\mu''_{r, \text{NiFe}}|$ decreases for higher applied magnetic fields; however, the $|\mu''_{r, \text{NiFe}}| \times f_{\text{FMR}}$ remains almost constant for all frequencies. In other words, the amount of increased loss compared to regular Cu reference conductors should be relatively equal in all frequencies. This statement is experimentally verified in the measurement results shown in Figure 5-22A as the slope of the measured ohmic resistance peak points is the same as the

reference Cu conductors; or, the amount of increased ohmic resistance due to usage of NiFe thin films remains the same as predicted by LLG theory (Figure 5-23).

The maximum peak points of the transmission lines are highly tunable from 1 GHz to 7 GHz ($> 700\%$) where an increased ohmic resistance of up to 200% compared to reference Cu conductors is achieved and the multi-layer conductors could be tuned to have a variable resistance for the given range of frequency.

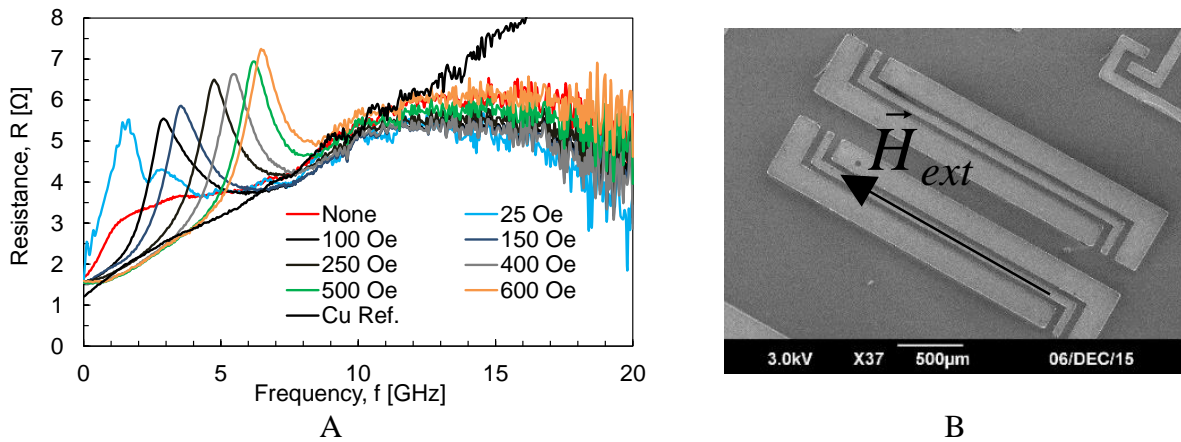


Figure 5-22. A) The measurement results of the extracted resistance of the Cu/Ni₈₀Fe₂₀ (150 nm/25 nm) transmission lines with various DC magnetic fields, B) the SEM of the transmission lines with the direction of the applied magnetic field which is indicated.

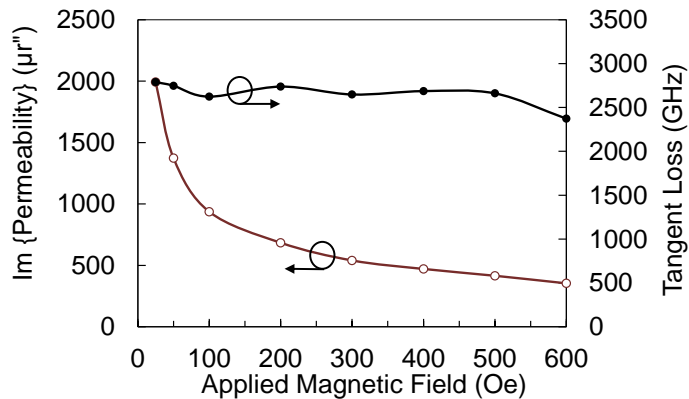


Figure 5-23. The peak point values versus applied magnetic field.

For frequencies above 10 GHz, the Cu/NiFe conductors are acting as low loss conductors. In overall, the proposed artificially fabricated M-FET conductors have an increased

ohmic resistance in low frequency region (< 10 GHz) and a reduced ohmic resistance in high frequency region (> 10 GHz), unlike regular existing solid conductors where their resistance continuously increases with frequency, as they could be also called as “metaconductors”.

Figure 5-4 shows the theoretical imaginary part of the permeability using the LLG dynamic model where the variation of the peak point of $|\mu''_{r, NiFe}|$ is depicted versus frequency. As estimated by the LLG theory, the peak point of the imaginary part of the permeability of the 25 nm Ni₈₀Fe₂₀ thin film shifts towards higher frequencies while the amplitude of resonance decreases almost exponentially below magnetic fields of 5 mT and linearly after 10 mT. Figure 5-24 shows the correlation between the peak resonance frequency of $|\mu''_{r, NiFe}|$ or f_{FMR} based on LLG model and the measurement results of the peak resonance frequency of the extracted RF resistance (Figure 5-22A) of the transmission lines from two different samples. As a result, the experimental results considering ferromagnetic losses as the major loss factor in the nano superlattice conductors verify the LLG model up to 7 GHz.

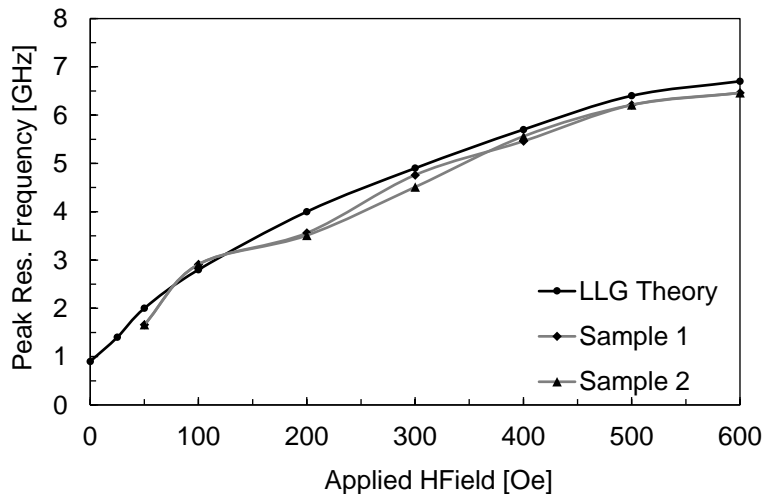


Figure 5-24. The correlation of the LLG theory and the measured samples with Cu/Ni₈₀Fe₂₀ (150 nm/25 nm) in terms of the peak of the ohmic resistance near f_{FMR} .

Figure 5-25 shows the extracted ohmic resistances of the M-FET conductors at a single frequency, where two popular frequency bands of 2.4 GHz and 5.8 GHz are shown. The

resistance of the transmission lines is tunable versus an applied magnetic field while operating at a single frequency. In order to increase the dynamic range of the M-FETs, the range of the minimum and maximum achievable ohmic resistances for the given range of applied DC magnetic field, other combination of Cu/NiFe M-FET conductors could be used. The other noticeable property of the M-FET which is shown in Figure 5-25 is the slope of the ohmic resistance of them where a negative slope is observed when operating in 2.4 GHz bands while a positive slope is achieved when operating in 5.8 GHz center frequency. This ability to set the slope based on frequency is another factor giving rise to the proposed M-FETs to be called metaconductors, since this property could not be achieved using conductors existing in nature.

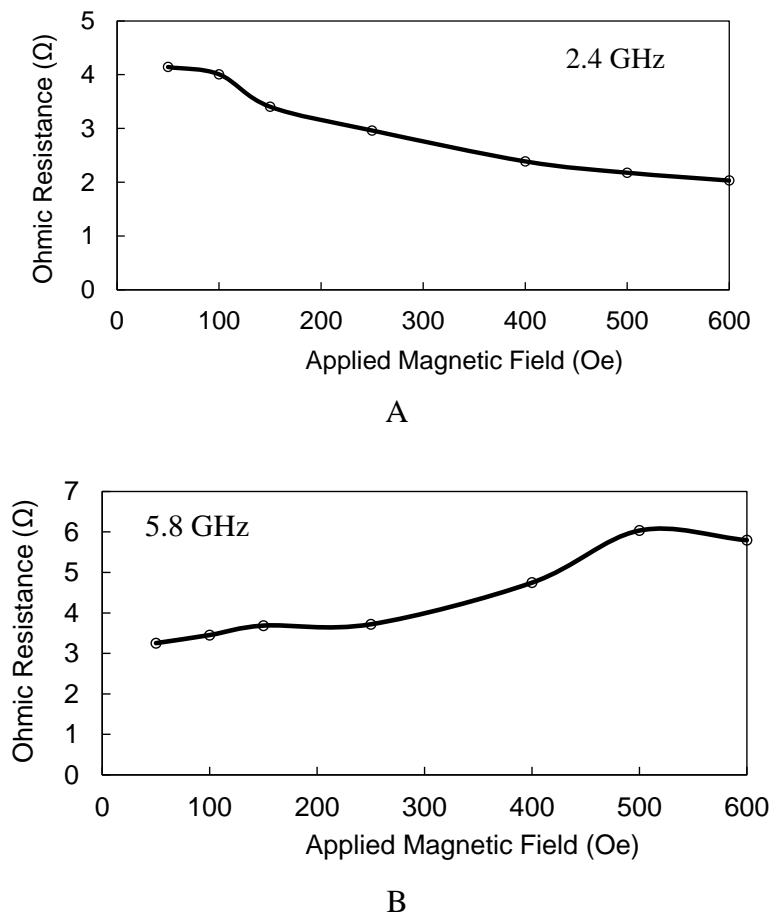


Figure 5-25. The extracted ohmic resistance of the M-FET with Cu/Ni₈₀Fe₂₀ (150 nm/25 nm) versus applied magnetic field. A) At 2.4 GHz, B) at 5.8 GHz.

The Effects of the Layer Thickness

In previous section, the experimental demonstration of the M-FET conductors using a Cu/NiFe of 150 nm/25 nm has been demonstrated. The spin torque transfer from the ferromagnetic materials producing the magnetic losses which are used in proximity to the Cu layers is used as the dominant factor of loss. Therefore, the ratio of the thickness of the ferromagnetic material to the thickness of the non-ferromagnetic material will define how the ferromagnetic materials are affecting the adjacent non-ferromagnetic layers.

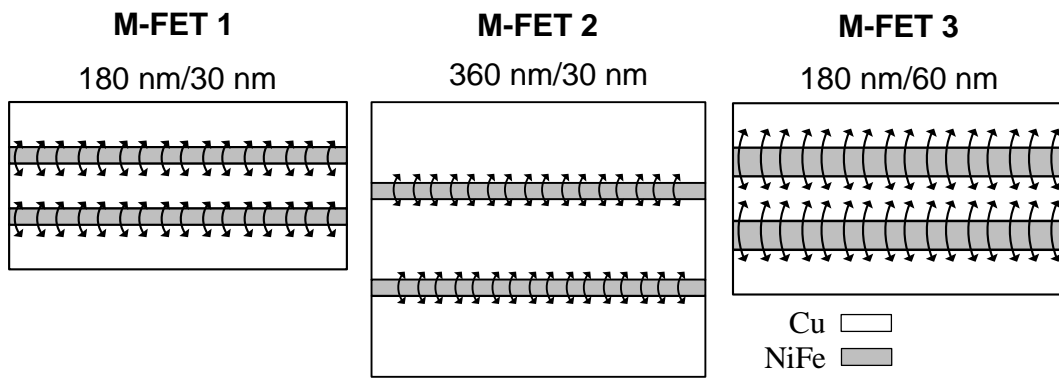


Figure 5-26. The ferromagnetic nano-layers affecting neighboring Cu layers in Cu/NiFe superlattice conductors, showing two paired layers for each.

In order to verify the effects of the layers' thicknesses compared to a Cu/NiFe initial configuration of 180 nm/30 nm (M-FET 1), two multi-layer conductor types are designed. In the second conductor (M-FET 2), the thickness of NiFe is kept the same while the thickness of Cu is increased by a factor of two which results in a Cu/NiFe architecture of 360 nm/30 nm. In the third conductor (M-FET 3), the thickness of Cu is kept the same while the thickness of NiFe is increased by a factor of two resulting in a Cu/NiFe architecture of 180 nm/60 nm. Figure 5-26 shows an intuitive demonstration of the M-FETs and how the ferromagnetic layers affect the neighboring conductors. Once the EM field frequency is close to ferromagnetic resonance, FM material will have maximum loss and M-FET 3 is expected to have maximum loss near

ferromagnetic resonance. Subsequently, M-FET 2 should have minimum loss near resonance since the ratio of Cu to NiFe is larger (which is 12) compared to other two M-FET structures (ratio of 6 for M-FET 2 and ratio of 3 for M-FET 3).

The other two M-FET structures in Figure 5-26 are nano machined using the same microfabrication process explained in Figure 5-16A. Number of layers is fixed for all three conductors; however, with different layers' thicknesses and different total thickness. Also, the same mask has been used for the fabrication of three M-FET conductors as CPW-based structure shown in Figure 5-22B. The TEM micrographs of the conductors' cross section views are depicted in Figure 5-13 and Figure 5-14.

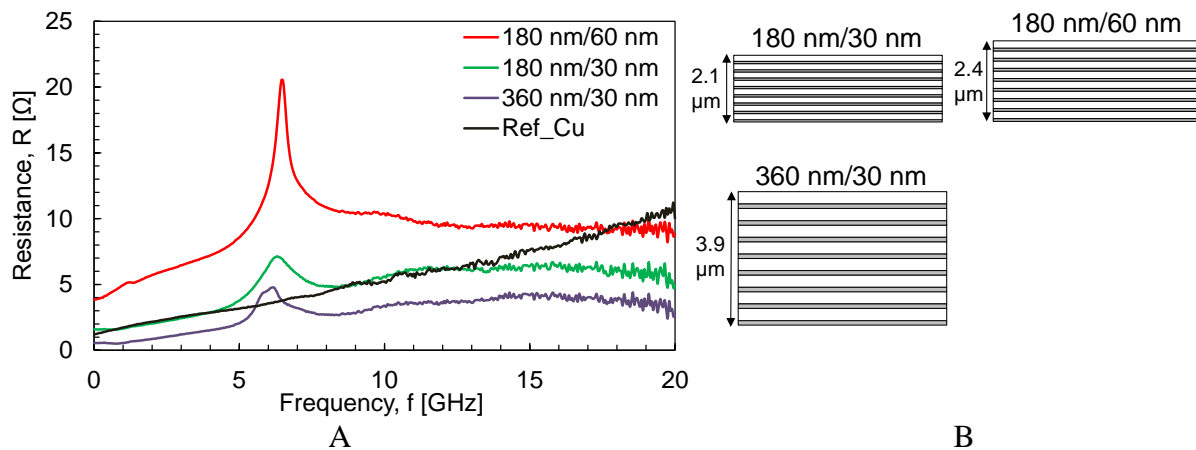


Figure 5-27. The measurement results of the M-FET conductors. A) The extracted ohmic resistance versus frequency given an applied DC magnetic field of 550 Oe, B) the schematic of the conductors.

Figure 5-27A shows the measurement results of the M-FET conductors using the same test setup in Figure 5-19 under an applied DC magnetic field of 550 Oe. The ohmic resistance of the devices is depicted versus frequency up to 20 GHz. The reference Cu conductor shown in Figure 5-27 is made of solid Cu with a thickness of 2 μm . Since the same ferromagnetic material is used for all three conductors, the peak of the ohmic resistance occurs at the same frequency for all. However, M-FET 2 with a Cu/NiFe thickness of 360 nm/30 nm has the lowest ohmic point

since it has the highest thickness ratio and the Cu layers are less affected by NiFe layers. M-FET 3 with a combination of Cu/NiFe thickness of 180 nm/60 nm gives the highest ohmic peak where more than 6 times ohmic peak (> 600%) at 6.5 GHz has been recorded with respect to the solid reference Cu conductor. As a result, the Cu/NiFe thickness ratio has been experimentally verified to operate like a dopant in a semiconductor concept where modifying the ratio changes the absolute value of the peak of the ohmic loss.

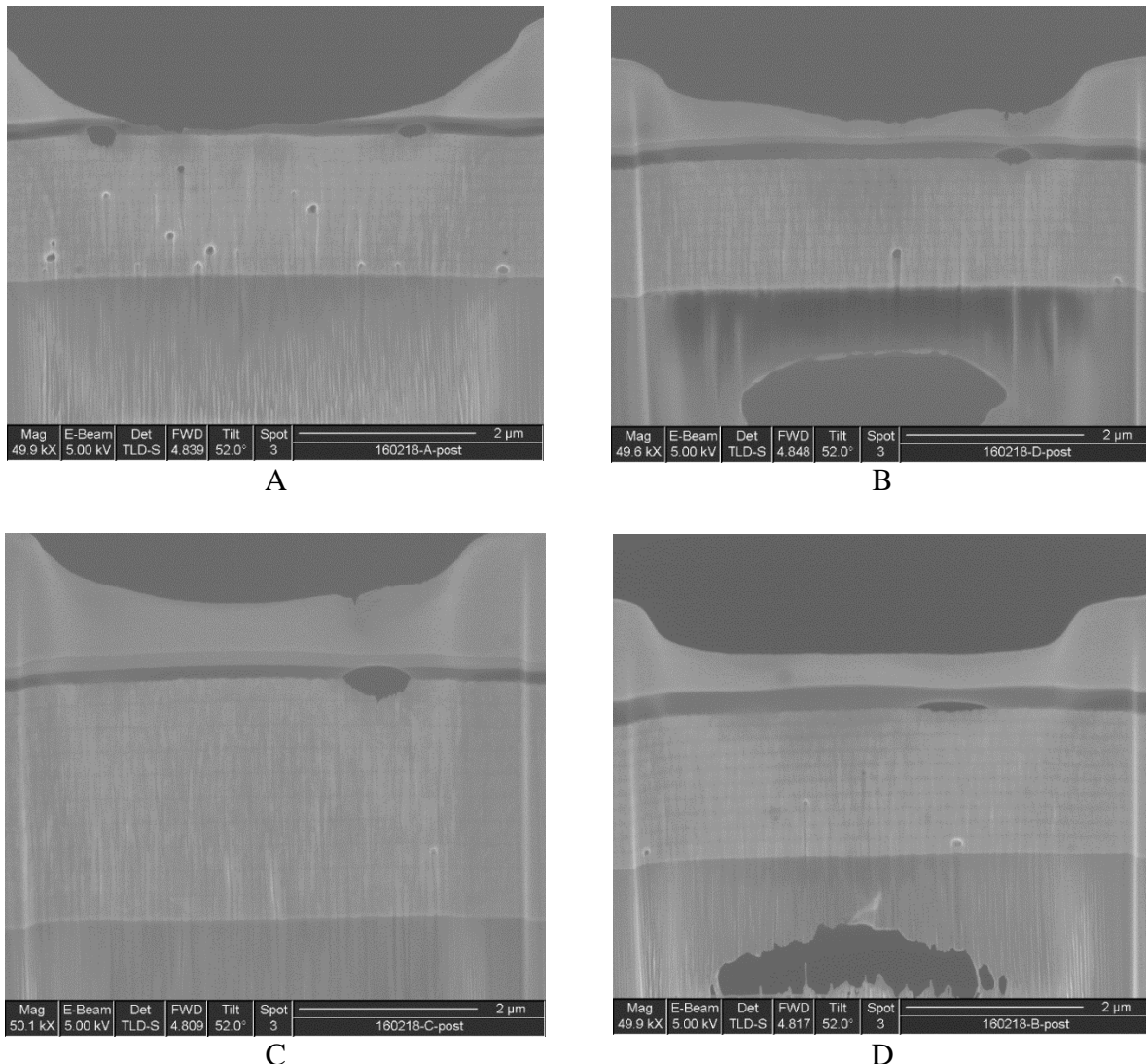
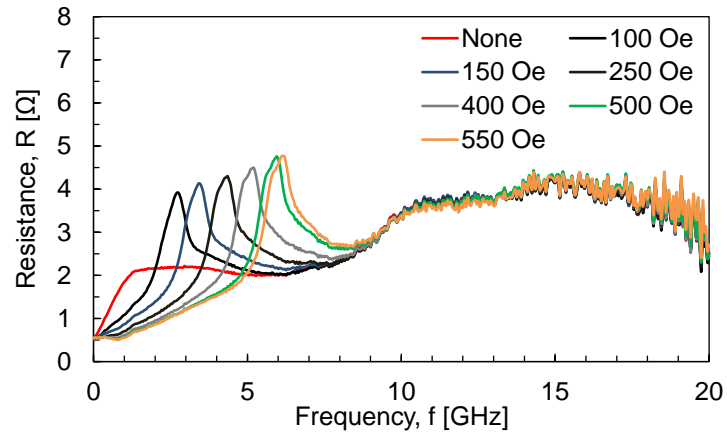


Figure 5-28. The SEM micrographs of the M-FET conductors. A) M-FET 1 with Cu/NiFe (180 nm/30 nm) on a Si substrate, B) M-FET 1 with Cu/NiFe (180 nm/30 nm) on a glass substrate, C) M-FET 2 with Cu/NiFe (360 nm/30 nm) on a Si substrate, D) M-FET 3 with Cu/NiFe (180 nm/60 nm) on a Si substrate.

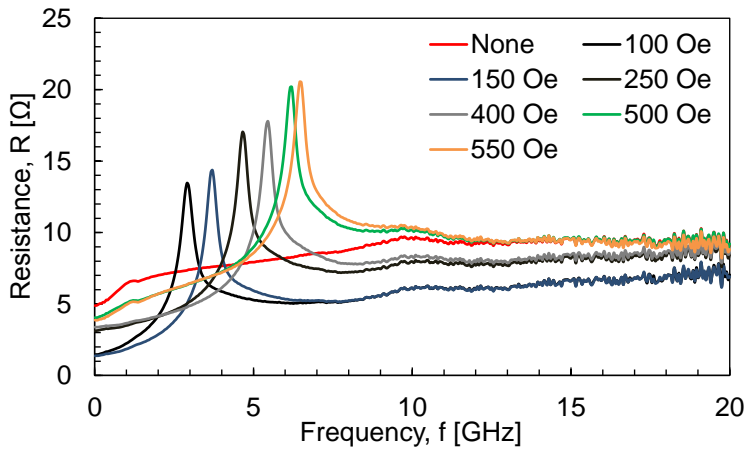
The SEM micrographs have also been taken from three conductor M-FETs as shown in Figure 5-28.

The tunability of M-FETs 2 and 3 versus an applied magnetic field has also been verified.

Figure 5-29 shows the extracted ohmic resistance of the M-FETs using an external magnetic field of 100 Oe to 550 Oe. Similar to M-FET 1, the M-FET are highly tunable versus frequency and the ohmic peak point will depend on the combination of the Cu/NiFe thicknesses.



A



B

Figure 5-29. The tunability of the M-FET conductors. A) The M-FET 2 with Cu/NiFe (360 nm/30 nm), B) the M-FET 3 with Cu/NiFe (180 nm/60 nm).

The Effect of Line Width

As shown in Figure 5-18A and Figure 5-18B, the CPW transmission lines with a width (W in Figure 5-18C) of $60 \mu\text{m}$ and $30 \mu\text{m}$ are fabricated. Figure 5-30A shows the comparison of the measurement results of these two conductors. The ohmic resistance depends directly on the width of the conductors where the M-FET with $W = 30 \mu\text{m}$ shows an almost twice resistance as the one with $W = 60 \mu\text{m}$.

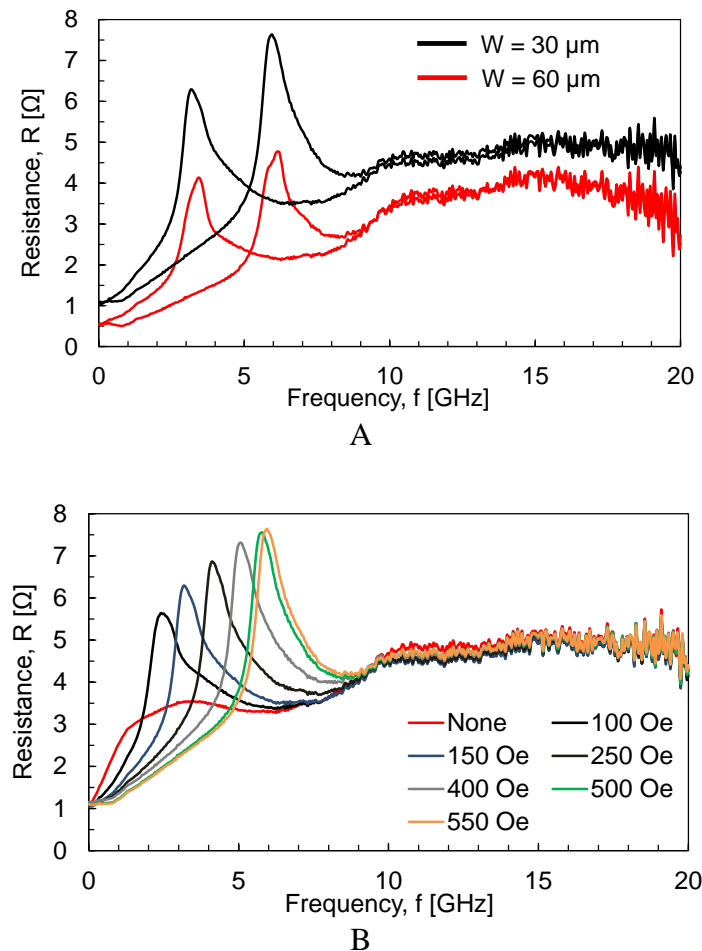


Figure 5-30. The comparison of the M-FET conductors with different signal width, W . A) The comparison of the M-FETs with $W = 30 \mu\text{m}$ and $W = 60 \mu\text{m}$ under an applied magnetic field of 150 Oe and 550 Oe , B) the tunability demonstration of the M-FET with $W = 30 \mu\text{m}$ under variable magnetic fields.

Although the peak of the ohmic resistance could be manipulated by modifying the conductor's width, in many applications such as transmission lines, a specific width is required

for impedance matching purposes. As a result, the other way to control the ohmic resistance, while keeping the same width, is to use the conductors with a different thickness ratio as explored in previous section. Figure 5-30B shows the tunability of the M-FET with $W = 30 \mu\text{m}$ under variable magnetic fields. Similar to the M-FETs with $W = 30 \mu\text{m}$, the ohmic resistance is tunable versus frequency.

Applied Magnetic Field in Hard Axis

As mentioned earlier, the principle of operation and the theory of spin torque transfer for ferromagnetic materials is valid when the applied DC magnetic field is perpendicular to the alternating electromagnetic H field, so the ferromagnetic absorption occurs that will be wasted as heat. Another measurement to be performed to verify the spin torque transfer is to apply a DC magnetic field in out-of-plane (hard axis) of the ferromagnetic material.

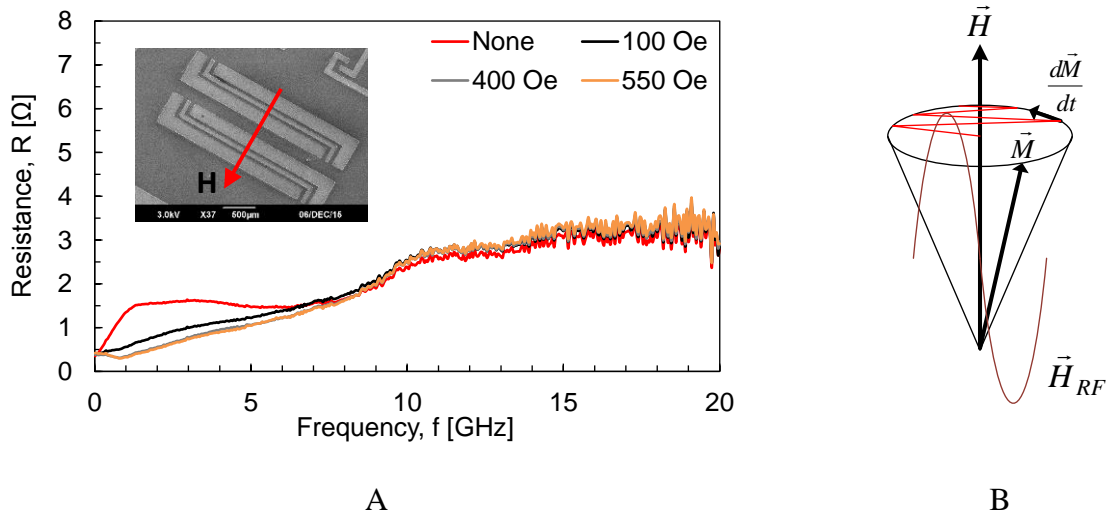


Figure 5-31. The effect of applied magnetic field in hard axis. A) The measurement results of the ohmic resistance of Cu/NiFe (360 nm/30 nm) M-FET, B) demonstration of the applied DC magnetic field in the direction of magnetic moment.

Based on magnetic moment theory, there should not be any spin torque transfer and as a result, no increase in the ohmic loss of the conductors. Figure 5-31 shows the measurement results of the M-FET conductor of Cu/NiFe (360 nm/30 nm) when a DC variable magnetic field

is applied through the hard axis (Figure 5-31B). The DC magnetic field has been varied from 100 Oe to as high as 550 Oe; however, since it's being applied out-of-plane, no noticeable change in the extracted resistance of the lines is observed. This is in result of the fact that the EM H-field is applied in the same direction as the DC field and no loss mechanism could be achieved using this configuration.

Summary

As the frequency of operation increases, current will be confined in the outmost areas of the conductor. As a result, by utilizing conductors which are a few time thinner than the skin depth of the conductor in those frequencies, that would be possible to microscopically modify the current flow in a conductor. This phenomenon opens a new area in device physics by using dynamical materials which have three requirements:

- 1) Frequency-dependent properties,
- 2) Electrically conductive,
- 3) The ability to be deposited in nm-range thicknesses.

Ferromagnetic materials are known to satisfy the mentioned requirements and are used in this work to realize magnetic field effect transconductor (M-FET). Similar to semiconductors, M-FETs could be tuned using a field (magnetic field) and could be designed to have a different conductivity. The theory of operation, design, fabrication, and measurements of these devices are covered in this Chapter. The applications include the tunable transmission lines, RF loads, and the microwave absorbers.

CHAPTER 6

LOW LOSS DIELECTRIC MATERIALS FOR RF COMPONENTS

Introduction

The dielectric materials are insulators that the metallic conductors are built on top of them realizing the RF passive components and systems. As detailed discussion is given in Chapter 2, the dielectric materials are imperfect and there is an energy loss associated with them which is wasted in terms of heat in vicinity of electromagnetic waves, diminishing the total efficiency of RF circuits in microwave regime. Meanwhile, the conductors couldn't be typically constructed on air and dielectric materials are required to mechanically support them.

Table 6-1. The comparison of some common manufacturing dielectric materials.

Material	Loss Tangent at 1 GHz	Dielectric Permittivity (ϵ_r)	Photo-Patternable
BCB	0.002	2.65	✓
LCP	0.002	2.9	✗
SU-8	0.03	3.4	✓
Polyimide	0.012	3.1 - 4.1	✓
Avatrell	0.009	2.55	✓
Corning Glass*	0.004	5.8	✗

The dielectric loss would be reduced by removing the dielectric materials forming air-lifted architectures ([17],[18]) or using very low loss dielectric materials ([20]-[21]). A variety of ceramic and composite-based dielectric materials with low dielectric loss are used in the printed circuit board (PCB) and monolithic microwave integrated circuits (MMIC) industries where the patterning is mechanically performed using a milling machine with a limited resolution, not compatible with standard MEMS and CMOS processes. However, as the frequency increases targeting next-generation communication systems, the dimensions of the RF devices will shrink requiring a micromachining technique for realization of high performance and optimized systems. Therefore, the development of dielectric materials compatible with standard manufacturing processes is critical. Table 6-1 shows some of the common manufacturing

dielectric materials mostly compatible with the standard microfabrication processes. SU-8 is a widely available dielectric material which could be coated and patterned in a variety of different thicknesses up to mm-range making it a potential candidate for RF applications. However, due to its relatively high dielectric loss tangent and corresponding RF loss, the overall RF performance might not be very promising [36]. The liquid crystalline polymer (LCP) [37] which is a flexible substrate is a family of polymers which are extremely inert to most chemicals while showing relative low dielectric loss and moderate permittivity and could be used in many wearable and flexible applications [38]. LCP is synthesized by dissolving a polymer into a solvent or by heating a polymer above its glass or melting transition point. Benzocyclobutene (BCB) [39] is another excellent dielectric material with low dielectric constant (low-k) which is used in a variety of microelectronic packaging and interconnects. The BCB hydrocarbon can be made by pyrolyzing process followed by treatment of the hydrocarbon with bromine which provides 4-bromo-BCB in an excellent yield [40] and also could be fabricated as a photo-sensitive material compatible with standard MEMS lithography processes.

Modern wireless systems, such as ground penetrating radar (GPR), automotive radar systems, ultra-wideband body area networks, and high-resolution sensing and imaging devices, have a great demand for broader bandwidth to support multiple band communication systems, including those working at K-Ku frequency bands [41]. Bandpass filters, with low insertion loss and compact sizes, are the key components for those modern wireless broadband and narrow band communication systems [61]. The substrate integrated waveguide (SIW) and half mode substrate integrated waveguide (HMSIW) technologies [57]-[58] have emerged as attractive alternatives to implement planar, integrable bandpass filters with performance comparable to those of the conventional waveguide counterparts. However, when broadband filters with more

than 5% fractional bandwidth (FBW) are needed, the SIW and HMSIW are not quite useful due to their high quality factors and low achievable inter-cavities coupling coefficients [59]. Not much work has been reported on broadband bandpass filters working with evanescent mode cavities, especially at millimeter wave frequencies. This chapter gives the details about the broadband microwave and mm-wave components that are proposed for current and next-generation frequency bands. Multiple low loss dielectric materials are used as the structural material for these filters.

Implemented Passive Components on LCP

During the last decade, the organic Liquid Crystal Polymer (LCP) has emerged as a low cost, low processing temperature alternative substrate for implementing highly integrated planar and multilayer RF devices mainly due its unique electrical ($\epsilon_r = 2.9$ to 3, $\tan \delta < 0.004$), thermal and mechanical properties [42]-[43][45]. In this work, the substrate integrated waveguide (SIW) architecture using a flexible liquid crystal polymer (LCP) substrate is explored for wearable RF component applications. For compact device realization, a metamaterial-based complementary split ring resonator (CSRR) unit cell is integrated with the SIW architecture. Furthermore, quarter mode SIW (QMSIW) is exploited instead of a conventional SIW or half mode substrate integrated waveguide (HMSIW) which has the advantage of broader bandwidths compared with the SIW and HMSIW counterpart because of the nature of its lower Q-factors and the higher values of magnetic coupling between neighboring resonators, which is easily controlled by changing the device dimensions [36]. As a test vehicle, CSRR-loaded QMSIW resonators and broadband bandpass filters for compact and wearable RF applications are demonstrated.

Substrate-Integrated Waveguide Structures

Figure 6-1 shows the resonance modes of the comparison of the electric field distribution for the conventional SIW cavity, the original QMSIW cavity and the CSRR-loaded QMSIW

cavity in this work. Eigenmode simulations using High Frequency Structure Simulator (HFSS 15, ANSYS Inc.) is performed here to obtain the resonance modes of the cavities. In Figure 6-1A, the electric field distribution of the TE₁₀₁ mode in a conventional substrate integrated waveguide cavity is presented. The cavity is designed and optimized on the LCP substrate to have a resonant frequency of 48 GHz. As observed, the resonance mode resembles the TE₁₀₁ mode of a conventional rectangular waveguide cavity. Arrays of metalized via holes with a spacing s of 0.3125 mm are used as the side walls of the waveguide cavity.

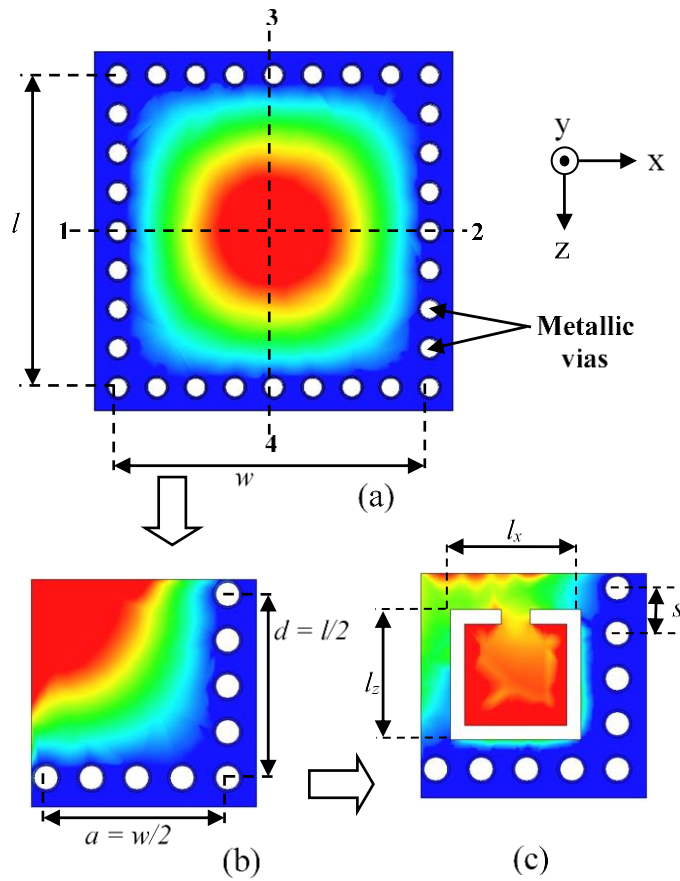


Figure 6-1. E-Field for the quasi-TE₁₀₁ mode in A) A conventional SIW cavity, B) the E-Field for the Quasi-TE_{0.25,0,0.25} mode in the resulting QMSIW cavity at 48 GHz, C) the E-Field for the main resonance mode at 25.5 GHz in the QMSIW cavity loaded with a single ring CSRR. Geometrical parameters are $w = l = 2.7$ mm, $l_x = l_z = 0.95$ mm, $s = 0.3125$ mm, $c = 0.1$ mm, $g = 0.18$ mm.

The two fictitious magnetic walls 1-2 and 3-4 allow to split the SIW into four independent square cavity resonators [62]. Each cavity represents one-quarter of the original SIW cavity, or a 75% size reduction, and then it is named the quarter-mode substrate integrated waveguide cavity (QMSIW) [36]. As observed in Figure 6-1B, the QMSIW propagates one-quarter of the quasi- TE_{101} mode in the original SIW cavity, called here the quasi- $TE_{0.25, 0, 0.25}$ mode. Next, the size of the waveguide cavity is further reduced by using a CSRR structure which will have a resonance frequency below the cut-off frequency of the SIW waveguide. As shown in Figure 6-1C, the electric field distribution is depicted for the resonator which shows the electric field distribution around the CSRR structure which occurs at 25 GHz.

Filter Design Methodology

After studying the QMSIW resonators, they will be used as building blocks in actual passive RF components such as bandpass filters. The design parameters are the external quality factor (Q_e) and the coupling coefficients of the resonators (M). The filter design methodology which is adopted here, is based on controlling the BW and return loss [61] as follows,

- Step 1: The circuit synthesis to find out the required Q_e and M to implement the filter with desired BW and return loss.
- Step 2: Physically implement the resonators as building blocks to achieve the required Q_e .
- Step 3: Realization of the bandpass filter by incorporating the designed resonators and modification of the dimensions to achieve required BW.

External Quality Factor

The variation of the external quality factor (Q_e) of the CSRR-loaded QMSIW cavity is obtained by exciting the cavity with one of the open sides, as shown in Figure 6-2. Since the first propagating mode is completely different from a TE_{101} mode in an SIW cavity, direct connection

of a microstrip $50\ \Omega$ transmission line is used to excite the cavity. In order to vary the external quality factor, the distance L_Q is used, which represents the distance from the top corner of the cavity to the center point of the feeding line. In comparison with a conventional SIW cavity, the obtained external quality factors Q_e are smaller where a Q_e as low as 5.2 has been obtained. Further, as observed in Figure 6-2, the resonant frequency of the CSRR-loaded QMSIW cavity has been reduced from 48 GHz to 25.5 GHz, which represents 47% reduction. In terms of the guided wavelength, λ_g at 25.5 GHz, the size of the proposed CSRR-loaded QMSIW cavity on LCP is $0.195\lambda_g \times 0.1954\lambda_g$.

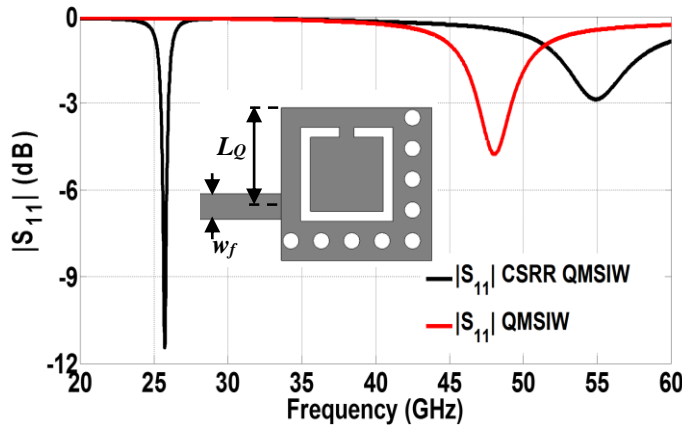


Figure 6-2. Frequency responses of the conventional QMSIW and the CSRR-loaded QMSIW cavities. Geometrical parameters are $L_Q = 1$ mm, $w_s = 0.26$ mm. A microstrip $50\ \Omega$ feeding line is used to excite the cavity.

Internal Coupling Coefficients

The internal coupling occurs when two resonators are placed next to each other where the electromagnetic coupling will displace the original resonance frequency of each individual resonator (Figure 6-3). The coupling coefficient of the new mode of resonance between two stages, i , and j , is calculated as,

$$M_{ij} = \frac{f_1^2 - f_2^2}{f_1^2 + f_2^2} \quad (4-1)$$

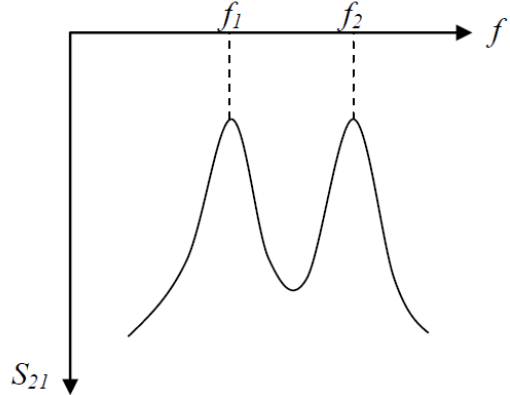


Figure 6-3. The illustration of electromagnetic coupling between two identical resonators [36].

Two-Pole and Three-Pole Filter Implementation

In this section, the designed resonator and filter methodology in previous section is adopted to design and implement bandpass filters for 25 GHz band using LCP as the structural dielectric material.

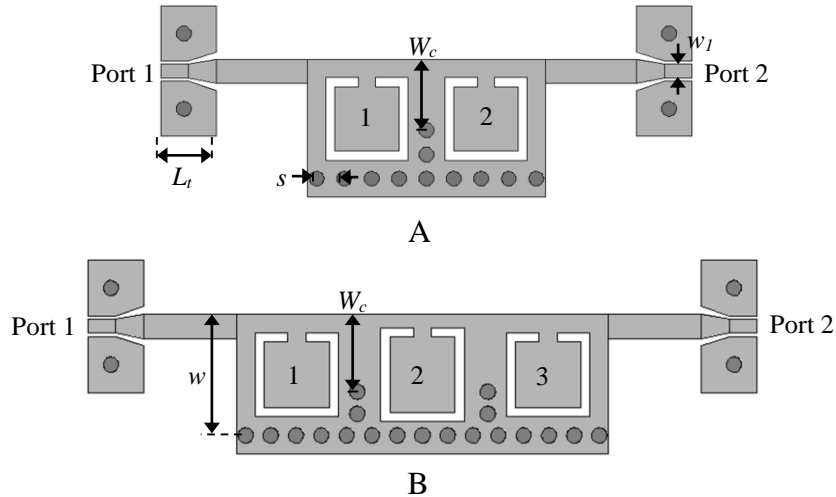


Figure 6-4. The schematic of the designed bandpass filters for 25 GHz frequency band, A) Two-pole bandpass filter, B) three-pole bandpass filter.

The mechanically drilled vias on LCP with 200 μm diameter are used to realize the QMSIW structure. Table 6-2 summarizes the calculated design parameters following the

methodology. Grounded coplanar waveguide (G-CPW) launching feeding lines are used with a Cascade Microtech probe station with GSG (ground-signal-ground) probes and a pitch distance of 150 μm .

Table 6-2. The summary of design parameters for the bandpass filters on LCP.

Bandpass Filter	f_0 (GHz)	20 dB RL FBW	Q_e	M_{12}	M_{23}
Two-pole	25.5	11%	6.044	0.1828	-
Three-pole	25.5	16%	5.320	0.1650	0.165

Implementation and Experimental Results

The designed resonators and bandpass filters are fabricated using a hybrid fabrication process since the LCP substrates cannot be etched chemically. The LCP substrates are initially prepared using a milling machine to create the vias. Then, they will go under a surface micromachining process for fabrication of the passive components for 25 GHz band.

Figure 6-5 shows the fabrication process of the passive components on LCP substrate. The LCP substrates used in this research are Ultralam 3850 from Rogers Corporation ($\epsilon_r = 2.9$, $\tan \delta = 0.002$) with a thickness of 100 μm and a metal thickness of 18 μm . The top copper layer of a double clad LCP sheet is etched by using standard wet chemical etching procedures. For this purpose, one layer of the LCP substrate is covered with photoresist AZ5214 and heated in the flat top surface of a hot plate. Then, the exposed copper layer is removed using diluted piranha bath ($\text{H}_2\text{SO}_4:\text{H}_2\text{O}_2:\text{H}_2\text{O}$). Also, because the LCP substrates are flexible, they are placed on a dummy 1.5 mm-thick glass wafer prior to surface micromachining (step (d) in Figure 6-5). A thin SU-8 layer is used for adhesion of the LCP substrate to the glass wafer while a heavy pressure is applied on the substrates during the soft-bake. Next, the seed layers are deposited followed by coating and patterning of 17 μm -thick NR9-8000P photoresist (Futurrex Inc.). The devices go over an electroplating process where 15 μm is deposited. Finally, the LCP substrates

are released using an acetone bath for cleaning both SU-8 and NR9 photoresists followed by removal of seed layers using diluted piranha bath and HF solutions.

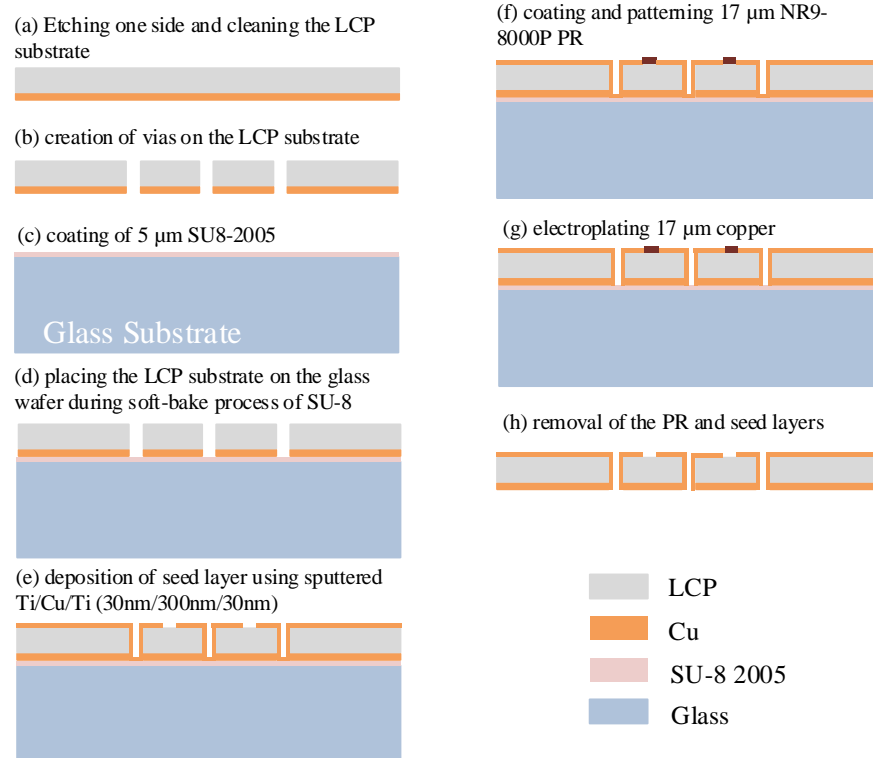


Figure 6-5. The fabrication process flow for the bandpass filters on LCP.

Figure 6-6 shows the SEM micrographs of the fabricated filters. The size of the two pole and three pole filters are $0.37\lambda_g \times 0.18\lambda_g$ and $0.56\lambda_g \times 0.18\lambda_g$, respectively; where λ_g is the guided wavelength at 25 GHz. Measurements are performed with a vector network analyzer Agilent E8361A (Agilent, Inc.) and a Cascade Microtech probe station with a probe pitch of 150 μm. Conventional SOLT (Short, Open, Load, Thru) calibration is done from 10 GHz to 40 GHz. Figure 6-7 shows the measurement results of the implemented bandpass filters where a comparison of the simulated and measurement results are done.

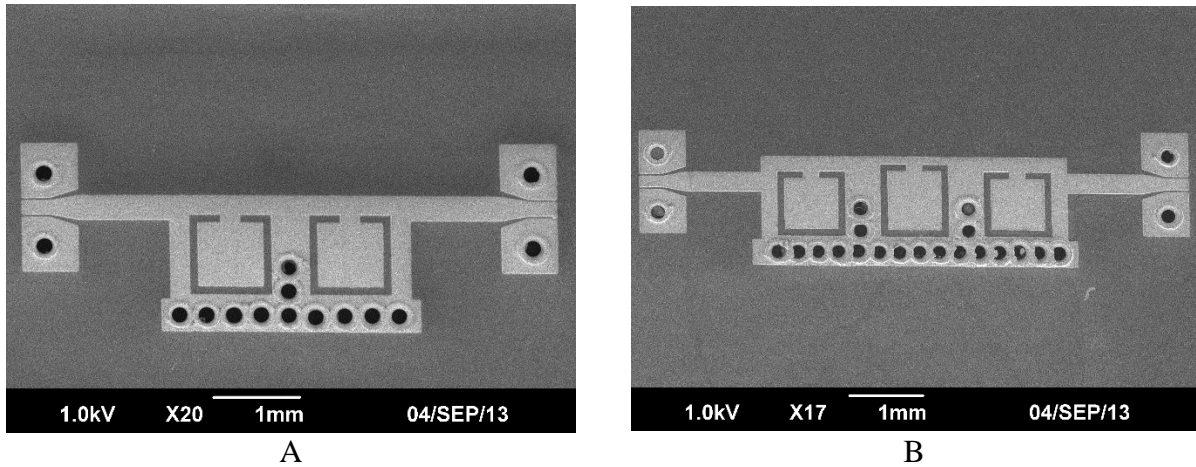


Figure 6-6. The SEM micrographs of the fabricated bandpass filters on LCP. A) two-pole filter, B) three-pole filter.

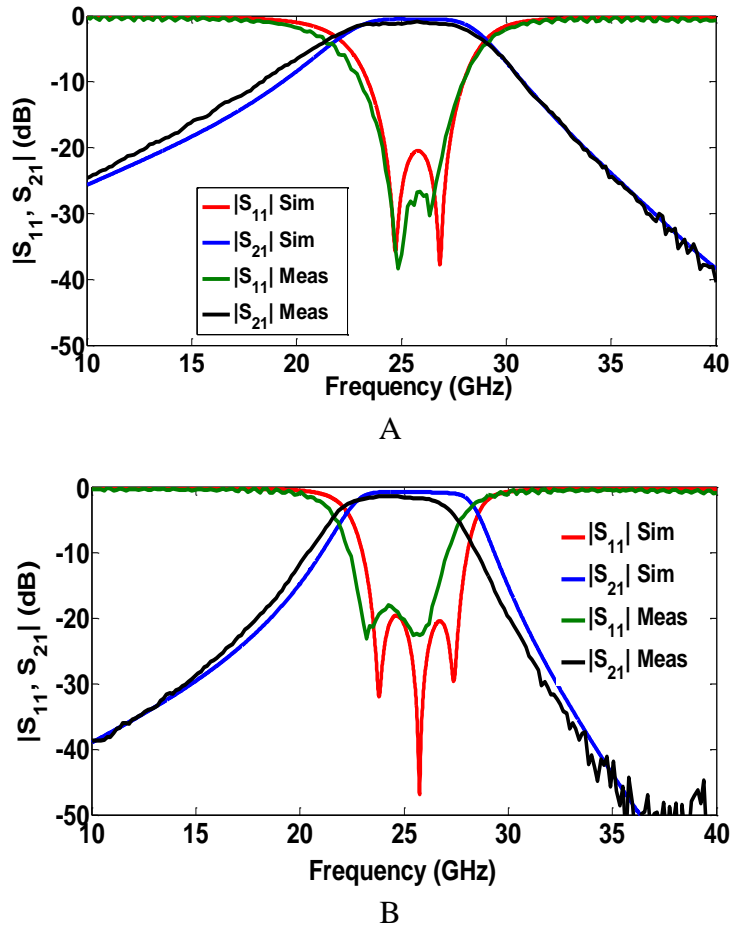


Figure 6-7. The Simulated and measured results of the implemented bandpass filters on LCP. A) Two-pole filter, B) three-pole filter.

Less than 1.6 dB insertion loss with in-band return loss better than 20 dB, including the transitions and feeding lines, are achieved in both cases. More than 11.6% 20 dB return loss

FBW is obtained for the two-pole filter and 17% 20 dB RL FBW is obtained for the three pole BPF. Measured results are in good agreement with the 3D structure simulations in HFSS.

Implemented Passive Components Using BCB

In previous section, the design and fabrication of passive components on LCP substrate for 25 GHz band were presented where a hybrid fabrication process was used. However, for systems operating in higher frequencies (i.e. V band), the wavelengths will shrink and a complete microfabrication process might be required for high performance and optimized device implementation. As a result, the dielectric materials compatible with standard MEMS processing with low dielectric loss at high frequencies are required. In this research, the photo-sensitive BCB (Benzocyclobutene from Cyclotene 4026-46; Dow Chemical, $\epsilon_r = 2.65$, $\tan \delta = 0.002$) has been selected as the dielectric material for implementation of test vehicles with low loss in 60 GHz band. The 60 GHz band is an excellent choice for wireless applications requiring gigabit-plus data rates especially considering the large bandwidth and high allowable transmit power. As a result, it is a potentially favorable band to demonstrate RF passive components to be used by next-generation communication systems.

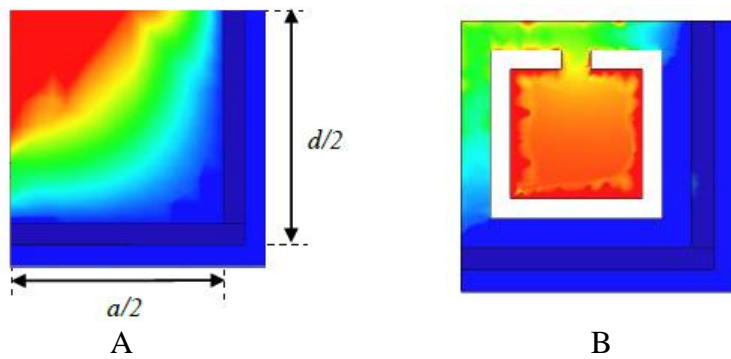


Figure 6-8. The field distribution graphs. A) QMSIW module before at resonance (102 GHz), B) the QMSIW loaded with a CSRR structure with resonance at 60 GHz.

In this research, two-pole and three-pole bandpass filters in 60 GHz band are designed and implemented using BCB as the dielectric material. Previously in our group [36], BCB has

been used for implementation of composite right/left handed (CRLH) metamaterial transmission lines up to 40 GHz where deposition and patterning of BCB with a thickness of 7 μm has been demonstrated. In this work, an optimized process has been developed for deposition and patterning of BCB with a thickness of 30 μm which is eventually used for passive components implementation at 60 GHz.

The design approach is similar to resonators and bandpass filters design discussed in previous section. Figure 6-8 shows the electric field distribution before and after loading the CSRR structure. The resonator has been designed to have 60 GHz resonance frequency. The two-pole and three-pole Chebishev bandpass filters with 10% 20-dB return loss FBW are then demonstrated at the unlicensed 57 GHz to 64 GHz band using inductively coupled CSRR-loaded QMSIW cavities. Table 6-3 summarizes the design parameters used for the two-pole and three-pole bandpass filters for 60 GHz band.

Table 6-3. The summary of design parameters for the bandpass filters using BCB.

Bandpass Filter	f_0 (GHz)	20 dB RL FBW	Q_e	M_{12}	M_{23}
Two-pole	60	10%	6.7	0.164	-
Three-pole	60	10%	-	0.09	0.06

Implementation and Experimental Results

The designed resonators and bandpass filters are fabricated using a full microfabrication process. Figure 6-9 shows the microfabrication process flow for the bandpass filters in 60 GHz band using BCB. The fabrication starts with a clean glass wafer which is used as the substrate in this work. The bottom ground plane of 2 μm has been deposited using sputtered Cu to have maximum uniformity and minimum RF loss in 60 GHz band. Next, the adhesion promoter AP3000 has been spin coated and soft baked to increase the adhesion quality of the BCB to the bottom ground plane. After that, the BCB has been spin coated with 850 rpm spin to achieve a 29 – 30 μm thickness followed by the soft baking process which occurs at 105 °C for 90 seconds.

The BCB-coated substrates will be exposed to i-line UV light with an intensity of 2200 mJ/cm² using the first mask. The negative BCB resist doesn't have a post-exposure-bake (PEB) step; however, the most challenging step in the fabrication is the development. The substrate with soft-baked BCB is transferred to a DS3000 solution which is in a temperature of 37 °C (with hotplate temperature set to 39 °C) for 8 min. Right after that, the substrates will be developed with DS3000 solution in room temperature for 2 minutes. The BCB goes under another step of development to etch the unexposed areas in DS3000 solution in 37 °C for another 2 min and finally rinsed with DI water. This will give the maximum reliability in successfully patterning the BCB of 30 µm. The substrates with BCB will be hard baked in an inert environment at 250 °C for 90 min; this is because the BCB has silicon in it which easily get oxidized in an oxygen environment in high temperature. To ensure the maximum cleanness, the substrates will be dry etched using reactive ion etching (RIE) with O₂ and SF₆ gasses. The SF₆ is used to dry etch the unfavorably generated silicon dioxide during descum. The last step is deposition of seed layers followed by electroplating to fabricate the top layer.

Figure 6-10 shows the SEM micrographs of the microfabricated 60 GHz bandpass filters. The two-pole and three-pole bandpass filters are shown in Figure 6-10. The 50 Ω grounded CPW (G-CPW) transmission lines are used as feedings.

Measurement results up to 67 GHz are shown in Figure 6-11 which are done with a PNA network analyzer (Agilent N5227A) and a Cascade Microtech probe station with a probe pitch of 150 µm. On wafer TRL (Thru, Reflect, Load) calibration is used from 40 GHz to 67 GHz. Less than 1.7 dB insertion loss and return loss better than 15 dB are achieved within the desired passbands. More than 10% 20-dB insertion loss FBW is obtained in both two-pole and three-pole bandpass filters.

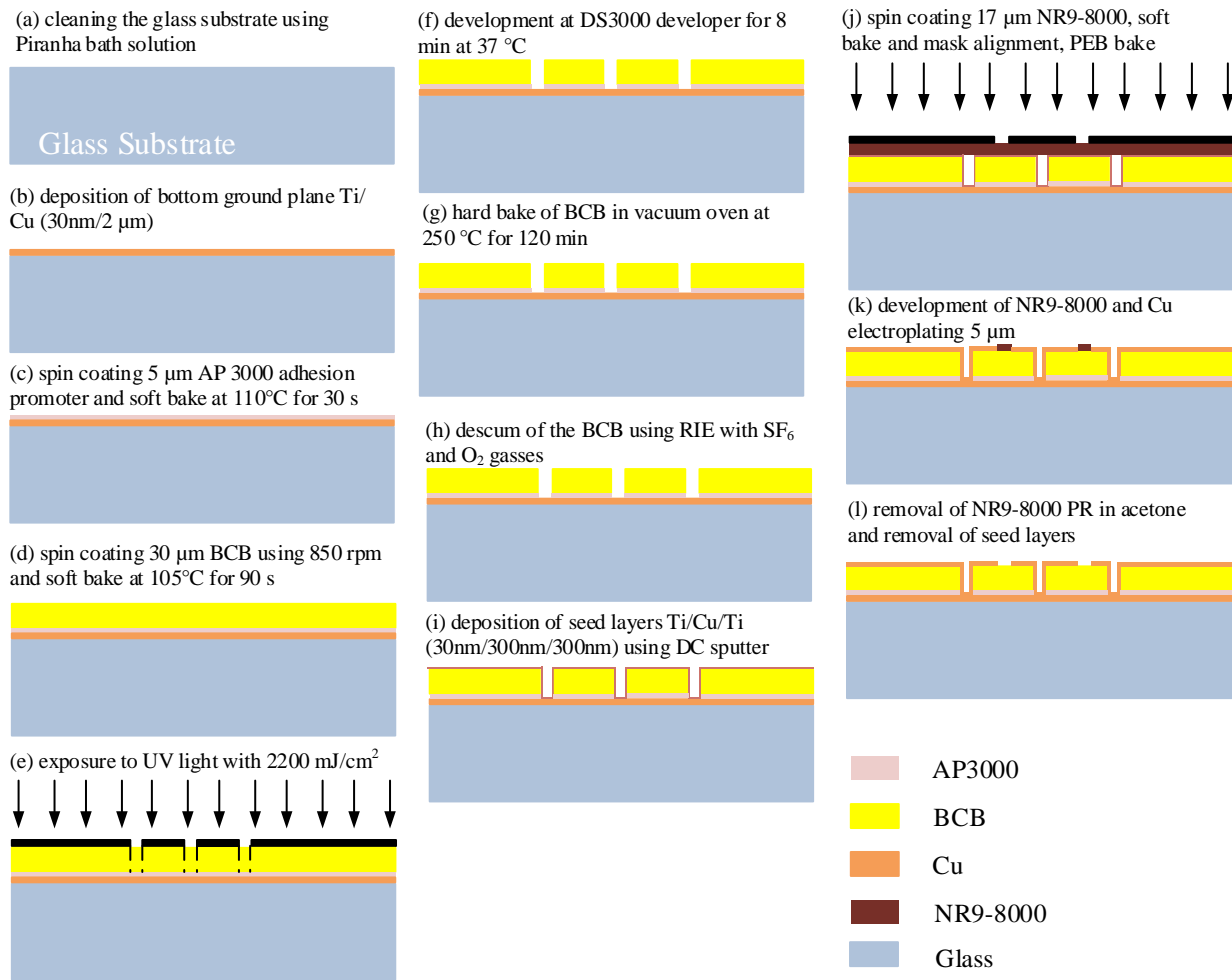


Figure 6-9. The fabrication process flow of the broadband bandpass filters using BCB.

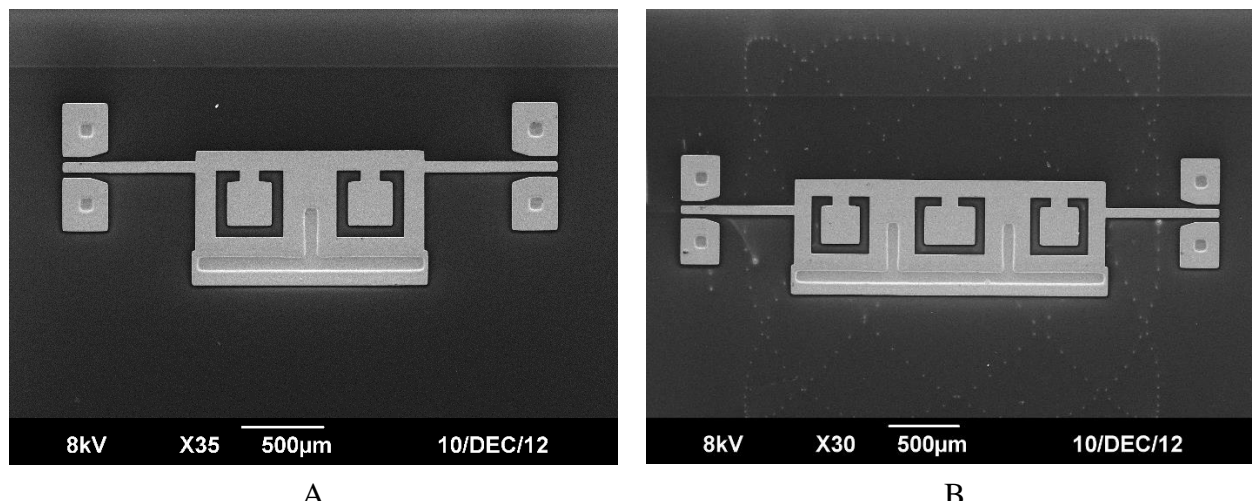


Figure 6-10. The microfabricated bandpass filters for 60 GHz band. A) two-pole bandpass filter, B) three-pole bandpass filter.

Measurements results agree well with those of the full wave structure simulations.

Frequency shift and additional loss are due to the tolerances in the fabrication process, and the variation in the thickness and electrical properties of the BCB. The results are promising, proving that the combination of metamaterial concepts with the QMSIW on a repeatable post-CMOS surface micromachined process with low loss polymer as dielectric layer is useful for low profile, integrable millimeter wave broadband filters.

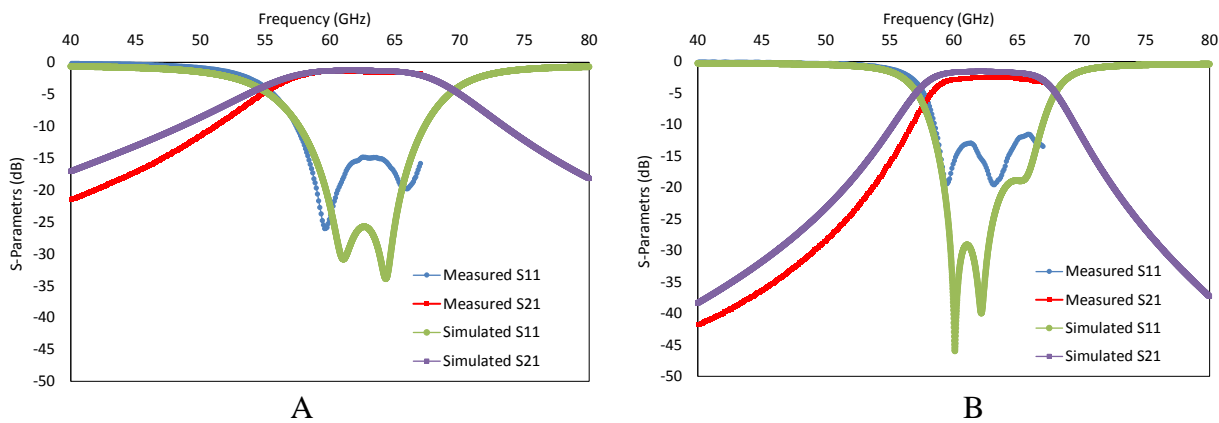


Figure 6-11. The measurement results of A) Two-pole filter, B) three-pole filter. Less than 2 dB insertion loss is obtained in the passband.

Summary

In this chapter, the implementation of passive components using low dielectric loss materials compatible with standard MEMS fabrication process has been demonstrated. A hybrid fabrication process using LCP is presented where 25 GHz resonators and bandpass filters embedded in LCP are realized. Also, a modified fabrication process is shown using single-coated BCB with a thickness of 30 μm as the photosensitive material suitable for implementation of low loss devices operating in 60 GHz band. In summary, the feasibility of implementing RF passives using aforementioned polymers as the structural material up to 60 GHz is experimentally verified.

CHAPTER 7

PACKAGING AND INTERPOSER TECHNOLOGY

The next-generation consumer electronic devices will mainly require low power, compact, and high performance (high data transfer rate and visual quality) components including active integrated circuits (IC's) and passive devices to be incorporated in wireless and communication systems. As a result, the high performance and compact packaging and interconnection of different active/passive modules of a system has a critical impact on the system's overall efficiency and maximum operation speed/frequency. In recent years, an interposer technology for packaging is introduced due to its reliability, higher scale of integration and feasibility of the so called 3D/2.5D packaging which enables the capability of replacing conventional wire bonding in integrated circuits with large number of I/O's [46] and utilization as a structural substrate for implementation of passive microwave components [49], [53]. Silicon and glass interposer technologies have been chosen as a high quality, reliable, highly integrable method of packaging by research institutes and industries [50]-[51]. This allows realization of RF passive off-chip components next to other active on-chip components and enables the high performance connectivity. On the other hand, the unique properties of glass interposer substrates in RF regime compared to their silicon counterparts include their intrinsic high signal isolation, mechanical and thermal robustness, lower dielectric loss and superior signal integrity, which enable the implementation of in-substrate passive components greatly enhancing overall system integration.

In this Chapter, low loss packaging solutions are proposed for high performance RF packaging and system integration. A CRS conductors presented in Chapter 3 is proposed as a low loss conductor for RF analog and RFIC chips packaging where wire bondings are used as auxiliary components for impedance matching purposes. Also, a glass interposer layer has been

used as the low loss structural medium for the implementation of high performance integrated RF passive components. High frequency characterization of the glass interposer layer, and the design, fabrication, and characterization of glass interposer integrated bandpass filters are detailed. Ring resonators with grounded coplanar waveguide (G-CPW) feedings and different dimensions are used to characterize the glass interposer substrates up to 50 GHz where the relative permittivity and loss tangent could be extracted. At last, the combination of high performance glass interposer substrates and the low loss conductors is provided where in-substrate passive components using the low loss conductors (in Chapter 4) are reported for K and Ka bands.

Proposed Packaging Schemes

Wire Bonding

Many RF applications still rely on wire-bonding as the analog IC's usually do not have so many pads and wire-bonding is still a useful packaging method for analog and RFIC's. Therefore, the CRS conductors presented in Chapter 3 could be directly used as a low loss conductor for RF packaging and impedance matching for RF active components. The inductance value could be modified by changing the length of the conductor to design different inductance values depending on the requirement of the system. The implemented CRS wire bonding in Chapter 3 could be used as an external high-Q inductor for impedance matching purposes.

Interposer Technology

As the number of input/output's (I/O's) in the recent integrated circuits is quadratically increasing, a silicon or glass interposer technology for packaging is preferred compared to the conventional wire bonding technology due to its reliability, higher scale of integration and feasibility of the so called 2.5D packaging. The glass interposer technology possesses superior signal integrity to its silicon counterpart such as its high signal isolation (dielectric material),

lower dielectric loss in the RF/microwave regime, low cross talk, and low material cost and complexity. Also, the non-conductive feature of glass interposers compared to silicon substrates will allow implementation of passive RF components with little substrate loss and therefore higher overall quality factor. Moreover, depending on the utilized glass composition, several mechanical and thermal properties of the glass interposer are adjustable that could be used to minimize the fabrication mismatches between different layers in a standard manufacturing process. Through silicon/glass vias (TSV/TGV) are the essential structures that make the realization of interposer and 3D packaging technology feasible. While the fabrication of TSV's requires more complex processes (i.e. Bosch process [46]) which might add to the overall cost and complexity of the system; the TGV's could be fabricated in-house using the direct UV lithography and standard wet etching using a photosensitive glass [49] or fusion process and laser machining utilized by Corning Incorporated [50]. In overall, the TGV technology allows RF passive components to be integrated in the low loss glass interposer layer and easily connected to other components, enhancing system integrability and reliability.

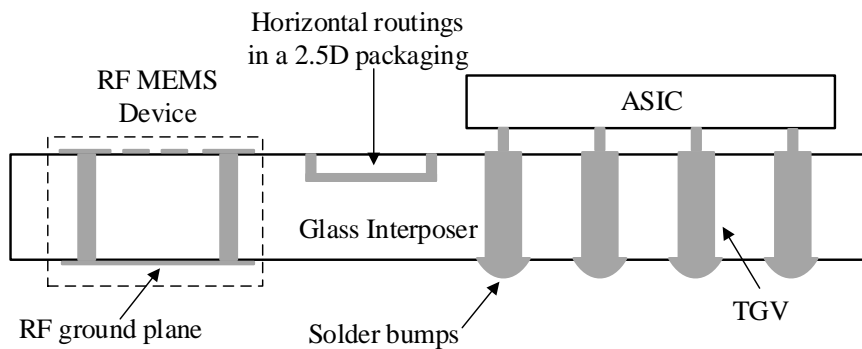


Figure 7-1. The interposer-based packaging scheme for integration of RF components (off-chip) and other components (integrated on-chip) of a system front-end using glass interposer and through glass vias (TGV's).

Figure 7-1 shows the proposed interposer-based low loss packaging method for RF and 2.5D integration of RF off-chip components and application specific integrated circuit (ASIC)

chips using horizontal routings and transmission lines as interconnections. By utilizing this packaging method, the off-chip RF passive components, typically occupying large on-chip area that cannot be directly embedded inside ASIC, are implemented by employing the glass interposer as their dielectric hosting medium. The vertical interconnections are made by metallizing through the TGV's for both RF MEMS devices and the ASIC connections. In order to maximize the performance of RF passive components and the total system (Figure 8-1),

- 1) A high quality glass interposer substrate with low dielectric loss and excellent surface smoothness is employed,
- 2) High performance TGV's are fabricated with high accuracy in dimensions and minimum roughness inside the TGV's which ease the metallization process using a physical vapor deposition (PVD) method,
- 3) Low loss Cu/NiFe multi-layer superlattice conductors are used for realization of interconnects and passive elements, in order to suppress the skin effect reducing the conductor loss and improving the insertion loss property of the passive components in K-band,
- 4) A highly integrable RF system with low parasitics is realized.

Figure 7-2 shows the four types of passive components' implementation using glass interposer substrates for different operation frequencies.

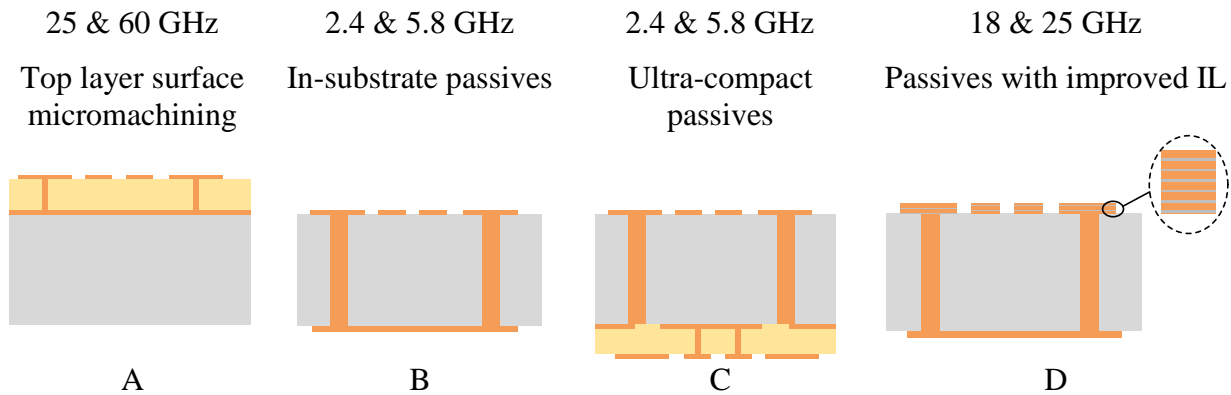


Figure 7-2. The different types of device implementation using glass interposer technology. A) The passives using glass as the carrier wafer and top surface micromachining, B) the in-substrate passives using glass as the structural material, C) the ultra-compact passives using glass as the structural material and backside micromachining, D) the passives with improved IL using low loss conductors.

In this chapter, the potential application of glass interposers to be used as structural dielectric substrates to implement RF passive components for next-generation interposer-based RF systems' packaging has been explored. The utilization of photo-sensitive glass interposer from TS Inc. [49] and semiconductor fusion glass from Corning Inc. [50] with detailed fabrication process flows are demonstrated. First, high frequency characterization (up to 50 GHz) of the glass interposer to extract the electrical properties of the substrates are provided. Second, based on the extracted glass properties, the compact resonators and bandpass filters for frequency bands of 2.4 GHz and 5.8 GHz integrated in the glass interposer layer as a hosting medium are designed and implemented. In order to maintain compactness and integrability with other parts of the system in interposer-based packaging, the planar substrate-integrated waveguide (SIW) structure has been selected for the implementation of RF resonators and filters. The complementary split-ring resonators (CSRR's) embedded in a half-mode SIW (HMSIW) operating in evanescent mode are used for further size reduction to realize extra compact planar in-substrate RF components.

Also, in-substrate passive components using a high performance glass interposer and through glass via (TGV) technology and a multi-layer superlattice conductor architecture are reported. Minimal RF loss is achieved using low dielectric loss glass substrates and superlattice conductors featuring skin effect suppression. Half mode substrate integrated waveguide (HMSIW) resonators and two-pole bandpass filters, embedded inside a glass interposer substrate, are used as test vehicles for the demonstration of insertion loss improvement in K-band. The utilized conductor is made of 20 layers of Cu/NiFe with each pair of 360 nm/30 nm, respectively, where NiFe layers with negative permeability in frequency range of interest are used for eddy

current cancelling and improving the conductor loss. Control devices using the same glass substrate and conductor made of pure copper are fabricated for comparison purposes.

TGV Technology and Proposed Microfabrication Processes

Photosensitive Glass Interposer

The photosensitive glass (TS Technology [49]) composed of ZnO, Ce and Ag has a dielectric constant and loss tangent of 5.53 and 0.0036 at 2.1 GHz with a thickness of 400 μm , which makes it suitable for low loss integrated passive devices.

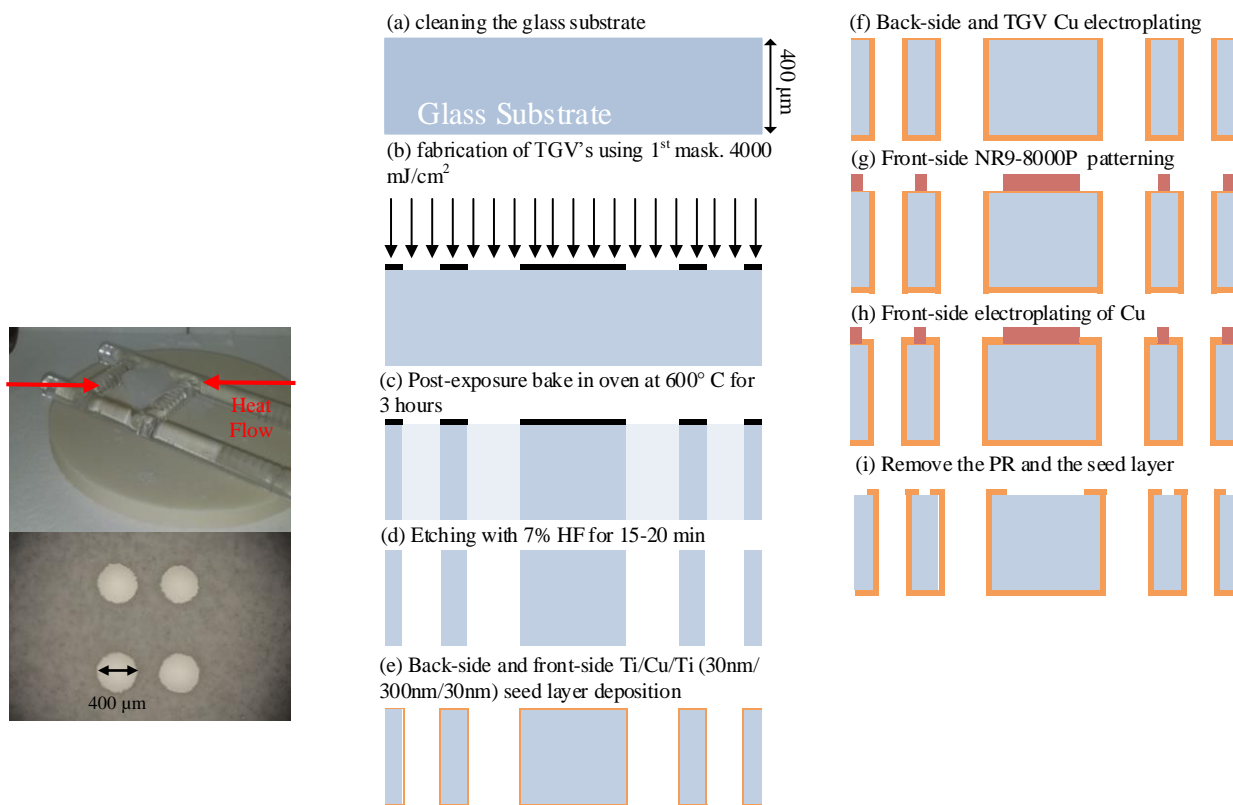


Figure 7-3. The fabrication process flow for the photosensitive glass.

Figure 7-3 shows the fabrication process flow for the photosensitive glass and its double side surface micromachining. The glass substrates are first cleaned and dehydrated and then exposed using a photolithography system (UV i-line, 365 nm) with 4000 mJ/cm^2 UV light power. The substrates are then heated for post-exposure bake process for 180 minutes at 600 °C

in an oven in oxygen environment. The glass substrate is placed vertically (inset in Figure 7-3) inside the oven to allow heat transfer as showed to effectively heat the substrate for efficient TGC etching. The substrates are then transferred to a 7% HF solution for etching purposes. The photosensitive glass is a positive resist where exposed areas will be removed inside the HF solution. The 7% HF solution will etch both non-exposed areas of the glass and the exposed areas with a ratio of 1:20.

Corning Glass Interposer

The SGW3 glass [50] with a thickness of 300 μm and 130 μm , and a coefficient of thermal expansion (CTE) of $31.7 \times 10^{-7}/^\circ\text{C}$ from Corning has been selected as the glass interposer layer for the implementation of integrated passive RF components. The glass interposers have an excellent surface roughness ($< 1.0 \text{ nm}$) suitable for implementation of high quality RF components and the TGV's are fabricated using Corning laser machining with high internal surface smoothness and accurate sizing. Figure 7-4 shows the optical views of the glass interposer substrate and the fabricated TGV's and their dimensions.

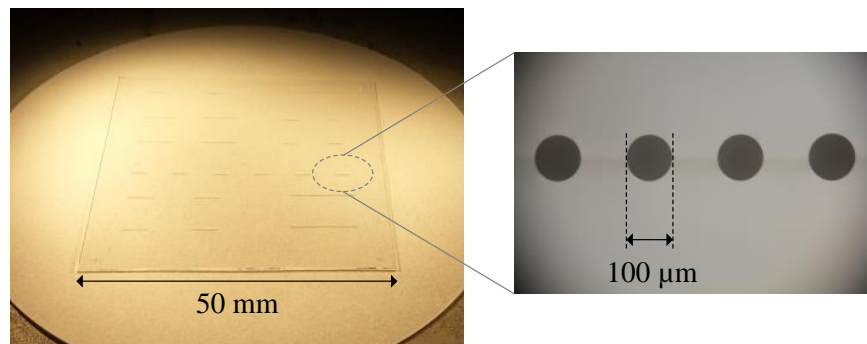


Figure 7-4. The series of laser-machined TGV's on Corning SGW3 50 mm \times 50 mm with a TGV diameter of 100 μm .

A surface micromachining technique has been utilized to fabricate the RF passive components on the glass interposer layer whose detailed fabrication process flow is given in Figure 7-5.

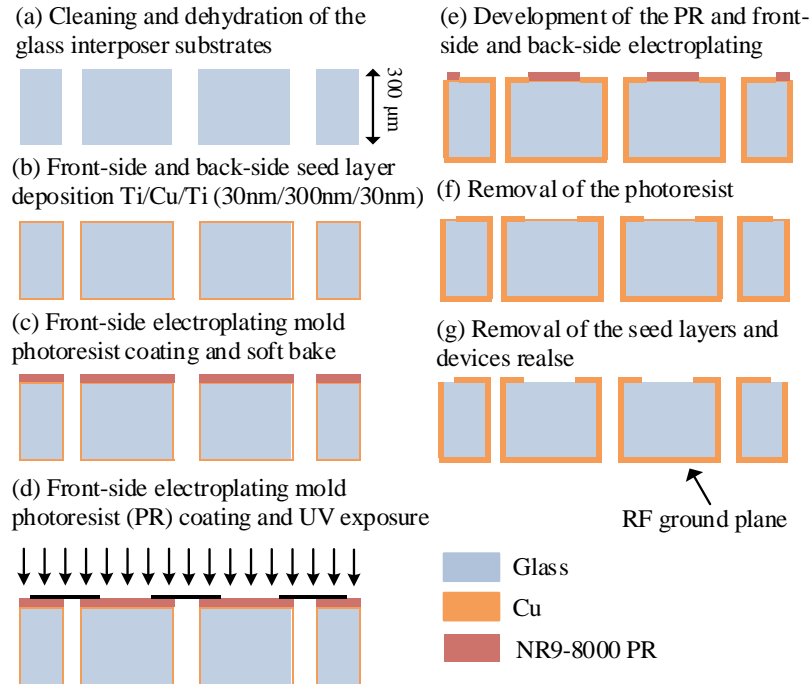


Figure 7-5. The microfabrication process using the Corning glass substrates.

After cleaning and dehydration of the glass substrate, the seed layers (Ti/Cu/Ti with 30 nm/300 nm/30 nm) are DC sputtered (Kurt J. Lesker CMS-18) on both the front-side and back-side of the glass substrate. Then, photoresist for an electroplating mold is coated on the front-side which contains the top-layer of the actual RF devices. After mask alignment, soft bake and photoresist development, the front-side and back-side of the glass substrate which contain the ground plane are electroplated at the same time. A 15 μm thick Cu layer has been electrodeposited during this step to ensure minimum conductor loss at the lowest operating frequency of 2.4 GHz. The devices are finally released by removing the photoresist mold and the seed layers in sequence.

The most challenging step of the fabrication is metallizing though the TGV's due to their relatively high thickness (300 μm) which makes it difficult to grow metal layers vertically on the walls of the TGV's. This problem has been addressed by the suggested microfabrication process flow in Figure 7-5. At step (b), the seed layers are deposited on both the front-side and back-side

of the glass substrate at the same time without further wet processing. This would not allow any polymer residue inside the TGV's and ensures a reliable connection of the seed layers on both sides of the glass as the thickness of the sputtered seed layers will decrease deeper into the TGV's. Also, the electroplating of the bottom ground plane and top layer is performed at the same time (step (e)); so, the seed layers will be removed in a single step which decreases the chance of removal of thinner metal layers inside the TGV's while removing the seed layers and increases the reliability of fabrication and better interconnection inside the TGV's. Figure 7-6 depicts the tilted angle view of the scanning electron microscopy (SEM) images of the fabricated TGV before and after metallization.

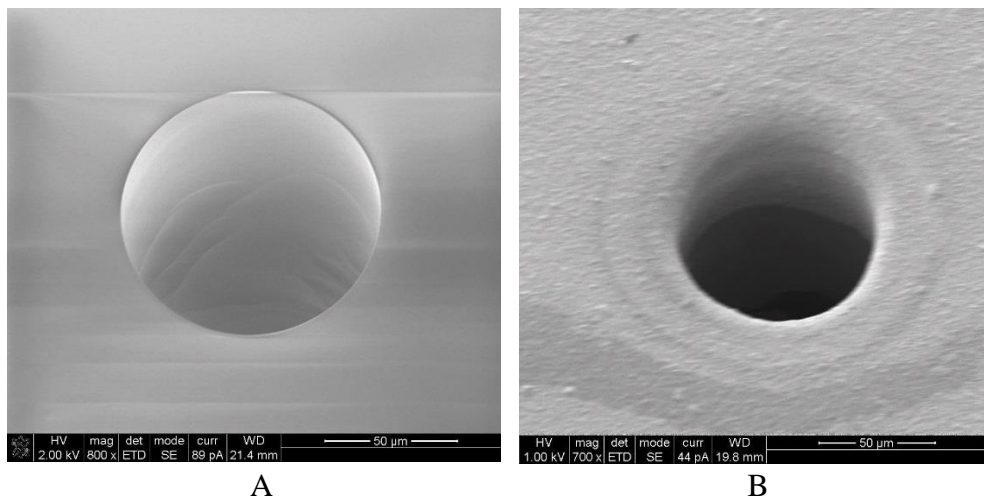


Figure 7-6. The SEM micrographs of a single TGV before and after thick metallization. A) The TGV before metallization, B) seed layer deposition and subsequent electroplating through the TGV.

Glass Interposer Characterizations

The electrical properties of the glass interposer layer have an important effect on their microwave performance and the RF components to be implemented on it. Therefore, high frequency characteristics of the glass interposer layer including the electrical permittivity and loss tangent are performed. The high quality factor micromachined microstrip ring resonators

with grounded coplanar waveguide (G-CPW) feedings are designed for high frequency characterization up to 50 GHz.

Ring Resonator Design

A ring resonator is a transmission line formed in a closed loop having multiple resonances depending on its perimeter size which is well modeled previously [52] and could be used to characterize the dielectric glass medium. Our group has previously reported the characteristics data for two glass interposer media from Corning up to 10 GHz [53] using a ring resonator architecture with microstrip feeding lines. In this work, smaller sized ring resonators with grounded coplanar waveguide (G-CPW) feeding lines are employed where measurements are performed by use of high frequency mm-wave probes characterizing the glass interposer layer up to 50 GHz. This allows to extend the design of the glass interposer integrated passive components to the mm-wave regime.

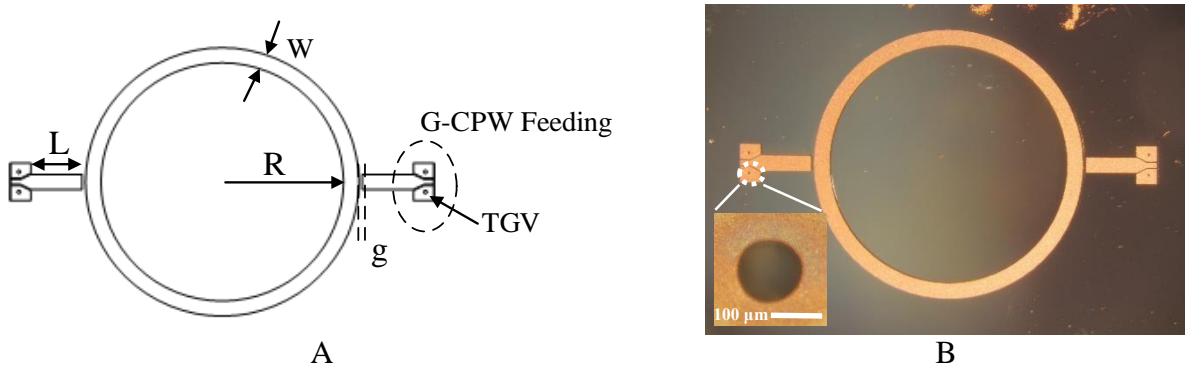


Figure 7-7. The ring resonators. A) The schematic of the ring resonator for electrical characteristics extraction of the utilized glass interposers, B) the fabricated device with the magnified view of the electroplated TGV.

Figure 7-7 shows the schematic of the implemented ring resonator which is used for high frequency glass characterization. A capacitive coupling (capacitive gap “ g ”) has been chosen to externally excite the ring resonator using two 50Ω CPW feedings. Three ring resonators with different dimensions of line width (W), ring’s radius (R) and length (L) (shown in Figure 7-7A)

to have multiple resonance frequency peaks between DC to 50 GHz are fabricated on the glass interposer medium using surface micromachining shown in Figure 7-5.

Table 7-1. Dimensions of the implemented ring resonators using the glass interposer layer.

Ring Resonator	W	R	g	L
RR_1	1 mm	7 mm	0.1 mm	2.2 mm
RR_2	0.6 mm	4.5 mm	0.1 mm	1.5 mm
RR_3	0.45 mm	3.5 mm	0.1 mm	1.5 mm

Glass Characterization

The electrical properties of the glass substrates will be extracted from the S-parameters, namely, insertion loss of the ring resonators from port 1 to port 2. Two-port measurements (E8361A PNA, Agilent Inc.) have been performed after standard short-open-load-through (SOLT) calibration to characterize the glass substrates. A Cascade Microtech probe station with ground-signal-ground (GSG) probes (150 μm pitch) are used for testing.

Figure 7-8 shows the measurement results of the ring resonators where the insertion loss versus frequency sweeping are given. The results in Figure 7-8A show 13 resonance peaks up to 40 GHz for RR_1 at which, the glass interposer parameters could be calculated. Also, the measurement results in Figure 7-8B show multiple peaks for ring resonators of smaller dimensions which could be used for characterization up to 50 GHz. From the measured S-parameters, the effective dielectric constant $\epsilon_{eff}(f_n)$ at each resonance frequency of f_n is given by [54],

$$\epsilon_{eff}(f_n) = \left(\frac{nc}{2\pi R_{ave} f_n} \right)^2$$

where f_n is the n^{th} resonance frequency of the ring resonator (where n is a natural number), $c = 3 \times 10^8 \text{ m/s}$ is the speed of light in free space, and R_{ave} is the average radius of the ring resonator

which will be equal to $(R+(R+W))/2$. The relative dielectric permittivity of the microstrip ring resonator will be given by,

$$\varepsilon_{eff}(f_n) = \frac{\varepsilon_r(f_n)+1}{2} + \frac{\varepsilon_r(f_n)-1}{2} / \sqrt{1+12\frac{h}{w_{eff}}} \quad (7-1)$$

$$W_{eff} = W + 1.25 \frac{t}{\pi} \left[1 + \ln \left(\frac{2h}{t} \right) \right] \quad (7-2)$$

where W is the width of the ring resonator, t is the thickness of the metal, and h is the thickness of the glass substrate. The tangent loss of the glass substrate could be calculated from the permittivity information and the quality factor of the resonator [53],

$$\tan \delta = \frac{\alpha_d \times \lambda_0 \times \sqrt{\varepsilon_{eff}} (\varepsilon_r - 1)}{8.6 \times \pi \times \sqrt{\varepsilon_{eff}} (\varepsilon_r - 1)} \quad (7-3)$$

The total loss of the system including the dielectric loss, conductor loss, and the radiation loss is given by,

$$\alpha_{total} = \alpha_d + \alpha_c + \alpha_r \quad (7-4)$$

$$\alpha_{total} = \frac{\pi}{Q_0 \lambda_g} [Np/m] \quad (7-5)$$

where Q_0 is the unloaded Q-factor of the ring resonator, and λ_g is the guided wavelength. The loaded Q-factor of the resonator could be directly calculated from measurement results in Figure 7-8,

$$Q_L = \frac{f_0}{BW_{3dB}} \quad (7-6)$$

$$Q_0 = \frac{Q_L}{1 - 10^{\frac{(-IL)}{20}}} \quad (7-7)$$

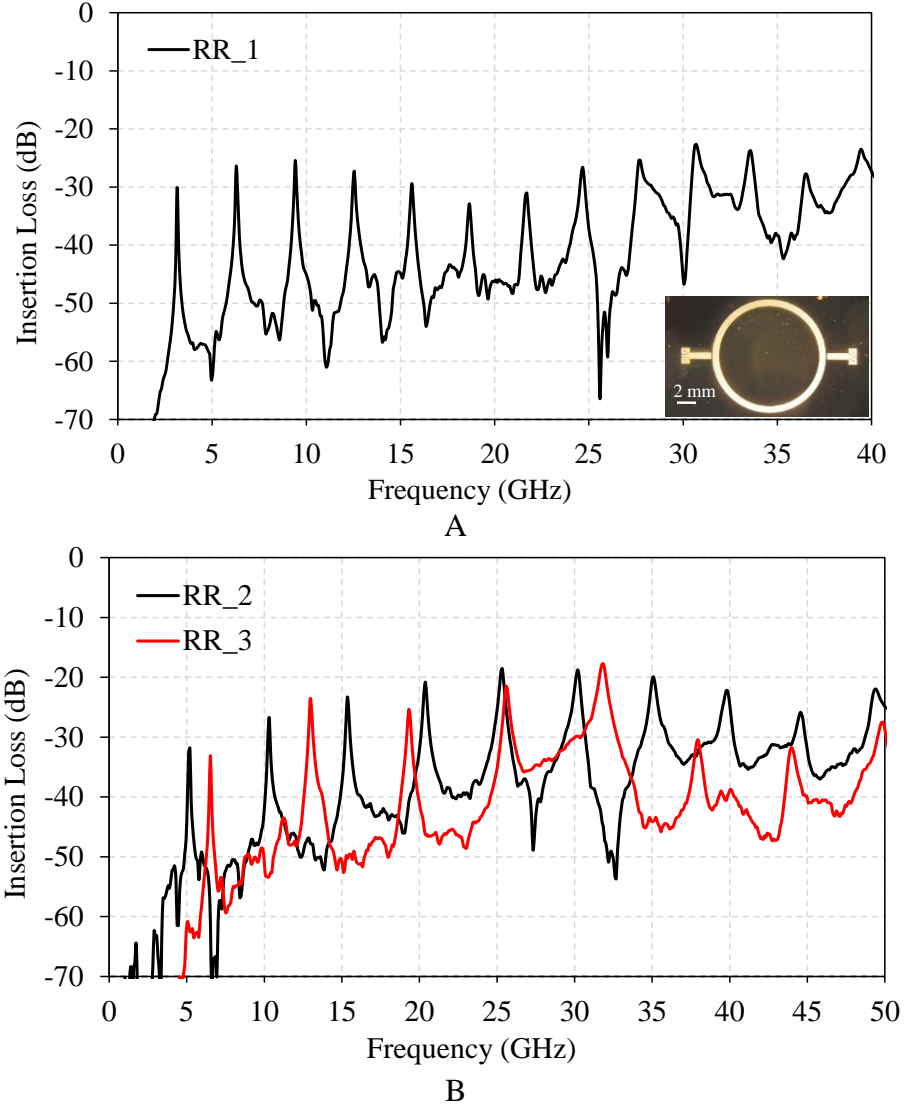


Figure 7-8. The measurement results of the insertion loss. A) RR_1 up to 40 GHz, and B) RR_2 & RR_3 up to 50 GHz. The inset in A shows the fabricated ring resonator RR_1.

To calculate the loss tangent from (7-3), the dielectric loss, α_d , should be first calculated from (7-4). The radiation loss could be normally ignored because its small compared to other losses as the devices are electrically small and do not radiate in the operation frequencies. The conductor loss, α_c , of a microstrip line could be approximated by the Schneider's approximation [55]. In [56], a numerical modelling has been reported for considering the effects of surface roughness on the conductor loss in microwave region. The mentioned theory in [56]

has been utilized by an study in [1] for an automated insertions loss and impedance calculation which gives,

$$\alpha_{c,surface_roughness} = \alpha_{c,smooth} \times K_{SR} \quad (7-8)$$

$$K_{SR} = 1 + \frac{2}{\pi} \arctan \left(1.4 \left[\frac{R_{RMS}}{\delta} \right]^2 \right) \quad (7-9)$$

where K_{SR} is a multiplicative factor accounting for surface roughness, R_{RMS} is the *rms* value of surface roughness, and δ is the skin depth. Based on the measured data and analytical discussion above, Table 7-2 tabulates the measured characterization data for the Corning SGW3 glass interposer layer up to 50 GHz. The 3dB BW, IL, and resonance frequency information from Figure 7-8 are used to extract the electrical permittivity and tangent loss values.

Table 7-2. The extracted characterization data for Corning SGW3 glass.

n	Frequency (GHz)	3dB BW (GHz)	Measured IL (dB)	ϵ_r	$\tan \delta$
1	3.1	0.07	30.1	5.3775	0.0051
2	6.3	0.1	26.5	5.1968	0.0051
3	9.4	0.1	25.4	5.2561	0.0053
4	12.5	0.14	27.3	5.2861	0.0056
5	15.6	0.18	29.4	5.3042	0.0058
6	18.6	0.18	32.9	5.3775	0.0049
7	21.7	0.23	31.1	5.3775	0.0054
8	24.7	0.23	26.6	5.4241	0.0046
9	27.6	0.36	25.4	5.503	0.0063
10	30.7	0.36	22.7	5.4902	0.0056
11	33.6	0.39	23.8	5.5496	0.0055
12	36.5	0.41	27.8	5.5998	0.0055
13	39.5	0.66	23.5	5.6123	0.0079
14	44.6	0.56	25.9	5.6299	0.0063
15	49.3	0.86	22	5.6931	0.0084

Micromachined Components on Corning Glass Substrates

Half-mode substrate integrated waveguide (HMSIW) architecture loaded with the complementary split ring resonators (CSRR) is chosen to realize compact resonators and bandpass filters for two ISM bands of 2.4 GHz and 5.8 GHz. Through glass via (TGV) structures

are fabricated using a laser fusion process on a glass interposer from Corning Incorporated. Surface micromachining techniques are used for the fabrication of the proposed devices. The measurement results show less than 1.8 dB insertion loss for the 2-pole bandpass filters in 2.4 and 5.8 GHz bands.

In this section, the extracted glass parameters ($\epsilon_r = 5.3$ and $\tan\delta = 0.0058$ at frequencies < 6 GHz) after implementation and measurements of the ring resonators are used to design RF resonators and bandpass filters for the bluetooth band of 2.4 GHz and the ISM band of 5.8 GHz.

The waveguides have the advantage of high performance operation and high power capability which make them a suitable candidate for implementation of many microwave circuit components. A waveguide as a transmission line could be operated as a filter by inserting an additional structure or could radiate energy and operate as an antenna using a slot. The substrate-integrated waveguide (SIW) structures will allow integration of waveguides into planar technologies that could be further integrated with other parts of a microwave circuit and also compatible with standard fabrication processes [60]. In order to further reduce the size of the resonators and filters, the SIW structures are operated in the evanescent mode where the operation frequency is smaller than the cut-off frequency of the waveguide; therefore, the overall dimensions of the devices will depend only on the size of the resonator and not that of the waveguide. The complementary split-ring resonators (CSRR's) are used to implement the compact resonators that will be embedded into the SIW structure to realize RF resonators and filters.

Resonator Design

Figure 7-9 depicts the schematic of the designed resonator which consists of a HMSIW structure that CSRR-based resonator is etched on its surface. The CSRR could be assumed as an LC tank where its resonance frequency is a function of its dimensions.

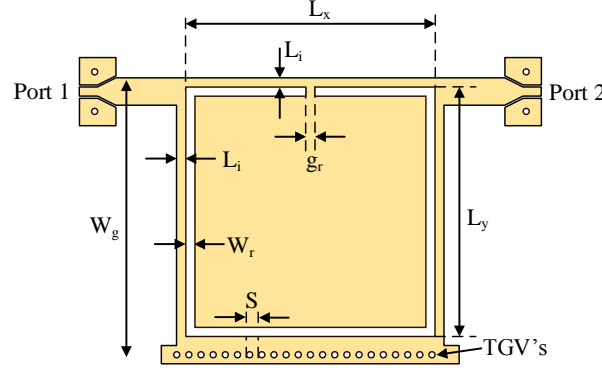


Figure 7-9. The schematic view of the CSRR-loaded HMSIW resonator on glass interposer layer and its dimensions.

The W_g is the width of the HMSIW waveguide which defines its cut-off frequency, f_c .

The L_x , L_y , W_r and g_r are the dimensions of the CSRR which change its LC lumped element components and define its resonance frequency. The utilized resonator and filter design methodology in this work are based on obtaining the required external quality factor, Q_e , for the coupled resonator design and the coupling coefficient, M , between the resonators for the bandpass filter design [61]. Then, the physical parameters of the design is changed to achieve the required values of Q_e and M . Two 50Ω CPW transmission lines are employed to externally excite the resonator. The external quality factor Q_e could be modified by changing the distance between the CPW feeding and the HMSIW ($L_o = 0$ in Figure 7-9). Figure 7-10 shows the simulation results of the resonator using ANSYS HFSS v. 15.0. The electric field at resonance, $f_o = 2.4$ GHz, is completely confined around the CSRR which will make a pass-band pole below the cut-off frequency of the waveguide (Figure 7-10A). Also, the coupling between the HMSIW and the CSRR will make a zero at 6 GHz. The second pass-band coming from the 2nd order harmonic of the CSRR occurs at frequencies above 15 GHz.

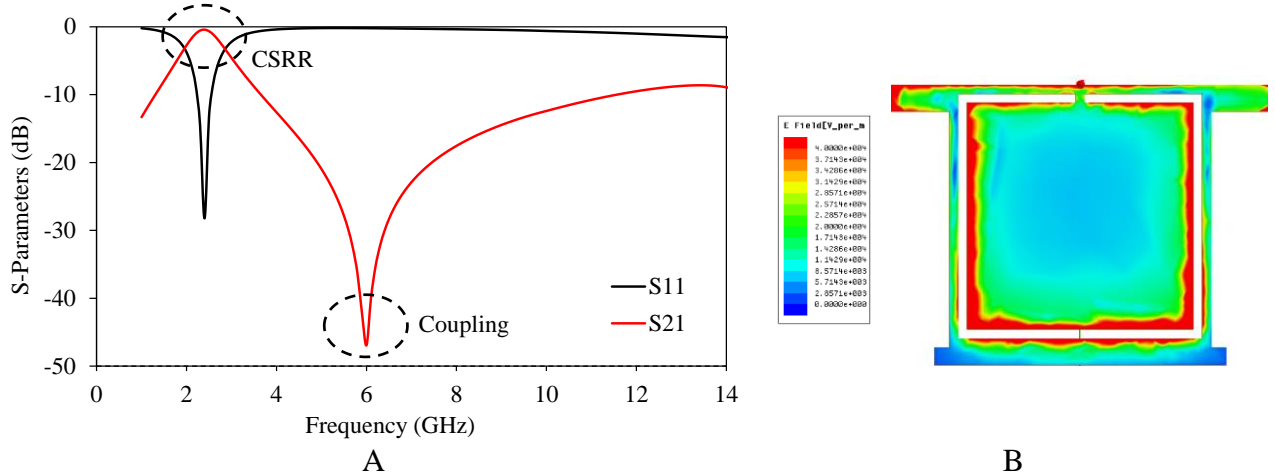


Figure 7-10. The simulation results of the CSRR-loaded HMSIW resonator. A) The S-parameters versus frequency, B) the electric field distribution at resonance.

The extracted external quality factors of the resonator as a function of the distance L_o , Q_e , is calculated as,

$$Q_e = \frac{2f_o}{BW_{3dB}}$$

where f_o is the resonance frequency and BW_{3dB} is the 3dB bandwidth of the resonator. $L_o = 0$ has been selected in this work in order to maximize the bandwidth of the resonators and filters where minimum external quality factor of 5 has been achieved.

Bandpass Filter Design

Based on the resonator design in the previous section, a bandpass filter could be designed where the pass-band could be achieved by using the mutual coupling between the resonators. Figure 7-11 shows the schematic of the two-pole bandpass filter which is used as the test vehicle in this paper. The pass-band below the cut-off frequency of the waveguide will be the result of mutual coupling between two resonators. The CSRRs' dimensions in Figure 7-11 are based on the resonator designed in the previous section. The distance L_c defines the mutual coupling between the resonators. In this work, the resonators and bandpass filters for two center

frequencies of 2.4 GHz and 5.8 GHz are designed and implemented. Table 7-3 tabulates the summary of dimensions used.

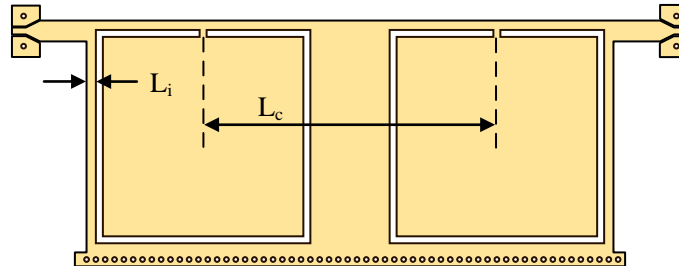


Figure 7-11. The schematic of the two-pole bandpass filter based on mutual coupling of two CSRR resonators.

Table 7-3. Summary of dimensions of the designed RF components in [mm].

Frequency	Device	W_g	L_x	L_y	L_i	W_r	g_r	L_c
2.4 GHz	Resonator	4.5	4.1	4.1	0.15	0.15	0.15	-
	Filter	5.2	4.6	4.6	0.2	0.15	0.15	6.3
5.8 GHz	Resonator	2.9	2.3	2.3	0.2	0.1	0.1	-
	Filter	2.9	2.4	2.4	0.2	0.1	0.08	3.5

Fabrication and Experimental Results

The designed RF components have been fabricated using the glass interposer substrate where the TGV's are fabricated using Corning laser machining and the surface micromachining technique proposed in Figure 7-5.

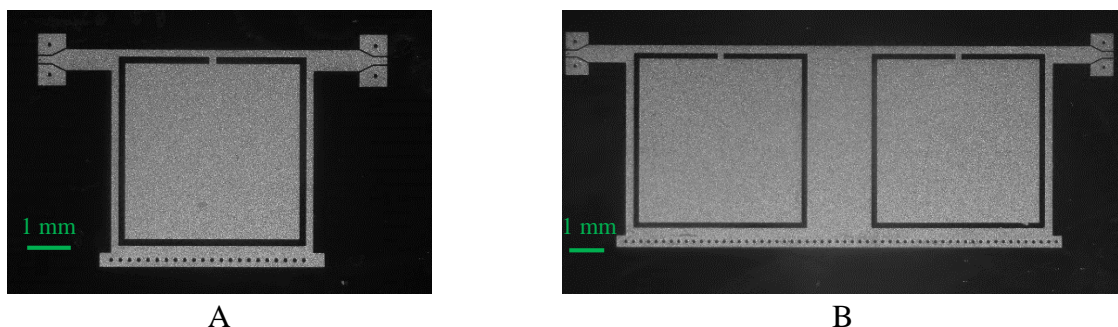


Figure 7-12. Optical micrographs of the fabricated 2.4 GHz devices. A) The CSRR-loaded resonator, B) the 2-pole bandpass filter.

Figure 7-12 shows the optical micrographs of the fabricated devices for the 2.4 GHz frequency band. Measurements have been performed using a vector network analyzer (E5071C,

Agilent Inc.) after standard two-port SOLT calibration between 1 GHz and 15 GHz. Figure 7-13 shows the measurement results of the resonator for 2.4 GHz. There is a slight shift of the frequency (0.1 GHz) where an insertion loss of 0.91 dB has been obtained at 2.5 GHz. The inaccurate thickness of electroplated Cu is attributed to the main cause of the frequency shift as the inductive components of the devices will be slightly deviate from simulations. The size of the implemented resonator is $0.094 \lambda_g \times 0.094 \lambda_g$ and the bandpass filter is $0.227 \lambda_g \times 0.102 \lambda_g$ at the design frequency of 2.4 GHz.

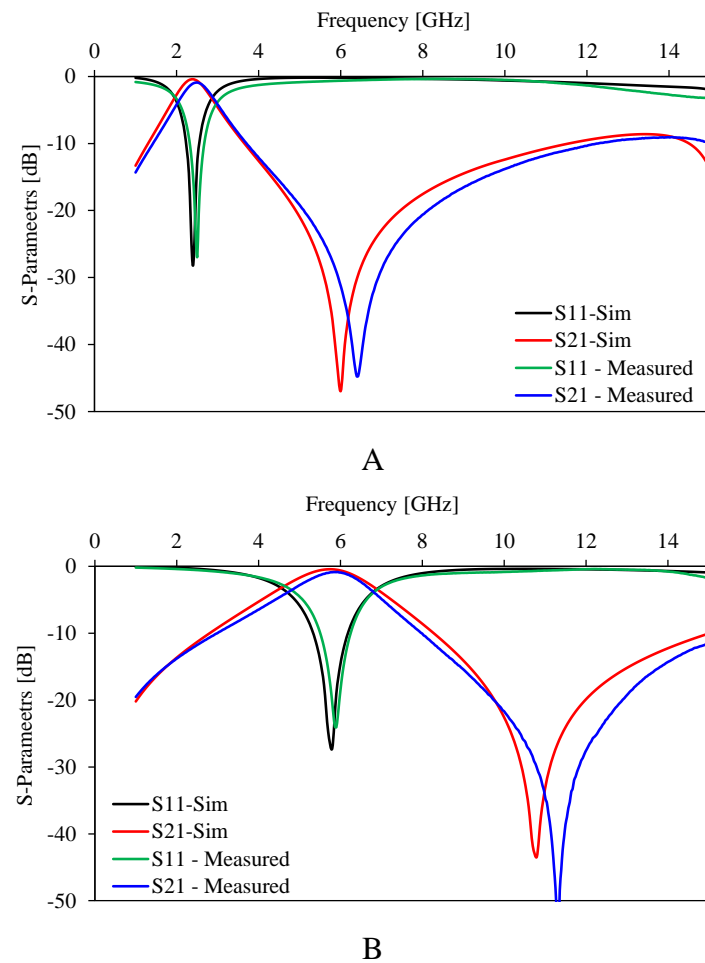


Figure 7-13. The simulation and measurement results of the CSRR-loaded HMSIW resonator. A) The 2.4 GHz band, B) 5.8 GHz band.

Figure 7-13 shows the measurement results and Figure 7-14 shows the SEM images of the fabricated devices for the 5.8 GHz frequency band. An insertion loss of 1.8 dB has been

achieved for the 2-pole bandpass filter at 5.76 GHz. The size of the implemented resonator is $0.149 \lambda_g \times 0.149 \lambda_g$ and the bandpass filter is $0.317 \lambda_g \times 0.144 \lambda_g$ at the design frequency of 5.8 GHz.

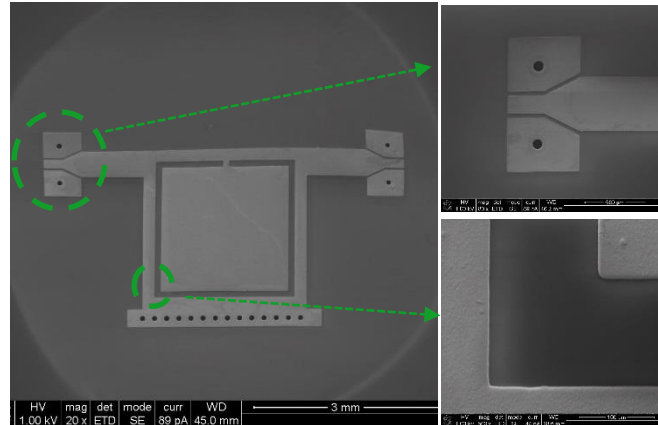


Figure 7-14. The SEM images of the fabricated resonator for the 5.8 GHz frequency band.

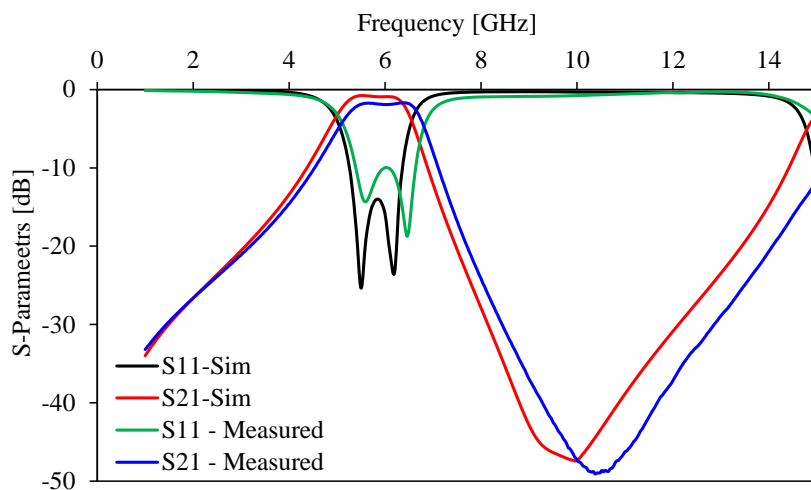


Figure 7-15. The simulation and measurement results of the 5.8 GHz 2-pole band-pass filter.

Towards Compactness for Higher Integration

In this work, micromachining techniques are exploited to fabricate low loss and compact components to satisfy the high scale of system integration of next-generation circuits and systems. The capability of MEMS manufacturing will decrease the total cost of the system and more compact devices will contribute towards highly efficient, low cost, highly integrable

systems. As an example, the resonators with dual ring CSRR's could be designed which have a higher equivalent lumped-element resonant components in the same HMSIW hosting medium and could reduce the total resonator area for the frequency band.

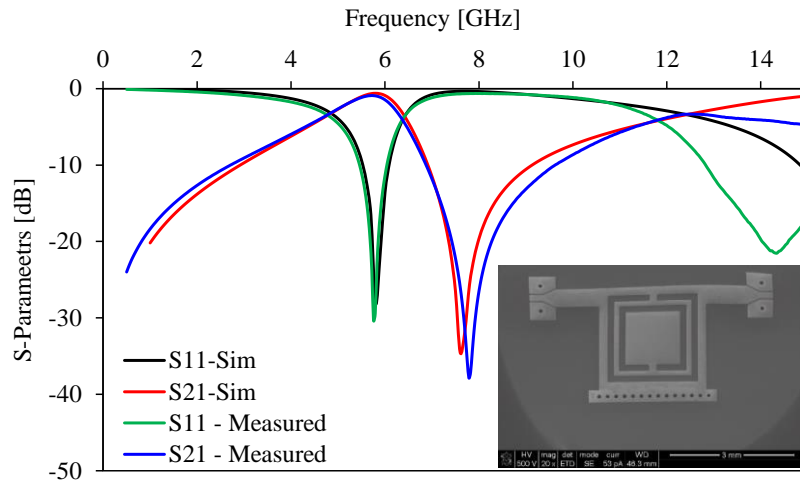


Figure 7-16. The simulation and measurement results of the 5.8 GHz double-ring CSRR-loaded HMSIW resonator.

For the 5.8 GHz band, the design, fabrication and measurement results of a double-ring CSRR is also demonstrated where the simulation and measurement results are shown in Figure 7-16. Due to employment of a double-ring resonator, the LC equivalent lumped-element equivalent circuit values of the resonator will be increased which leads to a 10% area reduction for the same operation frequency of 5.8 GHz with respect to regular single-ring resonator. This will also result in a narrower band response of the resonator which will be more suitable for narrow-band filter design. However, this will happen at the cost of a degraded out-of-band response because the second harmonic of the double-ring CSRR will occur at a lower frequency (around 15 GHz) compared to single-ring CSRR. In next section, a new architecture is proposed to further reduce the size of the RF passive resonators and bandpass filters with an improved spurious band rejection.

Ultra-Compact Multi-Layer Micromachined Components on Corning Glass Substrates

In previous section, the metamaterial-based CSRR structures are used inside the HMSIW to realize resonators and bandpass filters operating in evanescent mode for maximum size reduction. In this section, the combination of glass interposer technology and the low dielectric loss materials (BCB) is proposed for a multi-layer micromachined ultra-compact and high performance resonators and bandpass filters. The presented structures show a very high spurious band rejection suitable for implementation of high performance and highly integrable RF passive components.

Design and Simulations

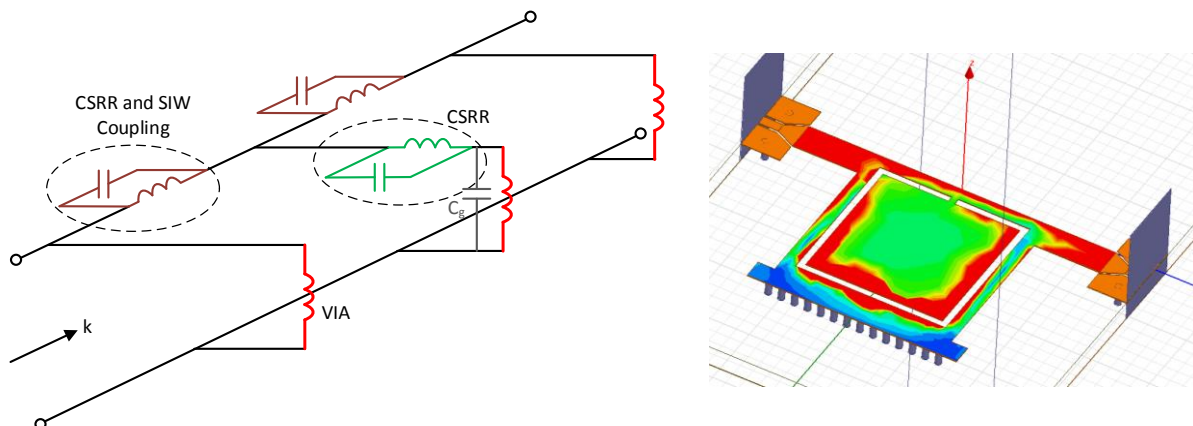


Figure 7-17. The schematic and lumped-element equivalent circuit of a CSRR-loaded HMSIW resonator for 5.8 GHz band.

Figure 7-17 shows the schematic view with electric field distribution and the lumped-element equivalent circuit model of a CSRR-loaded HMSIW resonator where the brown LC tank models the coupling between the waveguide and the CSRR resonator (circuit's zero) and the green LC tank is the CSRR equivalent circuit (circuit's pole). The proposed idea is to increase the capacitance of the circuit's pole to decrease the total area of the resonator while improving the out-of-band rejection performance. Therefore, an extra metal-insulator-metal (MIM)

capacitor is demonstrated to be added to the circuit which could be modeled as a parallel capacitor to help mitigate the resonance frequency given a much smaller area.

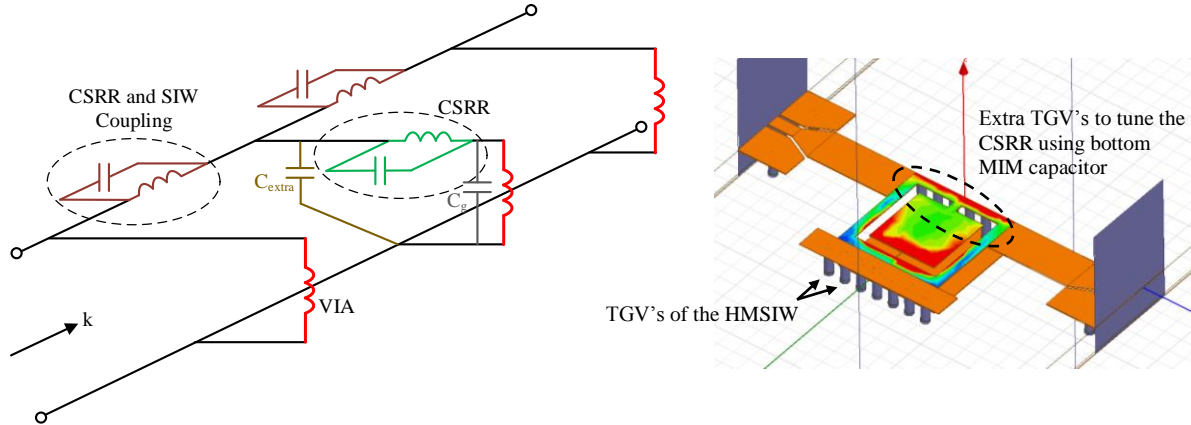


Figure 7-18. The schematic and lumped-element equivalent circuit of a CSRR-loaded HMSIW multi-layer and ultra-compact resonator for 5.8 GHz band.

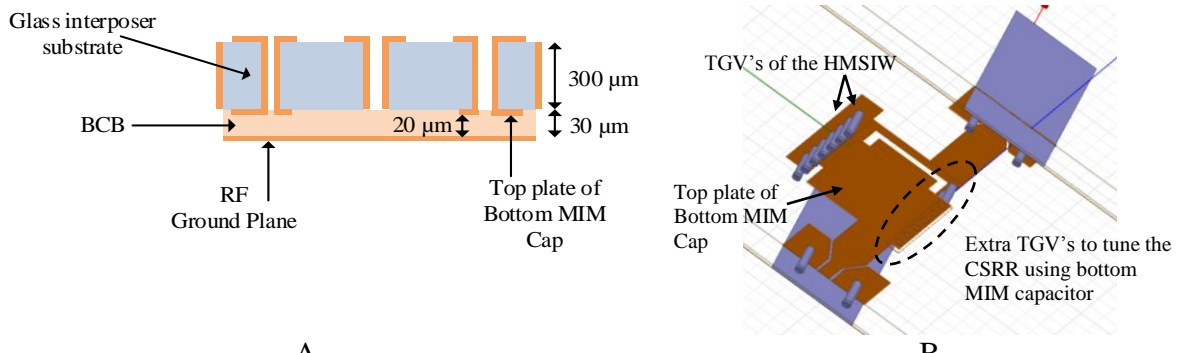


Figure 7-19. The proposed ultra-compact resonator. A) The cross section view of the multi-layer resonator, B) the bottom 3D view.

Figure 7-18 shows the equivalent circuit model and the schematic of the multi-layer ultra-compact resonator in which extra TGV's on the upper part of the HMSIW structure are used for connecting the HMSIW module to the bottom MIM capacitor. The HMSIW body is micromachined on the front side of the glass interposer layer and the bottom MIM capacitor is realized using an extra 30 μm BCB coating on the backside of the glass interposer layer. Figure 7-19A shows the cross section view and Figure 7-19B shows the backside 3D view of the resonator.

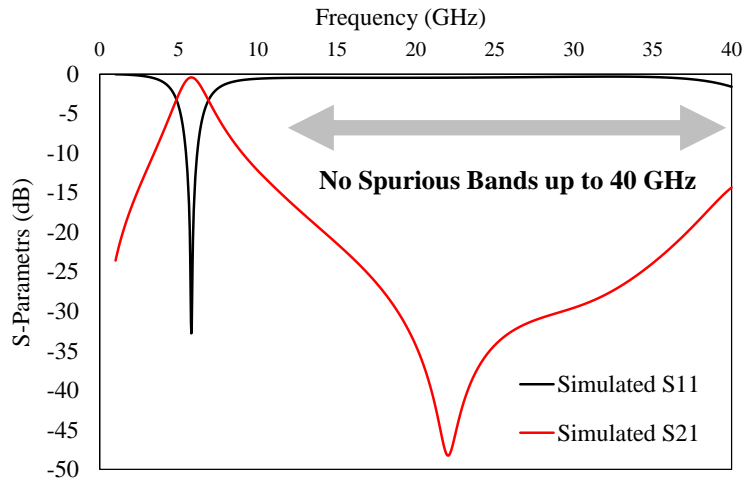


Figure 7-20. The simulation results of the CSRR-loaded HMSIW multi-layer 5.8 GHz resonator.

Figure 7-20 shows the simulation results of the 5.8 GHz multi-layer ultra-compact resonator up to 40 GHz with a size of $0.05 \lambda_g \times 0.05 \lambda_g$. The response is very clean without any spurious bands up to 40 GHz. Compared to regular CSRR-loaded HMSIW resonator which has spurious band at 15 GHz, the ultra-compact one has 8 times smaller area and at least 3 times improved $f_{\text{spurious}} / f_{\text{resonance}}$ which makes it suitable for high performance compact RF passive components.

The presented idea could be applied for designing resonators at other frequency bands which could be further extended as building block for other high performance and compact RF components including band-pass filters.

Fabrication and Experimental Results

Figure 7-21 shows the microfabrication process for the ultra-compact resonators where both sides of the glass interposer layer are micromachined. Since an electroplating method has been used for this fabrication, both sides of the substrate will be exposed to an electrolyte solution during the electrodeposition. As a result, the seed layers composed of Ti/Cu with a thickness of 30 nm/1 μm are deposited on both sides. The top layer lithography (the mold for electroplating) is performed first, followed by oxygen plasma (Asher, 2 minutes with 300W and

a gas flow of 600 SCCM) and 30 nm Ti deposition. Next, the back-side of the glass substrate is coated and patterned forming the top layer of the bottom MIM capacitor and both sides are electrodeposited with Cu simultaneously at step (i). After removal of NR9-8000P photoresist, the BCB is coated, soft-baked, patterned and hard-baked to make the MIM capacitor. Finally, the last photoresist is deposited on the back side of BCB to ensure an isolation in the MIM capacitor, between the ground plane and the top plane of the capacitor. Figure 7-22A shows the results of the front view of the microfabricated 5.8 GHz resonator after first mask. In order to perform simultaneous electroplating, the photoresist on the backside is coated and patterned. Also, the photoresist of the top layer is protected from overdevelopment (of the backside photoresist) using a sacrificial Ti layer at step (f). At the soft-bake step of the bottom photoresist, the top photoresist will experience some wrinkling (Figure 7-22B); however, since both photoresists will be removed at step (j), no defects were observed during the fabrication.

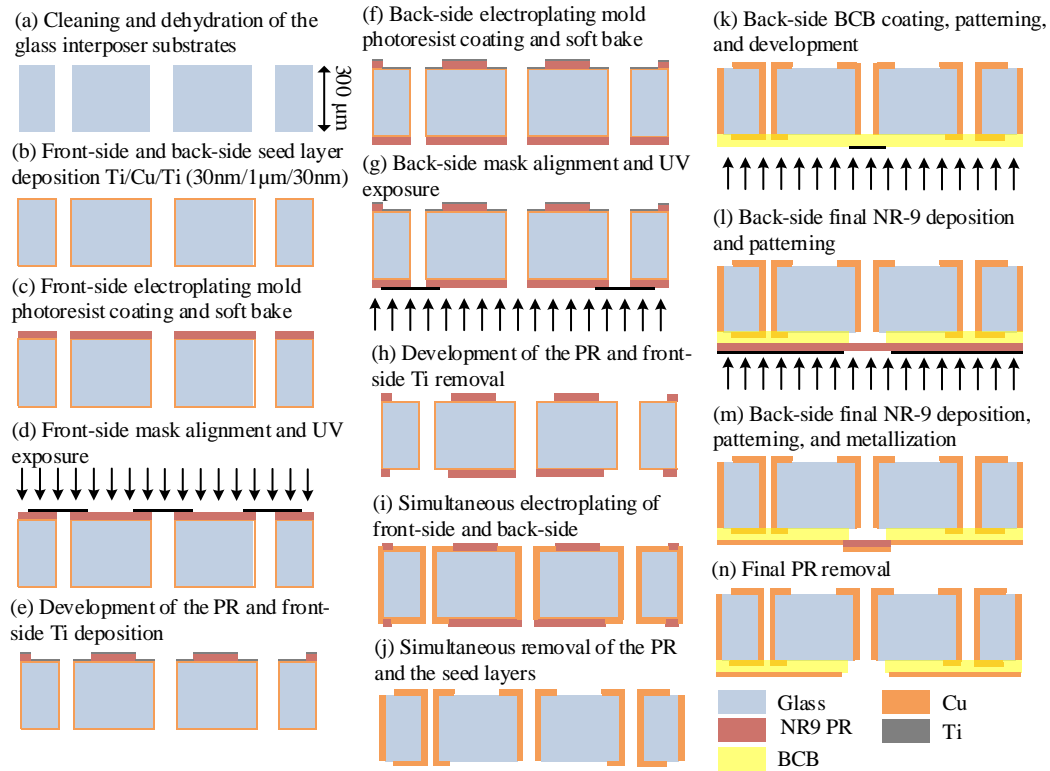


Figure 7-21. The fabrication process flow for the ultra-compact multi-layer resonators.

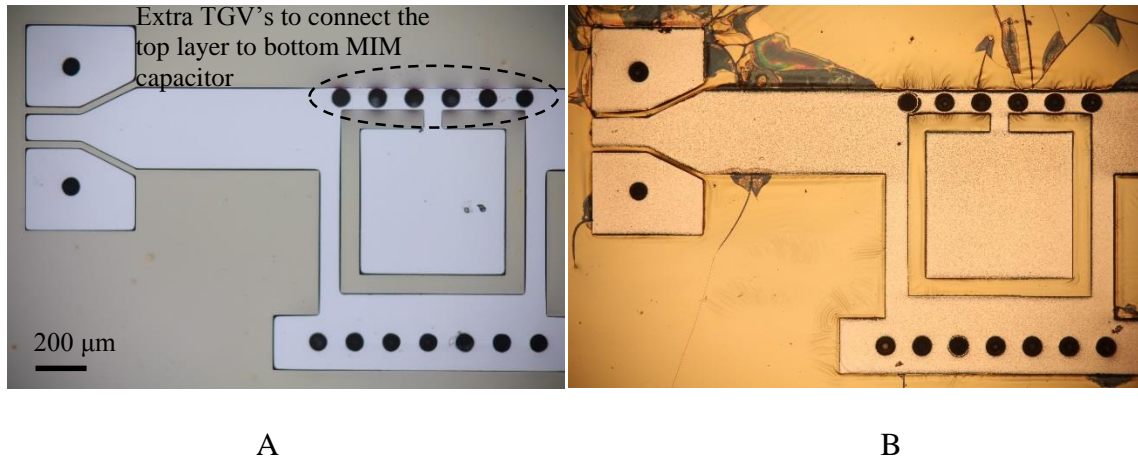


Figure 7-22. The front view of the microfabricated 5.8 GHz resonator. A) The optical view after first mask, B) the optical view after simultaneous electroplating of top and bottom sides.

In-Substrate Resonators and Bandpass Filters with Improved Insertion Loss in K-band

In this section, we report on in-substrate passive components using a high performance glass interposer and through glass via (TGV) technology and a multi-layer superlattice conductor architecture. Minimal RF loss is achieved using low dielectric loss glass substrates and superlattice conductors featuring skin effect suppression. Resonators and two-pole bandpass filters, embedded inside a glass interposer substrate, are used as test vehicles for the demonstration of insertion loss improvement in K-band. The utilized conductor is made of 20 layers of Cu/NiFe with each pair of 360 nm/30 nm, respectively, where NiFe layers with negative permeability in frequency range of interest are used for eddy current cancelling and improving the conductor loss. Control devices using the same glass substrate and conductor made of pure copper are fabricated for comparison purposes. The glass interposer substrate (SGW3, Corning Incorporated) has a thickness of 130 μm and the TGV's with a diameter of 80 μm . Up to 0.3 dB reduction in the insertion loss is achieved by using the proposed superlattice approach on glass substrates.

Design and Characterization

In-substrate passive resonators and broadband, with larger than 10% fractional bandwidth (FBW), bandpass filters are implemented for the 18 GHz frequency band (K-band) suitable for future telecommunication systems including next-generation 5G communication. The half mode substrate-integrated waveguide (HMSIW) approach is selected as the resonator/filter architecture where two metallic plates are employed on the top and the bottom of the glass substrate with an array of through glass vias (TGV's) as the sidewall. Also, metamaterial unit cells consisting of complementary split-ring resonators (CSRR) have been embedded on the HMSIW structures to further reduce the size, which lowers external quality factors ultimately contributing to broadband operation. As glass is used as the structural material, accurate characterization of glass substrates is performed to extract their electrical properties up to 25 GHz with test ring resonators. Copper (Cu) has been used for metallization through the TGV's and ground planes, ensuring a reliable electrical connection inside TGV's. The top metal layer of the actual devices is made of 10 layers of 300 nm/50 nm thick Cu/NiFe superlattice conductors, which are designed to have eddy current canceling and therefore low conductor loss in the K-band region of operation. The single-band resonators with a center frequency of 18 GHz are realized using a CSRR which is patterned in the top metal layer of a half-mode substrate integrated waveguide (HMSIW) cavity. The same method is used to fabricate two-pole bandpass filters.

In this section, glass interposer substrate, SGW3 (Corning Incorporated) in 50 mm × 50 mm dimension is used; however, with a different thickness and TGV's diameter compared to devices which were reported earlier in this Chapter allowing the implementation of SIW-based passive components in 18 GHz and 25 GHz bands. A thickness of 130 μm and TGV's with a diameter of 80 μm are used for the implementation of integrated passive RF components. The glass interposer substrates with excellent surface roughness and mechanical strength are suitable

for the implementation of the superlattice structures with ultra-thin metallic layers. Figure 7-23 shows the optical views of the fabricated TGV's and their dimensions where the top and bottom views of the TGV's are shown.

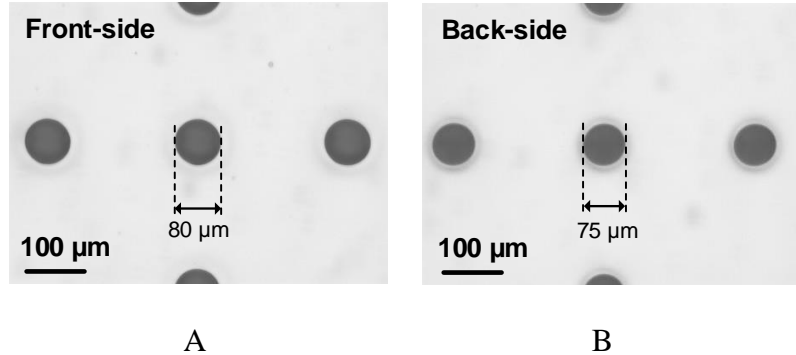


Figure 7-23. The optical micrographs of the fabricated TGV's by Corning with 80 μm diameter. A) The front-side view, B) the back-side view of the interposer substrate.

The electrical properties of the glass interposer substrate including the dielectric constant and tangent loss have a crucial effect on their microwave performance and the RF components to be implemented on it. Therefore, high frequency characterization results of the glass substrates up to 30 GHz in Table 7-2 are used to design the RF passive components.

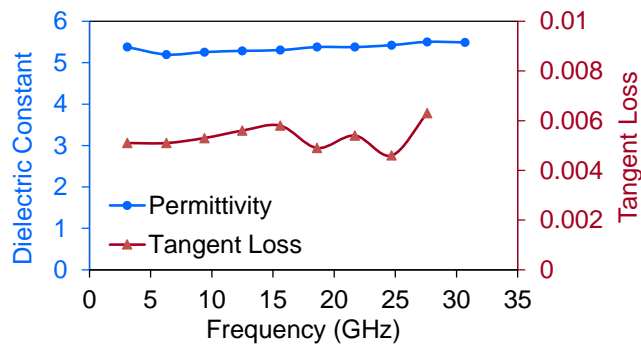


Figure 7-24. The extracted measurement results of the glass electrical properties up to 30 GHz.

Figure 7-24 depicts the extracted electrical properties of the glass. The values of the insertion loss (IL) and the 3dB bandwidth of the resonance peaks are used to specify the dielectric constant and the tangent loss of the glass substrate in the resonance frequency. Both the

electrical permittivity and the loss tangent values are relatively constant in frequencies from 3 GHz to 30 GHz resulting in a flat dielectric loss in the given frequency range.

As the operation frequency of the RF systems increases, the associated RF loss including the dielectric and conductor losses will also increase. Although the utilized glass interposer substrate in this work is designed to have relatively low tangent loss in frequencies up to 30 GHz, the other limiting factor affecting the efficiency of the RF circuits and systems in higher frequencies is the conductor loss as a result of the skin effect. Although copper and silver are known as high electrical conductivity materials, their high conductivity is not as effective in higher operation frequencies such as in K-band. In the devices operating in ISM bands of 2.4 GHz and 5.8 GHz bands, the pure thick electroplated Cu is used as the actual conductor. However, as the frequency increases, the electromagnetic wave propagating through a conductor will decay in a depth inside the conductor known as the skin depth. This confinement of current at the outmost areas of the conductor will result in a reduced effective cross section area and eventually an increased ohmic loss. To overcome that, in this work, a Cu/NiFe (360 nm/30 nm) metaconductor is used as the actual conductor for the implementation of the in-substrate passive components. The employed ferromagnetic material, NiFe, layers, will have a negative magnetic permeability above its ferromagnetic resonance frequency (f_{FMR}), cancelling out the generated eddy currents from copper layers to suppress the skin effect and improve the insertion loss property of the RF passives in the operation frequencies.

Figure 7-25 shows the simulation results of a unit-cell of the multi-layer conductor using ANSYS HFSS v. 15.0. In this simulation, the Cu/NiFe nano-superlattice conductors with 10 layers and a thickness of 360 nm/30nm, respectively, are used. A reference copper conductor with the same total thickness of 3.9 μm has been simulated for comparison. In the lower

frequency bands (< 5 GHz) near the f_{FMR} frequency of the ferromagnetic material, the permeability of the NiFe layers is high leading to a lower skin depth and a higher ohmic resistance. As the frequency increases and when $|\mu_{r, \text{NiFe}}|$ approaches the Cu/NiFe thickness ratio (which is 6 in this simulation), the conductor will have its maximum eddy current cancelling effect and the lowest ohmic loss is achieved. The resistivity of the Cu/NiFe will remain lower than that of the reference copper conductor in the K-band paving the way to implement passive components with the reduced conductor loss in the given frequency band.

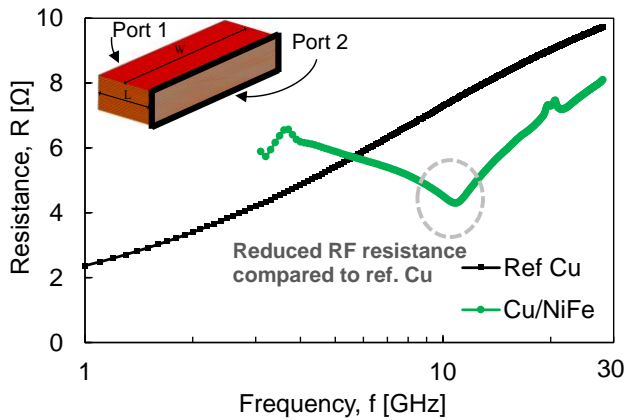


Figure 7-25. The simulation results of the planar Cu/NiFe (360 nm/30 nm) multi-layer (superlattice) conductor and the corresponding reference copper conductor in ANSYS HFSS v. 15.0.

RF Passive Components Design in K-Band

Resonators and bandpass filters are the RF passive components that are used as test vehicles in this work to demonstrate the feasibility of implementing passive components using low loss glass interposer and multi-layer metaconductors technologies for maximum possible loss reduction. The waveguide components are used for the implementation of the proposed RF passives because of their advantages including the high performance and high power capability. In order to maintain compactness and integrability with other parts of the system in interposer-based packaging, the planar half mode substrate-integrated waveguide (HMSIW) structure has been selected for the implementation of RF resonators and filters. The HMSIW structures are

realized using the metallic plates on both sides of a dielectric substrate which are connected to each other using a side wall made of an array of through substrate vias. To fabricate ultra-compact resonators using HMSIW components, they will be operated in the evanescent mode below the cut-off frequency of the waveguide by having the complementary split-ring resonators (CSRR's) patterned on the top surface of a HMSIW as the governing resonance scheme.

The glass characterization results (shown in Figure 7-24) have been used to design an in-substrate resonator and a wide-band two-pole bandpass filter with CSRRs at the 18 GHz band. The single loop CSRR structure will provide a higher-frequency second resonance response compared to other CSRR implementations including the double or triple loop designs and an improved out-of-band rejection performance. Two sets of devices using the same substrate are reported which use different conductor architectures. First, the devices are fabricated using the reference solid copper conductor for the top and ground planes. The devices using the proposed Cu/NiFe multilayer superlattice conductors are also fabricated to study the insertion loss improvement in K-band. Glass wafers with a thickness of 130 μm and a dielectric constant of 5.9, and a tangent loss of 0.0045 at 18 GHz have been used for the design.

The schematic of the designed resonator is the same as in Figure 7-9. Similarly, the HMSIW cavity has the width, W_g , which controls the cut-off frequency of the waveguide, while the dimensions of the CSRR resonator control the main resonance frequency. The CSRR structure could be thought of an LC tank where it's inductive and capacitive elements are controlled via changing its width (W_r) and gap (g_r). The CSRR structure patterned on the top metal layer of the HMSIW cavity is excited inductively using the 50Ω transmission lines. As a result, the external quality factor of the resonator is controlled by moving the position of the transmission lines from the array of TGV's towards the center of the waveguide cavity.

Due to the small size of the resonator, the external quality factor would be small leading to a high bandwidth of the resonator. For filter implementation, it could be used as an advantage for the implementation of broadband bandpass filters [63]. On the other hand, higher bandwidth will result in the lower selectivity of the filter which could be solved by increasing the number of poles of the filter achieving highly selective filters. Figure 7-26 shows the schematic of the two-pole bandpass filter to demonstrate the in-substrate passive component with improved insertion loss. The mutual coupling between the resonators will produce a passband where the coupling coefficient (M) and the corresponding passband depend on the distance between the resonators (shown as L_c in Figure 7-26).

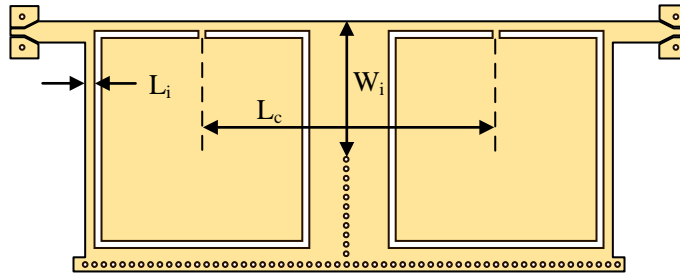


Figure 7-26. The schematic of the two-pole bandpass filter.

Table 7-4 shows the dimensions of the designed resonator and bandpass filters. The design parameters are optimized to reach maximum performance in terms of matching and insertion loss in the passband center frequency using full-wave electromagnetic simulations. For 18 GHz band, simulations show an external quality factor, Q_e of the resonator of 4.64 which is achieved using the proposed structure. Also, the simulated 15 dB FBW of the bandpass filter is more than 10%, suitable for broadband applications. The size of the implemented resonator is $0.18 \lambda_g \times 0.18 \lambda_g$ and the bandpass filter is $0.33 \lambda_g \times 0.18 \lambda_g$ assuming that λ_g is the guided wavelength at the design frequency of 18 GHz.

Table 7-4. Summary of design parameters for the RF passive components. The given dimensions are in mm.

Frequency	Device	W_g	L_x	L_y	L_i	W_r	g_r	W_i	L_c
18 GHz	Resonator	1.2	0.8	0.8	0.08	0.05	0.05	-	-
	Filter	1.2	0.8	0.8	0.08	0.05	0.05	0.72	1.1
25 GHz	Resonator	0.8	0.6	0.6	0.08	0.05	0.05	-	-
	Filter	0.8	0.6	0.6	0.08	0.05	0.05	0.72	1.1

Fabrication and Measurement Results

Surface micromachining processes have been utilized to fabricate the RF passive components. Prior to microfabrication, the TGV holes through the glass substrates are fabricated by Corning Incorporated where the via holes have a diameter of 80 μm and a thickness of 130 μm . The detailed microfabrication process is shown in.

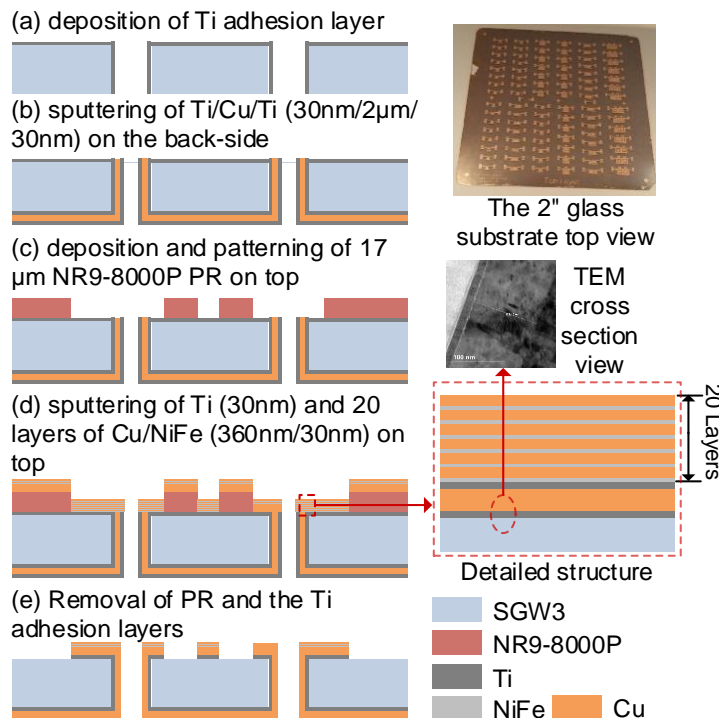


Figure 7-27. The microfabrication process for passive resonators and bandpass filters using Cu/NiFe conductors.

The glass substrates are first cleaned using a wet process and subsequently dehydrated to avoid any moisture. A PVD film deposition method is used for both the front-side and back-side of the glass substrates. Ti/Cu/Ti with a thickness of 30 nm/2 μm /30 nm are DC sputtered (Kurt J.

Lesker CMS-18) on the back-side to form the ground plane of the devices. The high surface smoothness of the TGV holes allows the reliable metallization through TGV holes using the PVD method. Then, 17 μm thick NR9-8000P photoresist for a front-side lift-off process is spin-coated which contains the top-layer of the actual RF devices. After mask alignment, exposure, soft bake and photoresist development, multiple Cu/NiFe are sputter-deposited on the front-side. An over-developed photoresist patterning is used to ensure a reliable lift-off process after front-side thick film metal deposition (up to 4 μm) using sputtering. A 99.9% Ni₈₁Fe₁₉ sputtering target (Kurt J. Lesker) is used for ferromagnetic material deposition. The devices are finally patterned by removing the photoresist and the Ti adhesion layers in sequence. The insets in Figure 7-27 show the detailed transmission electron microscopy (TEM) view of the deposited Ti/Cu on glass substrate and the optical image of the top view of the 2-inch substrate which has the final devices.

Figure 7-28 shows the micrographs of the fabricated devices using Cu/NiFe conductors of 360 nm/30 nm. Figure 7-28A shows the SEM images of the fabricated devices where Figure 7-28B shows the delaminated film due to relatively high amount of stress after PVD deposition. Figure 7-28C shows the SEM image with the tilted angle view of the series of the fabricated TGV's after PVD metallization and Figure 7-28D shows the detailed view of a single TGV where the smooth inside of the TGV's is observed.

Measurements have been performed using a vector network analyzer (E8361A, Agilent Inc.) after standard two-port SOLT calibration between 10 GHz and 30 GHz. A Cascade Microtech probe station with ground-signal-ground (GSG) probes (150 μm pitch) are used for testing. Figure 7-29 shows the measurement results of the resonator for 18 GHz. Figure 7-29A depicts the comparison of the simulation and measurement results where a solid copper

conductor has been used for simulations and the Cu/NiFe superlattice conductors with a Cu/NiFe thickness of 360 nm/30 nm, respectively, has been used for the fabricated devices. There is a slight shift of the frequency (0.6 GHz) comparing the simulation and measurement results, which is stemming from the fact that Cu/NiFe conductors have smaller inductive components. The Cu/NiFe multi-layer conductors have smaller resistivity in K-band because of the eddy current cancelling effect and more uniform current distribution into volume of the conductor in those frequencies compared to the solid copper conductor which is more largely affected by the skin effect. As a result, Cu/NiFe conductors have slightly smaller inductance which affects the inductive elements of the resonator shifting the center frequency to higher frequencies.

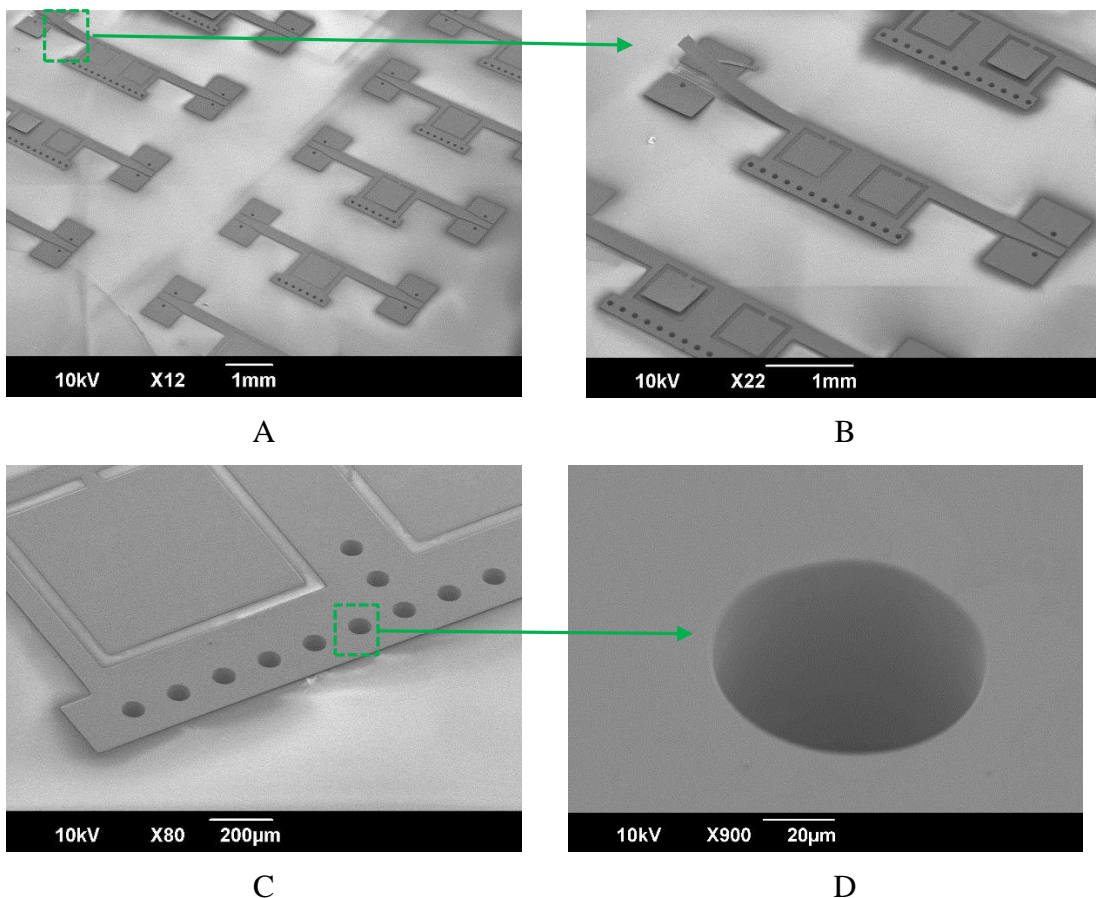
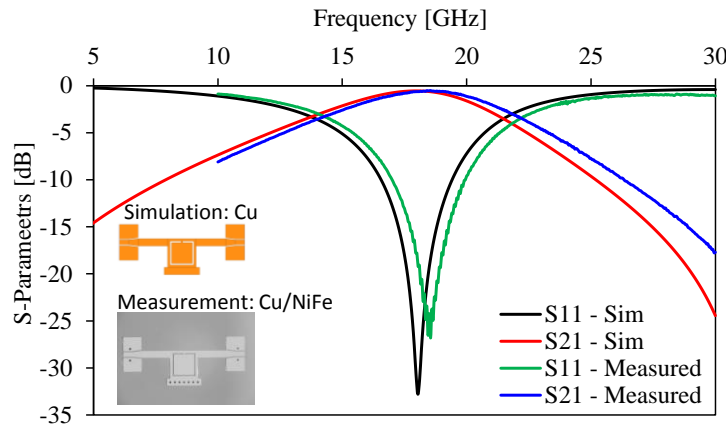
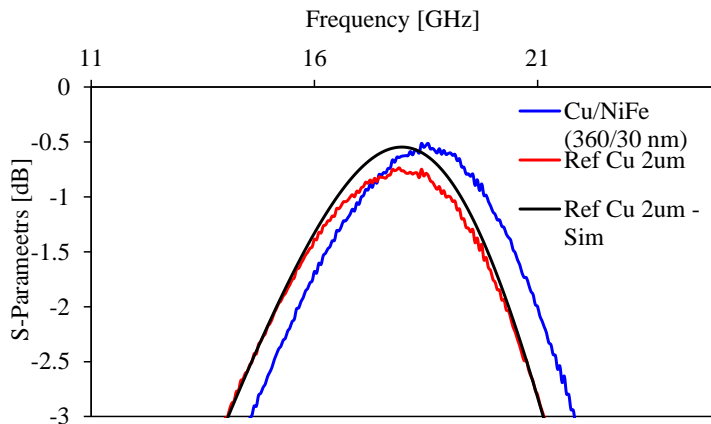


Figure 7-28. The SEM micrographs of the passive RF components. A) The substrate holding the devices, B) the two-pole bandpass filter with delaminated film, C) a series of fabricated TGV's with a tilted angle view, and D) the single TGV detailed view after metallization.



A



B

Figure 7-29. The measurement results of the resonator for 18 GHz band. A) The comparison of the simulation and measurement results of the designed resonator. The measurement results are performed for the devices using nano-machined Cu/NiFe conductors while the simulations utilize a reference solid copper conductor, B) the zoomed version of the insertion loss where comparison of the measurement results of the devices made of Cu/NiFe conductors and solid copper conductor is given.

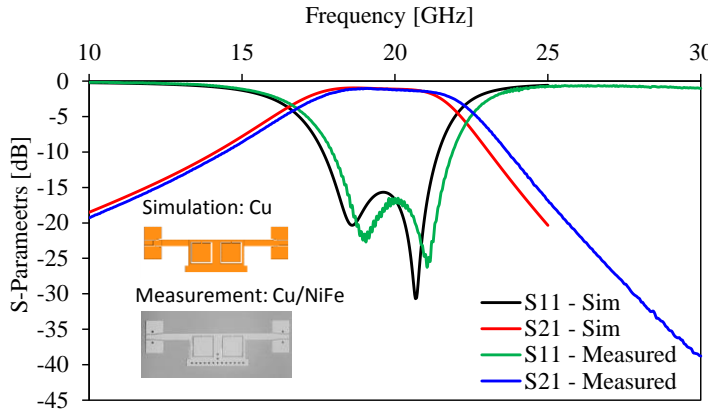
The same devices are fabricated using solid copper as a reference conductor with the microfabrication process given in Figure 7-27 except step (d) where solid copper has been deposited instead of Cu/NiFe. Figure 7-29B shows the measurement results comparison of the insertion loss of the devices made of Cu and Cu/NiFe conductors. As expected, the devices made of the reference copper conductor experience no shift in the frequency verifying that simulation

and measurement results are in good agreement for devices made of copper. However, a 0.2 dB insertion loss shift is observed stemming from idealities which are assumed for the simulation model including the glass and conductor losses, surface roughness of the glass and deposited film and fabrication tolerances.

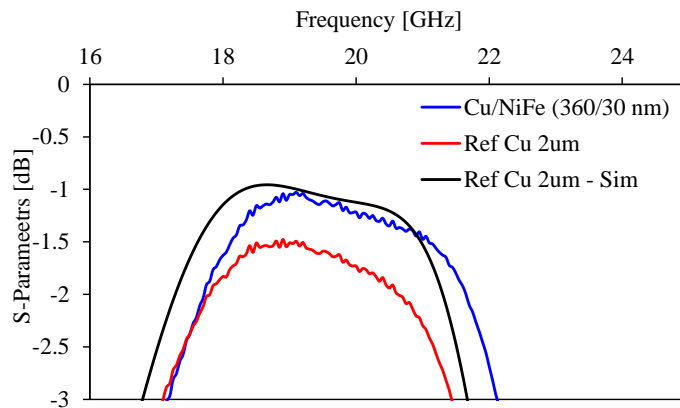
Although a frequency shift is observed, the devices made of Cu/NiFe conductors show more than 0.2 dB improvement in insertion loss compared to solid copper devices as shown in Figure 7-29B where an insertion loss of 0.51 dB is recorded for Cu/NiFe resonators at 18 GHz while an insertion loss of 0.73 dB is measured for solid copper resonators. As a result, the proposed Cu/NiFe conductors were superior to the reference copper conductor to reduce the loss of the passive components in the K-band region of operation.

Figure 7-30A shows the measurement results of the two-pole bandpass filter for the 18 GHz frequency band. Similar to the designed resonator, a frequency shift is observed in Figure 7-30A due to the smaller inductive elements of the Cu/NiFe conductors compared to the solid copper conductor. Figure 7-30B presents the comparison of the insertion losses of the fabricated devices using the reference solid Cu and Cu/NiFe conductors. A good agreement is observed for the simulation and measurement results of the devices made of solid copper. Due to the ultra-high surface smoothness of the utilized glass substrates, the deposition of ultra-thin Cu/NiFe layers in thicknesses in the nm range are feasible and the insertion loss improvement compared to the devices with reference copper conductors is observed.

Also, the Cu/NiFe bandpass filters show a 0.3 dB improvement compared to reference copper conductors. A 5.8 GHz (16.7 GHz – 22.5 GHz) 3dB bandwidth is measured for the bandpass filters translating to a 32% 3 dB FBW where an in-band return loss of more than 15 dB is measured.



A



B

Figure 7-30. The measurement results of the bandpass filter for 18 GHz band. A) The comparison of the simulation and measurement results of the designed bandpass filter. The measurement results are performed for the devices using nano-machined Cu/NiFe conductors while the simulations utilize a reference solid copper conductor, B) the comparison of the insertion loss.

The second set of devices are designed to target a 25 GHz band which is a popular band for next-generation communication systems including 5G protocol [2]. The same Cu/NiFe structure with a thickness of 360 nm/30 nm are used to realize resonators and bandpass filters with the similar structure as the 18 GHz devices on the same glass interposer substrate as in Figure 7-27. Figure 7-31 shows the measurement results of the resonator for the 25 GHz frequency band. Similarly, due to a different current flow inside the conductors comparing solid

Cu and Cu/NiFe conductors, a frequency shift is observed, while a 0.12 dB improvement in the 25 GHz band is recorded.

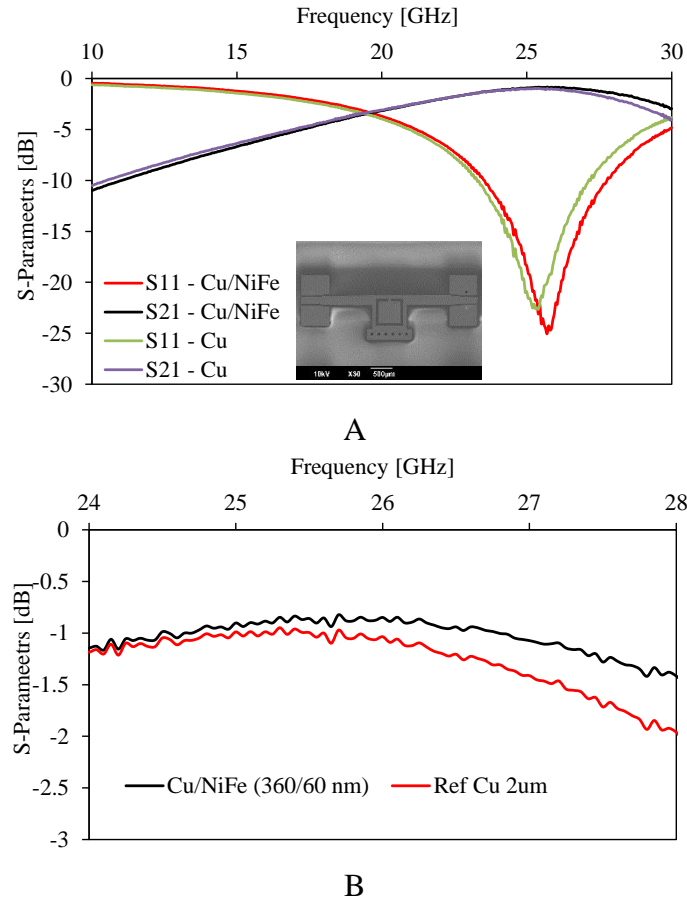


Figure 7-31. The measurement results of the resonator for 25 GHz band. A) The comparison of the resonator made of solid Cu and Cu/NiFe conductors, B) the comparison of the insertion losses in the passband.

Dual-Band Passives Using Cu/NiFe Conductors

In the previous section, single-band resonators and bandpass filters for the center frequency of 18 GHz and 25 GHz bands are designed and experimental results were shown. In this section, we report on a dual-band design to implement RF passives for the 12 GHz and 18 GHz bands. A capacitive metal path is integrated to the HMSIW structure which provides a capacitive path to the ground while inductively coupled to the HMSIW body. As a result, a series LC tank (shown in blue) will be added to the equivalent circuit model of the HMSIW resonator

as shown in Figure 7-32C. Figure 7-32A shows the schematic of the designed resonator where a capacitive path and a double ring CSRR resonator are integrated in a HMSIW waveguide cavity. Figure 7-32B shows the simulation results where two independent bands are generated below the cut-off frequency of the waveguide. The first band is designed to lie in the 12 GHz band using the CSRR structure; and the second band is on 19 GHz band controlled by the capacitive patch. The insertion loss of 0.71 dB and 0.94 dB are achieved in 12 GHz and 19 GHz bands, respectively.

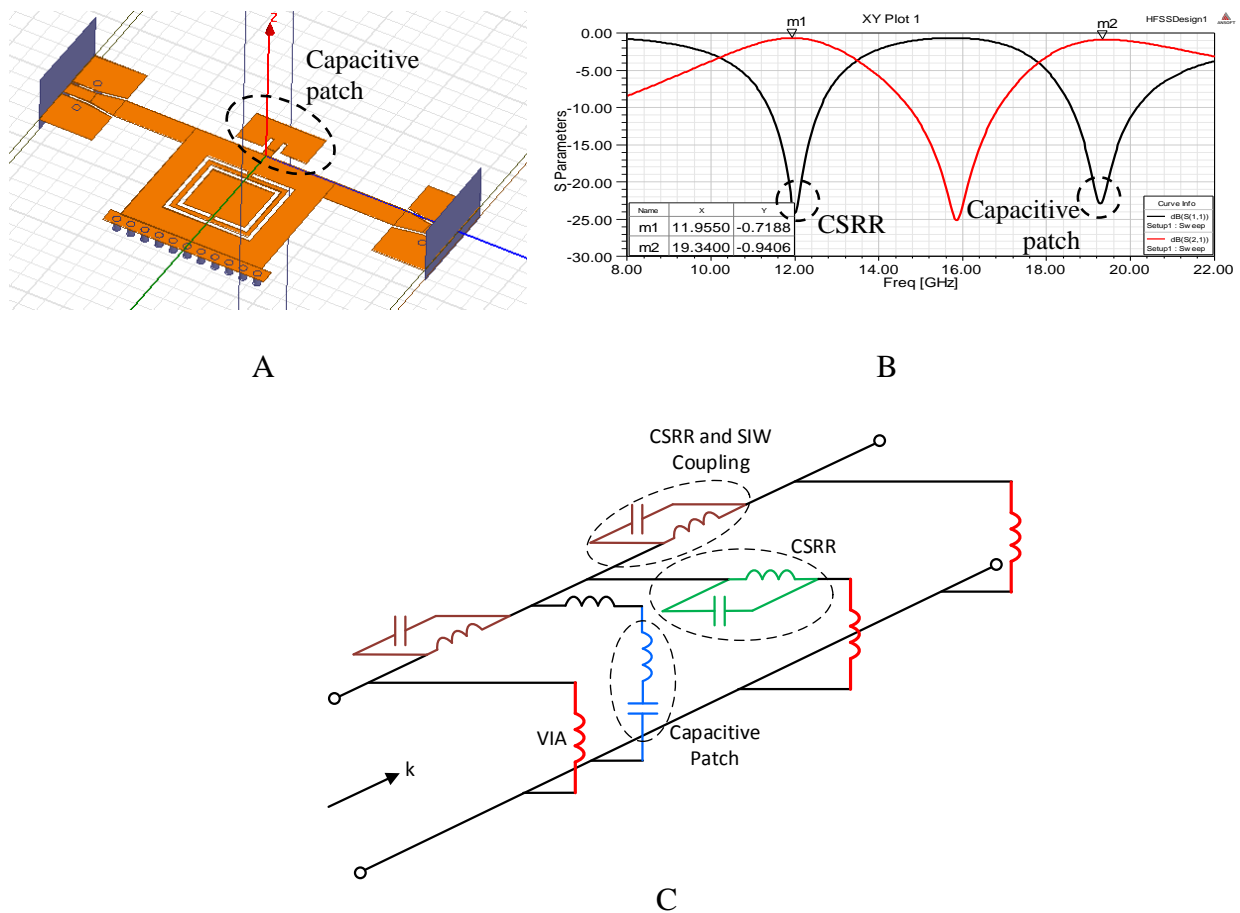


Figure 7-32. The dual-band capacitively-loaded HMSIW resonator. A) Simulation schematic, B) simulation results, and C) the equivalent circuit model.

The microfabrication process is the same shown in Figure 7-27 where the SGW3 glass wafer with a thickness of 130 μm and diameters of 80 μm diameter is used. The SEM

micrograph of the fabricated dual-band resonator for the 18 GHz band has been shown Figure 7-33.

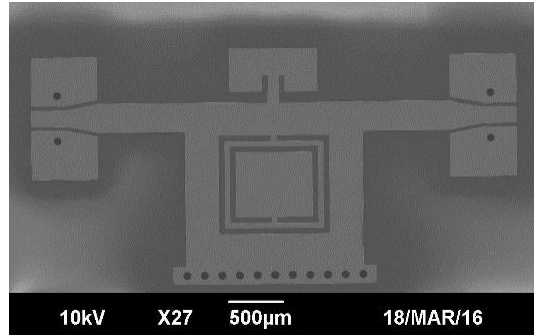


Figure 7-33. The SEM micrograph of the fabricated dual-band resonator for 18 GHz band.

Figure 7-34 shows the measurement results comparison of the insertion loss of the dual-band resonator made of Cu and Cu/NiFe conductors. The resonator made of the reference copper conductor experience almost no shift in the 12 GHz frequency band; although a small frequency shift is observed at 19 GHz band. Figure 7-34B and Figure 7-34C show the insertion loss comparison of the resonator made of reference Cu, Cu/NiFe and simulation results of the reference Cu. At 12 GHz band, a 0.5 dB improvement over reference Cu conductor is achieved mainly attributed to the thickness of the fabricated reference Cu which is 2 μm . This is because at lower frequency bands such as 12 GHz compared to 19 GHz, the skin depth of Cu is relatively lower (Table 5-1) and as a result, the higher thickness of Cu, 4 μm compared to 2 μm , will more improve the insertion loss. However, in 19 GHz band, 2 μm Cu is already 5 times of the skin depth and will capture almost all of the current. A 0.3 dB improvement in the insertion loss of the second band at 19 GHz occurs in result of using a Cu/NiFe conductor instead of a solid Cu conductor. Table 7-5 tabulates the summary of insertion loss values for the passive resonators and bandpass filters using Cu/NiFe and reference Cu conductors. As expected from extracted ohmic resistance of the transmission lines which were given in Chapter 4, at 18 GHz and 19 GHz bands, maximum loss improvement from the devices made of Cu/NiFe is achieved.

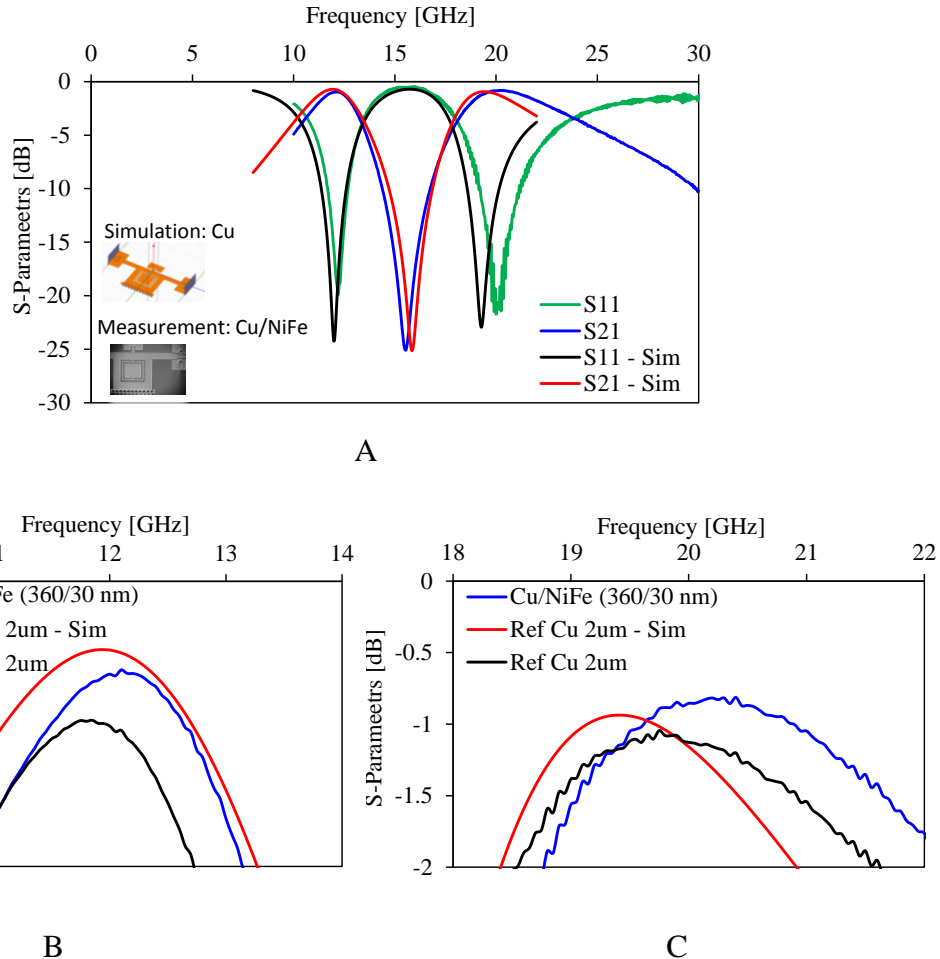


Figure 7-34. The measurement results of the dual-band resonator for 12 and 19 GHz band. A) The comparison of the simulation and measurement results of the designed resonator, B) the comparison of the insertion loss at 12 GHz band, C) the comparison of the insertion loss at 19 GHz band.

Further research is going on to find ferromagnetic materials with higher ferromagnetic resonance frequency that can improve insertion loss of the devices in higher frequencies.

Table 7-5. The summary of insertion loss values for the passive resonators and bandpass filters using Cu/NiFe and reference Cu conductors.

Frequency	Device	IL Cu/NiFe [dB]	IL Ref. Cu [dB]	IL Improvement [dB]
18 GHz	Resonator	0.51	0.73	0.22
	Passband filter	1.4	1.03	0.37
19 GHz	Resonator	0.81	1.04	0.23
	Passband filter	-	-	-
25 GHz	Resonator	0.82	0.94	0.12
	Passband filter	-	-	-

Summary

In this Chapter, a packaging scheme is proposed to reduce the total RF loss of the system by utilizing a high performance glass substrate in K-band, low loss conductors, and monolithic integration of off-chip RF passive components and on-chip integrated devices all on a glass interposer substrate.

The potential application of the glass interposer substrates to be used as the hosting medium for RF passive components is presented and experimentally verified. Glass characterization to extract the dielectric constant and tangent loss is performed using ring resonators and the resulting data is used to design resonators and bandpass filters in several frequency bands including the ISM 2.4 GHz, 5.8 GHz, and K-band of 18 GHz and 25 GHz bands. A resonator based on a complementary split ring resonator (CSRR) patterned on the top surface of the substrate-integrated waveguide (SIW) is designed and fabricated. Also, two-pole bandpass filters using CSRR structures are designed and fabricated using glass as the hosting medium and TGV's as the sidewall of SIW. While pure electroplated Cu is used for 2.4 GHz and 5.8 GHz devices, Cu/NiFe multi-layer conductors are used to suppress the conductor loss in K-band and to maximize the performance of the system. The measurement results show up to 0.3 dB improvement comparing the devices made of solid Cu and proposed Cu/NiFe conductors.

CHAPTER 8 CONCLUSIONS

In this work, passive component technologies are proposed for improving the overall performance of radio frequency (RF) circuits and systems using micro/nano machining. The main RF loss sources limiting the performance of passive components include the dielectric loss, the conductor loss, and the substrates loss. The main motivation is to develop solutions, suppressing all RF loss sources, for realization and integration of high performance passive components, typically occupying large on-chip area, including inductors, resonators, and band-pass filters, compatible with standard MEMS manufacturing processes, towards improving the More-than-Moore's law.

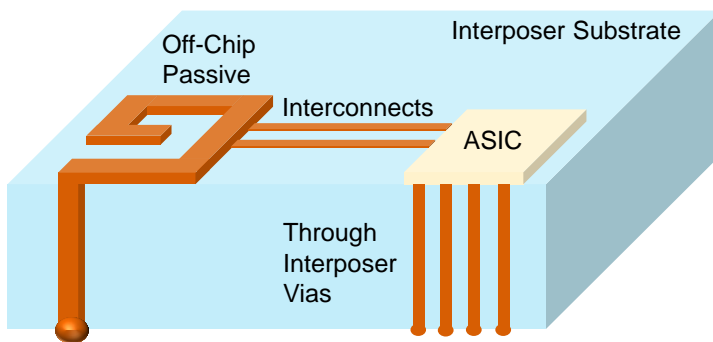


Figure 8-1. The proposed passive component technologies for implementation of high performance RF circuits and systems.

Figure 8-1 shows a summary of the passive component technologies which are used in this work. The application specific integrated circuit (ASIC) chips, using silicon as the substrate, are proposed to be implemented off-chip, allowing the implementation of other required passive components in a customized high performance platform. A glass interposer technology is used as the hosting medium incorporating all the required components of the RF systems, such as active and passive parts, with a high level of integration avoiding the wirebonding for ASICs and reduced RC delays for interconnects.

To realize a high performance system in Figure 8-1, low loss conductors in microwave regime to be used as the actual conductor for RF passives and as high performance interconnects are proposed. Also, a high performance glass substrate and through interposer via (TIV) technology is used. The RF passives implementation are explored embedded inside glass, using glass as the structural material, and also fabricated using a MEMS technology on top of the glass.

Firstly, the low loss conductor architectures including the cylindrical radial superlattice (CRS) and the planar multi-layer conductors are proposed for RF conductor loss reduction. The design, characterization, and experimental results of the passive components including transmission lines and inductors are then demonstrated. Device fabrication and RF characterization have been performed with an air-lifted inductor made of the CRS conductor using electroplated Cu/Ni₈₀Fe₂₀. The conductor loss reduction is clearly observed in the designed Ku-band frequencies. For the planar-type devices, the effects of the width and thickness of the Cu/Ni superlattice conductors have been studied for more effective eddy current cancelling. Pure Ni has been used as an appropriate ferromagnetic material to realize high performance multi-layer superlattice CPW transmission lines.

The design and fabrication of high performance resonators and bandpass filters is considered as they typically are required to be fabricated off-chip and most RF front-end systems require compact size and low insertion loss filters. A hybrid micromachining technique is exploited for the fabrication of passive resonators and bandpass filters operating in 25 GHz using LCP as the structural dielectric material. The broadband filters are realized using QMSIW cavities where extra size reduction is achieved using metamaterial-inspired structures where the results of two-pole and three-pole filters is demonstrated. Also, the 60 GHz frequency which is considered as a potential band for implementation of next generation RF systems with high data

transfer rates is selected for implementation of broadband bandpass filters. BCB is used as a high performance dielectric material suitable for 60 GHz implementation which is photo-sensitive and could be gone over standard microfabrication processes. Two-pole and three-pole filters with smaller than 2 dB insertion loss and 10% FBW are demonstrated.

At last, the integration of the proposed passive components, fabricated off-chip, and on-chip active components is considered as the final research task to be addressed. For that, glass interposer substrates are considered as the low loss packaging solution for high system integration and miniaturization. Characterization of glass interposer substrates using G-CPW fed ring resonators up to 50 GHz are studied. The characterization data are then utilized for design and implementation of low loss components including the CSRR-embedded resonators and bandpass filters for two common ISM bands of 2.4 GHz and 5.8 GHz. For higher frequency bands, such as K-band, the RF resonators and bandpass filters using glass substrates and the low loss conductors are reported where an improved insertion loss is achieved compared to devices using reference solid conductors.

Future research plans for this dissertation are listed as follows,

1. Air-lifted architectures to achieve minimum amount of loss with no dielectric loss:

One of the future research goals in the area of RF loss suppression is to design and realize air-lifted architectures to completely suppress the dielectric loss. A thick polymer processing will be required to initially build the devices on top of that and releasing air-lifted structures by selectively removing dielectric material. For that purpose, SU-8 photoresist from Microchem is considered where coating and lithography up to mm-thick range is feasible. The soft-baking process of the SU-8 will be performed followed by the standard lithography steps with selective exposure. The metallization of the top layer is then performed prior to the development step. The

devices will then release by development of the SU-8 layers and final measurement results will be performed.

2. The implementation of low loss TGV's:

Through glass via (TGV) is an important component in highly integrated systems where interposer technology is utilized as a preferred method of packaging. In this work, TGV's with solid conductors have been used which will have a limited performance in high frequencies due to skin effect. However, implementation of high performance TGV's with improved conductor loss in high frequencies is highly demanded [64]. Because vias are vertical components, deposition of nano layers on the vertical walls of the TGV's is of great challenge.

Electrodeposition method is a preferred method for uniform deposition of metal layers; however, the uniformity of this method as well as the minimum achievable thickness might limit the overall performance. The other alternative is to use super-thin glass wafers and use a PVD method with high uniformity for deposition of nano layers.

3. The ultra-compact passive components using multi-layer MEMS design:

The fabrication of the proposed ultra-compact resonators and bandpass filters in Chapter 7 is currently under progress. The glass interposer substrates with fabricated TGV's and double side metallization are already processed and the fabricated substrates need to be gone over the back-side BCB coating and lithography. The final fabrication and experimental results are left as a future work and will be performed in near future.

LIST OF REFERENCES

- [1] “The evolution of a revolution”, an overview of Intel processor history, <http://www.intel.com/pressroom/kits/quickreffeam.htm>.
- [2] Andrews, Jeffrey G., et al, “What will 5G be?” *IEEE Journal on Selected Areas in Communications*, Vol. 32, No. 6, pp. 1065-1082, Jun. 2014.
- [3] B. Rejaei and M. Vroubel, “Suppression of skin effect in metal/ferromagnet superlattice conductors,” *Journal of Applied Physics*, 96.11 (2004): 6863-6868.
- [4] J. B. Youssef, N. Vukadinovic, D. Billet, and M. Labrune, “Thickness-dependent magnetic excitations in permalloy films with nonuniform magnetization,” *Phys. Rev. B*, 69, 174402 (2004).
- [5] Y. Liu, L. F. Chen, C. Y. Tan, H. J. Liu, and C. K. Ong, “Broadband complex permeability characterization of magnetic thin films using shorted microstrip transmission-line perturbation,” *Rev. Sci. Instruments*, 76, 063911 (2005).
- [6] S. H. Hall, G. W. Hall, and J. A. McCall, “High-speed digital system design: a handbook of interconnect theory and design practices,” New York: Wiley, 2000.
- [7] N. P. Pham, P. M. Sarro, K. T. Ng, and J. N. Burghartz, “IC-compatible two-level bulk micromachining process module for RF silicon technology,” *IEEE Transactions on Electron Devices*, vol. 48 no.8, pp. 1756-1764, Aug. 2001.
- [8] M. Rais-Zadeh, J. Laskar, and F. Ayazi, “High performance inductors on CMOS-grade trenched silicon substrate,” *IEEE Transactions on Components and Packaging Technologies*, vol. 31, no. 00, pp. 126-134, 2008.
- [9] N. Sato, E. Yasushi, and M. Yamaguchi “Skin effect suppression for Cu/CoZrNb multilayered inductor,” *Journal of Applied Physics*, 111, 07A501, Feb. 2012.
- [10] I. Iramnaaz, et al., “High quality integrated inductors based on multilayered semiconductors,” *IEEE Micro. & Wireless Comp. Letters*, vol. 22, no. 7, pp. 345-347, Jul. 2012.
- [11] Y. Zhuang, B. Rejaei, H. Schellevis, M. Vroubel, and J.N. Burghartz, “Magnetic-multilayered interconnects featuring skin effect suppression,” *IEEE Electron Device Letters*, vol. 29, no. 4, pp. 319-321, Apr. 2008.
- [12] M. Yamaguchi, N. Sato, and Y. Endo, “Skin effect suppression in multilayer thin-film spiral inductor taking advantage of negative permeability of magnetic film beyond FMR frequency,” *Proc. of the 40th European Microwave Conference*, 2010.
- [13] A. Rahimi, J. Wu, X. Cheng, and Y.K. Yoon, “Cylindrical radial superlattice conductors for low loss microwave components,” *Journal of Applied Physics*, 117.10 (2015): 103911.

- [14] A. Rahimi and Y.K. Yoon, "Study on Cu/Ni nano superlattice conductors for reduced RF loss," *IEEE Microwave and Wireless Components Letters*, Mar. 2016.
- [15] A. Rahimi and Y.K. Yoon, "High-Q K-band integrated inductors using Cu/Ni nano-superlattice conductors," *Proc. of IEEE/MTT-S International Microwave Symposium (IMS)*, Phoenix, AZ, May 2015.
- [16] Y. Gao, et al. "Significantly enhanced inductance and quality factor of GHz integrated magnetic solenoid inductors with FeGaB/Al₂O₃ multilayer films," *IEEE Trans. Electron Devices*, vol. 61, no. 5, pp. 1470-1476, May 2014.
- [17] Y.K. Yoon, J.W. Park, and M. G. Allen, "Polymer-core conductor approaches for RF MEMS," *IEEE J. of Microelectromechanical Systems*, vol. 15, no. 5, pp. 886-894, October 2005.
- [18] B. Pan, Y. Li, M. M. Tentzeris, and J. Papapolymerou, "A novel low-loss integrated 60 GHz cavity filter with source-load coupling using surface micromachining technology," *Microwave Symposium Digest, IEEE MTT-S International*, pp.639-642, Jun. 2008.
- [19] M. Rais-Zadeh, P.A. Kohl, and F. Ayazi, "MEMS switched tunable inductors," *IEEE J. of Microelectromechanical Systems*, vol. 17, no. 1, pp. 78-84, February 2008.
- [20] D. E. Senior, X. Cheng, and Y.K. Yoon, "Highly compact surface micromachined metamaterial circuits using multilayers of low-loss Benzocyclobutene for microwave and millimeter wave applications," *IEEE Electronic Components and Technology Conference (ECTC)*, pp. 2062-2069, Jun. 2012.
- [21] D. E. Senior, A. Rahimi, and Y.K. Yoon, "A surface micromachined broadband millimeter wave filter using quarter mode substrate integrated waveguide loaded with complementary split ring resonator," *IEEE/MTT-S International Microwave Symposium (IMS)*, Tampa, FL, Jun. 2014.
- [22] J. G. Kassakian, M. F. Schlecht, and G. C. Verghese, "Principles of power electronics, chapter 20, pp. 566–567, Addison-Wesley, Reading, MA, 1991.
- [23] G. Grandi, M. K. Kazimierczuk, A. Massarini, U. Reggiani, and G. Sancinetto, "Model of laminated iron-core inductors for high frequencies," *IEEE Trans. Magn.*, vol. 40, no. 4, pp. 1839–1845, Jul. 2004.
- [24] M. Izaki, "Electrodeposition of iron and iron alloys," *Modern Electroplating* 4 (2011): 461-481.
- [25] M. Chen, C. C. L. Chien, and P. C. Searson, "Potential modulated multilayer deposition of multisegment Cu/Ni nanowires with tunable magnetic properties," *Chemistry of materials* 18.6 (2006): 1595-1601.

- [26] Y. Gao et al, “Significantly enhanced inductance and quality factor of GHz integrated magnetic solenoid inductors with FeGaB/Al₂O₃ multilayer films, *IEEE Trans. Electron Devices*, vol. 61, no. 5, pp. 1470-1476, 2014.
- [27] J. O. Kim, et al, “Nanolaminated permalloy core for high-flux, high-frequency ultracompact power conversion,” *IEEE Transactions on Power Electronics*, 28.9, pp. 4376-4383, 2013.
- [28] O. Zorlu, P. Kejik, and R. S. Popovic, “An orthogonal fluxgate-type magnetic microsensor with electroplated permalloy core,” *Sensors and Actuators A: Physical* 135.1, pp. 43-49, 2007.
- [29] P. Chen et al, “Ultrathin broadband microwave absorbers using ferromagnetic films,” *Journal of Magnetism and Magnetic Materials* 349, pp. 259-263, 2014.
- [30] W. Hao, et al, “Improved high frequency response and quality factor of on-chip ferromagnetic thin film inductors by laminating and patterning Co-Zr-Ta-B films,” *IEEE Transactions on Magnetics*, 49.7, pp. 4176-4179, 2013.
- [31] U. Shah, et al., “Permeability enhancement by multilayer ferromagnetic composites for magnetic-core on-chip inductors,” *IEEE Microwave and Wireless Components Letters*, 24.10, pp. 677-679, 2014.
- [32] C. Kittel, “Ferromagnetic resonance,” *J. Phys. Radium*, 12 (3), pp. 291-302, 1951.
- [33] J. Walowski, “Non-Local/Local Gilbert Damping in Nickel and Permalloy Thin Films,” *Ph.D. thesis, University of Gottingen*, 2007.
- [34] The technical datasheet of BX8X84 NdFeB permanent magnet (found in www.kjmagnetics.com).
- [35] The technical datasheet of SU-8 product from Microchem (found in www.microchem.com/Prod-SU8_KMPR.htm).
- [36] D. E. Senior, “Advanced Metamaterial circuits for microwave and millimeter wave applications,” *A Ph.D. thesis, University of Florida*, 2012.
- [37] W. D. Callister, D. G. Rethwisch, “Materials Science and Engineering - An Introduction,” *John Wiley & Sons*, 2010.
- [38] D. E. Senior, A. Rahimi, P. Jao, and Y.K. Yoon, “Flexible liquid crystal polymer based complementary split ring resonator loaded quarter mode substrate integrated waveguide filters for compact and wearable broadband RF applications,” *IEEE 64th Electronic Components and Technology Conf. (ECTC)*, Lake Buena Vista, FL, May 2014.
- [39] J. P. Godschalk, D. R. Romer, Y.-H. So, Z. Lysenko, Z et al, *U.S. Patent 5,965,679*, 1999.
- [40] Liu, M. B. U.S. Patent 4,822,930, 1990.

- [41] A. Alomainy, A. Sani, A. Rahman, J.G. Santas, J.G., H. Yang, "Transient characteristics of wearable antennas and radio propagation channels for ultra-wideband body-centric wireless communications," *IEEE Trans. on Antennas and Propagation*, vol.57, no.4, pp.875,884, Apr. 2009.
- [42] D. C. Thompson, O. Tantot, H. Jallageas, G. E. Ponchak, M. M. Tentzeris, and J. Papapolymerou, "Characterization of liquid crystal polymer (LCP) material and transmission lines on LCP substrates from 30–110 GHz," *IEEE Trans. Microw. Theory Tech.*, vol. 52, no. 4, pp. 1343–1352, Apr. 2004.
- [43] S. Pinel, M. Davis, V. Sundaram, K. Lim, J. Laskar, G. White, and R. Tummala, "High Q passives on liquid crystal polymer substrates and _BGA technology for 3D integrated RF front-end module," *IEICE Trans. Electron*, vol. E86-C, no. 8, pp. 1584–1592, Aug. 2003.
- [44] D. E. Senior, A. Rahimi, and Y.K. Yoon, "Millimeter-wave bandpass filter on LCP using CSRR-loaded triangular-shape quarter-mode substrate integrated waveguide," *Microwave and Optical Technology Letters*, vol. 57 no. 8, pp. 1782-1784, Aug. 2015.
- [45] S. Hwangbo, A. Rahimi, C. Kim, HY Yang, YK Yoon, "Through glass via (TGV) disc loaded monopole antennas for millimeter-wave wireless interposer communication," *Proc. of Elec. Comp. and Technology Conf. (ECTC) 2015*, San Diego, CA, May 2015.
- [46] D. V. Sukumaran, T. Bandyopadhyay, Q. Chen, N. Kumbhat, F. Liu, R. Pucha, Y. Sato, M. Watanabe, K. Kitaoka, M. ono, Y. Suzuki, C. Karoui, C. Nopper, M. Swaminathan, V. Suzuki and R. Tummala, "Design, fabrication and characterization of low-cost glass interposers with fin-pitch through-package-vias," *Proc. of 61st Electron. Compon. Technol. Conf. (ECTC)*, Lake Buena Vista, FL, May 31-June 3, 2011.
- [47] A. Rahimi and Y.K. Yoon, "Low loss conductors for CMOS and through glass/silicon via (TGV/TSV) structures using eddy current cancelling superlattice structure," *IEEE 64th Electronic Components and Technology Conf. (ECTC)*, Lake Buena Vista, FL, May 2014.
- [48] A. Rahimi and Y.K. Yoon, "High Quality Ku band inductor using cylindrical radial superlattice conductor and air-lifted architecture," *IEEE Antennas and Propagation Society International Symposium (APSURSI)*, pp. 627-628, Memphis, TN, Jul. 2014.
- [49] J. M. Yook, D. Kim and J. C. Kim, "High Performance IPDs (Integrated Passive Devices) and TGV (Through Glass Via) interposer technology using the photosensitive glass," *Proc. of 64th Electron. Compon. Technol. Conf. (ECTC)*, Lake Buena Vista, FL, May 2014.
- [50] T. Dunn, C. Lee, M. Tronolone, and A. Shorey, "Metrology for characterization of wafer thickness uniformity during 3D-IC processing," *Courtesy of Corning Incorporated*, available online at: www.corning.com/semitrans.
- [51] A. Rahimi and Y.K. Yoon, "Integrated low loss RF passive components based on glass interposer technology," *Proc. of Elec. Comp. and Technology Conf. (ECTC) 2015*, San Diego, CA, May 2015.

- [52] P. A. Bernard and J. M. Gautray, "Measurement of dielectric constant using a microstrip ring resonator," *IEEE Trans. Microw. Theory Tech.*, vol. 39, no. 3, pp. 592-595, Mar. 1991.
- [53] C. Kim and Y.K. Yoon, "High frequency characterization and analytical modeling of through glass via (tgv) for 3d thin-film interposer and MEMS packaging," *Proc. of 63rd Electron. Compon. Technol. Conf. (ECTC)*, Las Vegas, NV, May 28-31, 2013.
- [54] K. Chang and L-H. Hsieh, *Microwave Ring Circuits and Related Structures*, 2nd ed., *John Wiley & Sons*, 2004.
- [55] E.O. Hammerstad and F. Bekkadal, Microstrip handbook, ELAB report, *The University of Trondheim*, pp. 3-8, Feb. 1975.
- [56] S.P. Morgan, "Effects of Surface roughness on eddy current losses at microwave frequencies", *J. Appl. Phys.*, vol. 20, pp.352-362, 1949.
- [57] D. Deslandes, and K. Wu, "Single-substrate integration technique of planar circuits and waveguide components," *IEEE Trans. Microwave Theory Tech.*, Vol. 51, pp. 593-596, Feb. 2003.
- [58] Y. Wang, et al. "Half mode substrate integrated waveguide (HMSIW) bandpass filter," *IEEE Microwave and Wireless Components Letters*, 17.4 (2007): 265-267..
- [59] Z. Zhang, N. Yang and K. Wu, "5-GHz bandpass filter demonstration using quarter-mode substrate integrated waveguide cavity for wireless systems," *Proc. IEEE Radio and Wireless Sym.*, pp.95-98, Jan. 2009.
- [60] Y. Dong, T. Yang, and T. Itoh, "Substrate integrated waveguide loaded by complementary split-ring resonators and its applications to miniaturized waveguide filters," *IEEE Trans. Microw. Theory Tech.*, vol. 57, no. 9, pp. 2211-2223, Aug. 2009.
- [61] J. S. Hong and M. J. Lancaster, "Microstrip Filters for RF/Microwave Applications," New York: Wiley, 2001.
- [62] S. Zhang, T. Bian, Y. Zhai, W. Liu, G. Yang, and F. Liu, "Quarter substrate integrated waveguide resonator applied to fractal-shaped BPFs," *Microw. Journal*, vol. 55, no. 5, pp. 200-208, May 2012.
- [63] C. Kim, D. E. Senior, A. Shorey, H.J. Kim, W. Thomas, and Y.K. Yoon, "Through-glass interposer integrated high quality RF components," *Proc. of Elec. Comp. and Technology Conf. (ECTC) 2014*, Lake Buena Vista, FL, May 2014.
- [64] A. Rahimi and Y.K. Yoon, "Low ohmic loss cylindrical radial superlattice conductors using alternatingly electroplated magnetic/nonmagnetic thin films for microwave applications, *Proc. of Solid-State Sensors, Actuators and Microsystems Workshop*, pp. 335-338, Hilton Head, SC, Jun. 2014.

BIOGRAPHICAL SKETCH

Arian Rahimi was born in Tehran, Iran in 1986. He received the B.S. degree from Shahid Beheshti University (SBU), Tehran, Iran in 2008, the M.S. degree from Middle East Technical University (METU), Ankara, Turkey in 2011, and is currently working towards the Ph.D. degree in University of Florida, Gainesville, FL, USA, all in electrical engineering. His research interests include the design of microelectromechanical systems (MEMS) and microfabrication technologies, radio frequency (RF) circuits and systems, semiconductors fabrication and testing, and analog and mixed-signal integrated circuits design.

Arian Rahimi is the recipient of several scholarships, fellowships, and awards including the honorable Erasmus Mundus scholarship from the European Union (EU) for supporting his M.S. studies at METU in 2009, and the Intel Corporation scholarship, Middle East Efficient Energy Research (MER), for supporting his Master's thesis project, in 2010. He received two honorable IEEE fellowships including the IEEE Antenna and Propagation Society (AP-S) doctoral research award in 2015, and the IEEE Microwave Theory and Techniques Society (MTT-S) graduate fellowship in 2016. He also received the honorable mention award in the IEEE Antenna and Propagation Symposium (AP-S/URSI), Memphis, TN in 2014, the best paper award finalist in the International Microwave Symposium (IMS), Phoenix, AZ in 2015, and the best paper award finalist in the International Microwave Symposium (IMS), San Francisco, CA in 2016.